Advanced Space Concepts Laboratory
Department of Mechanical and Aerospace Engineering
Faculty of Engineering
University of Strathclyde

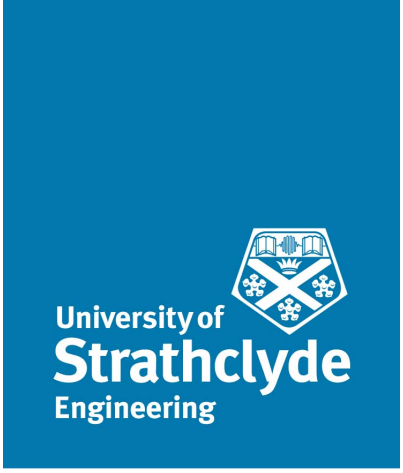

Space Mission Applications of High Area-to-mass-ratio Orbital Dynamics

Charlotte Bewick
formerly Charlotte Lücking

Submitted in fulfilment of the requirements for
the degree of Doctor of Philosophy (PhD)
2013

This thesis is the result of the author's original research. It has been composed by the author and has not been previously submitted for examination which has led to the award of a degree.

Charlotte Bewick

Bremen, Germany, June 2013

Supervisors

First supervisor:

Prof. Colin R. McInnes
Advanced Space Concepts Laboratory, University of Strathclyde
Glasgow, United Kingdom

Second supervisor:

Dr. Camilla Colombo
Astronautics Research Group, University of Southampton
Southampton, United Kingdom

Examiners

External examiner:

Prof. Vaios Lappas
Surrey Space Centre, University of Surrey
Guildford, United Kingdom

Internal examiner:

Dr. Massimiliano Vasile
Advanced Space Concepts Laboratory, University of Strathclyde
Glasgow, United Kingdom

Abstract

High area-to-mass-ratio spacecraft experience a significant perturbation due to surface forces, such as solar radiation pressure and aerodynamic drag. Hence, their orbits do not evolve in the manner of traditional satellites. They undergo strong changes in eccentricity and argument of pericentre due to solar radiation pressure, and in semi-major axis due to aerodynamic drag. These effects can be exploited for a number of applications, providing solutions to existing problems for space mission design.

In this thesis an analytical Hamiltonian model of the orbital evolution of high area-to-mass-ratio objects is used to identify potential mission applications on decreasing length-scale. These applications are then investigated using numerical methods and validated against high-precision orbit propagations.

On the metre-scale, applications for small satellites, of 100 kg mass or less, are developed. Firstly, a passive orbit manœuvre from geostationary transfer orbit to low Earth orbit is investigated. This method has the potential to enable a new range of piggy-back launches for small satellites. Using the same insights, the strategy of solar radiation pressure augmented deorbiting is presented. The deorbiting method can enable passive end-of-life removal from very high altitude orbits.

On the millimetre-scale, an orbit control method for so-called SpaceChips is developed. The method uses electrochromic coatings to allow the SpaceChip to alter its optical properties and thus modulate the perturbation due to solar radiation pressure. Different control algorithms are discussed and evaluated.

Finally, on the micrometre-scale, a dispersion strategy for a planetary dust ring extracted from a captured asteroid is presented. The long-lived dust ring is designed to reduce the solar input to the global climate system and mitigate global warming. *Heliotropic* orbits are used as a means of passively controlling the ring.

> Space is big. You just won't believe how vastly, hugely, mind-bogglingly big it is. I mean, you may think it's a long way down the road to the chemist's, but that's just peanuts to space.

Douglas Adams

Acknowledgements

My first and foremost gratitude goes to my supervisor, Prof. Colin McInnes, who was a fantastic and committed guide throughout my PhD. He taught me most of the skills I needed to produce this body of work and has supported me in all my endeavours, be it conference visits, journal submissions or student projects. Colin, thank you so much for all the time and energy you devoted to helping me become a better researcher and thank you especially for your counsel whenever I was unsure about what path to take.

Secondly, I wish to thank Dr. Camilla Colombo, my second supervisor. Camilla and I have been working closely during these three years. She has so often helped me selflessly with my research, taking time and care to proof-read my outputs and offer valuable suggestions. Camilla, in the last few months of my PhD, when you left Glasgow to your new position in Southampton, you were sorely missed in the office.

After thanking Colin and Camilla in particular, I would now like to express my gratitude to all the researchers in the Advanced Space Concepts Laboratory for providing inspiration at the weekly colloquia and lots of fun in the lunch breaks and pub nights. I will never forget the day Andreas lost his wig!

Next to my research I also worked on StrathSat-R, a student initiative for a microgravity experiment based on my deorbiting work and to be flown on-board a REXUS rocket in 2013. My thanks goes to the other students in this team for all their hard work and all the fun we had during the different events, and also of course to the institutions which made this experiment possible, the European Space Agency (ESA), the German Space Agency (DLR), the Swedish National Space Board (SNSB) and all the experts who supported us during the development of the project.

A number of institution have supported my research financially and otherwise. I would like to extend my foremost gratitude to the European Research Council (ERC) which funded my PhD through the Advanced Investigator Grant - 227571: VISIONSPACE: Orbital Dynamics at Extremes

of Spacecraft Length-Scale. Secondly I would like to thank the Institution of Engineering and Technology (IET) for the Hudswell International Research Scholarship and the USU/AIAA Conference on Small Satellites for the Frank J. Redd Student Scholarship I received. My gratitude further goes to the British Interplanetary Society (BIS), ESA, the Faculty of Engineering of Strathclyde University and again the IET for the different travel grants I have received and which allowed me to partake in a large range of space conferences. My special thanks goes to the committee of the ESA/CNES Small Satellite Systems and Services (4S) Symposium for granting me the unique opportunity to be part of the technical committee of the 20^{th} 4S Symposium. I would also like to thank the UK Space Agency for funding the UKUBE-2 feasibility study (FRODO and SAM, Mk. 2) from which the work on the passive GTO to LEO transfer presented in this thesis originated. Furthermore, I would like to thank Analytical Graphics, Inc. for kindly supplying a student license of STK for my research. And finally I wish to express my gratitude to the IAA Symposium on Small Satellites for the recognition in form of the best paper prize I received for my paper on solar radiation pressure augmented deorbiting, the International Astronautical Federation (IAF) for the Gold Medal I received for my paper on the GTO-to-LEO transfer and the Arthur C. Clarke foundation for the space student award I received in 2012.

On a more personal note, I wish to thank my family and friends for morally supporting me throughout my studies. My deepest gratitude goes to one person in particular, my husband. Russell, without you this PhD would have been this much harder and far less fun than it was. I am so glad, we went this path together. Thank you!

Contents

List of Figures

List of Tables

List of Acronyms

ASCL Advanced Space Concepts Laboratory

COTS Commercial-of-the-shelf

CSA Canadian Space Agency

DAD Drag-augmented deorbiting

EDT Electrodynamic tether

EOC Electrochromic orbit control

GEO Geostationary orbit

GNSS Global Navigation Satellite System

GPS Global Positioning System

GTO Geostationary transfer orbit

HAMR High area-to-mass-ratio

HPOP High-precision orbit propagator

IAC International Astronautical Congress

IAF International Astronautical Federation

IADC Inter-Agency Debris Coordination Committee

IPCC Intergovernmental Panel on Climate Change

ISO International Organization for Standardization

IR Infrared

LEO Low Earth orbit

LTAN Local time of the ascending node

MEMS Micro-electromechanical systems

MEO Medium Earth orbit

NASA National Aeronautics and Space Administration

OTM Orbit transfer module

PSZ Potentially stabilisable zone

SBGE Space-based geoengineering

SRM Solar radiation management

SRP Solar radiation pressure

STK Satellite Tool Kit

TRL Technology readiness level

VOP Variation of parameters

Nomenclature

Symbols which appear throughout the thesis are listed in the notation. Other symbols which appear only in a single section will not be listed. Some symbols are double defined. In that case the definition is clarified in the text. If there is no definition in the text, the standard definition in the nomenclature is valid.

a	Semi-major axis [km]
A	Cross-sectional area of the spacecraft [m^2]
a_{SRP}	Acceleration due to solar radiation pressure [$\mathrm{m\,s}^{-2}$]
c	Speed of light in vacuum [$\mathrm{m\,s}^{-1}$]
c_D	Drag coefficient
c_R	Coefficient of reflectivity
e	Eccentricity
E	Eccentric anomaly [rad]
e_0	Equilibrium eccentricity
e_{crit}	Critical eccentricity
f	True anomaly [rad]
$F_\odot$	Solar radiation flux at the position of the spacecraft [$\mathrm{W\,m}^{-2}$]
g_0	Acceleration due to the Earth's gravity on the surface of the Earth [$\mathrm{m\,s}^{-2}$]
h	Altitude over the surface of the Earth [m]
h_p	Perigee altitude [m]
H	Hamiltonian: orbital evolution due to solar radiation pressure and J_2
H_{SRP}	Hamiltonian:orbital evolution due to solar radiation pressure only
i	Orbital inclination [rad]

J_2	Second order gravitational harmonic coefficient
K	Any Keplerian orbital parameter
m	Spacecraft mass [kg]
M	Mean anomaly [rad]
$n_\odot$	Rate of the Earth's orbital motion around the Sun [$\mathrm{rad\,s^{-1}}$]
p	Semilatus rectum [km]
r	Radial distance of the spacecraft to the centre of the Earth [m]
R_E	Radius of the Earth [m]
r_g	Dust grain radius [m]
$_S$	(subscript) Stable orbit
t	Time [s]
T	Period in the phase space [s]
α	Solar radiation pressure parameter
$\alpha_\odot$	Right ascension of the position of the Sun on the Earth's equator with respect to the vernal equinox [rad]
$\delta_\odot$	Declination of the Sun with respect to the Earth's equatorial plane [rad]
δ_g	Density of dust grains [$\mathrm{kg\,m^{-3}}$]
Δv	Accumulated propulsive acceleration of a spacecraft over time [$\mathrm{m\,s^{-1}}$]
γ	Incidence angle of solar radiation on a surface [rad]
κ	J_2 effect parameter
$\lambda_\odot$	Angle between the position of the Sun on the ecliptic and the vernal equinox from Earth [rad]
μ	Standard gravitational parameter of the Earth [$\mathrm{m^3\,s^{-2}}$]
ω	Argument of perigee [rad]
Ω	Right ascension of the orbit's ascending node [rad]
ϕ	Angle between the direction of the Sun and the orbit's perigee vector [rad]
σ	Effective area-to-mass-ratio [$\mathrm{m^2\,kg^{-1}}$]

Chapter 1

Introduction

This thesis originated from the question: *how does orbital dynamics change as spacecraft length-scale shrinks?* As an object gets smaller at constant density, its area-to-mass-ratio, σ, increases. It can be seen that σ is inversely proportional to length-scale, as surface area is proportional to the square of length-scale and the mass or volume is proportional to length-scale cubed. Thus, the length-scale affects all surface forces, *e.g.* solar radiation pressure, aerodynamic drag, solar wind, particle collisions, and thermal emission. Also the Lorentz-force is dependent on length-scale, as the charge-to-mass-ratio depends on surface area and geometry.

The orbital dynamics of high area-to-mass-ratio objects have been studied for a number of applications, most notably planetary and interplanetary dust dynamics, space debris and solar sailing. Two of these applications, dust dynamics and space debris analysis, aim to predict the evolution of passive high area-to-mass-ratio objects under the effect of orbital perturbations. Solar sailing instead actively exploits these effects to achieve low thrust orbit transfers or non-Keplerian orbits.

The approach pursued in this thesis is to find new applications for the perturbed dynamics of high area-to-mass-ratio spacecraft. The thesis is split into three parts, each dealing with a different length-scale regime: from small-satellites to so-called SpaceChips, millimetre-scale satellites on a silicon chip, down to micrometre-scale asteroid dust. Each part contains a number of distinct, novel applications of high area-to-mass-ratio orbital dynamics and answers the following questions:

- How can spacecraft without a propulsion system transfer between orbits or perform an end-of-life manœuvre from high altitude orbits?

- How can SpaceChips control their orbits and perform active manœuves?

- How can dust from a captured asteroid be distributed in an Earth ring to maximise solar shading for climate engineering?

1.1 Orbital dynamics of high area-to-mass-ratio objects

The orbits of high area-to-mass-ratio spacecraft are affected strongly by surface force perturbations. Atchison and Peck [1] analyse the impact of perturbations on objects of different length-scale in different altitude Earth orbits. They identify three regions of length-scale over altitude. For most objects the Earth's oblateness is the most dominant perturbation. However, at small length-scales solar radiation pressure and aerodynamic drag are more dominant. In particular, drag dominates in low Low Earth Orbit while solar radiation pressure dominates above. The orbital dynamics of high area-to-mass-ratio objects have also been studied by the observation of planetary and interplanetary dust. Rings or clouds of dust particles display highly non-Keplerian behaviour due to the influence of orbital perturbations such as solar radiation pressure, aerodynamic drag, Poynting-Robertson drag, and electrostatic forces [2]. The range of forces acting on dust particles has so far not allowed a universal analytical model of their dynamics to be formulated. However, many reduced order models have been published, allowing an analytical investigation of certain aspects of the problem.

For example, the dynamics of dust particles in the interplanetary medium are investigated analytically by Gor'kavyi et al. [3] through the means of the continuity equation written in terms of semi-major axis and eccentricity. Howard et al. [4] analyse the phase space of the motion of positively charged particles in planetary magnetospheres. Grotta-Ragazzo et al. [5] analyse periodic orbits of charged dust grains in planetary rings. The long term effects of solar radiation pressure and planetary oblateness on Mars-orbiting dust particles was investigated by Krivov et al. [6] and expressed in the form of non-singular elements. Hamilton and Krivov [7] then introduced a Hamiltonian that for planar orbits combines solar radiation pressure and the J_2 effect to provide, analytically, the long-term evolution of the orbits of planetary dust grains in the eccentricity and Sun-perigee angle phase space. Krivov and Getino [8] also apply these equations to Earth orbiting balloon satellites and analyse their behaviour with respect to equilibria and bifurcations. This work provides the basis of much of the research presented in this thesis. The work of Hamilton and Krivov [7] and Krivov and Getino [8] is discussed in detail later in Sec. 2.1.1.

Aside from dust dynamics, although there have been investigations directly into the dynamics of high area-to-mass-ratio spacecraft, these remained sparse until recent interest fuelled by the

concept of solar sailing and the problem of space debris. Before this growing interest, work on high area-to-mass-ratio spacecraft stemmed from project Echo, an early experiment with reflective balloon satellites for passive terrestrial communications. Echo-1A (1960) and Echo-2 (1964) were large passive aluminium spheres with area-to-mass-ratios of $9.6\,\mathrm{m^2\,kg^{-1}}$ and $5.2\,\mathrm{m^2\,kg^{-1}}$ respectively [9]. They were intended to passively reflect communication signals. It was discovered that a periodic change in their orbital eccentricity occurred that could only be explained with the effects of solar radiation pressure [10]. A further early space mission which accidentally served as a study for high area-to-mass-ratio orbital dynamics was Project West Ford [11]. In order to enhance the reflective properties of the ionosphere, and thus to improve long wave radio communications, the Lincoln Laboratory of the Massachusetts Institute of Technology (MIT) launched approximately half a billion copper needles into an Earth orbit on behalf of the US military. The needles had a diameter of tens of micrometres and a length of approximately 2 cm. Their small length-scale caused the needles to be strongly perturbed by solar radiation pressure and drag and thus made a fascinating subject of study for contemporary astrodynamicists [12]. It was expected that the needles would re-enter the atmosphere after a few months. However, as of today there are still clusters of needles in orbit [13].

The study of these dynamics are the foundation of the work presented in this thesis. The Echo Balloons, the West Ford needles, planetary dust and debris collision fragments are strongly perturbed by solar radiation pressure and drag. However, since none of these objects are capable of active control, the utilisation of these dynamics has not been investigated in detail. Solar sailing is the exception. It exploits solar radiation pressure by controlling the attitude of a high area-to-mass-ratio sail with respect to the direction of the Sun [14]. However, in this thesis, other novel ways of utilising high area-to-mass-ratio orbital dynamics are investigated. In the first part of the thesis they are exploited semi-passively, simply by increasing the spacecraft area-to-mass-ratio at some optimum time. In the second part, the control of the optical properties is investigated, as a means of orbit stabilisation and transfer. Finally, for orbital dust, the orbit of dust release is studied, to achieve evenly distributed, long-lived Earth rings. The applications have been sorted by descending length-scale and the thesis is accordingly divided into three parts:

- **Metre-scale** conventional spacecraft with augmented area-to-mass-ratio: This can be achieved by deploying a large light-weight structure, for example a solar sail or deployable balloon. Possible applications discussed in this thesis are passive orbit transfers and deorbiting manœuvres.

- **Millimetre-scale** SpaceChips, are micro-electromechanical systems (MEMS) devices which have a high area-to-mass-ratio due to their small size: In this thesis a method of orbit control using electrochromic coatings to change their optical properties is investigated.

- **Micrometre-scale** planetary dust: the dust grains are perturbed by surface forces due to their naturally high area-to-mass-ratio. They can be extracted from Asteroids or the Moon. In this thesis a method of utilising Asteroid dust for Earth climate engineering is investigated.

In the following sections the three size regimes and the domain of application of high area-to-mass-ratio orbital dynamics are discussed in more detail. The specific contributions of this thesis are then summarised in Sec. 1.5.

1.2 Orbit transfers for small satellites

Small satellites are defined as spacecraft with a mass of less than 1000 kg and further divided into mass categories of mini-, micro-, nano-, pico- and femtosatellites. While the first artificial satellites were by this definition small satellites – Sputnik-1 had a mass of 84 kg [15] – they have been ignored as a useful platform until the 1980s. Currently they are creating significant interest by space agencies, industry and academia [16]. Their capabilities are ever expanding and the number of small satellite launches are increasing year to year. Kramer and Cracknell [17] provide an overview of the history of remote sensing small satellites and the milestones in their development to ever smaller, cheaper and more capable systems.

Table 1.1 lists the small satellite classes with their mass range as given by Kramer and Cracknell [17]. Additionally, some notable examples of small satellites of different classes are given. Galileo is the European global navigation satellite system (GNSS). A constellation of 30 Galileo spacecraft will make up this system, each satellite having a mass of 675 kg [18, Chap. 10]. This makes them minisatellites. Another example for a minisatellite is SMART-1 (370 kg), a European low-thrust Moon orbiter [19].

Femtosatellites, on the other end of the small satellite spectrum, have a mass of less than 100 g and include so-called satellite-on-a-chip systems or SpaceChips. These spacecraft will be discussed in Sec. 1.3.

The most prominent type of very small satellite is the CubeSat. Depending on its structure, it is classed as either a nano- or a picosatellite. CubeSats consist of so-called units or Us, which measure 10 cm cubed and have a mass of approximately 1 kg. The standardisation of CubeSats makes them especially attractive as a template for a very small satellite mission. Their components can be bought cheaply off-the-shelf and compatibility is easily ensured. Furthermore, regular CubeSat launch opportunities are offered by space agencies for educational or scientific missions.

The CubeSat standerd was developed by teams at Stanford University [20] and California Polytechnical State University [21] in the late 1990s. Since then the platform has been steadily gaining popularity.

Both CubeSats and larger minisatellites have been gaining acceptance in the last decades, not as a replacement for conventional large-scale space missions, but as a complement. Verhoeven et al. [25] discuss this under the name of *satellite ecosystems*. The core idea is that, while large satellites have the power and size to deliver data of a high spectral and spatial resolution, small satellites can be used in large numbers and thus supply high temporal resolution. Using both systems together allows the user to track changes in an area which can be imaged more accurately by the large spacecraft and then kept up-to-date by the smaller spacecraft. The low image quality of the latter can be improved using the high resolution data and applying image post-processing with this information. Furthermore, specific niche applications have been identified as more suited to a small satellite constellation than a large space mission. Typically these applications focus on just one payload instrument, which has moderate power, mass, volume and pointing requirements, and profit greatly from increased revisit times. In these cases a small satellite mission would fulfil the payload requirements and is still affordable in a multi-satellite constellation. A good example for this type of application is a maritime surveillance system receiving automatic identification system (AIS) messages from transatlantic ships [26]. Shipping vessels are required to send out AIS signals on an RF frequency that can be received in orbit using a standard VHF antenna.

In general, the main advantages of small satellites are their low cost and short development time. The low cost is partly due to the extensive use of commercial-of-the-shelf (COTS) components which are orders of magnitude cheaper than built-to-purpose parts in exchange for being less reliable. The capability of small satellite COTS components are constantly increasing because of the immense progress that has been made in the field of technology miniaturisation fuelled by the terrestrial market of mobile computing devices. These technologies have then been adapted for use in space allowing powerful computation and communications in a small and low-cost system.

Table 1.1: Small satellite classification by mass as defined by Kramer and Cracknell [17]

Satellite class	Mass range	Notable examples
Minisatellite	$100 - 1000\,\mathrm{kg}$	Galileo ($675\,\mathrm{kg}$) [18], SMART-1 ($370\,\mathrm{kg}$) [19]
Microsatellite	$10 - 100\,\mathrm{kg}$	Sputnik ($84\,\mathrm{kg}$) [15]
Nanosatellite	$1 - 10\,\mathrm{kg}$	Multi-U CubeSats: e.g. UKUBE-1 ($4\,\mathrm{kg}$) [22]
Picosatellite	$0.1 - 1\,\mathrm{kg}$	1U CubeSat ($1\,\mathrm{kg}$) [20]
Femtosatellite	$< 0.1\,\mathrm{kg}$	Satellite-on-a-chip ($0.015\,\mathrm{kg} \sim 0.055\,\mathrm{kg}$) [23], Sprite ($8 \times 10^{-6}\,\mathrm{kg}$) [24]

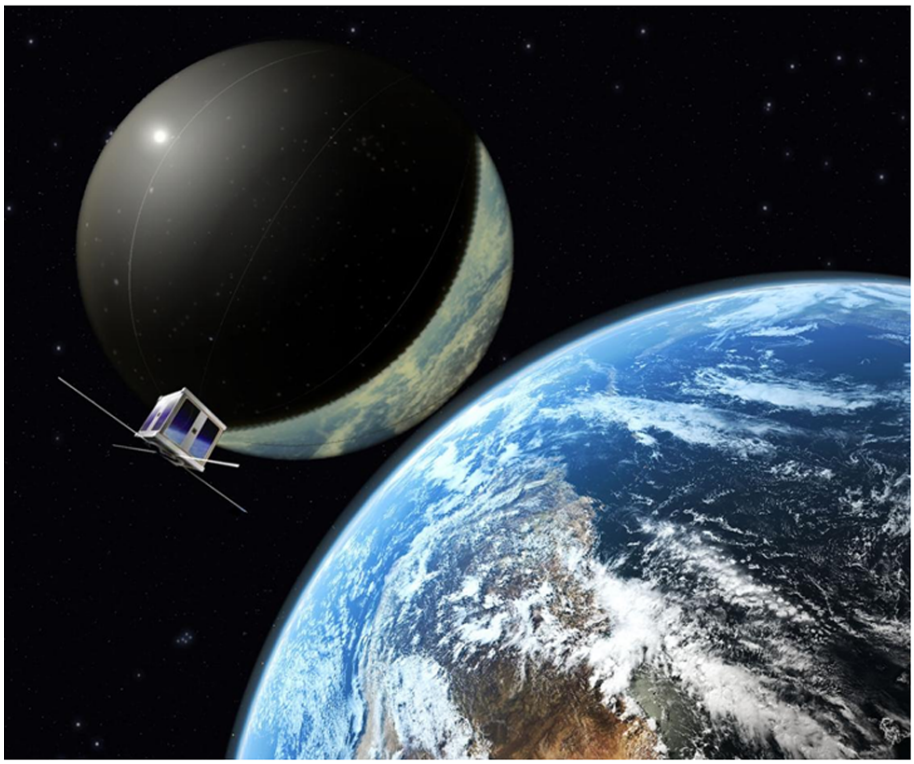

Figure 1.1: Artist's impression of a CubeSat with inflatable balloon (Image material: ESA, Clyde Space)

Another factor reducing the cost of small satellites is the availability of piggy-back launches. This is a type of shared launch in which the main payload has full choice over insertion orbit while the small satellite is launched for less than its relative mass share of the total launch cost. For CubeSats the standardised launcher interface and dispenser, P-POD, can be used [21]. Space Agencies occasionally even offer free CubeSat launches to public educational or research institutions. The very low cost of small satellite missions make them feasible for small companies, universities and research institutes, for which the cost of a conventional spacecraft mission is likely prohibitive. In the past decades a number of small satellite start-ups and university spin-off companies have been founded, fuelling the growing market with innovative new technology and applications.

Two problems facing these systems are approached in this thesis: the transfer to Low Earth Orbit (LEO) for spacecraft launched to geostationary transfer orbit (GTO) and end-of-life deorbiting from high altitude orbits. It is shown that by artificially increasing the area-to-mass-ratio using an inflatable balloon (see Fig. 1.1) or deployable sail, the effects of solar radiation pressure, J_2 and aerodynamic drag can be exploited passively to perform these orbit transfers. The use of solar radiation pressure for deorbiting has previously been studied as an active technique in which the attitude of the spacecraft with respect to the Sun is changed twice per orbit to maximise the altitude loss [27]. The method presented in this thesis differs significantly from this approach as

it is entirely passive and designed to increase the orbit eccentricity instead of decreasing the orbit semi-major axis.

1.2.1 GTO to LEO transfer

The main operational regime for CubeSats is LEO. This is due to their limited communications capability, caused by low transmitter power and low-gain antennae, and also their deorbit requirements forcing them into naturally decaying orbits [28]. With the increasing interest in CubeSat missions, demand for piggy-back launches to LEO is exceeding availability [29]. In order to tap into the many GTO launches, a strategy is therefore needed to transfer CubeSats from GTO to LEO. The transfer needs to be passive due to the absence of a propulsion subsystem. Instead, orbital perturbations will be exploited which do not require active manœuvring.

Fleeter et al. [30] have suggested transfers from GTO to LEO using aerodynamic drag and a final propulsive manœuvre. In their design a spacecraft would deploy a drag brake to lower the orbit apogee. Once the apogee is at the desired orbital altitude, a propulsive perigee raising manœuvre is performed to insert into a circular LEO. The perigee raising manœuvre is necessary, as without it the final altitude would be too low for normal operations (below 300 km). This is disadvantageous for CubeSats which would otherwise not need a propulsion subsystem. A propulsion subsystem is complex and costly, while small satellites tend to be low-cost and simple [31].

The new method used in this thesis is a solar radiation pressure augmented, passive GTO to LEO transfer, initially discussed by Colombo and McInnes [32]. It exploits the effect of solar radiation pressure to raise the orbit perigee while simultaneously using aerodynamic drag for apogee lowering. This novel concept is investigated in Chapter 3.

1.2.2 Deorbiting of small satellites

Space debris consists of in-operational satellites, disused rocket upper stages and in-orbit collision fragments. Collisions between debris objects creates more fragments, potentially causing a collisional cascade. This is known as the Kessler Syndrome after Donald J. Kessler who investigated this phenomenon in the 1970s [33]. In order to reduce the amount of new debris created, the Inter-agency space debris coordination committee (IADC) issued guidelines which require a spacecraft to be removed from its orbit within 25 years after the end of operations [34]. In 2007 the International Organization for Standardization (ISO) started adapting these guidelines into an ISO standard which was issued in 2010 [35]. As common with ISO standards, the requirements

are not mandatory, however, they do provide a baseline for the adaptation of stricter control by different national space agencies.

Larger spacecraft usually employ propulsion for the end-of-life manœuvres [36]. This is not an attractive option for small spacecraft for two reasons. Firstly, it requires active orbit and attitude control which is not usually integrated into very small satellites. Secondly, deorbiting has inherently high reliability demands. The ISO standard requires a 90 % chance of successful deorbit within the given time frame [35]. For propulsive manœuvres, the reliability of the deorbiting system depends on the integrity of many other subsystems at the end-of-life. Both issues will increase the costs of the system and go against the small satellite philosophy of low-cost spacecraft. Therefore, a simple fail-safe passive deorbiting system is needed which initiates the deorbit manœuvre automatically when the satellite fails, thus guaranteeing a deorbit in every failure mode.

Passive deorbiting technologies which have previously been investigated make use of either aerodynamic or electrodynamic drag forces. They are generally considered a useful alternative for small satellites for the reasons stated before, but are not deemed attractive for larger systems. This is because they cause an uncontrolled deorbit which is not appropriate for large spacecraft, where satellite components can survive the re-entry and impact on the ground [37]. Small satellites will deorbit passively within a reasonable time frame if they are operating at altitudes below approximately 400 km.

Drag augmented deorbiting (DAD) can increase the use of passive deorbiting to altitudes of approximately 800 km. This is achieved by increasing the spacecraft area-to-mass-ratio and thus enhancing the rate of loss of orbital energy due to atmospheric drag. Different DAD devices are being developed or have been proposed. Lappas et al. [38] are currently developing the Gossamer Deorbiter, based on CubeSail, which uses mechanically deployable booms unfolding a flat surface similar to a solar sail. A similar design is used by AEOLDOS, a CubeSat deorbiting device developed by the University of Glasgow and Clyde Space [39]. Instead Roberts and Harkness [40] proposed a conical device to exploit the shuttle-cock effect for attitude stabilisation, which occurs when an offset of centre-of-pressure and centre-of-mass create a stable equilibrium attitude. Maessen et al. [41] proposed a system which exploits the same effect, but consists of a an inflatable pyramid. Nock et al. [42] have developed the GOLD system, an inflatable balloon which has the advantage of being effective in any attitude. Andrews et al. [43] have investigated CubeSat re-entry and presented a tension-cone design which also acts as a heat shield to allow recovery of the CubeSat on ground.

Electrodynamic Tethers (EDT) are an alternative method for propellant-less deorbit. The movement of the EDT through the Earth's magnetic field induces a current in the tether. The

current results in a Lorentz force, which then alters the orbital energy over time. Both effects decrease rapidly with increasing distance from the Earth. A detailed study of the method was performed by Iess et al. [44, 45]. Since EDTs are dependent on the Earth's magnetic field, they are sensitive to initial orbital inclination. They work best in equatorial orbits and decrease in efficiency with increasing inclination and are inefficient for high altitude orbits above 74° inclination, as shown by Pardini et al. [46]. The Terminator Tether is a commercial product developed by Tethers Unlimited to make use of these principles [47].

While either of these methods, DAD or EDT, are applicable for lower altitudes they both rapidly lose efficiency as altitude is increased. This is due to the fact that both the atmospheric density and the magnetic field strength decrease dramatically with altitude. In this thesis two orbital regimes are investigated in which, as of today, no universal deorbiting solution exists for small satellites: medium Earth Orbit (MEO) in Chapter 4 and high altitude Sun-synchronous orbits (SSO) in Chapter 5. These regimes have an area of intersection but are treated individually.

Medium Earth Orbit

Medium Earth Orbit (MEO) is defined as a regime of orbits with altitudes between Low Earth Orbit (LEO) and the geostationary ring. This means the regime between 2000 km and 35 586 km altitude. In this section only orbits which lie entirely in the MEO region are considered, i.e. all orbits with a perigee altitude above 2000 km and an apogee altitude of less than 35 586 km, the upper boundary of LEO and lower boundary of GEO respectively. There are 546 NORAD tracked objects in the CelesTrak database which fulfil these requirements [48]. Just 12 of them have meanwhile decayed. All others are still in their orbits, although only 56 are categorised as operational. In the population of MEO six distinctive groups of spacecraft can be identified which make up 85 % of the total MEO spacecraft population:

- GLONASS, the Russian satellite navigation system can be found in circular orbits just below 20 000 km altitude [49].

- NavStar, the American GPS satellites occupy circular orbits with altitudes just above 20 000 km [50, 49].

- The Initial Defence Satellite Communications System (IDSCS) was the precursor constellation to the American Defence Satellite Communications System (DSCS). Twenty-six spacecraft were launched into circular orbits below GEO from 1966 to 1968 [51].

- Oko is the Russian defence constellation for early warning. It was launched over forty years ago into Molniya orbits with 600 km perigee altitude and 63.7° inclination. The Oko spacecraft appearing in this survey have drifted from their orbit, increasing in perigee altitude to now lie entirely within MEO [52].

- Future GNSS constellations: Galileo is the European satellite navigation system and is likely to make up a large part of total MEO launches in future. As of today, only two precursor satellites, GIOVE A and B, and four in-orbit verification (IOV) satellites have been launched. They occupy future Galileo orbits which are circular and inclined at an altitude of 23 222 km. Beidou is the future Chinese satellite navigation constellation in MEO and GEO. One MEO satellite has been launched so far in 2007. Beidou will occupy circular, inclined orbits at 21 500 km altitude [18, Chap. 11].

- The West Ford needle experiment is not strictly a satellite constellation. In the 1960s thousands of small metal needles were launched into high altitude polar orbits in a bid to improve long-range radio communications. Although some of these needles have meanwhile re-entered the atmosphere, large numbers still remain in their orbits as space debris [11, 12].

Figure 1.2 shows the number and type of catalogued launches into MEO per half decade. It can be seen that most of the MEO constellations have been stocked over long periods of time with Galileo and Beidou only just beginning. There was significant interest in MEO in the late 1960s, but satellite navigation constellations have made up the largest part of MEO launches in the last thirty years. The largest number of orbiting objects originated from Project West Ford needles in MEO, in the order of tens of thousands. However, they are not individually tracked. Instead cloud segments consisting of a large number of objects are tracked and appear in the diagram as a single object.

Figure 1.3 shows the inclination and altitude of different object groups with tracked space debris and rocket bodies shown in light grey in the background. The perigee and apogee altitudes of the spacecraft are marked with a filled circle. The eccentricity of a spacecraft's orbit can be seen by the distance between perigee and apogee. While circular orbits appear as just one point, eccentric orbits are long lines connecting the perigee and apogee. It can be seen that the main orbits of interest are circular GNSS-like orbits with altitudes of order 20 000 km and inclinations between 50° and 70° and highly eccentric Molniya-type orbits with high inclinations of 60° to 70° and semi-major axes of order 30 000 km.

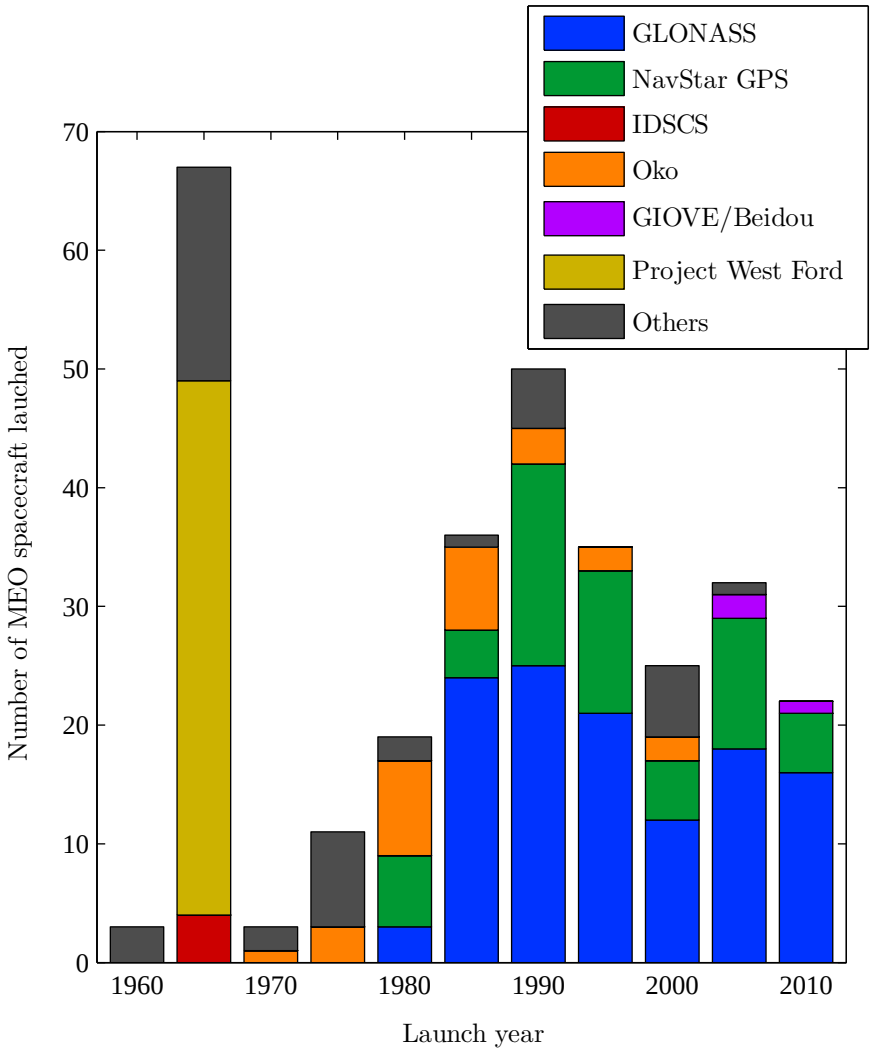

Figure 1.2: Number of tracked objects currently residing in MEO by launch date and category

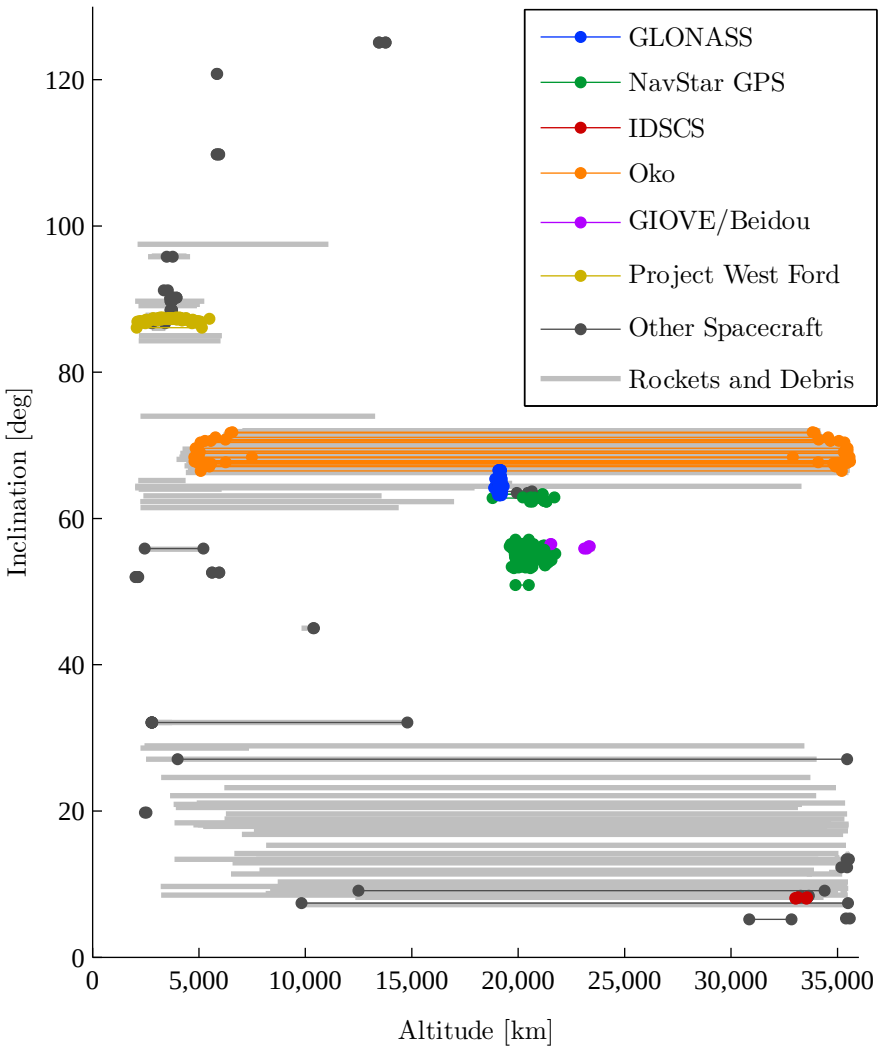

Figure 1.3: Objects currently in MEO by category on a graph of inclination and altitude: Perigee and apogee altitudes of spacecraft and Westford needles are marked with a circle.

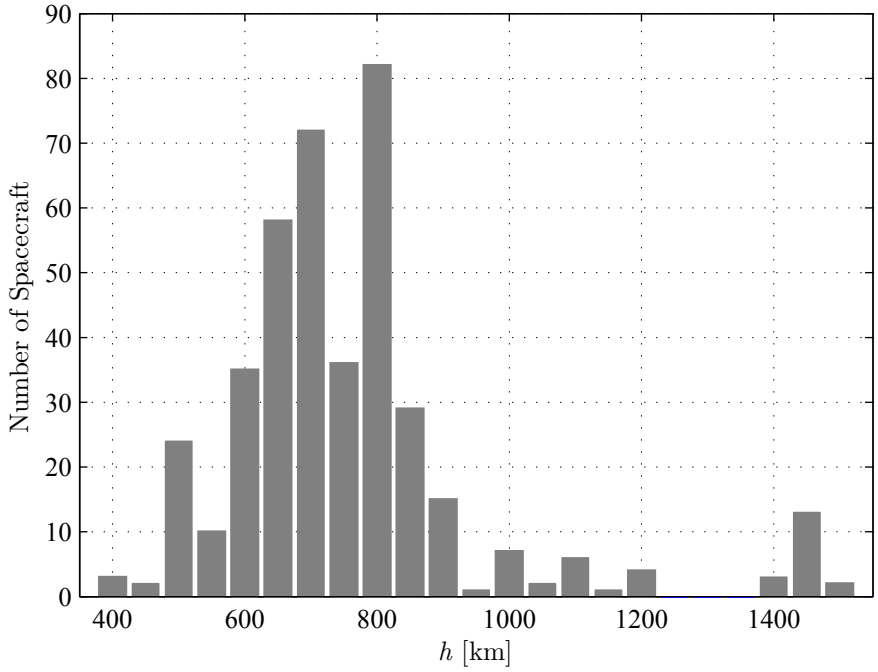

Figure 1.4: The number of spacecraft in the NORAD database in Sun-synchronous orbits of different altitudes

Sun-synchronous Orbits

The second regime investigated in this thesis for passive deorbiting are high altitude Sun-synchronous orbits (SSOs). SSOs are retrograde orbits of a fixed inclination ($i > 90°$) which depend on the orbit semi-major axis at which the J_2 effect causes the line of nodes to precess at the same rate as the Earth's orbital motion about the Sun [53]. Thus, the orbit plane always has the same aspect angle with respect to the Sun. This is useful for many Earth observation missions and makes SSOs the most popular of Low Earth Orbits (LEOs). One key advantage SSOs grant is even illumination conditions on the ground, providing a better comparison between image sets. Furthermore, dawn/dusk orbits require a less complex spacecraft architecture and thermal control system due to the almost constant configuration of Sun and the ground in the spacecraft's frame of reference. The popularity of Sun-synchronous orbits means that they are at a particular risk of space debris collisions and so end-of-life disposal is essential for spacecraft in these orbits.

Although current SSO missions favour 800 km orbits, high altitude SSOs have been used in the past as can be seen in Fig. 1.4, which shows the number of spacecraft in the CelesTrak database [48] which are in a Sun-synchronous orbit by their altitude. SRP-augmented deorbiting as an efficient passive deorbiting strategy can make these higher altitudes accessible for small spacecraft and enable new types of missions, as will be discussed in Chapter 5.

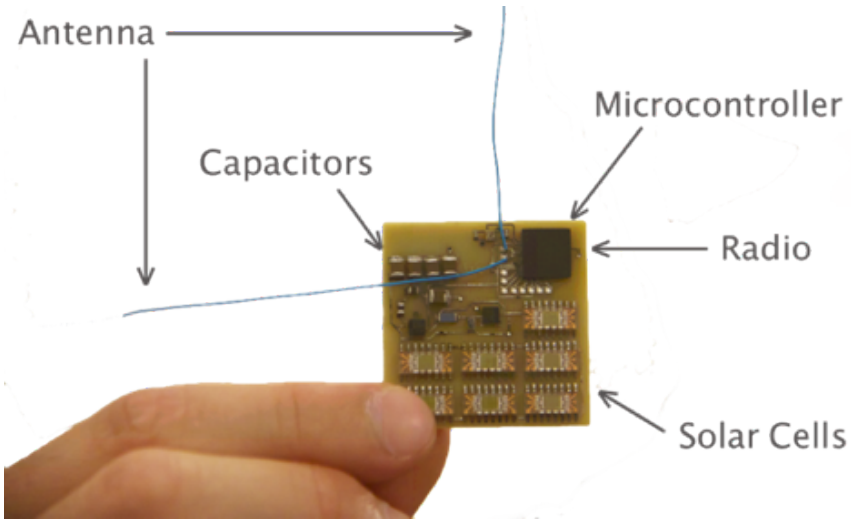

Figure 1.5: Photo of a breadboard model of a SpaceChip device (Credits: Cornell University)

1.3 Orbit control for SpaceChips

Moving down in length-scale, the orbital dynamics of so-called SpaceChips are investigated next in Chapter 6 and 7. Recent advances in miniaturisation make the prospect of these micro-electromechanical system (MEMS)-scale satellite missions realistic, employing system devices of length-scale 0.1 - 10 mm (see Fig. 1.5). These spacecraft offer cheap manufacture and launch, and can thus be deployed in large numbers providing multiple perspectives and real-time global information. The orbits of such satellites are influenced significantly by surface force perturbations such as solar radiation pressure and aerodynamic drag due to their high area-to-mass-ratio.

1.3.1 SpaceChip technology

Recently, a number of concepts for SpaceChip devices have emerged. Warneke et al. [54, 55] investigate the concept of "smart dust", multiple sensor nodes which have the ability to communicate with each other, while Sailor and Link [56] propose dust-grain-sized devices. SpaceChip devices function as independent agents in orbit but are contained on a single computer chip. They can generate power, gather and process information and communicate with other SpaceChips and a larger satellite or possibly the ground. Barnhart et al. [57, 58] propose small "femto-satellites" for space networks. They investigate the concepts both for a satellite on a printed circuit board and true SpaceChips.

The disadvantage of SpaceChips is their low survivability. The lack of any shielding from radiation will lead to quick deterioration of the on-board memory, with current technology. However,

their very low production and launch cost can see them deployed in large numbers as disposable detector networks [59]. Their very short production time make their use in rapid response scenarios attractive, and their short orbit lifetime in LEO prevents the creation of additional space debris. Some possible mission scenarios include space weather detectors or atmospheric sensors. It is, for example, envisaged, that a cloud of SpaceChips is deployed in LEO above the Earth's mesosphere sending out beacon signals, while slowly spiralling through the atmosphere until radiation events render them unresponsive [60]. The signal loss is then mapped and used to draw conclusions concerning radiation intensity in the upper atmosphere.

The SpaceChip used in this thesis is the Cornell University SpaceChip, *Sprite*, under development by Atchison and Peck [61]. It measures $1\,\mathrm{cm}^2$ by $20\,\mu\mathrm{m}$ thickness. This results in an area-to-mass-ratio of $17.8\,\mathrm{m}^2\,\mathrm{kg}^{-1}$ for the bulk density of Silicon.

1.3.2 Attitude and orbit control

MEMS spacecraft pose a challenge for orbit control since they are highly perturbed by surface forces such as SRP and drag, and are not suitable for conventional orbit control methods due to their small length-scale. They also present a risk of becoming a space debris hazard and endangering other satellites because of their lack of deorbiting capability and probable future deployment in large swarms. As the development of MEMS spacecraft advances, the need for a simple and effective orbit control method grows. Atchison and Peck [61] propose passive SRP control by etching patterns in the SpaceChip surface. Passive Lorentz-force propulsion is inspired by the motion of charged dust grains and uses natural charging of the SpaceChips to propel it to Earth escape [59]. Alternatively, methods to actively controlling the Lorentz force have been devised [62]. Bell et al. [63, 64] investigate the use of electrodynamic tethers for orbit control, while Schaub et al. [65] proposes to organise the spacecraft locally by exploiting Coulomb forces.

For attitude control, a range of passive techniques has been suggested. A structured surface can create an equilibrium attitude with respect to the Sun, while a thin wire or fin at the back of the spacecraft could produce the "shuttlecock effect" [61]. Alternatively permanent magnets could be used to exploit the Earth's magnetic field in a way similar to conventional LEO spacecraft.

1.3.3 Electrochromic control

The concept proposed in this thesis is to alter the coefficient of reflectivity of a SpaceChip device by using an electrochromic coating to control the spacecraft's orbit through modulation of the

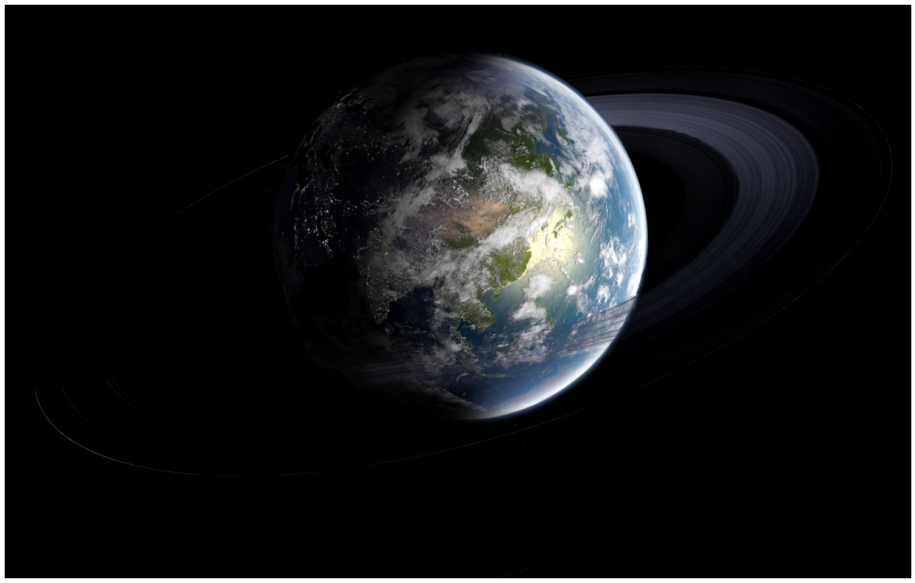

Figure 1.6: Impression of a dust ring around the Earth (image material: ESA)

SRP perturbation. This is advantageous for SpaceChip-scale devices since no moving parts are required. Electrochromic materials change their optical properties when an electrical current is applied. They are widely used in terrestrial applications, such as intelligent sunshades, tinting windows and flexible thin film displays, and have been used in space applications, albeit not for orbit control. The IKAROS solar sail demonstrator used electrochromic surfaces on the sail to adjust its attitude [66] and electrochromic radiators have been developed for thermal control [67]. A recent proposal by Ovelar et al. [68] to design the orbits of micro-particles by engineering their lightness number, the ratio between acceleration due to SRP and acceleration due to solar gravity, highlights current interest in the exploitation of orbital perturbations as a means of trajectory manipulation of micro-scale objects using simple control methods.

1.4 Geo-engineering using dust clouds

Finally, on a micrometre-scale the natural orbital evolution of dust is utilised to create, distribute and maintain a ring of dust around the Earth for solar radiation management (see Fig. 1.6). Solar radiation management (SRM) is one of the two main branches of geoengineering, the deliberate modification of the Earth's climate to mitigate anthropogenic climate change.

The consensus of the scientific community is that the Earth is currently experiencing human-driven climate change [69]. As concluded by the Intergovernmental Panel on Climate Change (IPCC), it is predicted to have serious impacts ranging from extreme weather events to the chang-

ing of coast lines threatening communities and biological diversity [70]. An increase in average temperature of between 1.1° and 6.4° is expected in this century [70].

In 2009 the Royal Society working group on geoengineering issued a survey of proposed strategies of geoengineering, ranking them in effectiveness, safety, affordability and timeliness [71]. In the report two main branches of geoengineering were distinguished: carbon capture and SRM. Carbon capture aims to reduce the amount of CO_2 in the atmosphere, while the goal of SRM is to lower the solar radiation input into the Earth's climate system. A reduction of 1.7 % would reduced the global rise in temperatures by an estimated 2 °C. SRM can be conducted on Earth via methods such as using reflective surfaces on roads and buildings to increase the Earth's Albedo [72] or cloud seeding [73]. While the former solution is not deemed to be effective, cloud seeding is considered to be risky as it may have unforeseen consequences on the environment. Most Earth-based geoengineering solutions are received with scepticism because of the complexity of the Earth's environmental system which makes precise prediction of the effects of any large-scale manipulation difficult or even impossible.

Space-based geoengineering (SBGE) is a form of SRM, describing strategies in which large-scale structures or clouds of particles are placed in strategic positions outside the Earth's atmosphere to filter out part of the incoming solar radiation and thus reduce the overall thermal input into the Earth's climate system [74]. It is argued that such a method, although costly and currently at a very low Technology Readiness Level (TRL), would be effective while minimising the side effects on the Earth's environment [71]. By moving geoengineering outside the atmosphere it can be conducted in a more controlled fashion.

Two key means of SBGE are proposed, either using large terrestrially manufactured reflector such as suggested by Angel [79] and McInnes [78] or using dust clouds sourced from the Moon or a

Table 1.2: Key properties of the different space-based geoengineering methods proposed in literature [75]

Position	Method	Insolation Red.	Req. Mass [kg]	Reference
Earth Ring	Dust ring	1.6 %	2.3×10^{12}	Pearson et al. [76]
Earth Ring	Solar reflector	1.6 %	5.0×10^{9}	Pearson et al. [76]
Earth-Moon L_4/L_5	Dust Cloud	1.4 %	2.1×10^{14}	Struck [77]
Sun-Earth L_1	Solar Reflector	1.8 %	2.6×10^{11}	McInnes [78]
Sun-Earth L_1	Solar Refractor	1.8 %	2.0×10^{10}	Angel [79]
Sun-Earth L_1	Dust Cloud	1.7 %	1.9×10^{10} /yr	Bewick et al. [80]

captured asteroid [77]. While the former method allows some degree of orbit control, which means that the system can be sustained in an advantageous position, it has the clear drawback with respect to the dust cloud method that all the material needs to be launched from Earth. Dust clouds are considered to require more mass than reflectors but this mass is more easily accessible in space. The material could be extracted from a captured asteroid, milled in order to achieve the required grain size and then expelled using a mass driver [81]. Otherwise the material could be ablated using lasers [82] or orbiting solar collectors [83].

Struck [77] proposed to place the dust clouds at the L_4 and L_5 points in the Earth-Moon system, while Bewick et al. [80] suggest the L_1 point of the Earth-Sun system. The former has the advantage of being a stable equilibrium, while the latter will decay over time. However, the L_1 position benefits from being fixed between the Earth and the Sun and thus allowing a continual reduction in insolation. This means that significantly less mass is required over time.

Pearson et al. [76] propose to place either reflectors or dust particles in Earth orbit rather than a Lagrange point. They estimate the masses required for such a scheme. In the positioning of the dust ring, aerodynamic drag is considered and the altitude is chosen so that the ring will not decay within a short time. However, solar radiation pressure was not considered and the ring deployment scenario was discussed only briefly. In this thesis the orbital dynamics of such a dust ring are investigated using a Hamiltonian dynamics approach in Chapter 8 and novel *heliotropic* orbits developed by Colombo et al. [84]. The resulting required mass is compared to the other schemes referenced in Table 1.2.

1.5 Contribution of the thesis

In this thesis the Hamiltonian model of the orbital dynamics of high area-to-mass-ratio objects investigated by Hamilton and Krivov [7] and Krivov and Getino [8] is exploited. In the first step, the analytical model is used to identify characteristic behaviour of high area-to-mass-ratio spacecraft which is then used to achieve specific mission goals. Next, the applications are assessed using a numerical model based on semi-analytical equations for the orbit evolution to account for the simplifications in the analytical model. Finally, test cases are run using a high precision orbit propagator. The methodology is explained in detail Chapter 2 in which the equations used in this thesis are developed and the analytical model is discussed.

The key contribution of this thesis is the investigation of novel applications of high area-to-mass-ratio orbital dynamics which are organised by the order of the governing length-scale, starting

at metre-scale with small satellites and CubeSats and going down to SpaceChips and then asteroid dust at a micro-metre scale. The unifying physics is the increase in area-to-mass-ratio, and hence surface forces, with decreasing length-scale.

1.5.1 Applications for small satellites

In part one of this thesis applications for small satellites such as nano- and picosatellites that can modulate their area-to-mass-ratio are discussed. The first application is a passive GTO-to-LEO transfer using solar radiation pressure and aerodynamic drag. The method was developed from the initial work discussed by Colombo and McInnes [32] for a specific scenario. Here it was proposed that a spacecraft could be launched into GTO where it remains until the orientation of the orbit with respect to the Sun is optimal for the passive manœuvre. Then the spacecraft deploys a structure to enhance its surface area and uses solar radiation pressure and drag to circularise into LEO while raising the orbit perigee. In this thesis the method is analysed in detail using a high precision orbit propagator and taking into account the variation of the orbital elements during the waiting time in GTO. It will be shown that these have a strong impact on the eventual success of the transfer.

In the Chapter 3 there is a discussion of the design of an area-to-mass-ratio increasing device for small spacecraft. Calculation of the effective coefficient of reflectivity is discussed with respect to device shapes and different deployment and rigidisation methods are evaluated. A recommendation is made for an inflatable balloon which is hardened using cold-curing resin.

Chapters 4 and 5 discuss the use of solar radiation pressure for deorbiting high altitude orbits, which is a fully original contribution in this thesis. The principle is the reverse of the GTO-to-LEO transfer. In the former the effects of SRP and the J_2 effect are used to decrease the orbit eccentricity and thus raise its perigee. For deorbiting, the perigee of initially circular orbits is lowered by using SRP to increase the orbit eccentricity. The method is first developed analytically and then analysed numerically for inclined orbits to identify areas in which the method is particularly effective and those where it cannot feasibly be applied. In Chapter 4 the deorbiting of medium Earth orbits (MEO) is investigated and in Chapter 5 high altitude Sun-synchronous orbits are discussed.

1.5.2 Applications for SpaceChips

In part two a different application of the perturbed dynamics, the orbit control of SpaceChips is presented. These are millimetre-scale satellites on a silicon chip with sensing, computing and communication capabilities. Different research teams are currently developing these *smart dust* devices. Although they cannot gather, process or send data comparable in quality or quantity to that of conventional spacecraft, their extremely low mass and fabrication costs allow them to be deployed in large numbers. This may enable distributed in-situ sensing with a high spacial resolution.

Due to their small size they lack an effective orbit control method. In this thesis electrochromic control is proposed, which again makes use of the naturally occurring orbital perturbations due to solar radiation pressure. Using electrochromic coatings the spacecraft can change their optical properties and thus gain control over their orbital evolution due to their large area-to-mass-ratio.

In Chapter 6 a general control algorithm based on an artificial potential field in the orbital element phase space is used to stabilise and navigate SpaceChips. The orbits which can be stabilised using this method are identified and an eccentricity and orientation changing manœuvre and an orbit raising manœuvre are investigated. In Chapter 7 the Hamiltonian model is applied to a specific type of manœuvre in the orbital element phase space and a control algorithm based on the Hamiltonian is developed. This algorithm is then applied to an eccentricity and orientation changing manœuvre and is shown to be more time-efficient for this type of manœuvre than the artificial potential field approach.

1.5.3 Applications for planetary dust

On a micrometre-scale, the natural evolution of dust grains was utilised to devise a deployment scheme for asteroid mined material to create a stable Earth-ring with Sun-pointing apogee for solar radiation management. Space-based geoengineering aims to mitigate climate change by reducing the amount of Sunlight reaching the Earth. In the proposed method a dust ring mined from a captured asteroid is used to filter out the required fraction of Sunlight. This research was conducted in collaboration with other researchers investigating macro-scale space systems. It is based on research on *heliotropic* orbits which use SRP and the J_2 effect to achieve a Sun-synchronous state. These orbits were discovered during an investigation of the Hamiltonian dynamics of the problem [84].

The contribution presented in this thesis is the analytical development of the dispersion scheme for the dust grains. The grains are produced on the asteroid which is in a given Earth orbit. The different sized dust grains are then expelled from the asteroid with a given Δv using a rail gun or mass driver. The insertion orbit is chosen in such a way to avoid rapid deorbiting due to the orbital evolution of the dust grains and, at the same time, to guarantee a best possible distribution of the grains to maximise the reduction of Sunlight. This is achieved by using *heliotropic* and approximately *heliotropic* orbits, so that the apogee of the grain orbits remains close to Sun-pointing.

1.6 List of publications

The work presented in this thesis has previously been published in a number of journal and conference papers:

1.6.1 Journal papers

- Colin R. McInnes, Matteo Ceriotti, Camilla Colombo, Joan-Pau Sanchez, Russell Bewick, Jeannette Heiligers and Charlotte Lücking. "Micro-to-macro: Astrodynamics at extremes of length-scale". *Acta Futura* **4**, 2011 [85].

- Charlotte Lücking, Camilla Colombo and Colin R. McInnes. "A passive satellite deorbiting strategy for medium Earth orbits using solar radiation pressure and the J_2 effect". *Acta Astronautica* **77**(1), 2012 [86].

- Charlotte Lücking, Camilla Colombo and Colin R. McInnes. "Electrochromic orbit control for SpaceChip swarms". *AIAA Journal of Guidance, Control and Dynamics* **35**(5), 2012 [87].

- Camilla Colombo, Charlotte Lücking and Colin R. McInnes. "Orbital dynamics of high area-to-mass-ratio spacecraft with J_2 and solar radiation pressure for novel Earth observation and communication services". *Acta Astronautica* **81**(1), 2012 [84].

- Camilla Colombo, Charlotte Lücking and Colin R. McInnes. "Orbit evolution, maintenance and disposal of SpaceChip swarms through electrochromic control". *Acta Astronautica* **82**(1), 2012 [88].

- Russell Bewick, Charlotte Lücking, Camilla Colombo, Joan-Pau Sanchez and Colin R. McInnes. "Heliotropic dust rings for Earth climate engineering". *Advances in Space Research*, **51**(7), 2013 [75].

- Charlotte Lücking, Camilla Colombo and Colin R. McInnes. "Solar radiation pressure augmented deorbiting: passive end-of-life disposal from high altitude orbits". *AIAA Journal of Spacecraft and Rockets*, in press, 2013 [89].

1.6.2 Conference papers

- Charlotte Lücking, Camilla Colombo and Colin R. McInnes. "Orbit control of high area-to-mass-ratio spacecraft using electrochromic coating" at the *61st International Astronautical Congress* in Prague, Czech Republic, October 2010 [90].

- Camilla Colombo, Charlotte Lücking and Colin R. McInnes. "Orbit evolution, maintenance and disposal of SpaceChip swarms" at the *6th International Workshop on Satellite Constellation and Formation Flying* in Taipei, Taiwan, November 2010 [91].

- Charlotte Lücking, Camilla Colombo and Colin R. McInnes. "A passive deorbiting strategy for high altitude CubeSat missions using a deployable reflective balloon" at the *8th IAA Symposium on Small Satellites for Earth Observation* in Berlin, Germany, April 2011 [92].

- Charlotte Lücking. "A passive high altitude deorbiting strategy" at the *25th AIAA/USU Conference on Small Satellites* in Logan (UT), United States of America, August 2011 [93].

- Charlotte Lücking, Camilla Colombo and Colin R. McInnes. "A passive satellite deorbiting strategy for MEO using solar radiation pressure and the J_2 effect" at the *62nd International Astronautical Congress* in Cape Town, South Africa, October 2011 [94].

- Russell Bewick, Charlotte Lücking, Camilla Colombo, Joan-Pau Sanchez and Colin R. McInnes. "Geo-engineering using dust grains in heliotropic elliptical orbits" at the *62nd International Astronautical Congress* in Cape Town, South Africa, October 2011 [95].

- Camilla Colombo, Charlotte Lücking and Colin R. McInnes. "Orbital dynamics of high area-to-mass-ratio spacecraft under the influence of J_2 and solar radiation pressure" at the *62nd International Astronautical Congress* in Cape Town, South Africa, October 2011 [96].

- Charlotte Lücking, Camilla Colombo and Colin R. McInnes. "Solar radiation pressure augmented deorbiting from high altitude sun-synchronous orbits" at the *4S Symposium* in Portorož, Slovenia, June 2012 [97].

- Charlotte Lücking, Camilla Colombo and Colin R. McInnes. "Mission and system design of a 3U CubeSat for passive GTO to LEO transfer" at the *63rd International Astronautical Congress* in Naples, Italy, October 2012 [98].

Chapter 2

Methodology

In this chapter the general methodology used for identifying and validating the applications for high area-to-mass-ratio (HAMR) orbital dynamics presented in this thesis is explained. A particular focus is laid on the basic dynamics governing HAMR objects and, more specifically, the Hamiltonian analytical model developed by Hamilton and Krivov [7] and Krivov and Getino [8] for natural dust grains and balloon satellites.

The new orbits and applications presented in this thesis were developed using a three-step approach:

- Firstly, the new orbits and applications were identified using the analytical Hamiltonian model discussed in Sec. 2.1. This model allows the identification of global behaviour in the evolution of HAMR objects and can be exploited to find analytical solutions for specific applications.

- Secondly, the orbits and applications identified were validated using numerical propagation of a set of equations for the secular orbital evolution. Two different models were used in the applications. These models are discussed in Sec. 2.2.

- Thirdly, a verification either using a propagation of the Gauss' equations in 3D introduced in Sec. 2.3.1, or an analysis with a high precision orbit propagator was performed for a sample of cases to confirm the results of the previous step as dicussed in Sec. 2.3.2.

The only exception is the geoengineering application presented in Chapter 8. In this work only the analytical analysis (step one) was performed as part of this thesis.

2.1 Orbital Dynamics with SRP and J_2

The dynamics presented in this section build the basis for the new orbits and applications presented in this thesis. They were developed by Hamilton and Krivov [7] and Krivov and Getino [8], and are particularly suitable for the analysis and design of high-area-to-mass-ratio applications in an Earth orbit. This is because they focus on the two most dominant perturbing effects for such spacecraft, solar radiation pressure and the J_2 effect, while neglecting other perturbations to arrive at an elegant Hamiltonian equation which can be adapted and transformed to investigate numerous applications as shall be shown in the later chapters of this thesis.

The model considers only the perturbations of solar radiation pressure and J_2. This is appropriate as Atchison and Peck [1] show that SRP and the Earth's oblateness are the dominant effects for high area-to-mass-ratio spacecraft in circular orbits above LEO ($a > 2000\,\text{km}$), with the next strongest perturbing force, the third body effects of the Moon and the Sun, which are orders of magnitude smaller. This is shown in Fig. 2.1, in which the relative accelerations experienced by a typical SpaceChip due to different perturbations are shown as a function of altitude. It can also be seen that the effect of aerodynamic drag, which is dominant over solar radiation pressure below approximately 600 km, is insignificant for altitudes above LEO.

Anselmo and Pardini [99] show in their work on the orbital evolution of high area-to-mass-ratio objects at GPS altitudes ($a \approx 27\,000\,\text{km}$, see Sec. 1.2.2) that short periodic variations of eccentricity due to solar radiation pressure occurs superimposed on the long periodic variation due to third body effects and higher order gravitational harmonics. Therefore, it is clear that SRP represents the key perturbing force. First the basic Hamiltonian model will be described and then an investigation into out-of-plane dynamics is presented.

2.1.1 Hamiltonian analytical model

This section will begin with the governing equations describing the Hamiltonian dynamics of HAMR objects. Next the resulting phase spaces are discussed, and finally out-of-plane behaviour is analysed.

Hamiltonian definition

An orbit which lies in the ecliptic plane can be described with three orbital parameters, the semi-major axis, a, the eccentricity, e, and the angle, ϕ, between the Sun-line and the orbit perigee, also

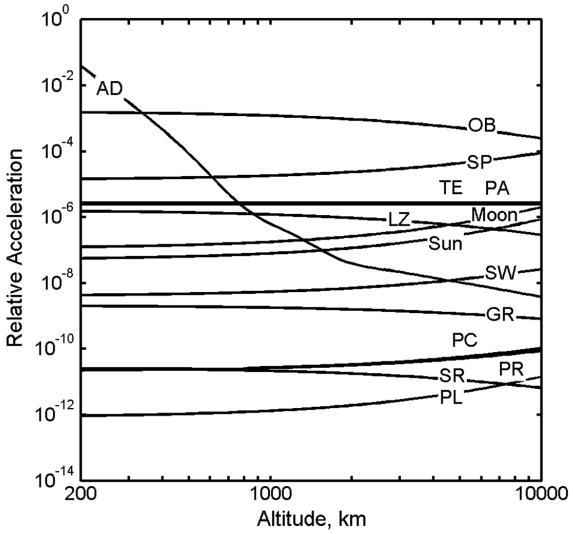

Initials	Acceleration
AD	Aerodynamic drag
EC	Eddy current drag
GG	Gravity gradient
GR	General relativity
LZ	Lorentz force
M	Magnetism
MT	Magnetism: torquer
MR	Magnetism: residual field
Moon	Lunar gravity
OB	Earth oblateness
PA	Planetary albedo
PC	Particle collisions
PL	Solar system planetary gravity
PR	Poynting–Robertson drag
SP	Solar pressure
SR	Special relativity
SW	Solar wind
Sun	Solar gravity

Figure 2.1: Relative acceleration of orbital perturbations on a typical SpaceChip as a function of altitude [1]

defined as the Sun-perigee angle, as shown in Fig. 2.2. Therefore, ϕ can be expressed as:

$$\phi = \Omega + \omega - (\lambda_{\odot} - \pi) \tag{2.1}$$

where Ω is the right ascension of the ascending node and ω the argument of perigee. For orbits in planes that are inclined with respect to the ecliptic, Eq.(2.1) is an approximation which loses accuracy with increasing inclination. When considering the J_2 Earth oblateness perturbation, it is necessary to reduce the geometry to a two dimensional planar model, neglecting the tilt of the Earth's rotational axis, to allow an analytical development of the problem.

The analytical model of the orbital dynamics developed by Hamilton and Krivov [7] and Krivov and Getino [8] uses an approximate Hamiltonian for planar orbits under the effects of solar radiation pressure and the Earth's oblateness. This analytical model does not consider eclipses and the tilt of the Earth's rotational axis with respect to the ecliptic plane. As a consequence, the semi-major axis remains constant and the evolution of the orbit can be described only by its eccentricity, e, defining the changing shape of the orbit, and Sun-perigee angle, ϕ, defining the orbit orientation with respect to the Sun. From Hamilton and Krivov [7], the change of orbital elements due to solar radiation pressure and J_2 with respect to the progression of the angle between the true longitude of the Sun on the ecliptic plane with respect to the first point of Aries, $\lambda_{\odot}$ (see Fig. 2.2), is:

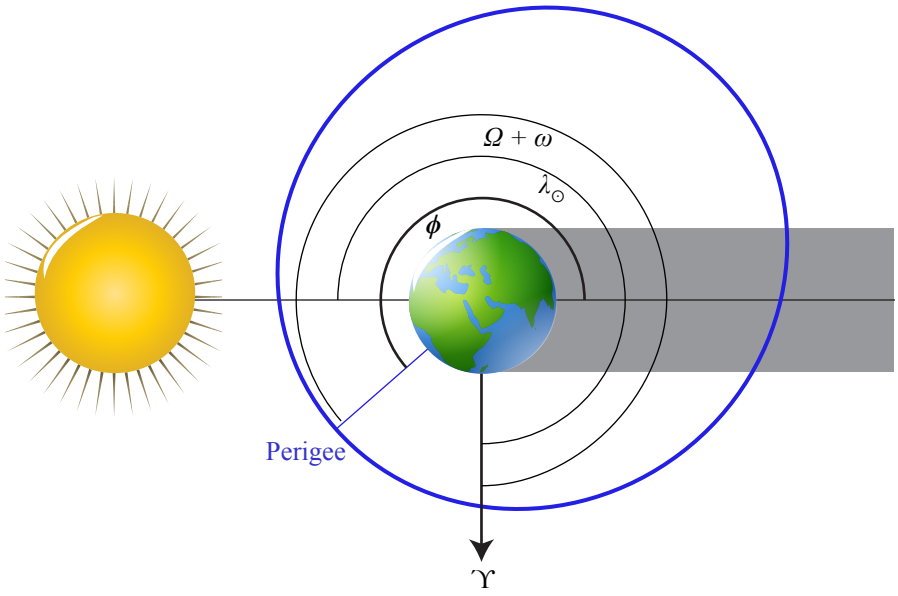

Figure 2.2: In-plane orbit geometry - Υ denotes the direction of the first point of Aries

$$\frac{\mathrm{d}e}{\mathrm{d}\lambda_\odot} = -\alpha\sqrt{1-e^2}\sin\phi \tag{2.2}$$

$$\frac{\mathrm{d}\phi}{\mathrm{d}\lambda_\odot} = -\alpha\frac{\sqrt{1-e^2}}{e}\cos\phi + \frac{\kappa}{(1-e^2)^2} - 1 \tag{2.3}$$

where α is the radiation pressure parameter and κ the J_2 effect parameter, defined by:

$$\alpha = \frac{3}{2n_\odot}a_{\mathrm{SRP}}\sqrt{\frac{a}{\mu}} \tag{2.4}$$

$$\kappa = \frac{3}{2n_\odot}J_2{R_E}^2\sqrt{\frac{\mu}{a^7}} \tag{2.5}$$

with $n_\odot = 2\pi\,\mathrm{rad\,yr}^{-1}$, the orbital rate of the Earth around the Sun, $J_2 \approx -1.08 \times 10^{-3}$, the second gravitational harmonic parameter of the Earth, $R_E \approx 6378\,\mathrm{km}$, the mean radius of the Earth, and a_{SRP}, the acceleration the spacecraft experiences due to solar radiation pressure. The term a_{SRP} can be calculated from the solar energy flux at 1 AU distance from the Sun, $F_\odot \approx 1370\,\mathrm{W\,m}^{-2}$, and the speed of light, $c \approx 3 \times 10^8\,\mathrm{m\,s}^{-1}$, as follows [53]:

$$a_{SRP} = \frac{F_\odot}{c}\sigma \tag{2.6}$$

The key spacecraft characteristic is the effective area-to-mass-ratio, $\sigma = c_R \frac{A}{m}$, the product of c_R, the coefficient of reflectivity, and $\frac{A}{m}$, the area-to-mass-ratio with respect to the Sun, which is assumed to be constant.

Hamilton and Krivov [7] show that Eqs. (2.2) and (2.3) can be written in a quasi-canonical form:

$$\frac{\mathrm{d}e}{\mathrm{d}\lambda_\odot} = \frac{\sqrt{1-e^2}}{e}\frac{\partial H}{\partial \phi} \tag{2.7}$$

$$\frac{\mathrm{d}\phi}{\mathrm{d}\lambda_\odot} = -\frac{\sqrt{1-e^2}}{e}\frac{\partial H}{\partial e} \tag{2.8}$$

with the Hamiltonian $H(\phi, e)$, defined as:

$$H(\phi, e) = \alpha e \cos\phi - \frac{\kappa}{3\sqrt{1-e^2}^3} - \sqrt{1-e^2} \tag{2.9}$$

H is not dependent on $\lambda_\odot$, which acts as a time variable in this model. Hence, the evolution of any orbit with initial eccentricity, e_0, and Sun-perigee angle, ϕ_0, is given by the set of orbits, (e, ϕ), with:

$$H(\phi, e) = H(\phi_0, e_0) = const. \tag{2.10}$$

Any orbit will evolve along phase lines of the same Hamiltonian value, either periodically returning to the initial orbit or, in special cases, converging towards an equilibrium orbit. The different phase space behaviours and equilibria that can occur are discussed in the following subsection.

Phase space behaviour and equilibria

A selection of phase space diagrams resulting from the Hamiltonian in Eq. (2.9) are shown in Fig. 2.3 for three different semi-major axes and three different area-to-mass-ratios in the range that is relevant for the applications discussed in this thesis. The diagrams were computed numerically. The shaded areas represent orbits where the radius of the perigee is smaller than the radius of the Earth. The values were chosen so that the most interesting behaviours could be shown. A reflectivity coefficient of $c_R = 1.8$ was chosen in an approximation of an imperfectly reflecting surface. The equilibrium eccentricities were found numerically and are marked with coloured circles, while the bold phase lines indicate the separatrices between rotational and librational behaviour. One of these is always a line passing through $e = 0$. Rotational behaviour describes an evolution in which

the angle ϕ performs a full rotation before returning to the original value. Librational behaviour occurs when an orbit librates around an equilibrium in the phase space.

Equilibria can only occur at $\phi = 0$ and $\phi = \pi$. This follows from Eq. (2.2) which clearly shows that the change in eccentricity for a non-zero SRP-parameter, α, can be only zero if $\phi = 0$ or $\phi = \pi$. Two types of equilibria can occur: stable centre equilibria and unstable hyperbolic equilibria. For low semi-major axes only one stable equilibrium exists at $\phi = 0$ (see Fig. 2.3(a-c)). At high semi-major axes a maximum of three equilibria exist for the given area-to-mass-ratios: the stable equilibrium at $\phi = 0$, an additional stable equilibrium at $\phi = \pi$ and, at a higher eccentricity, an unstable equilibrium also at $\phi = \pi$ (see Fig. 2.3(g-i)). The stable equilibrium at $\phi = \pi$ also exists when J_2 is neglected and only SRP is considered. It is the proposed orbit for the GEOSAIL mission [100]. This is a valid simplification for very high altitudes for which the Hamiltonian dynamics were investigated by Oyama et al. [101].

For semi-major axes in between these two regimes interesting behaviours can occur. Figure 2.3(d) shows a phase space in which all three equilibria occur. However, the two separatrices containing the librational zones around the two stable equilibria coincide. This way, for eccentricities below the eccentricity of the hyperbolic equilibrium no rotational behaviour exists. A spacecraft on a circular orbit would move towards the hyperbolic equilibrium on a stable manifold. This phase space behaviour is important for the solar radiation pressure augmented deorbiting method presented in Chapter 4 and 5.

A further behaviour of note can be observed in Fig. 2.3(e) where the stable and unstable equilibrium points coincide resulting in an unstable Bogdanov-Takens point [102]. For any semi-major axis there is an area-to-mass-ratio above which all equilibria at $\phi = \pi$ disappear. This is the case in Fig. 2.3(f).

In Fig. 2.4 the eccentricities of the equilibrium orbits are shown as a function of semi-major axis. The area-to-mass-ratios and reflectivity are selected in accordance with those in Fig. 2.3 and the three semi-major axes investigated there are marked by vertical black lines.

It can clearly be seen that for $a = 11\,000\,\text{km}$ there only exists the stable equilibrium at $\phi = 0$, regardless of how large the area-to-mass-ratio is chosen. At $a = 12\,350\,\text{km}$ the other two equilibria appear. First for small semi-major axes, and consequently at low eccentricities, but with increasing semi-major axes for higher area-to-mass-ratios as well. This effect could be seen in Fig. 2.3 where for low semi-major axes (a-c) just a single equilibrium appears and for high semi-major axes (g-i) all equilibria occur. Furthermore, the special case of Fig. 2.3 (e) where the hyperbolic

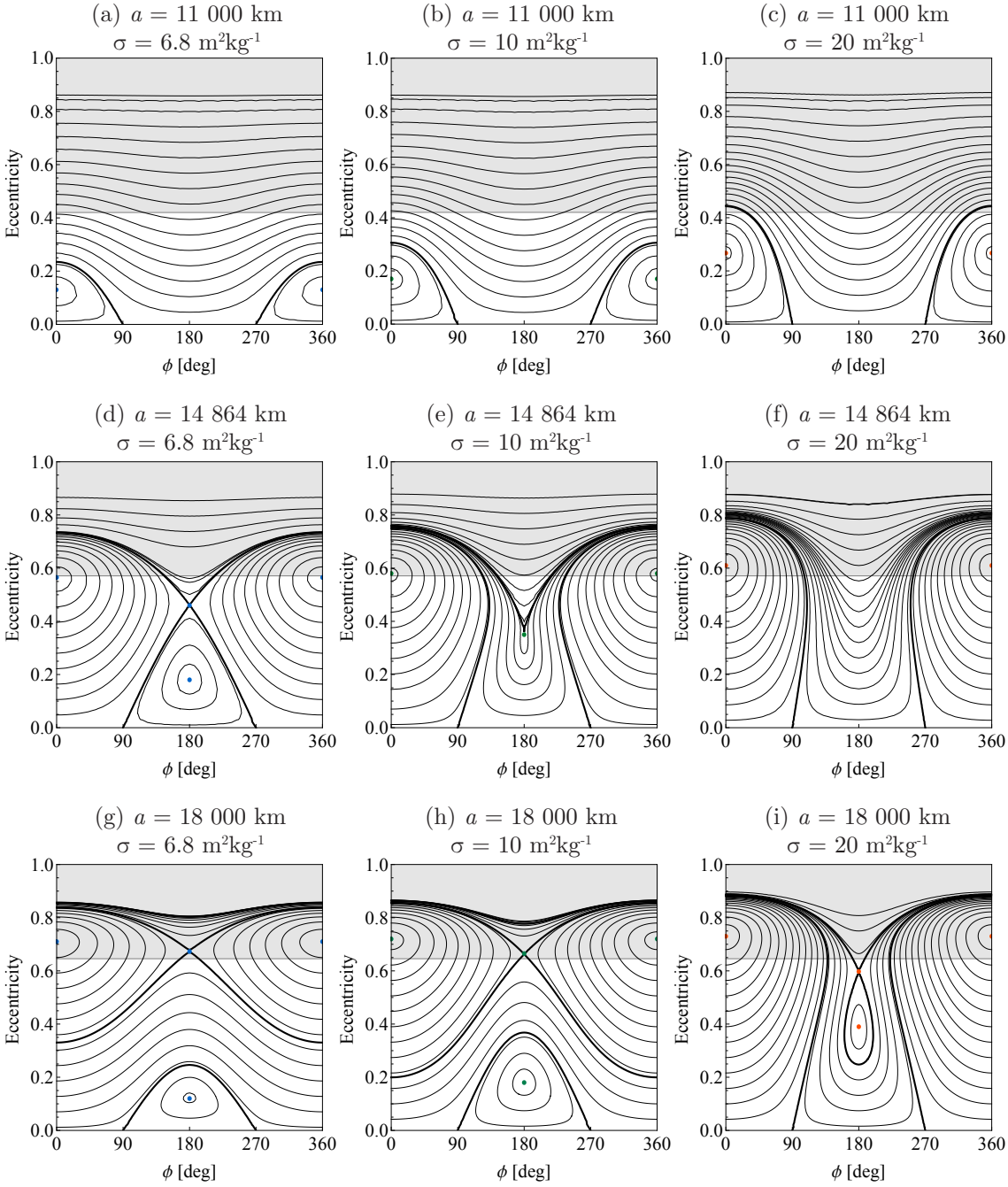

Figure 2.3: Hamiltonian phase space diagrams for three different semi-major axes a and three different area-to-mass-ratios σ ($c_R = 1.8$)

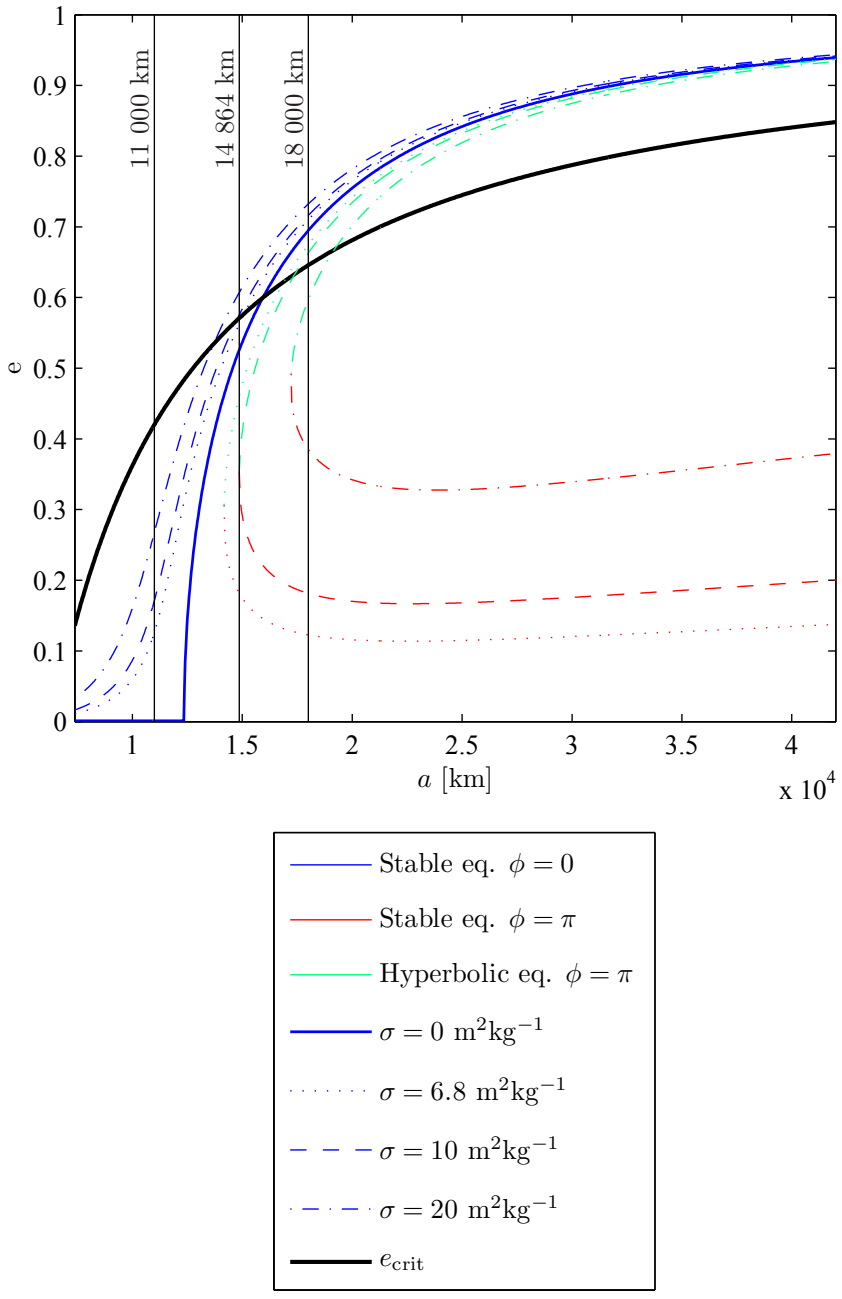

Figure 2.4: Eccentricity of equilibrium orbits in the Hamiltonian phase space as a function of semi-major axes a and for four different area-to-mass-ratios σ ($c_R = 1.8$)

and stable equilibrium coincided can be distinguished here as the position where the vertical line indicating $a = 14\,864\,\text{km}$ touches the lines for both equilibria at $\phi = \pi$ in the same position.

In Fig. 2.4 the critical eccentricity, e_{crit}, is also marked. This is the eccentricity for which an orbit perigee will intersect the Earth and is a function of semi-major axis and radius of the Earth, R_E, such that:

$$e_{\text{crit}} = 1 - \frac{R_E}{a} \tag{2.11}$$

Any equilibria above this line can thus not be used. Equilibria close below the line may not be feasible either as the drag at the perigee of these orbits could be too high. Because of this, for high semi-major axes only the stable equilibrium at $\phi = \pi$ is accessible.

Finally, it is interesting to note that equilibria also exist for $\sigma = 0\,\text{m}^2\,\text{kg}^{-1}$, i.e. without SRP. This is due to the fact that for $a \geq 12\,350\,\text{km}$, for high eccentricities the positive change of ϕ due to the J_2 effect is larger than the converse effect due to the progression of the Earth around the Sun, while for lower eccentricities it is the other way around. This means for each semi-major axis there exists an eccentricity for which the change in ϕ is zero, and the orientation of the orbit with respect to the Sun is thus constant. As SRP is neglected in this case, the orientation of the orbit with respect to the Sun is irrelevant.

2.1.2 Influence of obliquity and inclination

The Hamiltonian dynamics presented in the previous subsection are valid for zero inclination in-plane orbits. In-plane here means that the Earth's equatorial plane is assumed to lie in the ecliptic plane, i.e. the Earth obliquity is assumed to be zero rather than the actual 23.44°. That way the rotation of the orbit due to the J_2 effect and due to SRP and the progression of the Earth around the Sun share a common rotational axis. Thus a zero inclination orbit will never experience any out-of-plane forces due to SRP through-out its evolution. In this section the analysis by Colombo et al. [84] is summarised, which deals with the effects of non-zero obliquity and inclination on the evolution according to the Hamiltonian model by Hamilton and Krivov [7] and Krivov and Getino [8]. For the propagation of the orbits the expressions for the secular variation of orbital parameters due to SRP and J_2 found by Colombo and McInnes [103] and discussed later in 2.2 were used.

Figure 2.5 shows the change of the (e, ϕ) phase space as the obliquity is increased. It can be seen that the general shape of the phase space is retained. Despite the small divergences from

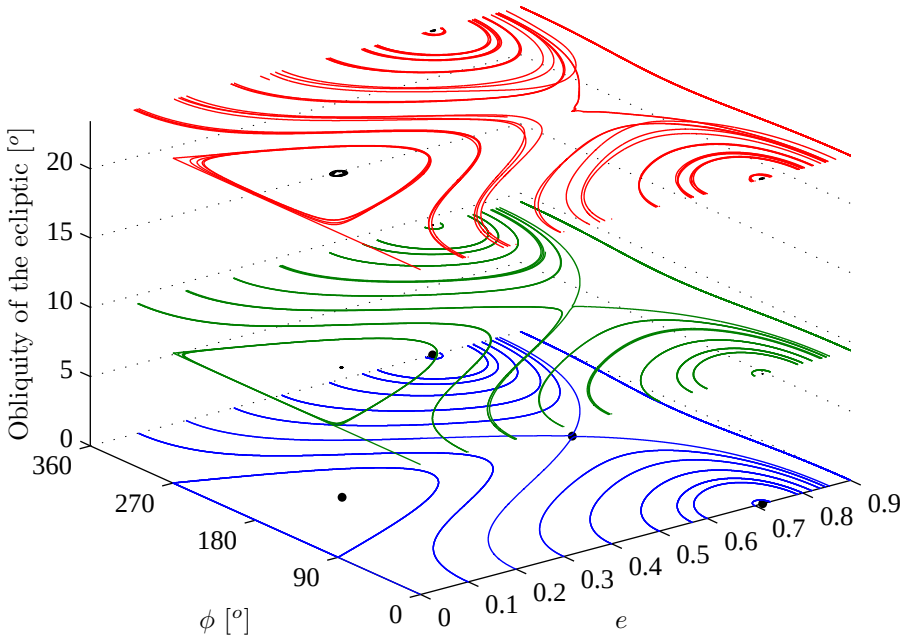

Figure 2.5: Orbital evolution due to SRP and J_2 of equatorial HAMR orbits in the (e, ϕ) phase space for different obliquity angles: $a = 18\,000\,\text{km}$, $\sigma = 10\,\text{m}^2\,\text{kg}^{-1}$ and $c_R = 1.8$ [84]

the analytical case, the equilibria still exist as quasi-frozen orbits. This means that the angle ϕ as defined in Eq. (2.1) remains close to constant while the angles Ω, ω and $\lambda_\odot$ vary.

Next, the occurrence and position of the equilibria is analysed for inclined orbits. Colombo et al. [84] use a numerical approach and apply a multi-objective minimisation to find the points in the phase space which vary the least in eccentricity, inclination and ϕ.

Figure 2.6 shows the eccentricity of the three types of frozen orbit corresponding to the equilibria discussed in Sec. 2.1.1 for a *Sprite* SpaceChip ($\sigma = 17.4\,\text{m}^2\,\text{kg}^{-1}$), as introduced in Chapter 1, at $a = 18\,000\,\text{km}$. It can be seen that the stable equilibrium at $\phi = \pi$ (blue) decreases in eccentricity for increasing inclination, while the other two types of frozen orbit experience an increase in inclination. Furthermore, it can be seen that the frozen orbits begin to disappear at higher inclinations.

2.2 Secular orbital evolution

In this section two sets of expressions for the secular variation of the orbital elements due to SRP and J_2 are described, which are used later in this thesis to verify any orbit families and

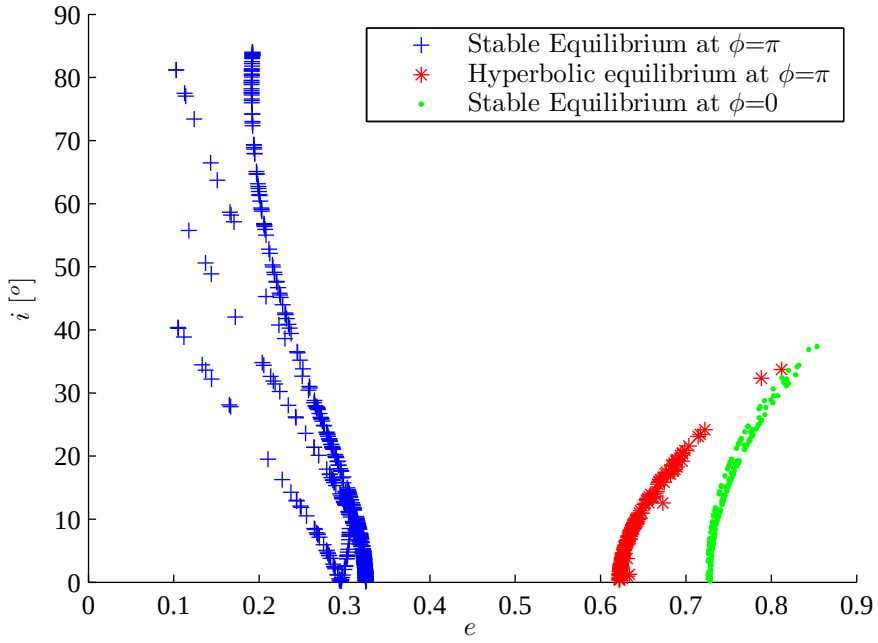

Figure 2.6: Quasi-frozen orbits in the (e, ϕ) phase space with frozen inclination for different inclined orbital planes: $a = 18\,000\,\text{km}$, $\sigma = 17.4\,\text{m}^2\,\text{kg}^{-1}$ and $c_R = 1.8$ [84]

applications developed using the analytical Hamiltonian model in Sec. 2.1.1. The first set uses Keplerian parameters and only applies to planar orbits. However, as opposed to the analytical model in Sec. 2.1.1, eclipses and aerodynamic drag are taken into account.

The second model takes into account inclination and the obliquity angle of the ecliptic with respect to the Earth's equator, $\varepsilon_E = 23.44°$. It is formulated in non-singular orbital elements to allow for the propagation of circular orbits. However, any perturbations apart from SRP and J_2 are not considered to minimise the computation time and thus allow the analysis of large sets of initial conditions. Additionally, both methods consider secular variations only. Secular variations are long term variations of the orbital elements averaged over one orbit disregarding the oscillations of the elements within one orbit. This vastly reduces the computational effort. However, it also means that any solutions are only approximate. To obtain high fidelity results a further verification step is needed as described later in Sec. 2.3.2.

2.2.1 Secular orbital in-plane evolution due to SRP, J_2 and drag

In this section the expressions found by Colombo and McInnes [103] for the orbit averaged variation of semi-major axis, eccentricity and Sun-perigee angle, ϕ, due to solar radiation pressure, the J_2 effect and drag are shown. These are a combination of an approximate integral of the Gauss'

equations of the perturbed Keplerian elements [53], the secular J_2 effect and the drag equations by King-Hele [104].

The orbit averaged change of the orbital elements due to solar radiation pressure found by Colombo and McInnes [103] was calculated by integrating the Gauss' equations. Then, the start and end angles of the integration interval $[f_1, f_2]$ are chosen as the exit and entrance angle of the eclipse. Therefore SRP only has an effect when the spacecraft is in Sunlight. The functions are applied as follows:

$$\begin{aligned}
\frac{\mathrm{d}a}{\mathrm{d}t}_{\mathrm{SRP}} &\approx \frac{1}{2\pi}\sqrt{\frac{\mu}{a^3}}\int_{f_1}^{f_2}\frac{\mathrm{d}a}{\mathrm{d}f}_{\mathrm{SRP}}(a,e,\phi)\mathrm{d}f = \frac{1}{2\pi}\sqrt{\frac{\mu}{a^3}}(\mathrm{fun}_a(a,e,\phi,f_2)-\mathrm{fun}_a(a,e,\phi,f_1))\\
\frac{\mathrm{d}e}{\mathrm{d}t}_{\mathrm{SRP}} &\approx \frac{1}{2\pi}\sqrt{\frac{\mu}{a^3}}\int_{f_1}^{f_2}\frac{\mathrm{d}e}{\mathrm{d}f}_{\mathrm{SRP}}(a,e,\phi)\mathrm{d}f = \frac{1}{2\pi}\sqrt{\frac{\mu}{a^3}}(\mathrm{fun}_e(a,e,\phi,f_2)-\mathrm{fun}_e(a,e,\phi,f_1))\\
\frac{\mathrm{d}\phi}{\mathrm{d}t}_{\mathrm{SRP}} &\approx \frac{1}{2\pi}\sqrt{\frac{\mu}{a^3}}\int_{f_1}^{f_2}\frac{\mathrm{d}\phi}{\mathrm{d}f}_{\mathrm{SRP}}(a,e,\phi)\mathrm{d}f = \frac{1}{2\pi}\sqrt{\frac{\mu}{a^3}}(\mathrm{fun}_\phi(a,e,\phi,f_2)-\mathrm{fun}_\phi(a,e,\phi,f_1))
\end{aligned} \tag{2.12}$$

with

$$\mathrm{fun}_a(a,e,\phi,f) = -\,a_{\mathrm{SRP}}\frac{2a^3(1-e^2)}{\mu}\left(\frac{\cos\phi + e\sin\phi\sin f}{e(1+e\cos f)}\right) \tag{2.13}$$

$$\begin{aligned}
\mathrm{fun}_e(a,e,\phi,f) = a_{\mathrm{SRP}}\frac{a^2(1-e^2)^2}{\mu e}\Bigg(&\sin\phi\left(-\frac{3}{\sqrt{1-e^2}^3}\arctan\left(\sqrt{\frac{1-e}{1+e}}\tan\frac{f}{2}\right)\right.\\
&\left.+\frac{\sin f(\cos f(-8e^4+10e^2-2)+6e(1-e^2))}{4(1-e^2)^2(1+e\cos f)^2}\right)-\cos\phi\frac{1+2e\cos f}{2e^2(1+e\cos f)^2+e^2}\Bigg)
\end{aligned} \tag{2.14}$$

$$\begin{aligned}
\mathrm{fun}_\phi(a,e,\phi,f) = -\,a_{\mathrm{SRP}}\frac{a^2(1-e^2)^2}{\mu e}\Bigg(&\cos\phi\left(\frac{3}{\sqrt{1-e^2}^3}\arctan\left(\sqrt{\frac{1-e}{1+e}}\tan\frac{f}{2}\right)\right.\\
&\left.-\frac{e\sin f}{(1-e^2)(1+e\cos f)}-\frac{1}{2}\frac{(e+\cos f)\sin f}{(1-e^2)(1+e\cos f)^2}\right)+\sin\phi\frac{1+2e\cos f}{2e^2(1+e\cos f)^2}\Bigg)
\end{aligned} \tag{2.15}$$

where $\mu \approx 3.986 \times 10^5\,\mathrm{km^3\,s^{-2}}$ is the gravitational parameter of the Earth.

The oblateness of the Earth and the Earth's motion around the Sun have a further effect on the progression of ϕ, such that:

$$\frac{\mathrm{d}\phi}{\mathrm{d}t}_{J_2} = \frac{3J_2R_E^2}{2(1-e^2)^2}\sqrt{\frac{\mu}{a^7}} - n_\odot \tag{2.16}$$

This term is later added to the Sun-perigee angle term in Eq. (2.12) to obtain the rate of change of the Sun-perigee angle. The semi-major axis and the eccentricity are not affected by the J_2 effect. However, they are perturbed by aerodynamic drag. Therefore, a term describing this effect has to be added to the semi-major axis and eccentricity terms in Eq. (2.12). The decay due to aerodynamic drag for a static atmosphere can be calculated using the modified Bessel functions according to King-Hele [104]:

$$\begin{aligned}
\frac{\mathrm{d}h_p}{\mathrm{d}t}_{\text{Drag}} &\approx -\sqrt{\frac{\mu}{a^3}}c_D\sigma a^2\rho_p \exp\left[-\frac{ae}{H_p}\right]\left(I_0 + 2eI_1 + 3\frac{e^2}{4}(I_0+I_2) + \frac{e^3}{4}(3I_1+I_3)\right) \\
\frac{\mathrm{d}e}{\mathrm{d}t}_{\text{Drag}} &\approx -\sqrt{\frac{\mu}{a^3}}c_D\sigma a\rho_p \exp\left[-\frac{ae}{H_p}\right]\left(I_1\frac{e}{2}(I_0+I_2) - \frac{e^2}{8}(5I_1-I_3) - \frac{e^3}{16}(5I_0+4I_2-I_4)\right)
\end{aligned} \tag{2.17}$$

with

$$\frac{\mathrm{d}h_p}{\mathrm{d}t}_{\text{Drag}} = \frac{\frac{\mathrm{d}h_p}{\mathrm{d}t}_{\text{Drag}} + a\frac{\mathrm{d}e}{\mathrm{d}t}_{\text{Drag}}}{1-e} \tag{2.18}$$

c_D is the drag coefficient, ρ_p is the atmospheric density at perigee and H_p is the scale height for the exponential model of the atmosphere at perigee. Furthermore, I_k are modified Bessel functions of the first kind of order k and argument $\frac{ae}{H_p}$. For planar orbits and neglecting the rotation of the atmospheric drag has no effect on ϕ.

To obtain the approximate secular change in planar orbital elements due to SRP, J_2 and drag, Eqs. (2.12), (2.16) and (2.17) can be added to yield:

$$\begin{aligned}
\frac{\mathrm{d}a}{\mathrm{d}t} &= \frac{\mathrm{d}a}{\mathrm{d}t}_{\text{SRP}} + \frac{\mathrm{d}a}{\mathrm{d}t}_{\text{Drag}} \\
\frac{\mathrm{d}e}{\mathrm{d}t} &= \frac{\mathrm{d}e}{\mathrm{d}t}_{\text{SRP}} + \frac{\mathrm{d}e}{\mathrm{d}t}_{\text{Drag}} \\
\frac{\mathrm{d}\phi}{\mathrm{d}t} &= \frac{\mathrm{d}\phi}{\mathrm{d}t}_{\text{SRP}} + \frac{\mathrm{d}\phi}{\mathrm{d}t}_{J_2}
\end{aligned} \tag{2.19}$$

This set of equations is used later in this thesis for determining the secular in-plane orbit evolution of high area-to-mass-ratio spacecraft with perigee altitudes in the drag regime.

2.2.2 Secular orbital evolution due to SRP and J_2 in non-singular elements

In this section a further set of expressions for the secular orbital evolution due to SRP and J_2 are introduced. The model presented here was developed by Krivov et al. [6] and includes a full 3D evolution of the orbit. However, as opposed to the planar model introduced in the previous section it does not include the effect of aerodynamic drag and does not consider eclipses. The orbital dynamics are propagated by numerically integrating the averaged Gauss' equations in non-singular Lagrangian elements:

$$\begin{aligned} h &= e\cos(\omega+\Omega) \\ k &= e\sin(\omega+\Omega) \\ p &= \sin i\cos\Omega \\ q &= \sin i\sin\Omega \end{aligned} \tag{2.20}$$

where the fifth element is the semi-major axis a.

The differential equations for the secular change due to the J_2 effect and solar radiation pressure were derived by Krivov et al. [6] and revised by Colombo et al. [84] as:

$$\begin{aligned} \frac{\mathrm{d}h}{\mathrm{d}\lambda_\odot} &= -k\kappa\frac{5I^2-2I-1}{2E^4} - \frac{\alpha}{E(1+I)}\Big(\left(E^2(1+I) - p(p-Hh)\right)\cos\varepsilon_E\sin\lambda_\odot \\ &\quad - \left(E^2(1+I)p - IKk\right)\sin\varepsilon_E\sin\lambda_\odot - (p-Hh)q\cos\lambda_\odot\Big) \\ \frac{\mathrm{d}k}{\mathrm{d}\lambda_\odot} &= h\kappa\frac{5I^2-2I-1}{2E^4} + \frac{\alpha}{E(1+I)}\Big(\left(E^2(1+I) - q(q-Hk)\right)\cos\lambda_\odot \\ &\quad - \left(E^2(1+I)q + IKh\right)\sin\varepsilon_E\sin\lambda_\odot + (q-Hk)p\cos\varepsilon_E\sin\lambda_\odot\Big) \\ \frac{\mathrm{d}p}{\mathrm{d}\lambda_\odot} &= q\kappa\frac{1}{E^4} + \frac{\alpha}{E(1+I)}(Hp-(1+I)k)\left((p\cos\varepsilon_E - I\sin\varepsilon_E)\sin\lambda_\odot - q\cos\lambda_\odot\right) \\ \frac{\mathrm{d}q}{\mathrm{d}\lambda_\odot} &= -p\kappa\frac{1}{E^4} + \frac{\alpha}{E(1+I)}(Hq-(1+I)k)\left((p\cos\varepsilon - I\sin\varepsilon_E)\sin\lambda_\odot - q\cos\lambda_\odot\right) \end{aligned} \tag{2.21}$$

where

$$\begin{aligned} E &= \sqrt{1-h^2-k^2} \\ I &= \sqrt{1-p^2-q^2} \\ H &= hp+kq \\ K &= hq-kp \end{aligned} \tag{2.22}$$

and α and κ are the solar radiation pressure parameter and the J_2 effect parameter defined in Eqs. (2.4) and (2.5). The orbit averaged secular change of the semi-major axis is zero as aerodynamic drag is not considered and the J_2 effect has no influence on the semi-major axis and eclipses are neglected. Krivov et al. [6] have shown that at high semi-major axes the effect of eclipses is small.

These equations are used later in this thesis to calculate the secular evolution of inclined high altitude orbits of high area-to-mass-ratio spacecraft.

2.3 Verification

As discussed earlier, the secular equations presented in the previous section offer very fast numerical propagation but lack some precision. This is because they only consider the secular change in orbital elements and because of the exclusion of perturbations other than SRP, aerodynamic drag and the J_2 effect. Furthermore, the expressions given in Eq. (2.19) are considering only a planar 2D model of the orbital geometry, while the expressions given in Eq. (2.21) do not consider aerodynamic drag. Therefore, a further verification step is necessary. This was performed for sample test cases in either of two ways. One option is the propagation of the orbit using the Gauss' equations of the variation of parameters in three dimensions, the other is a high precision propagation using the Analytical Graphics, Inc. STK HPOP tool. Both methods are described in this section.

2.3.1 Verification using Gaussian VOP equations

The Gaussian variation-of-parameters (VOP) equations are used for the verification of the electrochromic orbit control algorithm developed in Chapters 6 and 7. The expressions are used to calculate the rate of change of the osculating orbital parameters over time. This means that, as opposed to the orbit averaged models introduced in Sec. 2.2, they evaluate the changing parameters at each step of the orbit and are thus a more accurate model of the spacecraft dynamics. The

Gauss' equations were taken from Vallado [53] as:

$$\frac{\mathrm{d}a}{\mathrm{d}t} = \frac{2a^2}{\sqrt{\mu p}}\left(e\sin\left(f\right)a_r + \frac{p}{r}a_\theta\right) \tag{2.23}$$

$$\frac{\mathrm{d}e}{\mathrm{d}t} = \frac{p\sin f a_r + \left((p+r)\cos f + er\right)a_\theta}{\sqrt{\mu p}} \tag{2.24}$$

$$\frac{\mathrm{d}i}{\mathrm{d}t} = \frac{r\cos\omega + f}{\sqrt{\mu p}}a_n \tag{2.25}$$

$$\frac{\mathrm{d}\Omega}{\mathrm{d}t} = \frac{r\sin\omega + f}{\sqrt{\mu p}\sin i}a_n \tag{2.26}$$

$$\frac{\mathrm{d}\omega}{\mathrm{d}t} = \frac{-p\cos f a_r + (p+r)\sin f a_\theta}{e\sqrt{\mu p}} - \frac{r\sin\omega + f}{\sqrt{\mu p}\tan i}a_n \tag{2.27}$$

$$\frac{\mathrm{d}f}{\mathrm{d}t} = \frac{\sqrt{\mu p}}{r^2} - \frac{p\cos f a_r - (p+r)\sin f a_\theta}{e\sqrt{\mu p}} \tag{2.28}$$

where p is the semilatus rectum, $p = a\left(1-e^2\right)$, and a_r, a_θ and a_n are the accelerations experienced by the spacecraft in the radial, transversal and normal directions respectively.

2.3.2 High fidelity verification using STK

The other method of verification used in Chapters 3, 4 and 5 is the point-wise verification of the behaviour using a high precision orbit propagator. In this thesis the Analytical Graphics, Inc. STK HPOP tool was used for this purpose [105]. This propagator calculates the trajectory at each time step using a Runge-Kutta-Fehlberg algorithm [106]. It takes into account solar radiation pressure, aerodynamic drag, the Earth gravitational harmonics up to 21^{st} order, and third body perturbations due to the Sun and the Moon in addition to SRP. The atmospheric density model used is the Jacchia-Roberts model which accounts for seasonal and divisional variations of the density [107].

PART I

Metre-scale:

Passive Orbit Manœuvres for Small Satellites

Chapter 3

Passive GTO to LEO Transfer

In the first part of this thesis the dynamics introduced in Sec. 2.1 are applied to passive orbit transfer for small satellites. In particular, a passive geostationary transfer orbit (GTO) to low Earth orbit (LEO) transfer and later a passive deorbiting method are considered. In this chapter a passive orbit transfer for CubeSats from a GTO to LEO using solar radiation pressure and aerodynamic drag is investigated, and a surface area increasing device sized.

As discussed in Sec. 1.2, the need for a passive transfer method from GTO to LEO arises due to the limited availability of piggyback launches to LEO, the main operational regime for small satellite missions, and the typical lack of propulsion capabilities for CubeSats. The work in this chapter investigates further the method of solar radiation pressure augmented passive GTO to LEO transfer initially discussed by Colombo and McInnes [32]. It exploits the effect of solar radiation pressure to raise the orbit perigee while at the same time lowering the apogee using aerodynamic drag. Both effects are dependent on the area-to-mass-ratio of the spacecraft. By artificially increasing this ratio through the deployment of a large gossamer structure these effects can be enhanced. In the original work [32] an analysis of the sensitivity of the transfer time and final altitude of an SRP-augmented GTO to LEO transfer with respect to initial perigee angle of the GTO, and reflectivity and area-to-mass-ratio of the spacecraft was performed. The work presented in this chapter builds on and extends this research. In particular, the method is investigated using a high precision orbit propagator including secondary perturbations. It is shown that the time of the initial launch is important for the success of the manoeuvre, due to third body gravitational effects experienced by the CubeSat in GTO. These effects were not considered in the initial work by Colombo and McInnes [32].

The orbit transfer method uses a spacecraft fitted with an area-to-mass-ratio enhancing device. The design options for this device are discussed in Sec. 3.2.1, but an inflatable balloon is chosen as the baseline in this chapter. Any results will also work on a different shaped device as long as it is deployable at the start of the manœuvre, ejectable or retractable at the end, and its area-to-mass-ratio with respect to the Sun is fixed. As discussed in Sec. 1.2.1, once in GTO the spacecraft will wait until the correct time to start the manœvre. It will then deploy its transfer device. When the desired goal orbit is reached the device is ejected or retracted to avoid rapid deorbiting.

In Sec. 3.1 the basic orbital dynamics governing the scenario are discussed and the effectiveness of the method analysed. A test scenario is computed and the radiation environment investigated. Finally, in Sec. 3.2 possible design options for the area-to-mass-ratio enhancing device are discussed.

3.1 Orbital transfer

In this section the orbital dynamics of the passive GTO to LEO transfer are discussed in detail. Then, a mission scenario is designed using an arbitrarily chosen launch date. Finally, a radiation analysis for the manœuvre is performed and the consequences for the spacecraft design are discussed.

3.1.1 Orbital dynamics

The transfer method investigated in this chapter is based on the Hamiltonian dynamics discussed in Sec. 2.1.1, where it can be seen that the orbit of a high area-to-mass-ratio spacecraft perturbed by SRP will experience an increase or a decrease in eccentricity depending on ϕ, the angle between its perigee and the direction of the Sunlight, where ϕ is defined as is Eq. (2.1) in chapter 2. The angles for planar orbits can be seen in Fig. 2.2 in Sec. 2.1. This passive effect will be used for the transfer.

It can be seen in Eq. (2.2) that for $-\pi < \phi < 0$ the average change of eccentricity over one orbit is always positive and for $0 < \phi < \pi$ it is negative. The change in ϕ depends on the orbit and the area-to-mass-ratio of the spacecraft (see Eq. (2.3)). Without the effect of solar radiation pressure and the Earth's oblateness, ϕ, will always have an average rate of change of $\frac{\mathrm{d}\phi}{\mathrm{d}\lambda_\odot}_{\mathrm{rot}} = -1$ due to the Earth's motion around the Sun. The average rate of change of ϕ due to the J_2 effect

is always positive and dependent on the semi-major axis and eccentricity. For GTO the rate of change due to J_2 is $0 < \frac{\mathrm{d}\phi}{\mathrm{d}\lambda_\odot}_{J_2} < 1$. Therefore, the total rate of change $\frac{\mathrm{d}\phi}{\mathrm{d}\lambda_\odot} = \frac{\mathrm{d}\phi}{\mathrm{d}\lambda_\odot}_{\mathrm{rot}} + \frac{\mathrm{d}\phi}{\mathrm{d}\lambda_\odot}_{J_2}$ is negative and $\left|\frac{\mathrm{d}\phi}{\mathrm{d}\lambda_\odot}\right| < 1$, so that one full rotation of the Sun-perigee angle takes more than a year. The effect of solar radiation pressure on the average rate of change depends mainly on the semi-major axis and area-to-mass-ratio. Its sign however is dependent on ϕ. For $-\frac{\pi}{2} \leq \phi \leq \frac{\pi}{2}$ it is negative, otherwise it is positive.

It can be seen that the value of ϕ at the deployment of the area-to-mass-ratio enhancing device has a significant effect on the success of the manœuvre. Firstly, the transfer needs to be initiated when $0 < \phi < \pi$, so that the eccentricity decreases and the perigee is raised [32]. Secondly, the manœuvre needs to be performed in such a way that the perigee is within the drag region long enough to lower the apogee sufficiently. Therefore, a sharp increase in perigee altitude is not desirable. An analysis of a range of starting conditions performed by Colombo and McInnes [32] shows the achievable perigee altitude as a function of the initial Sun-perigee angle, ϕ_0, and the area-to-mass-ratio for GTOs with perigee altitude $h_p = 250\,\mathrm{km}$. In this analysis the simulation is performed by propagating the expressions for the secular variation of the orbital elements due to solar radiation pressure, the J_2 effect and aerodynamic drag in a planar 2D model introduced in Sec. 2.2.1. It is shown that the GTO to LEO transfer works best for $0 < \phi_0 < \frac{\pi}{4}$.

It is common for spacecraft to be launched into a midnight GTO. In this case the final insertion burn will be performed at midnight which means that the orbit perigee is on the opposite side of the Earth from the Sun, *i.e.* $\phi = 0$. This is disadvantageous for the GTO to LEO transfer because for it to be successful ϕ needs to be between 0° and 45°, while the change in ϕ is negative as shown before. Consequently, the spacecraft must remain waiting in GTO for almost a full rotation of ϕ which takes approximately 620 days. Although occasionally GTO launches have different initial orientations towards the Sun, the midnight launch is the most common and also a worst case scenario for the GTO to LEO transfer. Therefore, this type of launch is assumed here. In the next subsection an example mission scenario is defined for an arbitrarily selected launch date of the 1$^{\mathrm{st}}$ of October 2014.

3.1.2 Test scenario

The mission analysis on a test scenario is performed using two different orbit propagators. Analytical Graphics Inc. Satellite Tool Kit (STK) is used for high precision orbit propagation (HPOP) including an extensive set of orbital perturbations as detailed in Sec. 2.3.2. The propagation using this algorithm has a high fidelity but also a long computational run-time. It is used for the determination of the evolution of single scenarios. For the analysis of a large range of scenarios

MATLAB is utilised which uses the analytical equations for the secular variations of the 2D planar orbital elements under the effect of SRP, J_2 and aerodynamic drag, introduced in Sec. 2.2.1. This method of propagation is less accurate than STK but can be performed significantly faster.

Three steps are needed for the mission design. After choosing a launch date, the GTO is propagated in STK to reach the initial conditions for $0 < \phi_0 < \frac{\pi}{4}$. This is because luni-solar perturbations are assumed to have a significant effect on the orbit during the waiting time causing its perigee altitude to librate. In this propagation a 3U CubeSat is assumed with an area-to-mass-ratio of $0.01\,\mathrm{m^2\,kg^{-1}}$, a drag coefficient of 2.2 and a coefficient of reflectivity of 1.5, representative of a CubeSat with a stowed device. From the results of this simulation a table of starting conditions for the orbit transfer is extracted. These conditions are then imported into MATLAB and the 2D propagation is used to calculate the resulting final perigee altitude as a function of waiting time. From this, the best waiting time is chosen and the end-to-end scenario is run in STK. After the balloon ejection, the simulation is run for another year to ensure the spacecraft can maintain its operational orbit for such a period of time.

Waiting in GTO

Figure 3.1 shows the progression of ϕ from GTO insertion. The evolution is steady and it can be seen that after 540 to 620 days of waiting (grey band) ϕ will be in the appropriate zone for the manœuvre. In Fig. 3.2 the evolution of the semi-major axis, a, and the altitude of the perigee, h_p are shown. It can be seen that the orbit loses some energy during the waiting time due to aerodynamic drag at perigee causing the semi-major axis to decrease. The eccentricity and consequently the perigee altitude oscillate due to third body gravitational effects. This means that at the time of the start of the manœuvre the altitude of the perigee is different than at GTO insertion and measures between 220 km and 270 km.

Choosing the manœuvre starting time

The different initial parameters for the manœuvre are then propagated in MATLAB to find an approximation of the final perigee altitude after the orbit transfer with the device deployed to achieve an area-to-mass-ratio of $3\,\mathrm{m^2\,kg^{-1}}$. For this, the orbital parameters of the GTO after different waiting times are propagated until the eccentricity is lower than 0.05 and the orbit is thus quasi-circular. The results of this analysis are shown in Fig. 3.3. It can be seen that the final perigee is higher than the initial perigee for waiting times between 575 and 600 days. As a trade-off

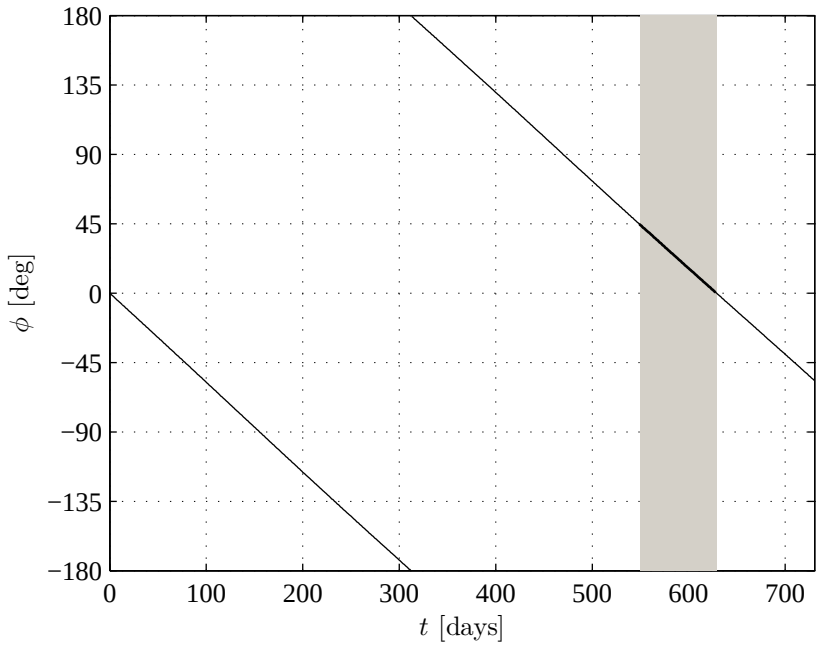

Figure 3.1: Evolution of the Sun-perigee angle of the GTO after launch - the grey band represents the waiting time corresponding to the manœuvre start window

between trying to maximise the final perigee altitude and choosing a time in the middle of the interval, a waiting time of 585 days is chosen.

It should be noted that the date at which the spacecraft is first inserted into GTO does have a significant impact on whether or not the manœuvre can be performed. A second analysis of the oscillations in waiting time and evaluation for the final perigee altitude of a different starting date has revealed that the intial perigee altitude at the start of the manœuvre is important for its success. This analysis is performed for a launch on the 1st of January 2015. Because of the different geometry of the Sun and the Moon at orbit insertion the eccentricity oscillates in a different phase to the previous simulation. The result is a higher perigee altitude in the manœuvre critical region of $0 < \phi < \frac{\pi}{4}$. While the October 2014 launch saw the perigee in the range of 220 to 270 km, it is now between 270 and 310 km for the January launch. This higher initial perigee altitude would suggest that the achievable final perigee altitude is higher than that of the October launch as well. However, it was shown that this is not the case.

Figure 3.4 shows the initial and resulting final perigee altitudes for different effective area-to-mass-ratios for the January launch. Counter-intuitively the higher initial perigee altitudes with respect to the October launch presented in Fig. 3.3 resulted in lower final perigees. The reason for this is the fact that the orbit does not receive a large semi-major axis reduction due to drag initially.

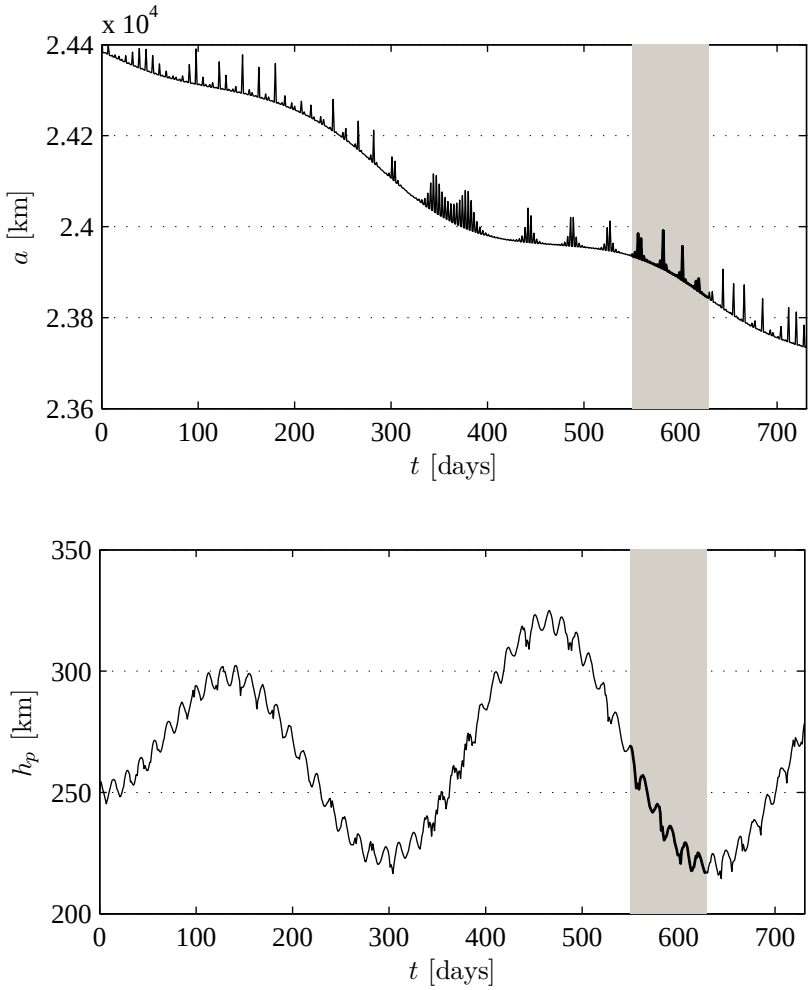

Figure 3.2: Evolution of the semi-major axis and perigee altitude of the GTO after launch on 01/10/2014 - the grey band represents the waiting time identified in Fig. 3.1

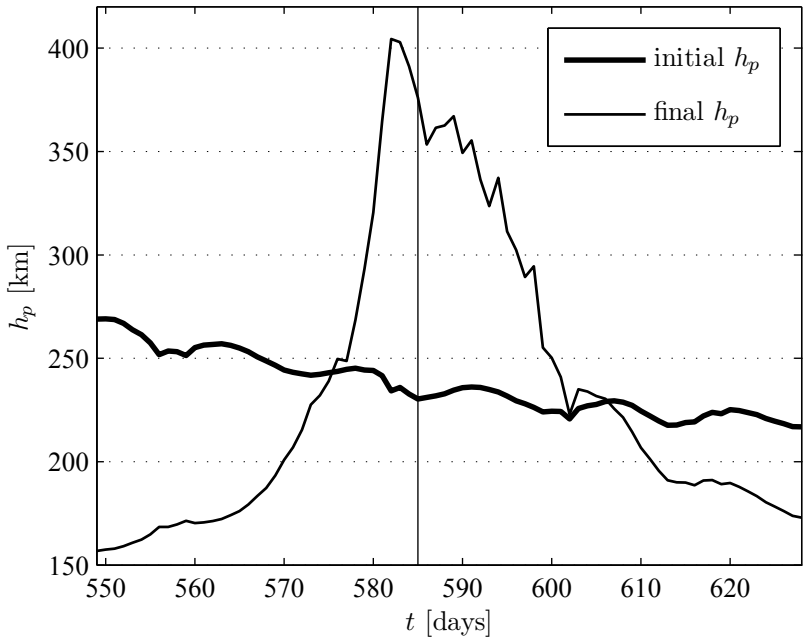

Figure 3.3: Initial perigee altitude and approximation of the final perigee altitude as a function of waiting time (launch on 01/10/2014)

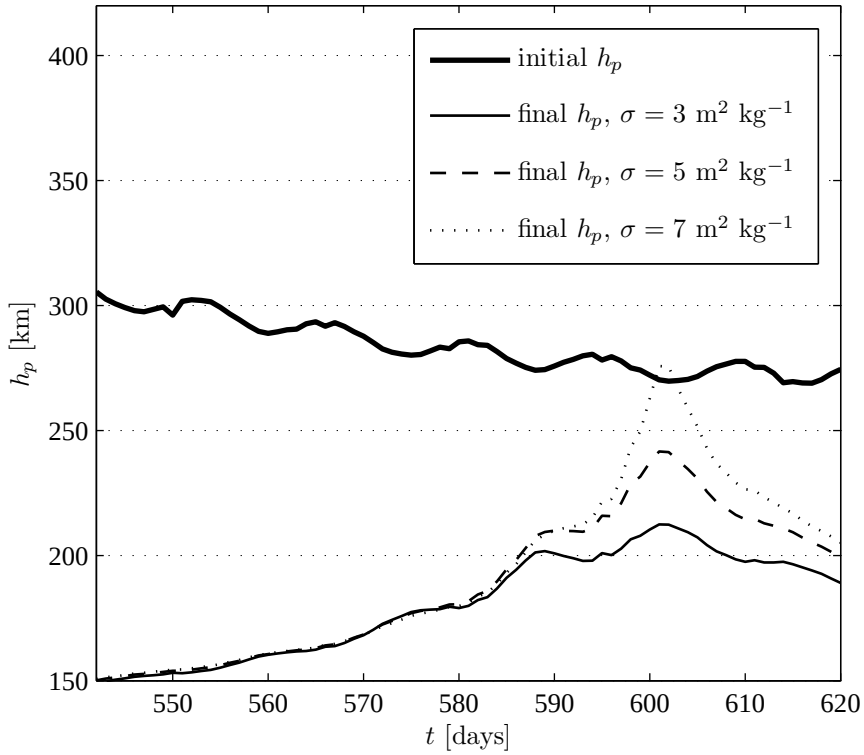

Figure 3.4: Initial perigee altitude and approximation of the final perigee altitude as a function of waiting time (launch on 01/01/2015)

It then experiences the increase in perigee altitude due to solar radiation pressure without having reached the correct semi-major axis. After initially decreasing the eccentricity, solar radiation pressure next causes it to increase again. When drag starts to take effect again it decreases the apogee while SRP continues to decrease the perigee resulting in a very low final orbit. Only high area-to-mass-ratios ($\sigma = 7\,\mathrm{m^2\,kg^{-1}}$) manage to gain a small increase in perigee altitude by reducing the semi-major axis fast in the first phase.

Complete manœuvre

Finally, the full manœuvre is simulated in STK (see Sec. 2.3.2). The initial parameters are those of a midnight launch GTO from Kourou on the 1$^{\mathrm{st}}$ of October 2014. The initial semi-major axis is 24 474 km and the initial perigee altitude 250 km. The inclination is 6°, the argument of perigee 178° and $\phi = 0°$. The orbit is propagated with a stowed area-to-mass-ratio of $0.01\,\mathrm{m^2\,kg^{-1}}$ and $c_R = 1.5$ for 585 days. After that time the area-to-mass-ratio is increased to $3\,\mathrm{m^2\,kg^{-1}}$ and c_R is changed to 1 to model a balloon shape. The device shape and resulting reflectivity will be discussed in detail in Sec. 3.2.1.

When the eccentricity reaches 0.05 the area-to-mass-ratio and coefficient of reflectivity are changed back to the original values to model the balloon jettisoning and the propagation is continued for another year.

Figure 3.5 shows the evolution of the semi-major axis and the perigee altitude during the manœuvre. It can be seen that the semi-major axis remains quasi-constant during the waiting time. When the area-to-mass-ratio changes it decreases rapidly, and finally in LEO the semi-major axis is stable again. The perigee altitude oscillates during the waiting time. When the balloon is deployed the effect of solar radiation pressure causes the perigee to rise before it decreases again slightly. At the end of the orbit transfer the perigee is 100 km above where it started.

The evolution of the eccentricity and Sun-perigee angle are shown in Fig. 3.6. It can be seen that whenever the area-to-mass-ratio is low the eccentricity, similar to the semi-major axis, is relatively stable. It can also be noted that the direction of the progression of ϕ changes when the device is deployed. This is due to the effect of solar radiation pressure on the rate of change of the Sun-perigee angle. In the final LEO the direction of change is still positive even after ejection of the device. This is due to the stronger influence of the J_2 effect on orbits with lower semi-major axis.

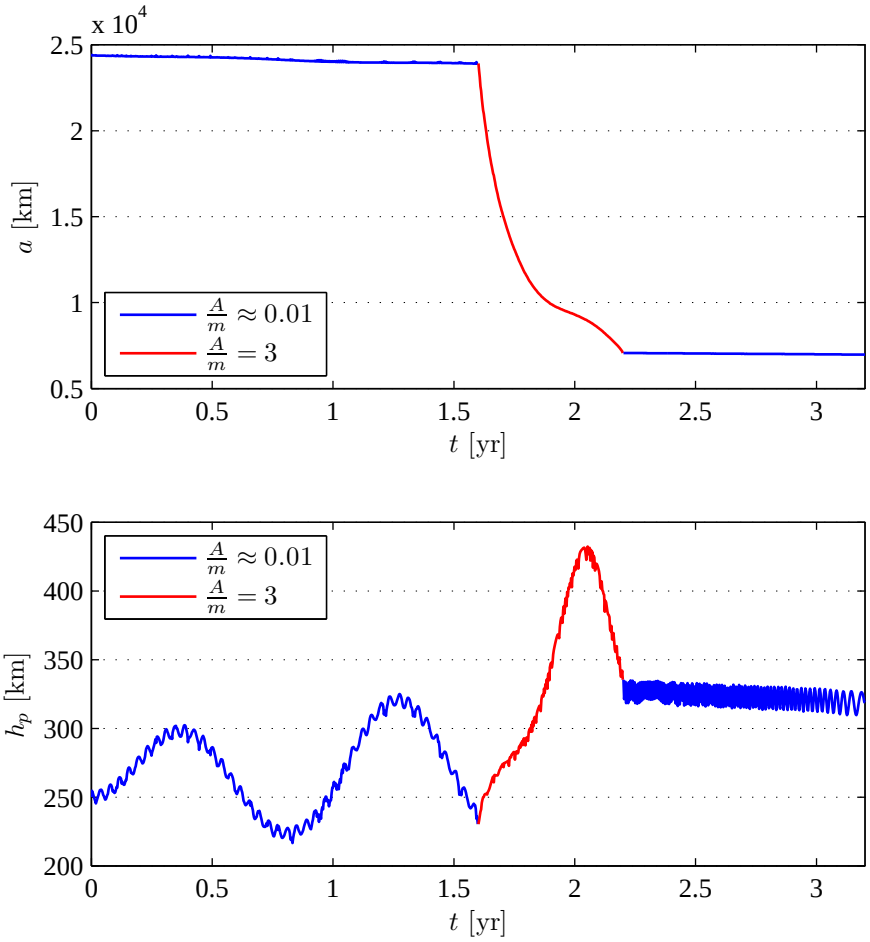

Figure 3.5: Evolution of the semi-major axis and perigee altitude during the mission (launch on 01/10/2014)

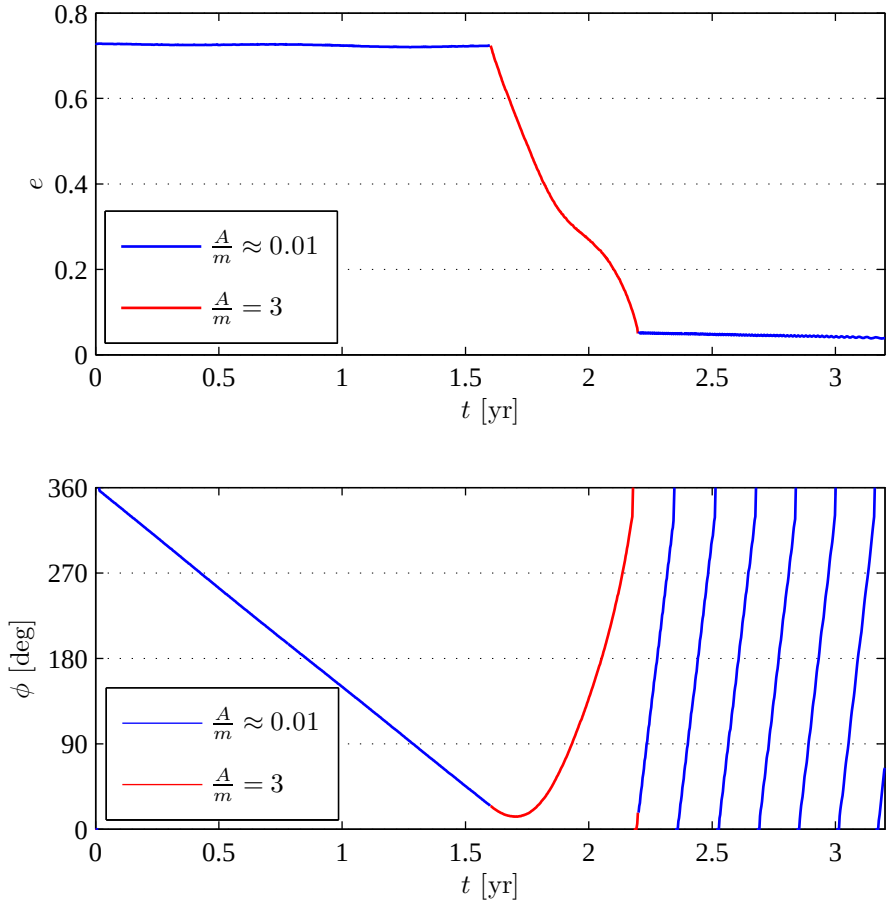

Figure 3.6: Evolution of the eccentricity and Sun-perigee angle during the mission (launch on 01/10/2014)

3.1.3 Radiation analysis

The long waiting time in GTO and the subsequent manœuvre mean that the spacecraft will spend approximately two years passing through the Van Allen belts. A radiation analysis is performed in ESA's space environment information tool (SPENVIS) [108]. A file with sampled coordinates throughout the mission lifetime is input into the tool, which then calculates the electron and proton fluxes on the spacecraft. The results are shown in Fig. 3.7 as a function of mission time (compare with Fig. 3.5). It can be seen that the fluxes are highest in GTO, during the transfer they decrease and are between two (electrons) and five (protons) magnitudes lower in LEO.

The fluxes are then used to calculate the total ionising dose on a Silicon component as a function of Aluminium shielding thickness d_S. Figure 3.8 shows the results. It can be seen that while the ionising dose due to trapped electrons decreases almost log-linearly with thickness the ionising dose due to *Bremsstrahlung* and trapped protons stagnates after an initial fast decrease. 7.5 mm spot shielding of sensitive vital components such as the flight computer and the flash memory reduces the total ionising dose to 1×10^{-4} rad. According to Wertz and Larson [109] common commercial of the shelf (COTS) components can withstand this dose of radiation.

3.2 Design of the transfer device

In this section design options for the orbital transfer device are discussed. The requirements for the module are defined. Then the main design choices are investigated and the baseline design introduced and analysed. The purpose of this design exercise is to gain an understanding of different design options and an idea of the achievable area-to-mass-ratios. The design presented here is very conceptual in nature. A more detailed design and a study of the technical feasibilty and maturity is future work.

The orbit transfer device consists of a deployable structure for enhancing the spacecraft's area-to-mass-ratio to increase the effect of solar radiation pressure and aerodynamic drag. The structure needs to be stowed completely within the spacecraft during launch and the waiting time in GTO. After deployment the structure needs to rigidise to ensure survival against micro-meteorite and debris impacts during the transfer. The structure also needs to be ejectable or retractable after the transfer is complete to avoid rapid deorbiting. If ejected, the device shall deorbit within a short time to avoid collision with other spacecraft. Three main design choices have to be made for the deployable structure: which shape should it have, how is it deployed and how is it rigidised and finally ejected. These choices are discussed in the following subsections.

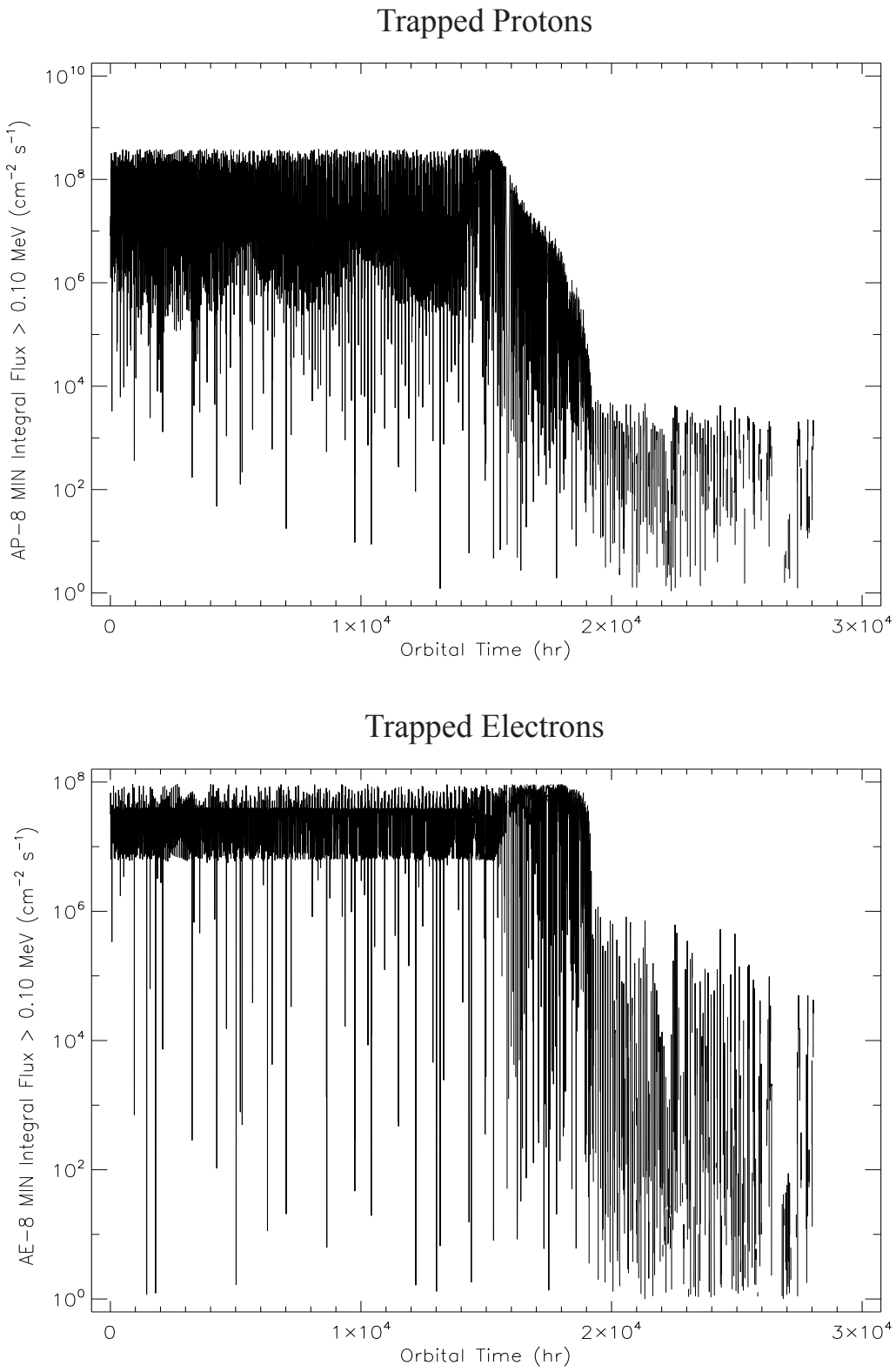

Figure 3.7: Electron and proton fluxes above 0.1 MeV as a function of mission time

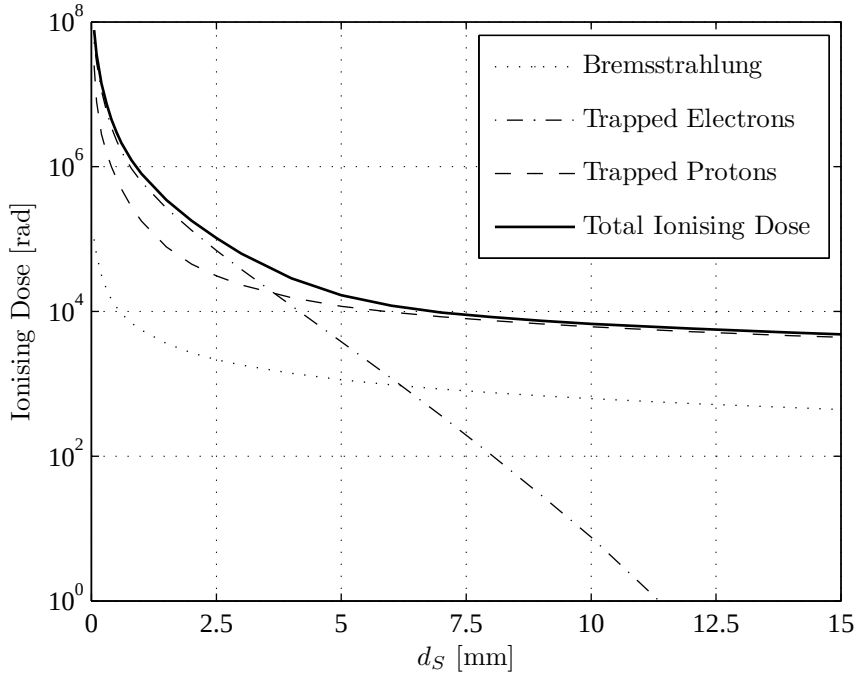

Figure 3.8: Ionising dose on silicon spacecraft component as a function of the thickness of the aluminium shielding

3.2.1 Device shape

The main options for the shape of the device are a balloon, a cone/pyramid or a flat sail. The cone and the sail need to be directed to face the Sun in order to experience the desired effect on the orbit evolution. Without a damping moment, of these three options only the balloon can be considered truly passive, however the balloon would also need eight-times more surface material than the flat sail. This is due to the ratio of surface area of a sphere to its cross-sectional area and because of the different reflection characteristics of the geometrical shapes.

The coefficient of reflectivity c_R determines the momentum an object gains from incident radiation. It is dependent on the optical properties of the surface material and on the geometrical shape of the object. It is assumed that the material is not transmissive. The incoming solar radiation is partly absorbed and partly reflected. The reflection is part specular and part diffuse. Specular reflection is directional and leaves the surface at an angle which depends on the angle of incidence of the radiation. Diffuse reflection is multi-directional. In this discussion both reflections are considered together as a reflectivity $\eta \in [0, 1]$, where $\eta = 0$ means fully absorptive and $\eta = 1$ is a perfect mirror. The material is assumed to be highly specular, which means that η is high

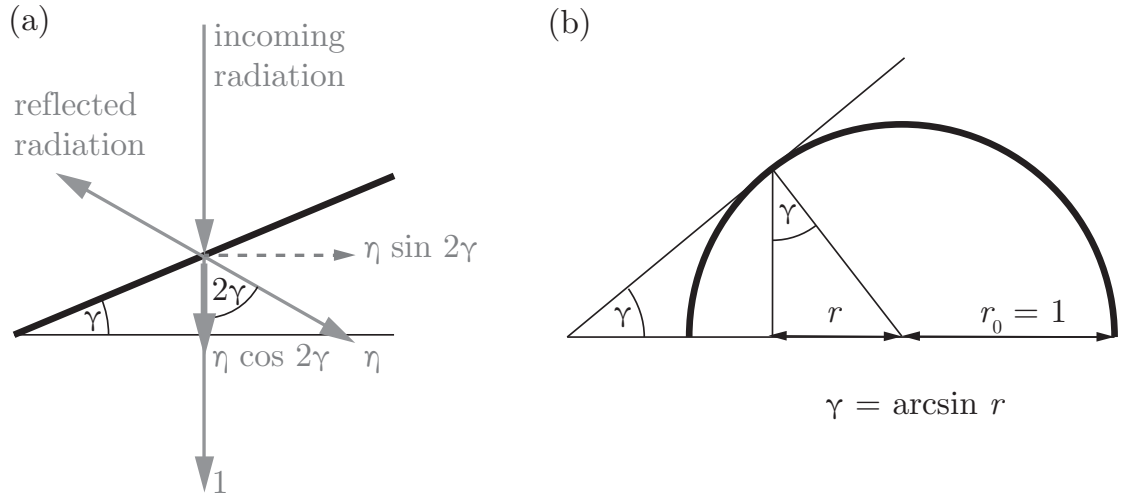

Figure 3.9: (a) Effective reflectivity of an inclined surface, (b) surface inclination of a sphere

and the vectors of the incoming and reflected radiation are symmetrical with respect to the local surface normal.

The effective coefficient of reflectivity of any sphere is one, as can be proven geometrically. First the impulse transmitted to a non-transmissive surface which is tilted by angle $\gamma \in [0, \frac{\pi}{2}]$ with respect to the radiation normal is determined. The incoming radiation is partly absorbed and partly reflected at an angle of 2γ. Figure 3.9a shows the geometry of this problem. It can be seen that the total impulse along the direction of the incoming radiation is proportional to $1 + \eta \cos 2\gamma$. The other part of the resulting force lies in the plane normal to the incoming radiation. This force can be neglected as it will be cancelled out in an axisymmetric shape. Next, the tilt dependent effective coefficient of reflectivity can be defined as a function of the in-plane radius from the centre of pressure of the sphere. Figure 3.9b shows that, for a sphere of radius 1, the tilting angle $\gamma = \arcsin r$. Therefore, the local coefficient of reflectivity is $1 + \eta \cos(2 \arcsin r)$. This can be integrated to find the total resulting coefficient of reflectivity $c_{R,\text{sphere}}$. The term for the local c_R is multiplied by the circumference at that position and integrated over $r \in [0, 1]$. The integral is then divided by the full cross-sectional area. The resulting value is not dependent on η and always equals one:

$$\begin{aligned} c_{R,\text{sphere}} &= \frac{1}{\pi} \int_0^1 2\pi r \left(1 + \eta \cos(2 \arcsin r)\right) \mathrm{d}r \\ &= 1 \end{aligned} \tag{3.1}$$

In the case of a cone or pyramid the tilt angle determines the effective coefficient of reflectivity as shown in Fig. 3.9a. For the sphere the orthogonal forces cancel each other out, and for a symmetrical cone or pyramid when the main axis is parallel to the direction of the radiation. The effective coefficient of reflectivity can be written as:

$$c_{R,\text{cone}} = 1 + \eta \cos 2\gamma \tag{3.2}$$

It is interesting to note that $c_{R,\text{cone}} = 1$ for $\gamma = \frac{\pi}{4}$, while $1 \leq c_{R,\text{cone}} \leq 1 + \eta$ for $\gamma < \frac{\pi}{4}$ and $1 - \eta \leq c_{R,\text{cone}} \leq 1$ for $\gamma > \frac{\pi}{4}$. The cone or pyramid is a flat sail if $\gamma = 0$. In that case the coefficient of reflectivity is $c_{R,\text{flat}} = 1 + \eta$.

To summarise, while a fully reflective, flat sail oriented normal to the incident Sunlight will have an effective coefficient of reflectivity of 2, a sphere will only have an effective coefficient of reflectivity of 1, and thus needs twice the cross-sectional area. The clear advantage of a sphere is that it has the same cross-sectional area from any aspect angle. Thus, after deployment and rigidisation no further control is needed until the device is ejected. The manœuvre will therefore occur completely passively. A flat sail would need to be controlled in order to constantly face the Sun, similar to solar sailing. However, a simple control algorithm can be implemented because no active orbit propagation needs to be performed on-board, and the only requirement is to keep the sail Sun-pointing. Another advantage over conventional solar sailing is that fast attitude changes do not need to be performed.

A cone or pyramid is a compromise between the balloon and the sail. They both require less surface material than the balloon and due to their conic shape experience a shuttlecock-type effect which creates an oscillation around a stable equilibrium attitude (when the centre of pressure is behind the centre of mass with respect to the acting force). These designs would, however, need a mechanism to dampen this oscillation. Then, a constant Sun-pointing attitude could be assured for altitudes outside the region of aerodynamic drag. A problem for the sail and the cone arises however when the spacecraft enters the drag region. In this region the force of drag and the force of SRP can act from different directions. The cone would naturally face the direction of the combined torque-inducing forces acting on the device.

As a baseline design for the structure the balloon shape is chosen and in further analysis it is assumed that the spacecraft to be transferred is a 3U CubeSat ($10\,\text{cm} \times 10\,\text{cm} \times 30\,\text{cm}$) with 1U dedicated to the orbit transfer device. Again, a balloon is the most promising shape for a simple, low-cost orbit transfer device, as it requires no active attitude control or passive stabilisation during the transfer and can be deployed through internal pressure.

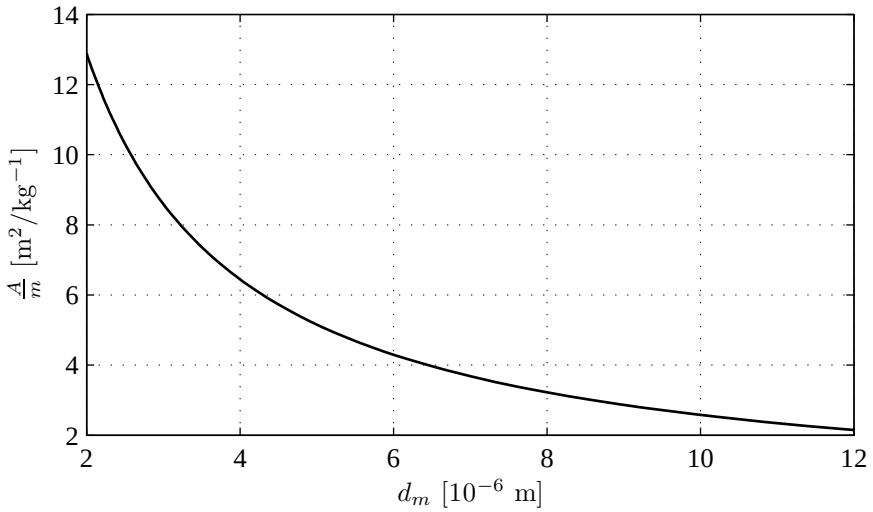

Figure 3.10: Achievable area-to-mass-ratio of the 3U CubeSat as a function of material thickness for a balloon shaped device

In order to gauge the possible area-to-mass-ratio supplied by a balloon, it is assumed that the surface material of the balloon is UV-proofed Mylar of thickness d_m. The balloon is stowed within 82 % of the volume of a 1U CubeSat module with a packaging efficiency of 50 %. This packaging efficiency is taken from physical tests at the University of Strathclyde [110]. The resulting area-to-mass-ratio as a function of material thickness can be seen in Fig. 3.10. State-of-the-art solar sail concepts use 2 µm thick Mylar [111], while 12 µm thick metallised PET rescue foil is easily available commercially. It is assumed that a material with a final thickness of 8 µm is plausible. Therefore, an area-to-mass-ratio of $3\,\mathrm{m^2\,kg^{-1}}$ for the whole system is used. Although the stowed balloon takes up 82 % of a 1U module, it weighs less than 200 g.

3.2.2 Inflation

Possible options for deployment of the balloon include mechanical methods and gas-based inflation. Mechanical methods extend strut elements using tensile forces by exploiting material properties or using micro-motors. However, they are not well suited for curved shapes such as a sphere. Inflation is the preferred method for the deployment of spherical shapes as the internal pressure can ensure an even deployment. The gas for the deployment can either be stored in compressed form or be generated in a cold gas generator. The former option is disadvantageous as the gas would need to be stored for a significant time without leaking, while pressurised containers can be a hazard during launch.

Therefore, a nitrogen gas generator is optimum for inflation of the balloon. This mechanism satisfies the key drivers since it can be manufactured cheaply, is very reliable and mass and volume efficient. For 0.5 g of nitrogen one micro gas generator is required which measures 15 cm^3 and weighs of order 8 g [112]. An inflation pressure of 1 Pa is assumed which leads to one generator per 43.5 m^3 of balloon volume using the ideal gas equation and assuming the nitrogen is at room temperature at inflation. This means that with a volume of order 31 m^3 only one generator is needed for inflation.

3.2.3 Rigidisation and ejection

Several alternative methods of rigidisation exist. Mechanical rigidisation was used by the Echo balloons, where an aluminium coating on the balloon surface was stretched beyond its yield point through inflation [113]. The advantage of this method is that it works regardless of storage time and under most environmental conditions. The disadvantage is the large mass it requires for the aluminium coating and the extra gas for high internal pressure. This disqualifies the method for use in the orbit transfer device.

Low mass methods of rigidisation use resin with which the surface material is impregnated and which hardens under given circumstances. Resins for use in rigidisation are not considered a mature technology. For the purposes of this thesis, however, we are neglecting the possible complications arising from low availability and technological maturity. A popular method is UV curing resin, which hardens when exposed to ultraviolet radiation [113]. This method, however, has a short shelf-life and is thus not applicable for this mission in which a long waiting time in GTO comes before inflation. Other resins will harden when they either heat up or cool down. The former is an irreversible chemical process which cannot be tested before launch. A cold curing resin is therefore seen as the best option. These resins are typically elastomers which harden when they cool below their glass transition temperature [114]. This is advantageous as the balloon will cool down passively after deployment due to its reflective surface material and low mass.

In order to be able to inflate the balloon, it needs to be heated prior to deployment using solar radiation. This is achieved by turning the spacecraft to face the Sun with the orbit transfer module (OTM). The lid of the OTM is coated with Nickel Oxide, which has a large solar absorptivity α a low infrared (IR) emissivity, ε: ($\alpha_{\mathrm{NiO}} = 0.9$, $\varepsilon_{\mathrm{NiO}} = 0.1$), and so will quickly heat up in the Sun. The heat is then transported via a copper casing around the stowed balloon. Copper has excellent heat conduction and low infrared emissivity, $\varepsilon_{\mathrm{Cu}} = 0.03$. To minimise the radiative heat transfer to the rest of the spacecraft, the structure is lined with Mylar which has a very low infrared absorptivity

of $\varepsilon_{\text{Mylar}} = 0.03$ and for bodies in thermal equilibrium the emissivity is the same as the absorptivity at a given wavelength [115]. Figure 3.11 shows an exploded view of the orbit transfer module.

Tensioned wires holding the lid to the module are cut using pyro-cutters and the balloon is forced out of the smooth casing through the pressure of the inflation gas. Upon reaching LEO another tension wire is cut which holds the frame and copper case to the spacecraft. The aerodynamic forces immediately separate the balloon from the spacecraft and the unit deorbits within 9 hr as can be seen in Fig. 3.12.

3.2.4 Thermal analysis

Thermal analysis is now performed on the system before and after inflation to ensure that the balloon can be sufficiently heated for deployment and then will cool enough for rigidisation.

Transient thermal analysis of heating process

A transient thermal analysis is performed in Matlab to determine the required time for the pre-deployment heating process. The lid, the copper casing, the Mylar lining and the stowed balloon are partitioned into nodes. The differential equations defining conductive and radiative heat exchanges between different nodes and the solar radiation input and infrared output are now given. $\sim$ symbol denotes a thermal node, where the spacecraft structure $\tilde{S}$ acts as a constant temperature heat sink. The set-up is visualised in Fig. 3.13.

The rate of change of thermal energy in node $\tilde{A}$ due to heat conduction with another node $\tilde{B}$ can be expressed as:

$$\left(\frac{\mathrm{d}E_{\tilde{A}}}{\mathrm{d}t}\right)_{\tilde{B}} = k_{(\tilde{A},\tilde{B})}(T_{\tilde{B}} - T_{\tilde{A}}) \tag{3.3}$$

where $k_{(\tilde{A},\tilde{B})}$ is the conductive heat exchange factor between the two nodes which is dependent on the material properties, the cross-sectional area of the link and the distance between the nodes. $T_{\tilde{A}}$ and $T_{\tilde{B}}$ are the temperatures of nodes $\tilde{A}$ and $\tilde{B}$ and a function of the heat capacity $c_{\tilde{A}}$ and $c_{\tilde{B}}$ of the nodes and their stored thermal energy $E_{\tilde{A}}$ and $E_{\tilde{B}}$. For example, for node $\tilde{A}$ the temperature is expressed as [116]:

$$E_{\tilde{A}} = \frac{T_{\tilde{A}}}{c_{\tilde{A}}} \tag{3.4}$$

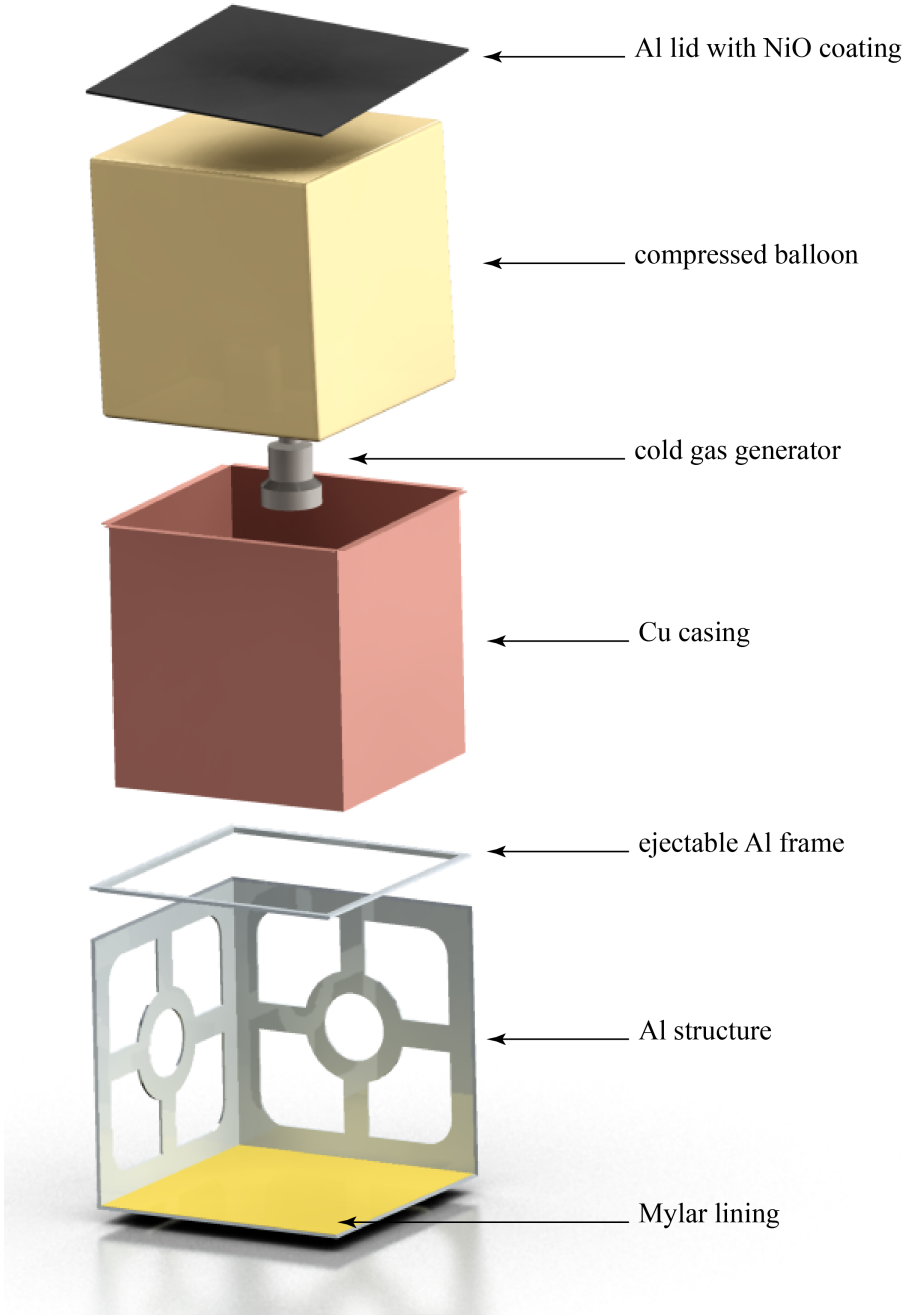

Figure 3.11: Exploded view of a possible orbit transfer module for CubeSats

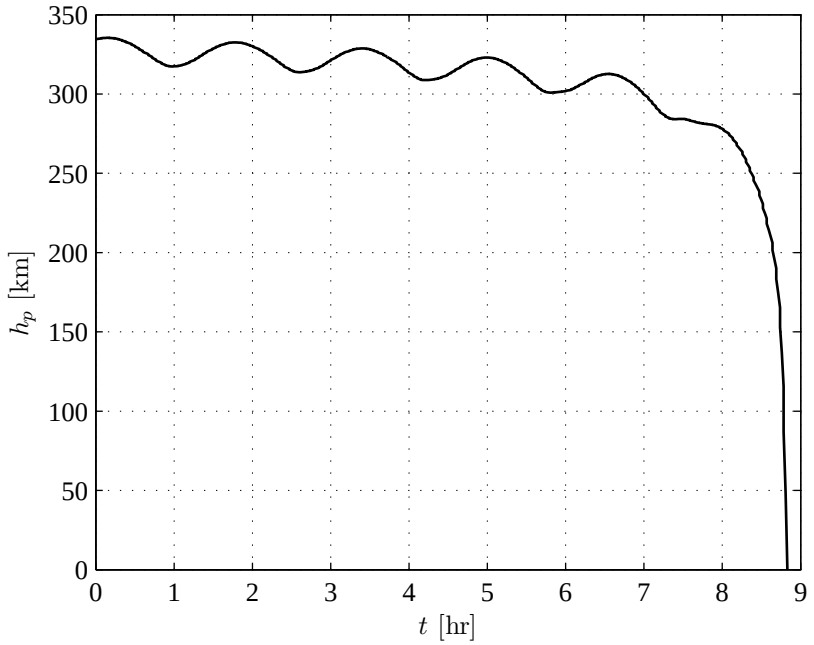

Figure 3.12: Perigee altitude, h_p, of the balloon over time after ejection for the scenario shown in Fig. 3.5. Simulated in STK with atmospheric model for January 2017.

Using these relations a system of differential equations is set up to express the conductive heat exchange within the whole system, the size and form of which depends on the number nodes and types of input.

All nodes in the system are conductively linked to their neighbouring nodes and all experience conductive heat exchange during the simulation. However, only specific nodes experience radiative heat exchange. The nodes of the copper casing and the nodes of the lid both radiate heat away, and only the nodes of the lid receive radiative heat from the Sun. The received solar thermal energy per node in the lid $\tilde{L}$ is:

$$\left(\frac{\mathrm{d}E_{\tilde{L}}}{\mathrm{d}t}\right)_{\odot} = \alpha_{\mathrm{NiO}} F_{\odot} A_{\tilde{L}} \tag{3.5}$$

where $F_{\odot}$ is the solar flux, $\alpha_{\mathrm{NiO}} = 0.9$ is the solar absorptivity of the Nickel Oxide coating and $A_{\tilde{L}}$ is the area of the node exposed to the Sunlight. As the lid is assumed to face the Sun directly no tilt angle needs to be considered.

Both the copper case and the lid radiate heat away externally in the IR spectrum. For the lid, the resulting flux can be calculated as:

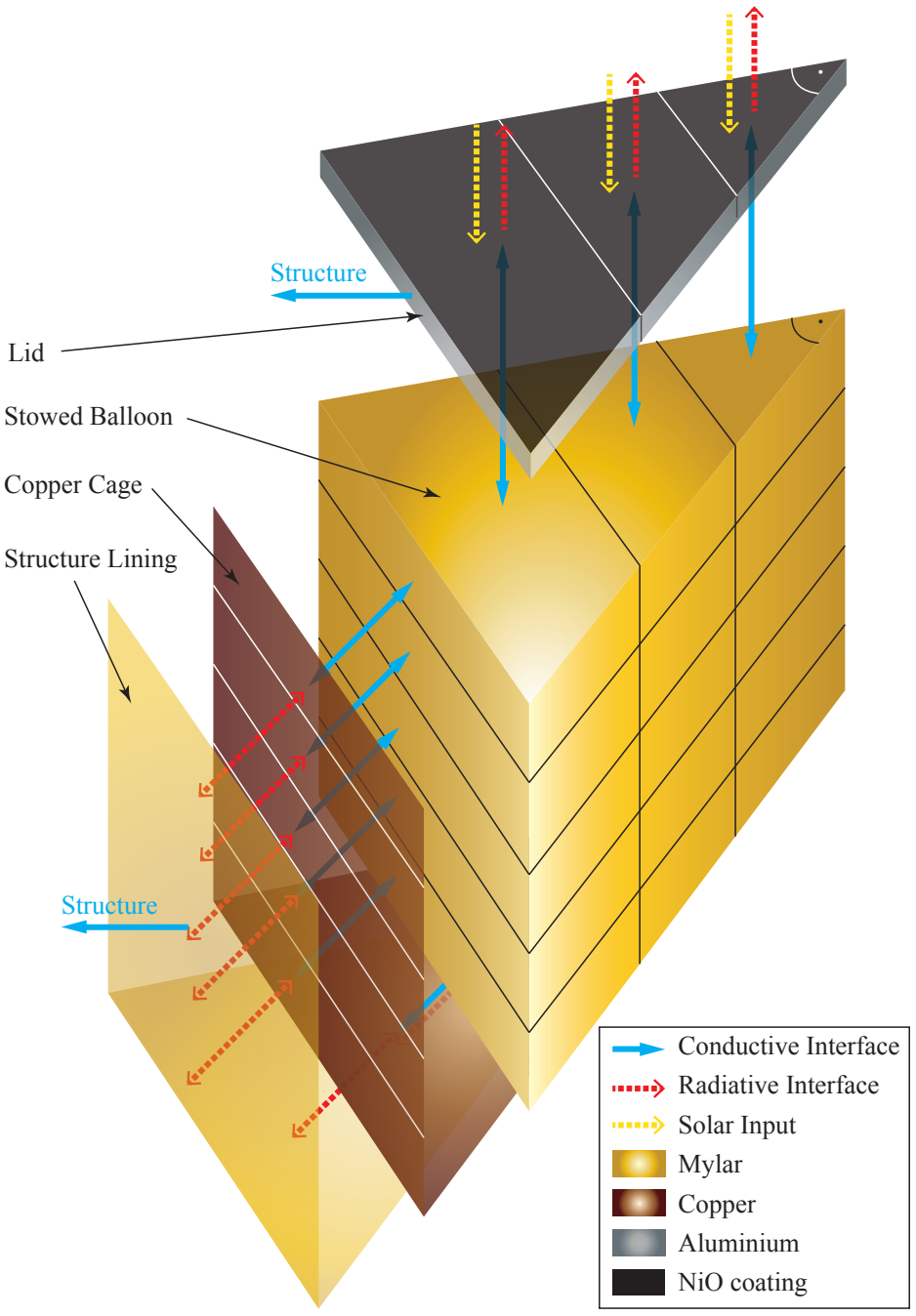

Figure 3.13: Thermal model of the pre-deployment heating process

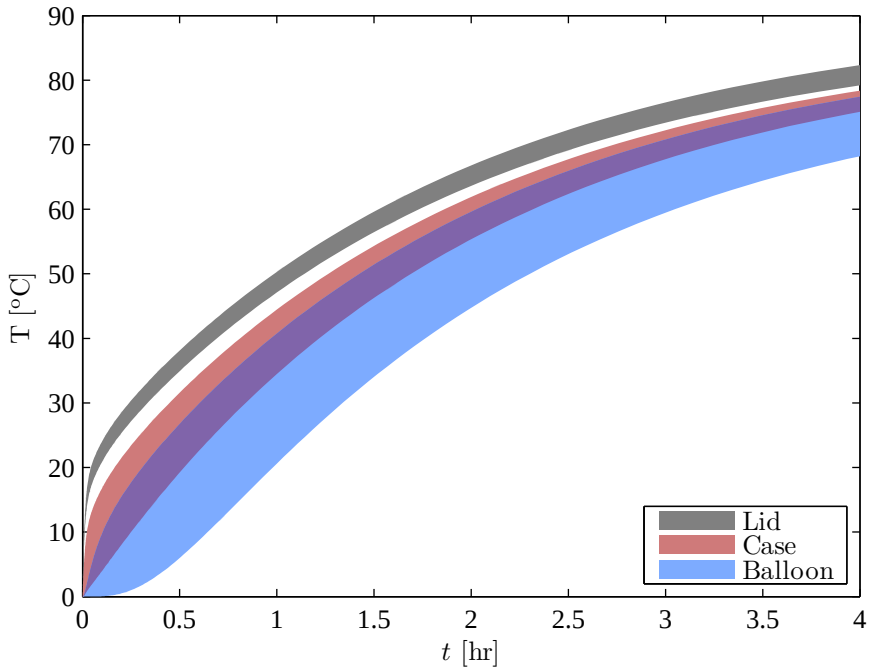

Figure 3.14: Temperatures during the pre-deployment heating process

$$\left(\frac{\mathrm{d}E_{\tilde{L}}}{\mathrm{d}t}\right)_{IR} = \sigma_{SB}\varepsilon_{\mathrm{NiO}}A_{\tilde{L}}T_{\tilde{L}}^4 \tag{3.6}$$

where $\sigma_{SB} \approx 5.67 \times 10^{-8}\,\mathrm{W\,m^{-2}\,K^{-4}}$ is the Stefan-Boltzmann-constant, $\varepsilon_{\mathrm{NiO}} = 0.1$ is the emissivity of the Nickel Oxide coating and $A_{\tilde{L}}$ the outward facing area of lid node $\tilde{L}$.

The thermal energy radiated away from the copper case will be partially reflected back by the Mylar lining of the spacecraft structure. This reflection will then again only be partly absorbed by the copper. Additionally the spacecraft structure will also radiate heat towards the copper case. The resulting exchange can be calculated as follows for a case node $\tilde{C}$ and the spacecraft structure $\tilde{S}$ [116]:

$$\left(\frac{\mathrm{d}E_{\tilde{C},\tilde{H}}}{\mathrm{d}t}\right)_{IR} = \frac{\sigma}{\frac{1}{\varepsilon_{\mathrm{Cu}}} + \frac{1}{\varepsilon_{\mathrm{Mylar}}} - 1}(T_{\tilde{C}}^4 - T_{\tilde{H}}^4) \tag{3.7}$$

These equations are then integrated using the ordinary differential equation solver ODE45 in MATLAB with an initial temperature of 0 °C. The results are shown in Fig. 3.14. It can be seen that after approximately three hours the whole balloon is predicted to be at a temperature above 60 °C. At this temperature the resin is very soft and pliable and the system is ready for inflation.

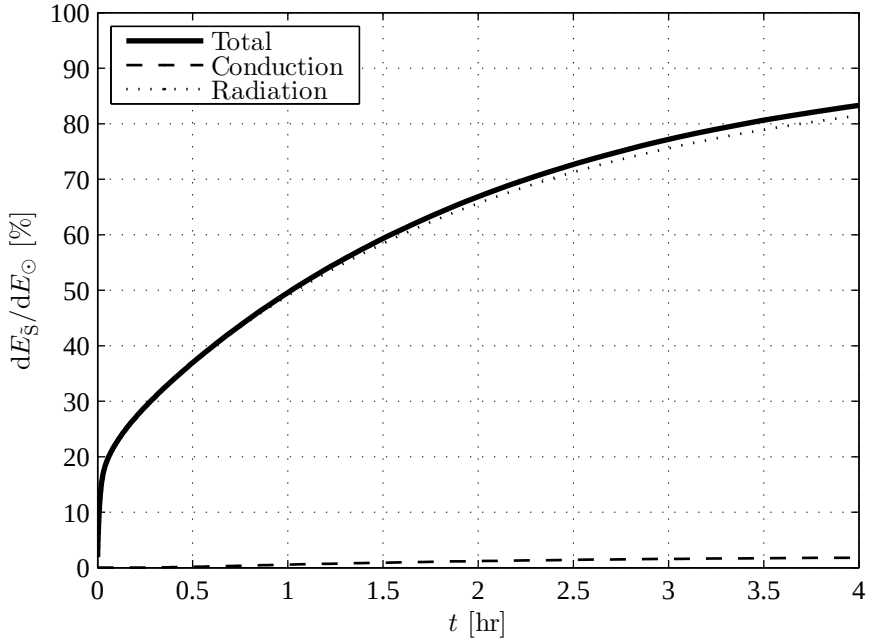

Figure 3.15: Percentage of the total thermal energy received from the Sun which is transmitted to the spacecraft structure

Figure 3.15 shows the percentage of the received solar radiation which is transmitted to the spacecraft structure. As the difference in temperatures between the internal components of the orbit transfer module and the rest of the spacecraft increases, so does the thermal flux to the spacecraft structure. The figure also shows the radiative and conductive parts of the heat transfer. It can be seen that the radiative exchange is dominant. This is because there is only a very small conductive interface between the spacecraft structure and lid which is also insulated with Mylar. Within the simulation time the transfer ratio never reaches 100%, which is when the steady state has been reached. If the link to the spacecraft were stronger, for example if there were more conductive interfaces or the low absorptivity Mylar were not used, the steady state would be reached sooner and at a lower internal temperature. In that case the balloon might not have reached the correct temperature for deployment.

Steady state thermal analysis after cooling

The temperatures after inflation can be determined to ensure that the device fully rigidises. To achieve this a worst case scenario is implemented in which the balloon's attitude is fixed with respect to the Sun and the thermal gradient highest. The balloon is assumed to be reflective Mylar on the outside and coated in nickel oxide on the inside to maximise the radiative heat exchange

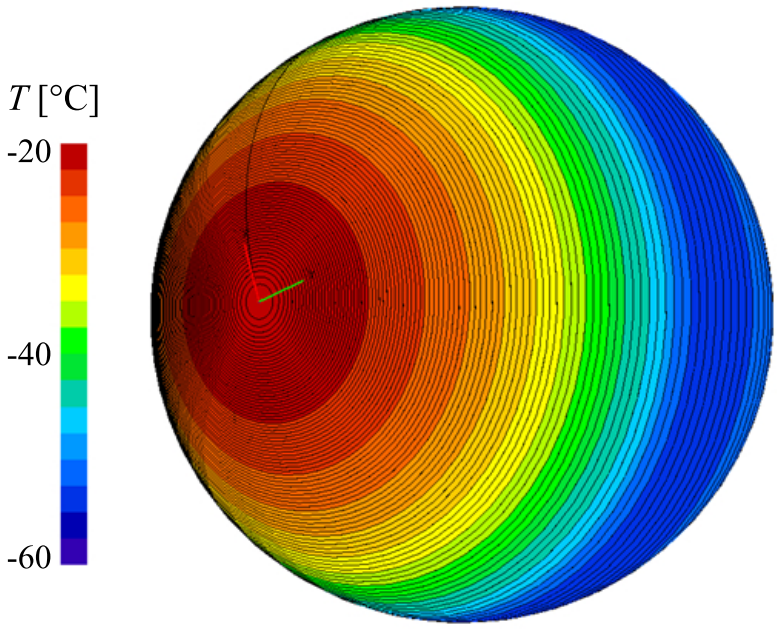

Figure 3.16: Steady state temperatures of the inflated balloon

between the Sun facing hot and the cold side. The scenario is computed using the ESATAN thermal modelling suite [117]. The results are shown in Fig. 3.16 where it can be seen that even in the worst case the maximum temperature is at $-20\,°\mathrm{C}$, cold enough for full rigidisation.

3.3 Conclusions

A novel mission and system design for a 3U CubeSat GTO to LEO transfer has been presented. This is seen as an alternative to LEO piggyback launches. The spacecraft increases its area-to-mass-ratio to use solar radiation pressure and the J_2 effect to simultaneously decrease apogee altitude and raise the perigee to passively reach a LEO orbit without the use of propulsion, exploiting the phase space dynamics discussed in Chapter 2. The detailed mission scenario is investigated using a high precision orbit propagator and a radiation analysis is performed.

An orbit transfer module for CubeSats has been designed, which contains a deployable Mylar balloon which when inflated increases the spacecraft area-to-mass-ratio to $3\,\mathrm{m}^2\,\mathrm{kg}^{-1}$. The balloon rigidises after inflation using a cold hardening resin and can be ejected when the final orbit is reached. This design task was performed to gain an insight into the mass required for auch a device, into its reflective properties and into the different technologies required for its realisation.

Different shapes for a deorbiting device were discussed and a spherical shape was chosen (akin to the GOLD device developed by the Aerospace Corporation [42]). This shape offers the same reflective properties and surface area from any aspect angle and thus requires no further attitude control. A disadvantage is its low mass efficiency: compared to a flat solar sail, about eight times the surface material is needed. Furthermore, will a balloon shape pose a greater challenge at construction than any flat shape.

An inflation system was proposed for the deployment which is the intuitive and most effective way of deploying a sphere. However, this also makes the device less scalable as a doubling in surface area would require four times the gas volume. For rigidisation a cold hardening resin was chosen. The technological draw-backs of such a resin were discussed in section 3.2.3. Additionally, while the hardening will protect the device from full collapse due to micrometeorite punctures, such impacts can create a thrust through the evacuating gas. This effect has not been analysed as part of this body of work.

In addition to delivery of payloads from GTO to LEO, the concept presented in this chapter also offers opportunities to fly payloads in the Van Allen belts to investigate the radiation environment. It is also a promising low-cost mission concept for a CubeSat technology precursor mission to demonstrate passive orbit transfers using area-to-mass-ratio enhancing technologies. In order to study the radiation belts the spacecraft would remain in an operational state throughout the transfer. However, due to its passive nature the transfer method will also work when the spacecraft is powered down during the manœuvre.

Chapter 4

SRP-Augmented Deorbiting from Medium Earth Orbits

In this chapter a new concept of solar radiation pressure augmented deorbiting is introduced and applied to medium Earth orbits (MEO). Passive deorbiting is another manœuvre which can be performed by exploiting the effects of solar radiation pressure and the Earth's oblateness discussed in Chapter 2. As opposed to other passive methods discussed in Sec. 1.2.2, it can be applied to high altitude orbits in the MEO regime, thus enabling new types of missions for small satellites.

SRP-augmented deorbiting exploits the effect of solar radiation pressure (SRP) and Earth's oblateness in combination with aerodynamic drag to passively deorbit a satellite within a given time after its end-of-life without any further control requirements. This is achieved by making use of the interaction between SRP and the J_2 effect to increase the orbit eccentricity of any initially circular orbit until the perigee reaches an altitude at which aerodynamic drag causes the spacecraft to deorbit. The orbital evolution can be divided into two phases, as visualised in Fig. 4.1 for an initial orbit altitude of 7000 km and an area-to-mass-ratio of $3\,\mathrm{m}^2\,\mathrm{kg}^{-1}$. In phase one, solar radiation pressure is dominant over drag and is used to increase the orbit eccentricity until drag becomes the dominant force. The first phase requires approximately 90 % of the total manœuvre time. Then phase two begins in which aerodynamic drag decreases the orbital energy and thus the semi-major axis of the spacecraft orbit, and the eccentricity at the same time, so that the perigee altitude is kept almost constant. In the final phase of the manœuvre the orbit is quasi-circular and at an altitude where drag decreases the orbit altitude rapidly. At this stage, the sail or balloon acts in the same manner as other drag devices, since at this stage solar radiation pressure is negligible compared to the drag force.

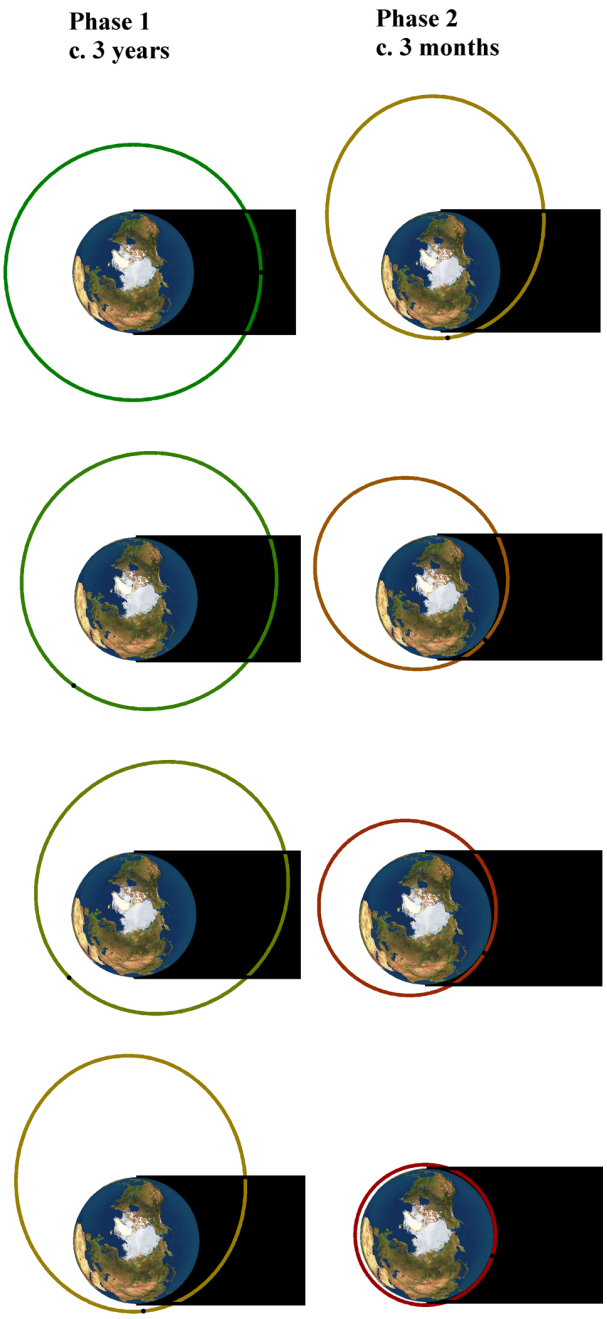

Figure 4.1: The two phases of the deorbiting manœuvre

In the first section of this chapter the method is analysed using the Hamiltonian, Eq. (2.9), introduced in Sec. 2.1. The analytical results are then verified numerically in Sec. 4.2. Next, the method is applied to inclined Medium Earth Orbits (MEO) in Sec. 4.3. In the next chapter the SRP-augmented deorbiting of high altitude Sun-synchronous orbits is investigated separately.

4.1 Analytical in-plane model

In this section the method of solar radiation pressure induced eccentricity increase is investigated analytically. This is done to obtain an initial guess for the required effective area-to-mass ratio to deorbit. The problem is first investigated using the analytical Hamiltonian model introduced in Sec. 2.1.1 in a reduced planar geometry. Then, the expression for the analytical first guess is derived from the Hamiltonian dynamics.

The Hamiltonian is used to approximate the global evolution in eccentricity and Sun-perigee angle of a high area-to-mass-ratio spacecraft. It contains information on the path in the orbital element phase space but not the time history of the orbit evolution. Krivov and Getino [8] present some examples for the orbit evolution. Again, in this section the Hamiltonian is used to obtain a first guess at the required area-to-mass-ratio to deorbit. This value is then refined numerically with a restriction on the manœuvre duration in Sec. 4.2.

4.1.1 Discussion of the Hamiltonian model

For increased area-to-mass-ratios the orbital element phase space of ϕ and e exhibits interesting behaviour, particularly in the region with a semi-major axis of 2 - 3 Earth radii [8, 84], with three possible behaviour patterns as shown in Fig. 4.2. In these figures the orbital evolution due to the effects of solar radiation pressure and J_2 according to the Hamiltonian is shown for orbits with a semi-major axis of 15 000 km for three different effective area-to-mass-ratios. In particular, the phase line corresponding to an orbit evolution passing through $e = 0$ is highlighted with a bold coloured line. Orange represents $5\,\mathrm{m^2\,kg^{-1}}$, purple for $20\,\mathrm{m^2\,kg^{-1}}$ and red for the bifurcation area-to-mass-ratio of approximately $12.9\,\mathrm{m^2\,kg^{-1}}$. These colour codes are used again in later figures.

For SRP-augmented deorbiting, the evolution of the orbit eccentricity is the most important information in these figures. The maximum eccentricity an initially circular orbit will reach for a given area-to-mass-ratio decides whether this area-to-mass-ratio is sufficient to cause the spacecraft to re-enter the atmosphere or not. In all three cases the initially circular orbit will start to become

eccentric at $\phi = \frac{3\pi}{2}$ and reach maximum eccentricity at either $\phi = 0$ (perigee Sun-pointing) or $\phi = \pi$ (apogee Sun-pointing), before returning to the circular state at $\phi = \frac{\pi}{2}$ if its perigee is not low enough for deorbiting. For lower area-to-mass-ratios, the maximum eccentricity in the evolution of an initially circular orbit can be found at $(0, e_{1,\max})$ (Fig. 4.2a). At the critical effective area-to-mass-ratio, σ_B, which is dependent on semi-major axis, the evolution of the initially circular orbit bifurcates and passes through a hyperbolic equilibrium point at (π, e_B) (Fig. 4.2b) to reach its maximum at $(0, e_{B,\max})$. For high effective area-to-mass-ratios the maximum eccentricity $e_{\max}$ in the evolution of an initially circular orbit can be found at $\phi = 0$ (Fig. 4.2c).

In the first case (Fig. 4.2a), a second line appears at high eccentricities with the same value of the Hamiltonian for the initially circular orbit. This line, however, does not pass through $e = 0$. It has a minimum eccentricity at $(\pi, e_{2,\min})$ and a maximum eccentricity at $(0, e_{2,\max})$. This double occurrence of equivalent yet unconnected phase lines requires some extra consideration when finding an analytical solution for the required area-to-mass-ratio to deorbit. This issue is dealt with in Sec. 4.1.2.

Figure 4.3 shows the three different types of behaviour introduced in Fig. 4.2 and where they occur depending on semi-major axis and effective area-to-mass-ratio σ. For a semi-major axis of lower than approximately 12 350 km the phase space will always follow behaviour (c). Above this semi-major axis the phase space can display any of the three behaviours depending on the area-to-mass-ratio. The thick black line dividing the regions of behaviour (a) in grey and behaviour (c) in white corresponds to the case in which the bifurcation of the initially circular orbit phase line occurs (b). The bifurcating behaviour allows spacecraft to deorbit with a particularly low area-to-mass-ratio as will be seen in the following section. This is because the evolution of the Sun-perigee angle ϕ causes the orbit to remain longer in a position with respect to the Sun where solar radiation pressure will cause an increase of eccentricity. Above a semi-major axis of approximately 20 000 km an area-to-mass-ratio of more than $40\,\mathrm{m^2\,kg^{-1}}$ is required to achieve the bifurcated behaviour. This cannot be feasibly achieved by a spacecraft with current deployable structures technology.

4.1.2 Required area-to-mass-ratio for deorbiting

An expression for the minimum required area-to-mass-ratio to deorbit a spacecraft on an initially circular orbit can be obtained by solving Eq. (2.9) for $e = 0$, which results in:

$$H_{\mathrm{circ}} = -1 - \frac{\kappa}{3} \tag{4.1}$$

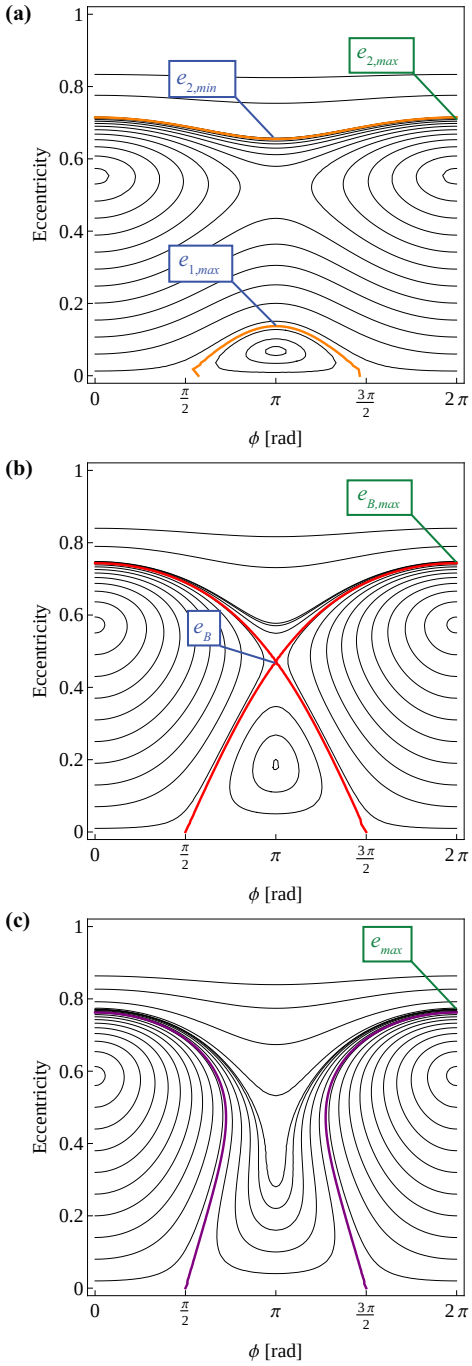

Figure 4.2: Phase plane diagram for a spacecraft with a semi-major axis of 15 000 km and three different values of effective area-to-mass-ratio σ: (a) $5\,\mathrm{m^2\,kg^{-1}}$, (b) $12.9\,\mathrm{m^2\,kg^{-1}}$ and (c) $20\,\mathrm{m^2\,kg^{-1}}$

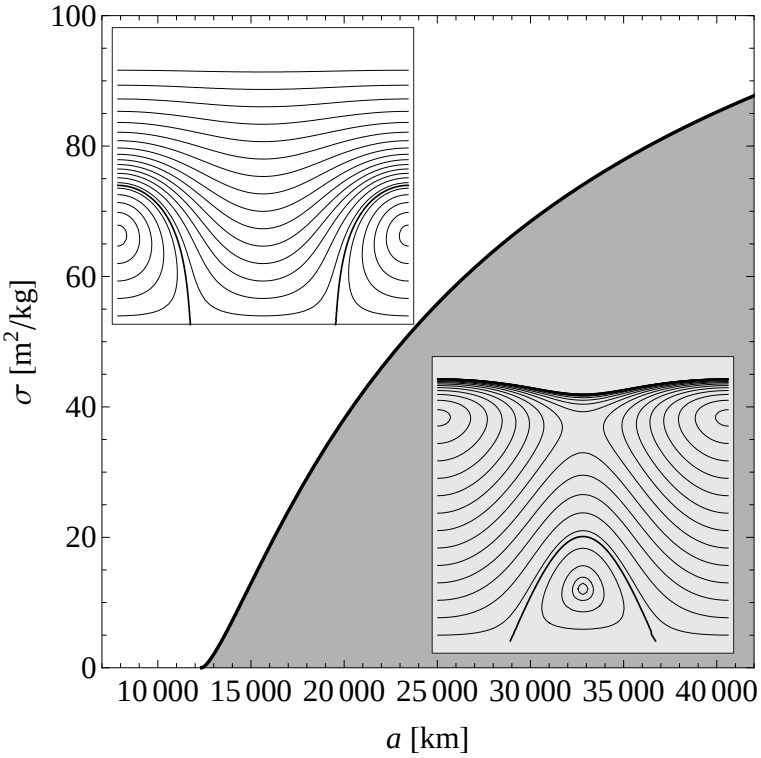

Figure 4.3: Behaviour of the phase space depending on area-to-mass-ratio and semi-major axis

By inserting Eq. (4.1) into Eq. (2.9) and considering that the maximum eccentricity from a circular orbit can be reached at $\phi = 0$ or $\phi = \pi$ (see Fig. 4.2), the resulting equation can be solved to give the required SRP-parameter α (Eq. (2.4)) needed to reach a certain eccentricity, e^*, from an initially circular orbit as a function of the semi-major axis:

$$\begin{aligned} \alpha_0 &= \frac{1-\sqrt{1-e^{*2}}}{e^*} + \left(\frac{1}{3e^*} - \frac{1}{3e^* 1 - e^{*2}{}^{\frac{3}{2}}}\right)\kappa \\ \alpha_\pi &= -\left(\frac{1-\sqrt{1-e^{*2}}}{e^*} + \left(\frac{1}{3e^*} - \frac{1}{3e^* 1 - e^{*2}{}^{\frac{3}{2}}}\right)\kappa\right) \end{aligned} \tag{4.2}$$

The term α_0 corresponds to $\phi = 0$ and α_π to $\phi = \pi$, the two perigee angles for which the eccentricity can reach its maximum starting from $e = 0$. Since the orbit semi-major axis is defined by the spacecraft's circular operational orbit, the required effective area-to-mass-ratio σ can thus be calculated using Eqs. (2.4 - 2.6) and (4.2). As the required effective area-to-mass-ratio cannot be negative it can be written as:

$$\sigma(e*, a) = \frac{2n_\odot c}{3F_\odot}\sqrt{\frac{\mu}{a}}\left|\frac{1-\sqrt{1-e^{*2}}}{e^*} + \left(\frac{1}{3e^*} - \frac{1}{3e^*\sqrt{1-e^{*2}}^3}\right)\kappa(a)\right| \tag{4.3}$$

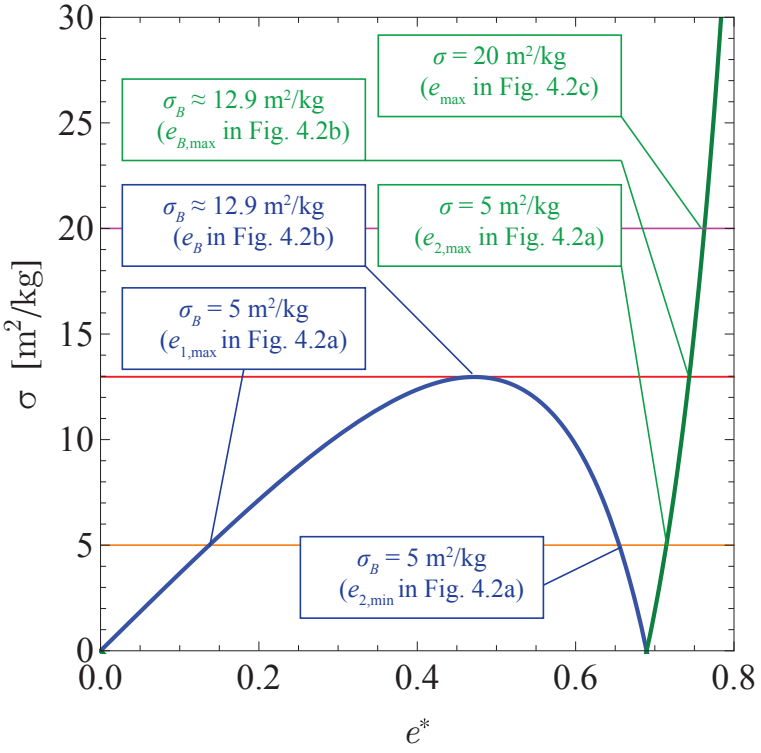

Figure 4.4: Area-to-mass-ratio computed through Eq. (4.3) for a semi-major axis of 15 000 km

The eccentricity needed to deorbit a spacecraft is defined as the critical eccentricity e_{crit}. This is the eccentricity at which the perigee of an orbit would lie on the surface of the Earth and is a function of the semi-major axis, as defined in Eq. (2.11). Figure 4.4 shows the solutions of Eq. (4.3) for a semi-major axis of 15 000 km. The solutions in which the maximum eccentricity e^* is reached at $\phi = 0$ are shown in green and for $\phi = \pi$ in blue.

The noteworthy eccentricities highlighted in Fig. 4.2 are marked in Fig. 4.4. The horizontal lines mark three different area-to-mass-ratios and their colours correspond to the colours of the bold phase lines in Fig. 4.2. The orange line indicates $\sigma = 5\,\text{m}^2\,\text{kg}^{-1}$ and the purple line indicates $\sigma = 20\,\text{m}^2\,\text{kg}^{-1}$. The red line is where the phase line for initially circular orbits bifurcates with the critical area-to-mass-ratio σ_B, which depends on the semi-major axis. A problem arises when solving for a maximum eccentricity e^* between e_B and $e_{B,\max}$ (see Fig. 4.2(b)). In this case Eq. (4.3) delivers values lower than σ_B. These correspond to the second phase line which never passes through $e = 0$ (see Fig. 4.2(a)). Thus, to reach values of eccentricity between the hyperbolic equilibrium point (e_B in Fig. 4.2(b)) and the maximum eccentricity reachable through the bifurcated zero-eccentricity phase line ($e_{B,\max}$ in Fig. 4.2(b)), the minimum area-to-mass-ratio solution corresponds to that for the bifurcated phase space.

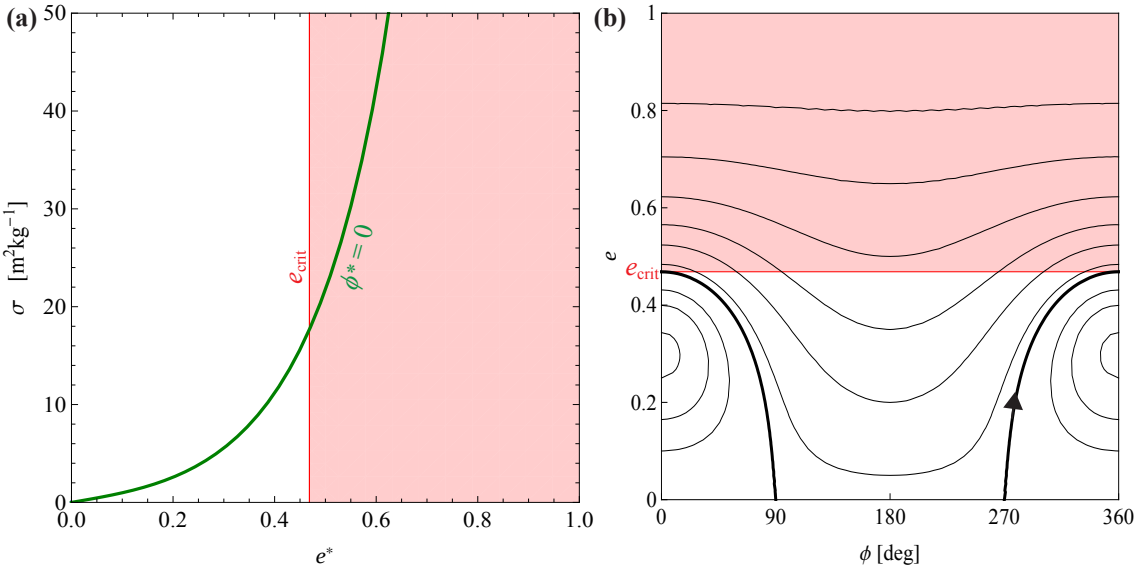

Figure 4.5: Deorbiting from 12 000 km: (a) Results of Eq. (4.3) with critical eccentricity e_{crit}, (b) (e, ϕ) phase space of the manœuvre

Figure 4.5a shows the results of Eq. (4.3) as a function of eccentricity for a semi-major axis of 12 000 km. The critical eccentricity e_{crit} at this semi-major axis is marked in red. The required area-to-mass-ratio to deorbit can be found where the e_{crit} line crosses the σ line, at $19\,\text{m}^2\,\text{kg}^{-1}$. Figure 4.5(b) shows the evolution of orbits at $a = 12\,000\,\text{km}$ with $\sigma \approx 19\,\text{m}^2\,\text{kg}^{-1}$ in the (e, ϕ) phase space. The thick line represents the evolution of an initially circular orbit. It can be seen that the maximum is reached when $\phi = 0°$. As can be seen in Fig. 4.3, there is only one type of phase space behaviour at 12 000 km.

Figure 4.6a shows the results of Eq. (4.3) as a function of eccentricity for a semi-major axis of 25 000 km. The results where the maximum is reached at $\phi = 180°$ are marked in blue and those for $\phi = 0°$ are marked in green. The required area-to-mass-ratio to deorbit can be found where the e_{crit} line crosses the σ line at $\sigma \approx 41\,\text{m}^2\,\text{kg}^{-1}$. In this case it crosses the blue part of the line. This means that the maximum eccentricity is reached when the perigee is Sun-pointing at $\phi = 180°$. Figure 4.6b shows the orbital evolution during this manœuvre.

At semi-major axes between approximately 13 000 km and 18 000 km the double occurrence of the $e = 0$ phase line prevents Eq. (4.3) from delivering the real required area-to-mass-ratio to deorbit. This can be seen in Fig. 4.7. Figure 4.7(a) shows the values of Eq. (4.3) for a semi-major axis of 15 000 km. It can be seen that the area-to-mass-ratio given by Eq. (4.3) to reach the critical eccentricity is lower than that for some lower eccentricities. This is unreasonable. Figure 4.7(b) explains this result. The orbit does not actually reach the critical eccentricity for the given area-to-mass-ratio, but instead the double occurrence of the $e = 0$ line crosses e_{crit} at $\phi = 180°$.

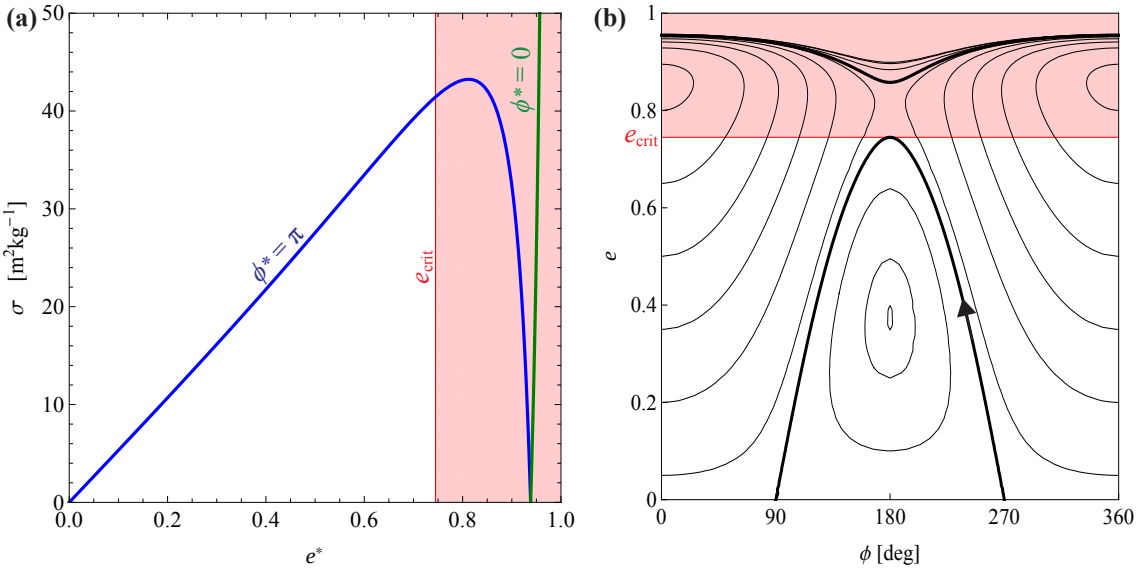

Figure 4.6: Deorbiting from 25 000 km: (a) Results of Eq. (4.3) with critical eccentricity e_{crit}, (b) (e, ϕ) phase space of the manœuvre

In order to account for the false results produced by the second identity of the circular orbit phase line, an analytical expression for the effective area-to-mass-ratio at which a circular orbit would pass through the bifurcation point needs to be found. This formula for $\sigma_B(a)$ is found through the bifurcating eccentricity e_B which is determined by locating the local extremum in Eq. (4.3):

$$\frac{\partial \sigma\left(e_B, a\right)}{\partial e_B} = 0 \tag{4.4}$$

Solving for $e_B \in [0, 1]$ yields:

$$\begin{aligned} e_B = \Bigg[& \frac{5}{4} - \frac{9}{4(3+\kappa)^2} - \frac{B(\kappa)}{4} \\ & - \Bigg(\frac{-4\kappa^2(3+\kappa)^4(648+441\kappa+77\kappa^2)B - 2(3+\kappa)^4 A(\kappa)^2 B(\kappa)}{24(3+\kappa)^6 A(\kappa) B(\kappa)} \\ & + \frac{\kappa A(\kappa)\left(17496\kappa + 29160\kappa^2 + 17064\kappa^3 + 4194\kappa^4 + 369\kappa^5\right)}{24(3+\kappa)^6 A(\kappa) B(\kappa)} \\ & + \frac{\kappa A(\kappa)\left(11664 + 15876\kappa + 7884\kappa^2 + 1647\kappa^3 + 102\kappa^4 - 5\kappa^5\right) B(\kappa)}{24(3+\kappa)^6 A(\kappa) B(\kappa)} \Bigg)^{\frac{1}{2}} \Bigg]^{\frac{1}{2}} \end{aligned} \tag{4.5}$$

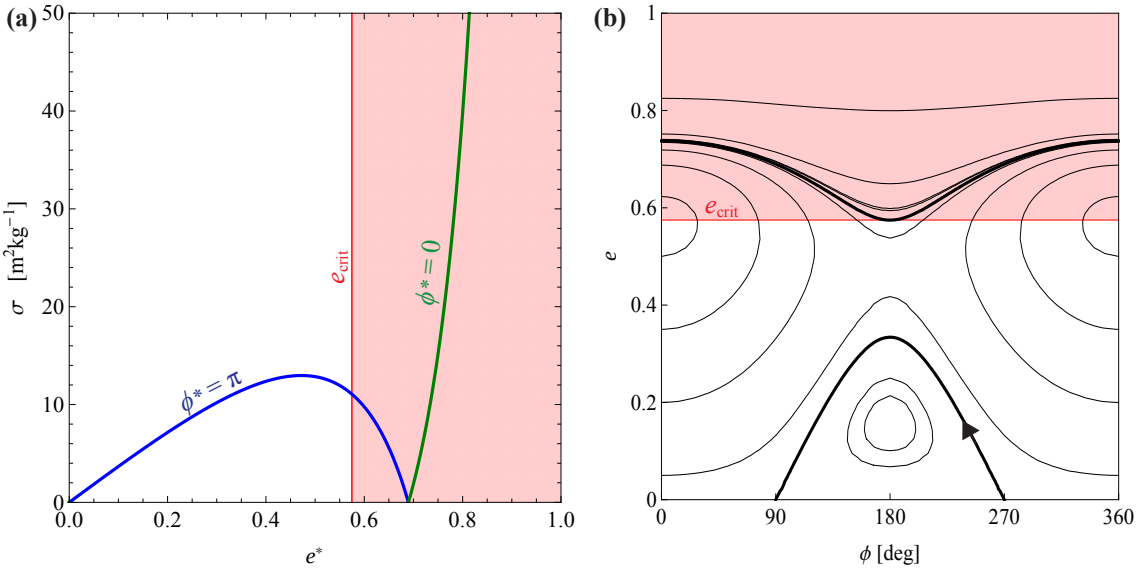

Figure 4.7: Failed deorbiting from 15 000 km: (a) Results of Eq. (4.3) with critical eccentricity e_{crit}, (b) (e, ϕ) phase space of the failed manœuvre

where κ is the J_2 effect parameter in Equation (2.5) and a function of the semi-major axis a. A and B are auxiliary parameters defined as follows:

$$\begin{aligned} A(\kappa) = \Big(&46656\kappa^3 + 57469.5\kappa^4 + 22707\kappa^5 + 2903.5\kappa^6 \\ &+ 40.5\sqrt{3\kappa^7(3+\kappa)^2\left(20736 + 22779\kappa + 8218\kappa^2 + 971\kappa^3\right)}\Big)^{\frac{1}{3}} \end{aligned} \tag{4.6}$$

$$B(\kappa) = \sqrt{\frac{(36 + 30\kappa + 5\kappa^2)^2}{(3+\kappa)^4} + \frac{8\kappa^2\left(648 + 441\kappa + 77\kappa^2\right)}{3(3+\kappa)^2 A(\kappa)} + \frac{4A(\kappa) - 16\left(27 + 18\kappa + 5\kappa^2\right)}{3(3+\kappa)^2}}$$

$\sigma_B(a)$ is found by using Eq. (4.3), such that:

$$\sigma_B(a) = \sigma\left(a, e_B\right) \tag{4.7}$$

The following expression for the minimum required area-to-mass-ratio $\hat{\sigma}(e^*, a)$ to deorbit can now be defined:

$$\hat{\sigma}(a) = \begin{cases} \sigma(e_{\text{crit}}(a), a) & \text{if } e_{\text{crit}}(a) \leq e_B(a) \\ \sigma_B(a) & \text{if } (e_{\text{crit}}(a) > e_B(a)) \wedge (\sigma(e_{\text{crit}}(a), a) < \sigma_B(a)) \\ \sigma(e_{\text{crit}}(a), a) & \text{if } (e_{\text{crit}}(a) > e_B(a)) \wedge (\sigma(e_{\text{crit}}(a), a) \geq \sigma_B(a)) \end{cases} \tag{4.8}$$

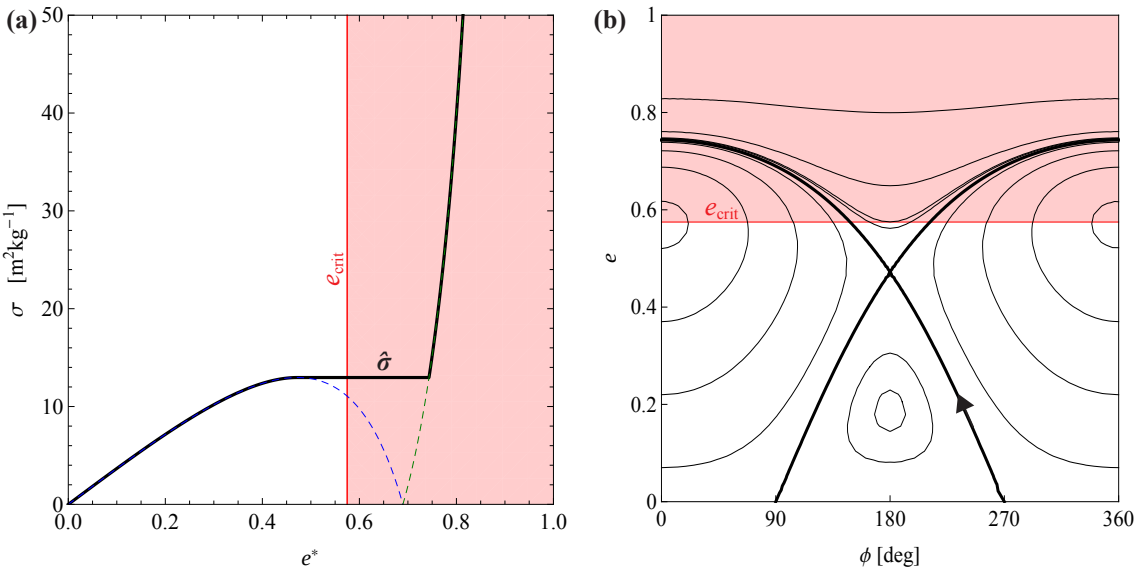

Figure 4.8: Deorbiting from 15 000 km: (a) Results of Eq. (4.8) with critical eccentricity e_{crit}, (b) (e, ϕ) phase space of the manœuvre

Figure 4.8 shows the result for a semi-major axis of 15 000 km. It can be seen that the revised area-to-mass-ratio is the value at which the $e = 0$ line passes through the bifurcation.

It must be noted that this analytical method does not take into consideration the duration for deorbit. It has already been established that at some semi-major axes the spacecraft orbit would move on a phase plane line which passes through a hyperbolic equilibrium point where it would slow down asymptotically (see Fig. 4.2b). In this case the time required for transferring the spacecraft from $e = 0$ to $e = e_{\text{crit}}$ becomes infinite. In the next Section numerical methods are used to limit the manœuvre time.

4.2 Numerical verification of the analytical model

In this section the analytical theory presented in Sec. 4.1 will be verified numerically for equatorial orbits in a three-dimensional reference frame using the expressions introduced in Sec. 2.2.2. The numerical propagation considers only the perturbations of solar radiation pressure and the J_2 effect. As drag is not considered in this model, a successful deorbiting is defined as reaching a perigee altitude of 0 km. The required area-to-mass-ratio can be increased by a margin to account for any unconsidered factors such as third body gravitational effects, drag, eclipses and higher order Earth gravitational harmonics.

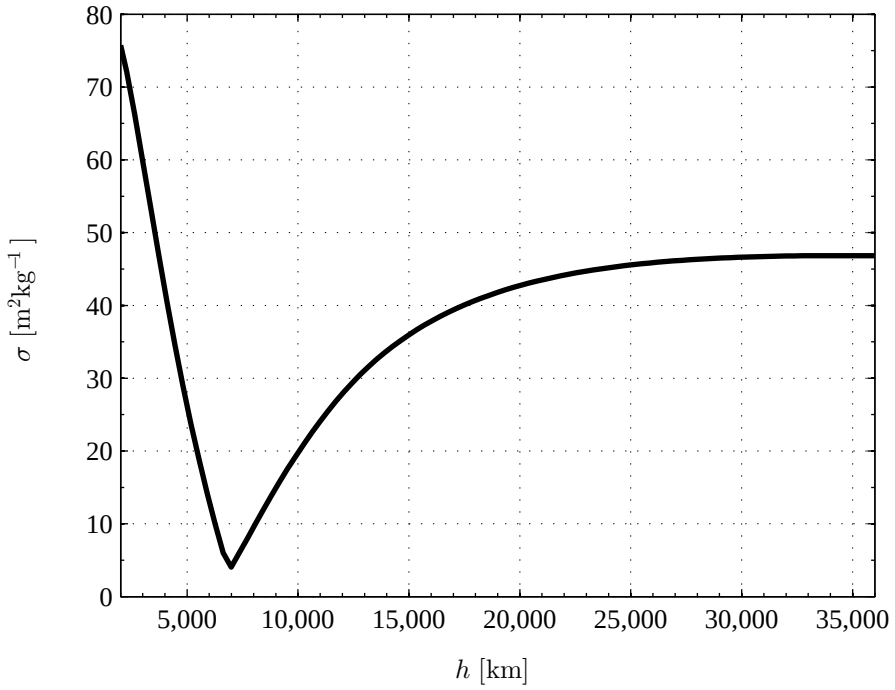

Figure 4.9: Analytical results for the required area-to-mass-ratio to deorbit as a function of semi-major axis

In three dimensions an equivalent Sun-perigee angle ϕ is defined in Eq. (2.1) as $\phi = \Omega + \omega - (\lambda_\odot - \pi)$ where Ω is the right ascension of the ascending node, ω is the argument of perigee and $\lambda_\odot$ defines the position of Sun on the ecliptic with respect to the vernal equinox, as also shown in Fig. 2.2 [84] (see section.

When deorbiting spacecraft from circular equatorial orbits, the initial right ascension of the ascending node Ω_0 and the initial argument of perigee ω_0 are irrelevant. However, the initial position of the Sun $\lambda_{\odot,0}$ influences the orbital evolution. To account for this, the required effective area-to-mass-ratios are found for a range of $\lambda_{\odot,0}$ for each semi-major axis. To determine the required effective area-to-mass-ratios to deorbit within a certain time limit, a stepwise search is performed. Starting with the analytical result obtained from Eq. (4.8) the orbit is propagated for a given amount of time or until the criterion for deorbiting is fulfilled (i.e., perigee altitude reaches 0 km). Depending on the result of the propagation a new value for the effective area-to-mass-ratio is chosen. If the searched value lies between the last two steps the step size is halved. This is continued until a minimum step size of $0.01\,\mathrm{m^2\,kg^{-1}}$ is reached and thus the effective area-to-mass-ratio can be determined with a given accuracy. The maximum deorbiting time is set as five years instead of the 25 years outlined by the IADC guidelines [34]. This is because the difference in area-to-mass-ratio required for the five year deorbit time as opposed to 25 years is small, while Lewis et al. [118]

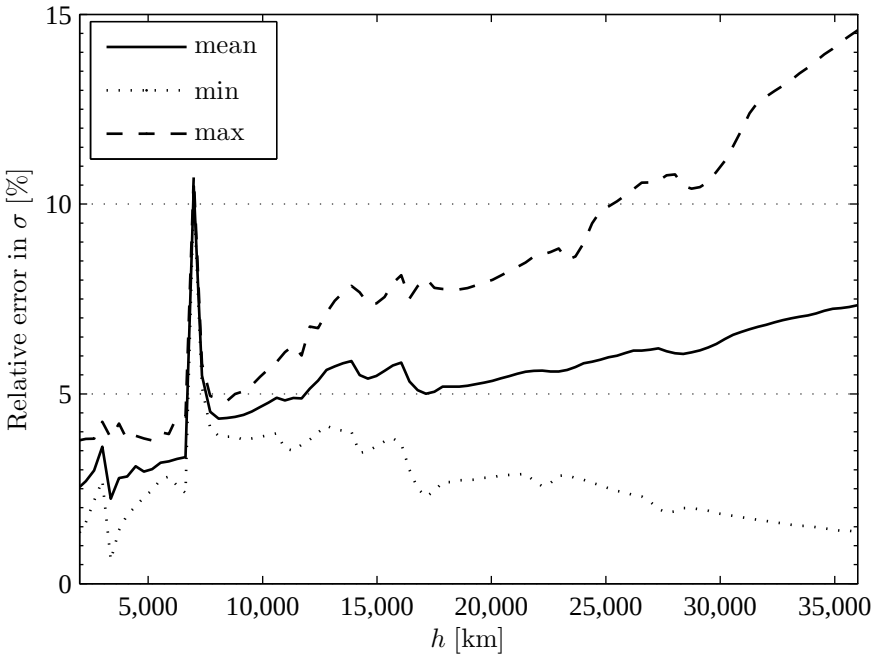

Figure 4.10: Relative error between analytical results for required area-to-mass-ratio to deorbiting calculated in 2D and numerical results in 3D limited to a five year deorbiting manœuvre

show that reducing the deorbit time to five years would be a necessary step towards stopping the growth of the space debris population.

Figure 4.10 shows the maximum, minimum and mean relative error between the numerical and the analytical results for different values of Ω_0 and $\lambda_{\odot,0}$. The mean required effective area-to-mass-ratio is approximately 5 % higher than previously estimated. The maximum overall relative error is 15 % and occurs at geostationary altitude. The maximum error increases with altitude because the effects of solar radiation pressure dominate over the Earth's oblateness for higher orbits. In addition, while in the analytical model the orbit is considered equatorial with respect to the J_2 effect, it is considered to be in the ecliptic with respect to solar radiation pressure. The peak at approximately 7500 km altitude occurs because of the five year maximum manœuvre time. For most altitudes the manœuvre time with the minimum required effective area-to-mass-ratio is below five years. However, for orbital manœuvres approaching the hyperbolic equilibrium in the orbital element phase space the manœuvre time will tend towards infinity. Therefore, in this region the required area-to-mass-ratio needs to be significantly increased over the analytical prediction to complete the manœuvre in the given maximum time.

4.3 Deorbiting inclined MEOs

In this subsection the results for the required effective area-to-mass-ratios to deorbit circular orbits of a range of inclinations and semi-major axes and the sensitivity towards initial orbit orientation $(\Omega_0, \lambda_{\odot,0})$ are presented and discussed.

4.3.1 Geometry of inclined orbit planes

For circular inclined orbits, apart from the initial position of the Sun $\lambda_{\odot,0}$, the initial right ascension of the ascending node Ω_0 is of importance. The initial argument of perigee ω_0 is irrelevant as the initial eccentricity e is zero. To determine the range of different initial conditions the orbit is visualised in a rotational reference frame shown in Fig. 4.11. The centre of the coordinate system lies at the centre of the Earth. The z-axis is fixed as the rotational axis of the Earth. The $x-y$ plane is consequently the Earth's equatorial plane. The x-direction is the fixed projection of the Sun-Earth line onto the ecliptic. This means that as time progresses the vernal equinox rotates around the centre of the coordinate system on the equatorial plane (not shown in the Figure). Meanwhile, the vector pointing towards the true position of the Sun librates in the $x-z$-plane. The angle between this vector and the x-axis is the declination of the Sun with respect to the equator $\delta_\odot$ which librates between $-\varepsilon_E$ and ε_E.

Figure 4.11 shows the position of the Sun and the geometry of the orbital plane with respect to the equatorial plane in an inertial reference frame. It can be seen that for a given inclination the orbit plane with respect to the direction of the Sun can be described by the declination of the Sun over the equator $\delta_\odot$, the right ascension of the Sun $\alpha_\odot$ and the right ascension of the orbit's ascending node Ω. Both $\alpha_\odot$ and $\delta_\odot$ are functions of $\lambda_\odot$ and the obliquity of the Earth's equator ε_E. The expressions can be derived geometrically as:

$$\tan\alpha_\odot = \tan\lambda_\odot \cos\varepsilon_E \tag{4.9}$$

$$\sin\delta_\odot = \sin\lambda_\odot \sin\varepsilon_E \tag{4.10}$$

Geometrically the result is the same for any $\lambda_\odot$ and $\pi - \lambda_\odot$. Therefore, only half of the $\lambda_\odot$ parameter space needs to be investigated.

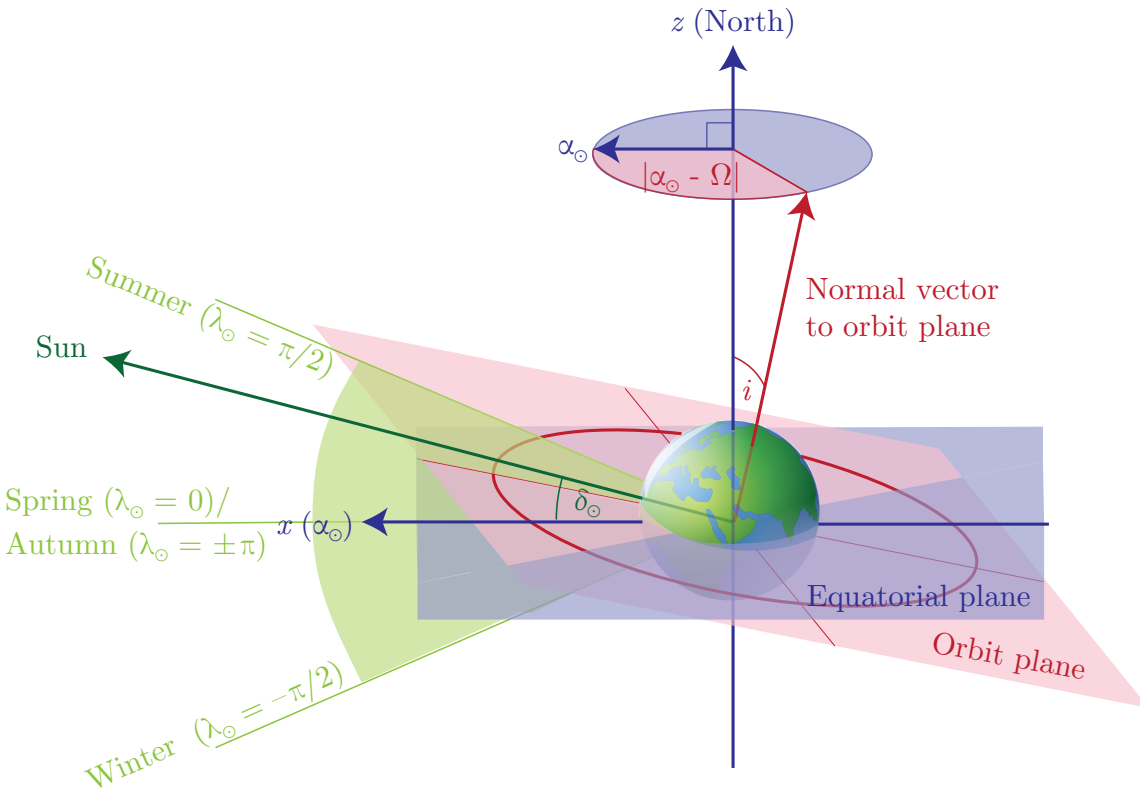

Figure 4.11: Diagram showing the orientation of the plane of an inclined orbit with respect to the incident Sunlight depending on $|\alpha_\odot - \Omega|$ and $\delta_\odot$

4.3.2 Numerical results for deorbiting inclined orbits

In this section the results of the numerical simulation are presented and discussed. The results have been obtained using the semi-analytical formulations of the orbit evolution under the effect of SRP and J_2 presented in Sec. 2.2.2. First the results for four selected semi-major axes are investigated to determine the dependence of the required effective area-to-mass-ratio to deorbit σ on the initial orientation of the orbital, equatorial and ecliptic plane. Then a full range of initial semi-major axes from LEO to GEO is investigated.

Dependence on plane configuration

First, the variation of the required area-to-mass-ratio with respect to the initial values of $\lambda_\odot$ and $|\alpha_\odot - \Omega|$ is investigated. For this, the method described in Sec. 4.2 is used with an accuracy of $1\,\mathrm{m^2\,kg^{-1}}$. The simulation is initially run for four different initial altitudes: 2000 km, 5000 km, 10 000 km and 36 000 km. At each of these altitudes the required area-to-mass-ratio is calculated for

an array of initial inclinations, four different initial $\lambda_\odot$ and eight different initial values of $|\alpha_\odot - \Omega|$. Again, a maximum manœuvre time restriction of five years is imposed.

Figure 4.12 shows the required maximum area-to-mass-ratio for different initial values of $\lambda_{\odot,0}$, i.e. time of year. The values for $\lambda_{\odot,0}$ range only from $[0, \pi]$ as both halves of the solution space are symmetrical, as shown in Sec. 4.3.1. It can be seen that the required area-to-mass-ratio depends strongly on the orbit inclination. There is not a clearly identifiably best time of year for deorbiting. It depends on the orbit semi-major axis and inclination. At 2000 km altitude the results stay within 10 % margin of each other. For 5000 km and 10 000 km there is more variation, particularly in the higher inclinations, and at 36 000 km strong variations can be seen at any inclination.

Figure 4.13 shows the required effective area-to-mass-ratio plotted over inclination for eight different initial values of $|\alpha_\odot - \Omega|$. It can be seen that for most orbits the required area-to-mass-ratio is lowest for $|\alpha_\odot - \Omega| = 90°$ or 270° and highest for $|\alpha_\odot - \Omega| = 0°$ or 180°. This effect is particularly strong for the higher inclined orbits at the altitudes of 5000 km and 10 000 km. Again it can be seen that variations at $h_0 = 5000$ km are smaller than at higher altitudes and distinct minima are identifiable, while at 36 000 km, i.e. near geostationary altitude, the average required effective area-to-mass-ratio shows only weak correlation to inclination and strong variations in the required area-to-mass-ratio.

Numerical results for inclined MEOs

Next the mean required area-to-mass-ratio is calculated for a range of initial altitudes and inclinations. The resolution is 500 km and 2° respectively.

Figure 4.14 shows the mean required effective area-to-mass-ratio to deorbit a spacecraft from a circular orbit as a contour plot of initial semi-major axis and inclination. While many of the values are very high and not feasible for near-term missions, two main regions can be identified in which the required area-to-mass-ratios are lower than $20\,\mathrm{m^2\,kg^{-1}}$. One of these regions is at very high inclination ($i > 70°$) low MEO orbits ($h_0 < 5000$ km). The other is shaped like an arch in the (a, i) plane spanning from $h = 2000$ km and $i \approx 40$ degrees of inclination to $h \approx 7500$ km and $i = 0°$.

Both regions are investigated at a higher resolution. The results for the arch-shaped region can be seen in Fig. 4.15. The parameter space has a resolution of of 100 km and 1°. In this figure the downwards shift of the minimum in inclination with increasing altitude becomes even more

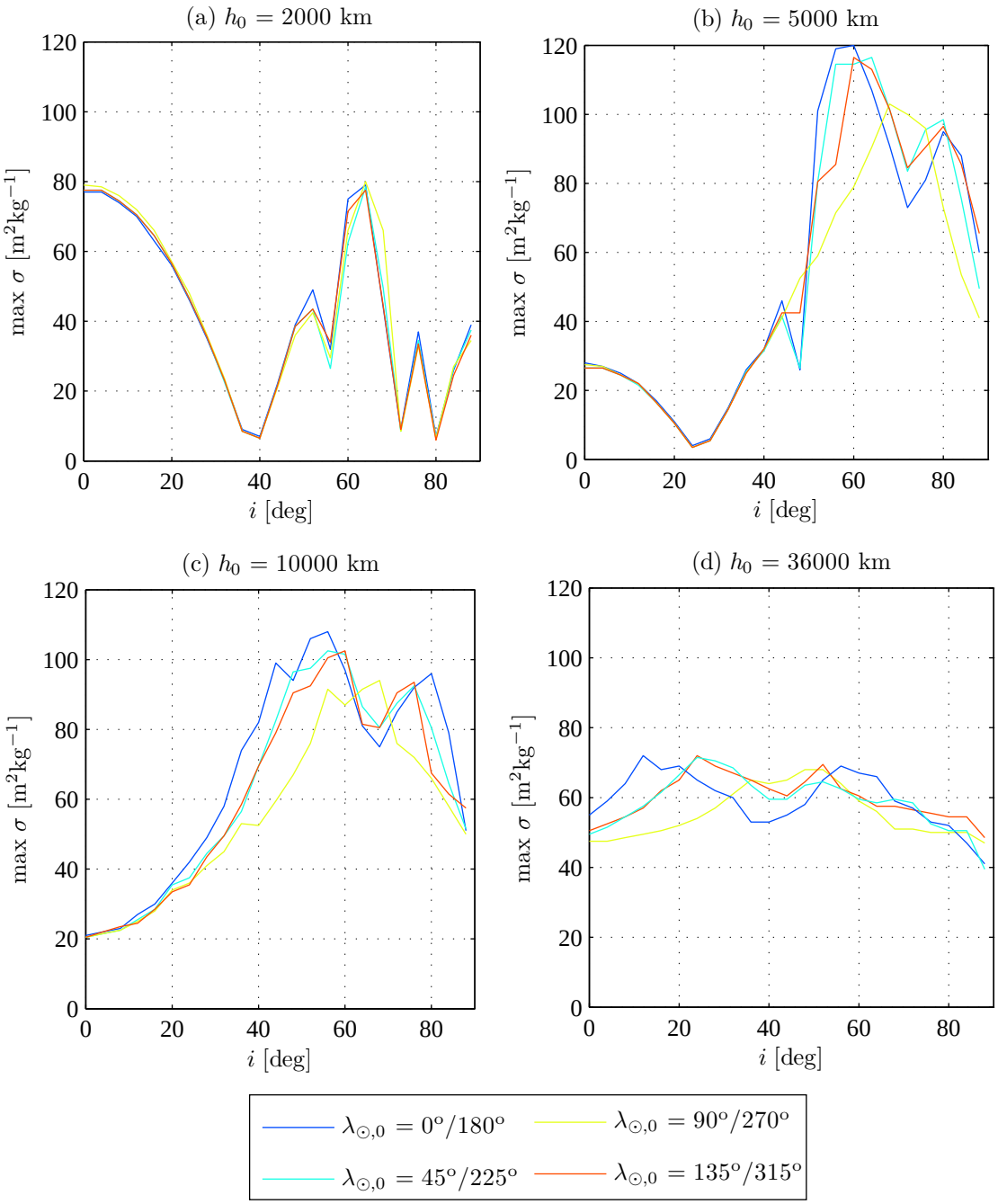

Figure 4.12: Numerical results for the maximum required area-to-mass-ratio to deorbit inclined circular MEO orbits as a function of inclination for four different initial altitudes and different values of $\lambda_\odot$

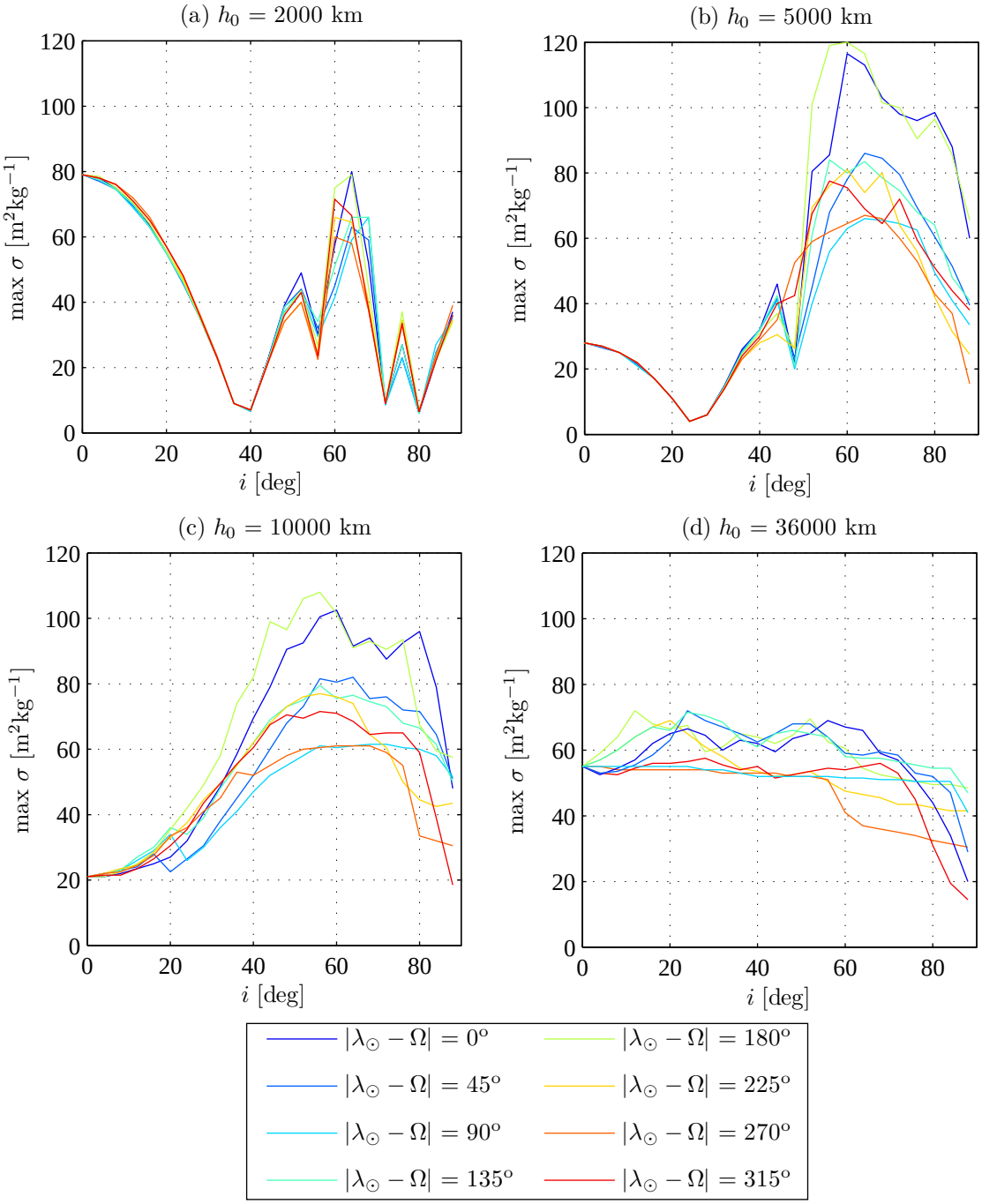

Figure 4.13: Numerical results for the maximum required area-to-mass-ratio to deorbit inclined circular MEO orbits as a function of inclination for four different initial altitudes and different initial values of $|\lambda_\odot - \Omega|$

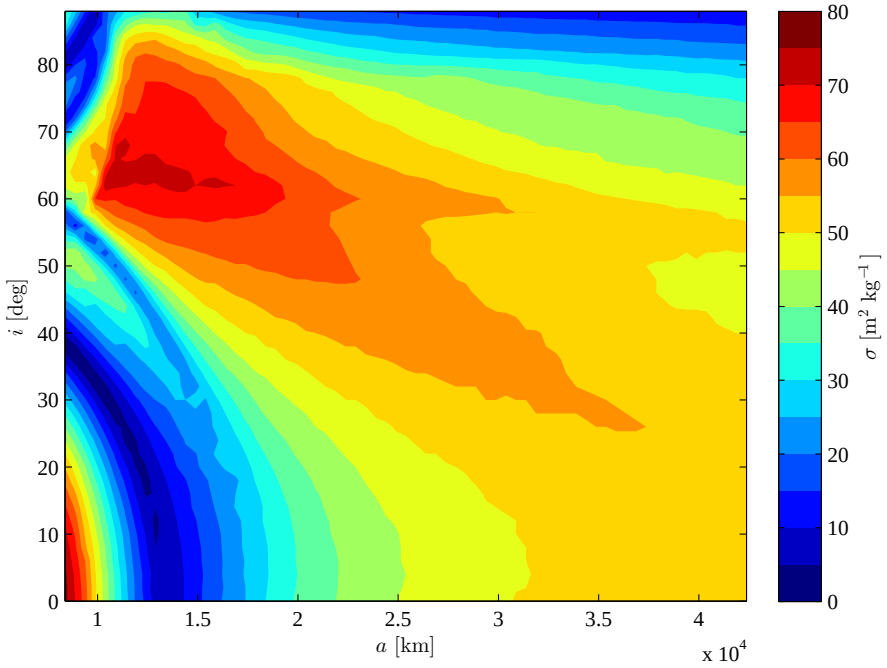

Figure 4.14: Mean results for the required area-to-mass-ratio to deorbit inclined MEOs obtained by numerical propagation

obvious. An explanation for the shifting minimum in this region can be found in Sec. 2.1.2 where the extension of the stationary points in the (e, ϕ) phase space is shown for non-zero obliquity of the ecliptic over the equator and non-zero inclinations. In the three dimensional SRP and J_2 dynamics problem an exact solution for equilibrium points does not exist; however, conditions for inclined quasi-frozen orbit can be found [84]. The eccentricity of the quasi-frozen point at $\phi = 0$, around which the lower altitude orbits librate, increases when the inclination is greater than zero (see Fig. 2.4). This is the reason why in Figs. 4.12a, 4.12b, 4.13a and 4.13b the required area-to-mass-ratio initially decreases with altitude. However, as shown by Colombo et al. [84] any quasi-frozen orbits are only true equilibria in the planar case (zero obliquity and zero inclination). They become increasingly unstable with higher inclination and eventually disappear completely. This is the reason for the increase of the required effective area-to-mass-ratio after the initial drop. The eccentricity of the quasi-frozen point at $\phi = \pi$, around which higher altitude orbits librate, decreases with increasing inclination. This explains why higher altitude orbits require an increasing effective area-to-mass-ratio for larger inclinations.

The results for the high-inclination region can be seen in Fig. 4.16. The area-to-mass-ratio requirements to deorbit near-polar low MEO orbits are small. Figure 4.17 show the minimum and maximum results for the required area-to-mass-ratio calculated over a range of initial $\lambda_\odot$ and Ω. A large discrepancy between the minimum and maximum signifies a strong sensitivity towards these

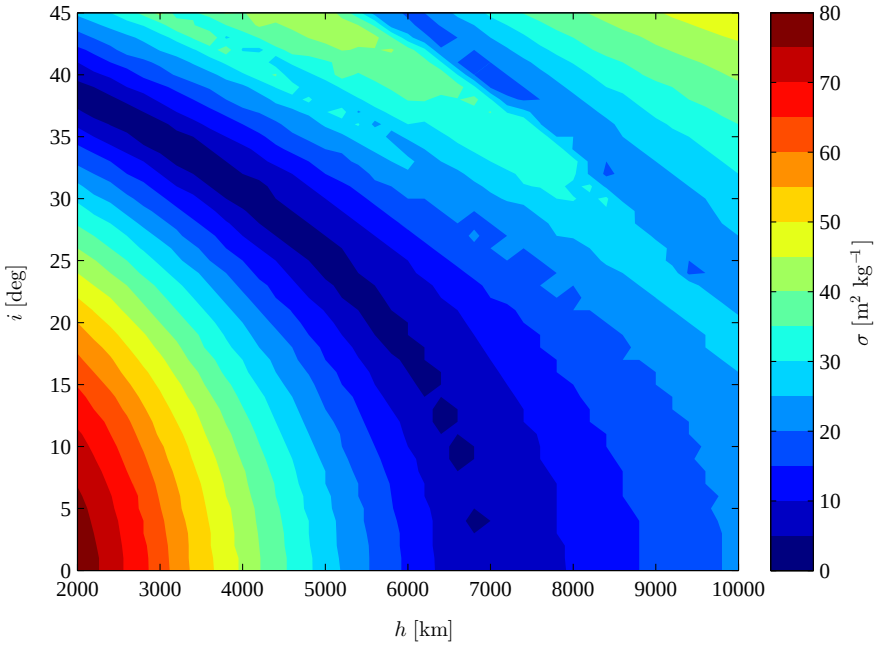

Figure 4.15: Mean results for the required area-to-mass-ratio to deorbit inclined MEOs obtained by numerical propagation: close-up of the low MEO regime with high effectiveness for SRP-augmented deorbiting

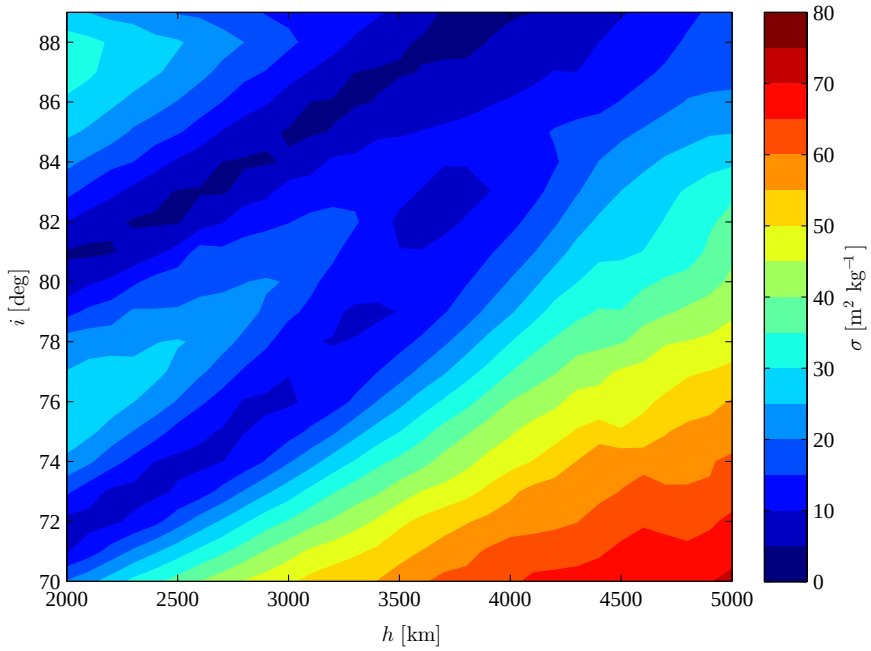

Figure 4.16: Mean results for the required area-to-mass-ratio to deorbit inclined MEOs obtained by numerical propagation: close-up of the polar orbit regime with high effectiveness for SRP-augmented deorbiting

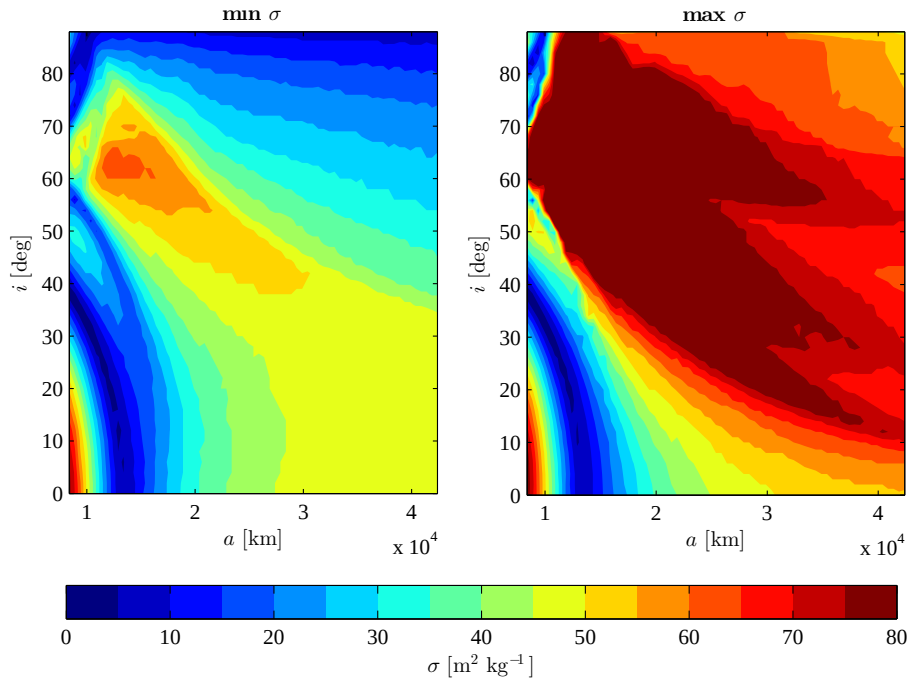

Figure 4.17: Minimum and maximum results for the required area-to-mass-ratio to deorbit inclined MEOs obtained by numerical propagation

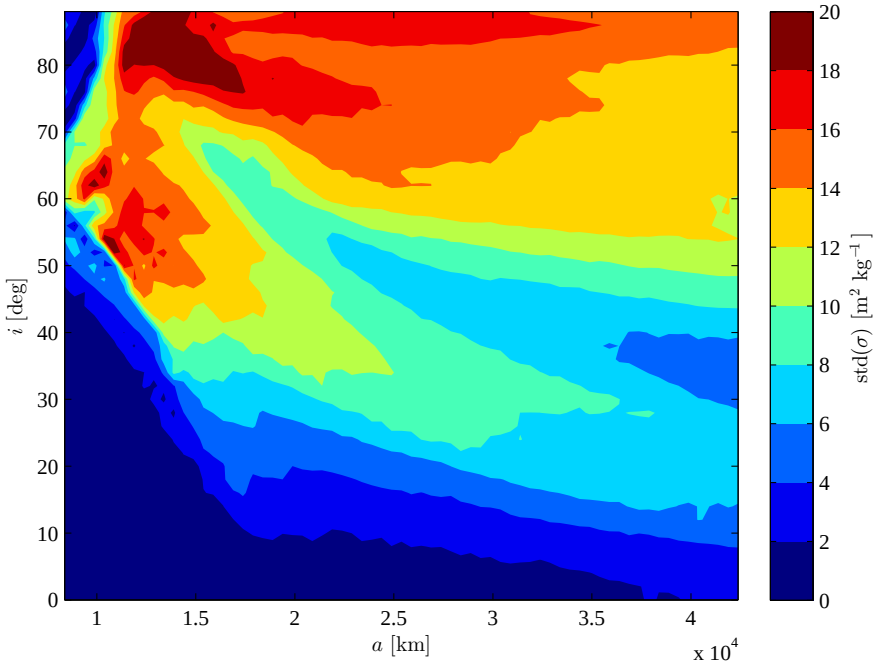

Figure 4.18: Standard deviation for the required area-to-mass-ratio to deorbit inclined MEOs obtained by numerical propagation for different initial $\lambda_\odot$ and Ω

two parameters which determine the initial orientation with respect to the Sun. It can be seen that orbits in the GNSS regime are very sensitive to the initial planar configuration. The GNSS regime spans from $a \approx 25\,000\,\text{km}$ to $a \approx 30\,000\,\text{km}$ with $50^\circ < i < 70^\circ$ (see Sec. 1.2.2). In the left graph it can be seen that GNSS satellites can be deorbited with $\sigma \approx 30\,\text{m}^2\,\text{kg}^{-1}$ in the minimum case. This means that at a certain time of the year for a certain right ascension of the orbit's ascending node a deorbiting manœuvre can be performed with a far lower area-to-mass-ratio than at other times. Thus, SRP-augmented deorbiting may still be an option for spacecraft in the GNSS regime if the date of the manœuvre initialisation can be freely chosen.

Figure 4.18 shows the standard deviation of the results for different initial planar configurations. This is a different way to express the sensitivity with respect to initial $\lambda_\odot$ and Ω. It can be seen that the areas in which deorbiting is most feasible are also the least sensitive to the initial planar configuration. This is advantageous when designing a fail-safe deorbiting system which deploys automatically when the spacecraft becomes unresponsive. It can be seen that the sensitivity is highest at high inclinations and in a region around $10\,000\,\text{km} < a < 15\,000\,\text{km}$, $50^\circ < i < 70^\circ$. This region is located in the fork between the two regions of high effectiveness identified before.

4.4 Comparison with propulsive end-of-life manœuvre

In order to assess the effectiveness of SRP-augmented deorbiting it is necessary to compare it to propulsive end-of-life manœuvres which are the main alternative. An approximate mass comparison is made to compare the two methods quantitatively. For the propulsive method the fuel mass fraction m_f is considered and compared to the ratio of mass of the SRP-augmented deorbiting device to the total spacecraft mass m_b for SRP-augmented deorbiting. A simple analytical approach is used.

4.4.1 Fuel mass fraction for propulsive deorbiting

Six different propulsion systems are considered, two high-thrust systems and three low-thrust systems (see Table 4.1). The higher the specific impulse I_{sp} of a system the more fuel-efficient it becomes. The values of specific impulse in this table are estimates and are taken from Wertz and Larson [109] and Mueller et al. [31]. Mono-propellant and bi-propellant are high-thrust systems which are both used on larger spacecraft. Bi-propellant systems are more effective but also more complex. Both tend to have a high dry mass due to the complexity of the system. Resistojets offer the lowest I_{sp} of the chosen high-thrust systems but are low in cost and complexity. They

Propulsion System	**Specific Impulse**	**Propulsion Type**
Mono-propellant	200 s	high-thrust
Bi-propellant	300 s	high-thrust
Resistojet	500 s	low-thrust
Hall effect thruster	1200 s	low-thrust
Xenon ion thruster	2500 s	low-thrust

Table 4.1: Different propulsion systems considered in comparison with specific impulse and propulsion type

work by heating a fluid with electric resistors which is then expelled through a nozzle. Hall effect and Xenon ion thrusters both work by accelerating ions through an electric and/or magnetic field. Efforts are made to make miniaturised versions of these systems affordable to the smalls satellite market. There are additional types of thrusters available which have not been considered in this study as the aim is to estimate the fuel mass required with very different systems.

Although low-thrust systems have higher specific impulses and are thus more fuel efficient, high-thrust systems can perform more effective impulsive manœuvres. Here it is assumed that a high-thrust spacecraft would perform a single impulse manœuvre to transfer from a circular orbit with semi-major axis a onto an elliptical orbit with a perigee altitude of zero. The required Δv can be found with the following expression:

$$\Delta v = \sqrt{\frac{\mu}{a}} - \sqrt{\mu \left(\frac{2}{a} - \frac{2}{a + R_E} \right)} \tag{4.11}$$

A low-thrust spacecraft on the other hand would thrust continuously and thus spiral down from its initial orbit until it reaches zero altitude. The Δv for this manœuvre can be estimated as follows [53]:

$$\Delta v = \sqrt{\frac{\mu}{R_E}} - \sqrt{\frac{\mu}{a}} \tag{4.12}$$

Atmospheric drag is not considered in either formulation. If added it would reduce the Δv requirements as the spacecraft would not need to reach zero altitude to deorbit. The higher the initial altitude, the smaller will be the difference between the drag-free case and the case considering drag.

With the Δv determined, next the ratio m_f of required fuel mass over the initial wet mass of the satellite can be calculated using the rocket equation [119]:

$$m_f = 1 - \exp(-\frac{\Delta v}{I_{sp} g_0}) \tag{4.13}$$

Figure 4.19 shows the results of these calculations. It can be seen that the Xenon ion thrusters is always the most effective of all methods followed by the Hall effect thruster and the bi-propellant system. In LEO (Fig. 4.19(a)) the Resistojet is more efficient than the mono-propellant system. However, in MEO (Fig. 4.19(b)) it is overtaken by mono-propellant at approximately 19 000 km semi-major axis.

4.4.2 Mass fraction of the passive deorbiting system

For the passive deorbiting system a design similar to the baseline design for the GTO to LEO transfer is used (see Sec. 3.2). In this investigation the mass of the surface material of an inflatable balloon is calculated. The material is assumed to have a thickness $d_b = 5\,\mu\text{m}$ and the density of polyethylene terephthalate (PET) $\rho = 1400\,\text{kg}\,\text{m}^{-3}$. PET film is commonly known as Mylar and is one of the main choices for solar sail material. The other main choice is Kapton which has a very similar density. The mass fraction m_b of the balloon subsystem over the total spacecraft mass for a reflectivity coefficient of $c_R = 1$ can then by calculated for a given effective area-to-mass-ratio σ as follows:

$$m_b = 4 d_b \rho \sigma \tag{4.14}$$

With this expression the balloon mass fraction as a function of σ can be calculated. The results for three different values of balloon material thickness can be seen in Fig. 4.20. As discussed in Sec.3.2.1, 2 µm Mylar is the state-of-the-art for solar sailing while 10 µm is in the range of the thickness of common rescue foil.

With Eq. (4.14) the results from Sec. 4.3.2 can then be converted into the balloon mass fraction. It is assumed that the spacecraft can initiate the manœuvre at the optimum time of year so that the minimum results with respect to $\lambda_\odot$ are used.

Figure 4.21 shows the converted plot. It can be seen that in large orbital regions SRP-augmented deorbiting is impossible with the given specifications. It could become more feasible for thinner material or a different deorbiting subsystem design, such as a flat sail granting higher geometric efficiency (see Sec. 3.2.1).

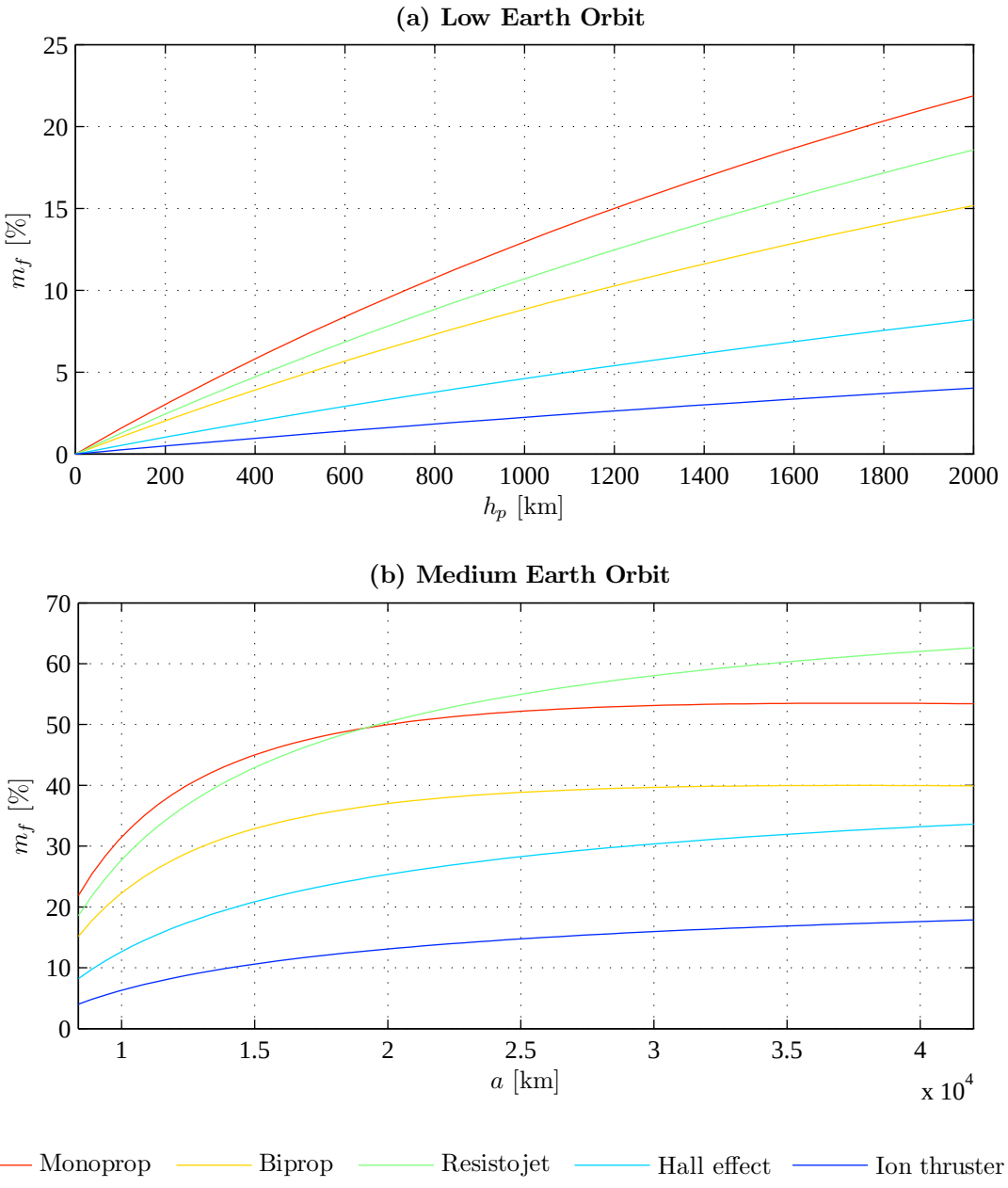

Figure 4.19: Mass fraction of fuel over total spacecraft wet mass for a propulsive end-of-life manœuvre as a function of altitude for different propulsion systems

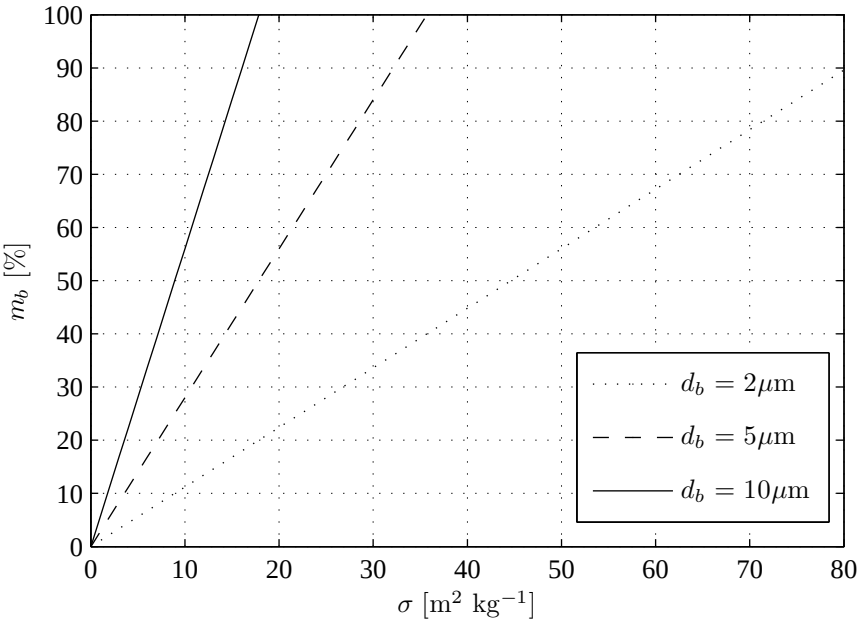

Figure 4.20: Mass of balloon material over total spacecraft mass as a function of effective area-to-mass-ratios for different values for balloon material thickness d_b

The mass fractions calculated for both the balloon and the fuel mass are approximate guidelines. For a real system, extra mass would have to be added for the propulsion subsystem on one hand and the balloon deployment system on the other. However, the results can provide an estimate of the mass advantages of SRP-augmented deorbiting over propulsive deorbiting in the most effective regions identified in Sec. 4.3.2. In these regions the balloon mass fraction is below 20 % and can thus only be matched by the ion engines, which are complex and expensive.

Other than mass advantages the balloons also offer low cost of components and operations, as after the signal for deployment no further control is required since the device is spherically symmetric and does not require either active or passive attitude control. Small satellite systems can profit from these significant advantages.

4.5 Verification of test scenarios

The results presented in the previous section are now verified for three test scenarios. The verification is performed using the high precision orbit propagator STK HPOP as introduced in Sec. 2.3.2. Three different MEO orbits are chosen.

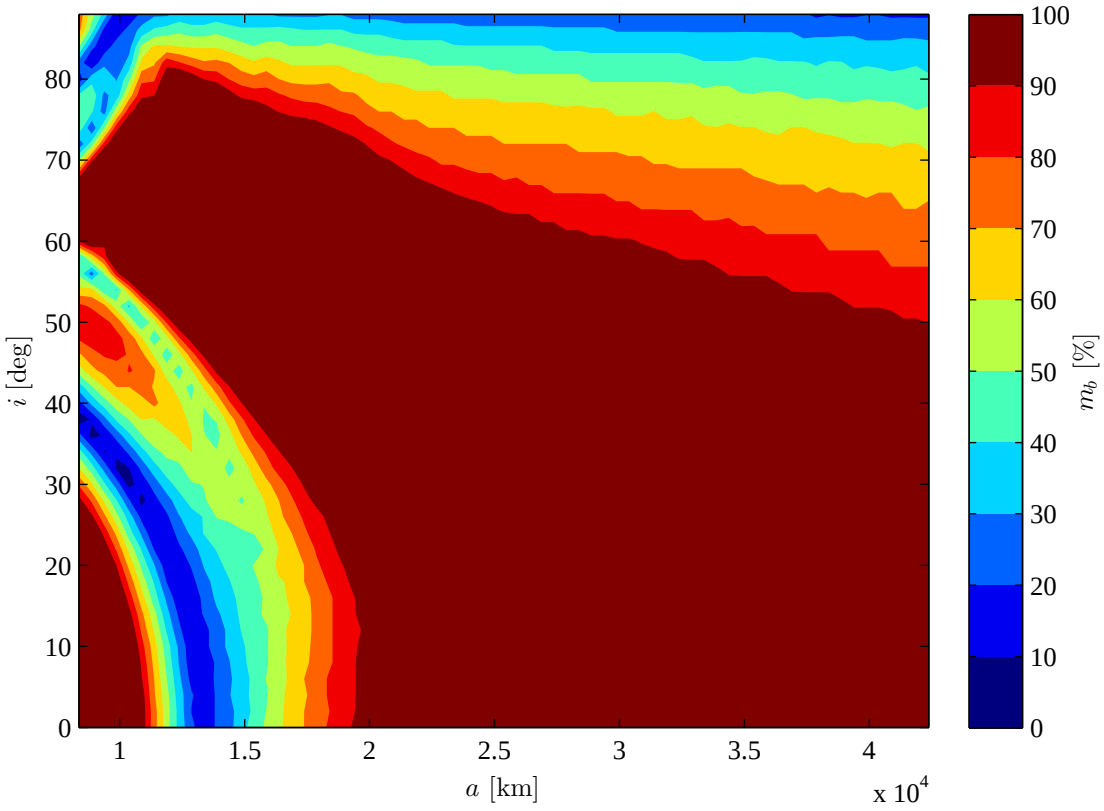

Figure 4.21: Mass of balloon material over total spacecraft mass of an SRP augmented deorbiting manœuvre initiated at the optimum time of year with $d_b = 5\,\mu\text{m}$

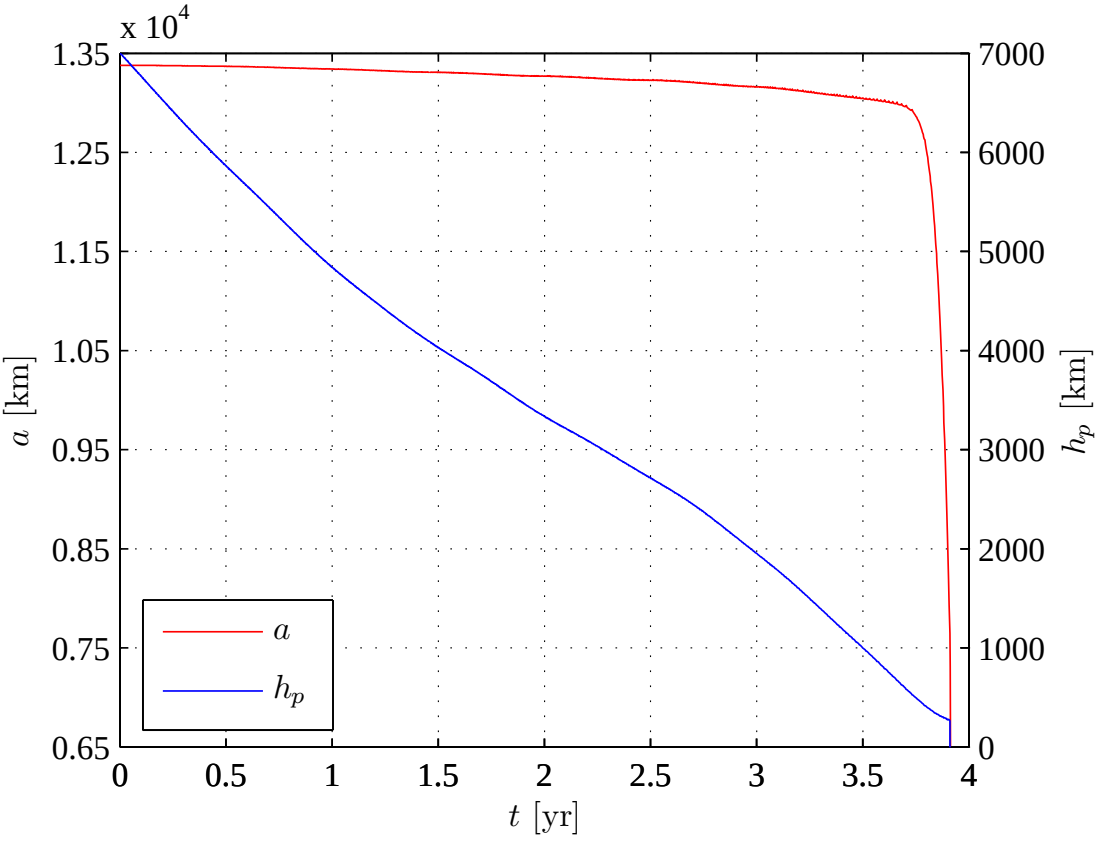

Figure 4.22: Evolution of the perigee altitude and semi-major axis of a 7000 km equatorial orbit for a spacecraft with an effective area-to-mass-ratio of $2\,\mathrm{m}^2\,\mathrm{kg}^{-1}$

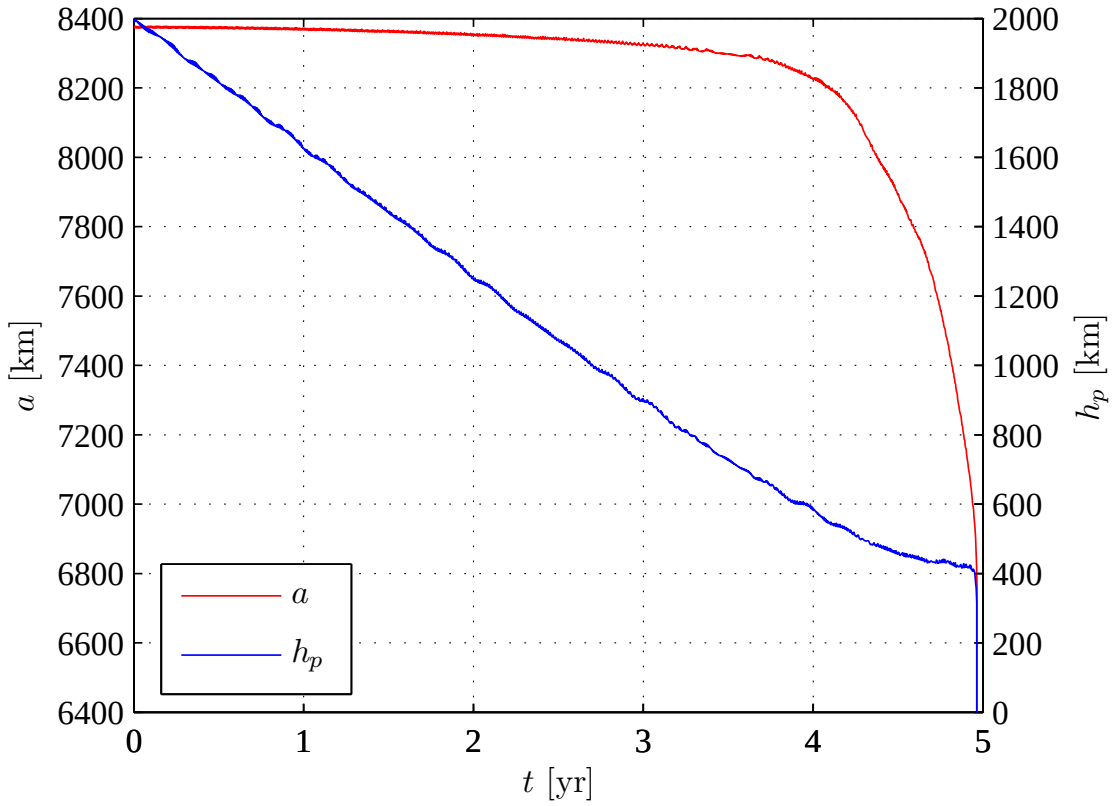

Figure 4.23: Evolution of the perigee altitude and semi-major axis of a 2000 km orbit with 40° inclination for a spacecraft with an effective area-to-mass-ratio of $5\,\mathrm{m}^2\,\mathrm{kg}^{-1}$

The first orbit is an equatorial orbit at 7000 km altitude. A comparison with Fig. 4.15 shows that SRP-augmented deorbiting is highly effective for this initial orbit. In the numerical model in Sec. 4.3.2 the required area-to-mass-ratio is $2\,\mathrm{m}^2\,\mathrm{kg}^{-1}$ for a deorbit within five years. Figure 4.5 shows the resulting evolution of the semi-major axis and perigee altitude. It can be seen that the numerical model is accurate in this case as the total manœuvre duration is just under four years. The two phases of the manœuvre are easily distinguishable. In the first phase the semi-major axis only decreases slowly and then drops sharply in the second phase. All the while the perigee altitude decreases quasi-linearly. This is because initially the eccentricity is increased while in the second phase the semi-major axis decreases. Both parameters affect the perigee altitude.

For the next case an orbit at 2000 km altitude is chosen. Figure 4.15 shows that this altitude orbit with $i \approx 40°$ requires the least area-to-mass-ratio. At $i = 40°$ the numerical model predicts that an effective area-to-mass-ratio of $5\,\mathrm{m}^2\,\mathrm{kg}^{-1}$ is needed to deorbit the satellite within five years. The propagation of a spacecraft with these properties is shown in Fig. 4.5. Again the numerical prediction is accurate, as the spacecraft deorbits within just under five years time. The evolution of semi-major axis and perigee altitude is similar to the 7000 km case presented in Fig. 4.5, however,

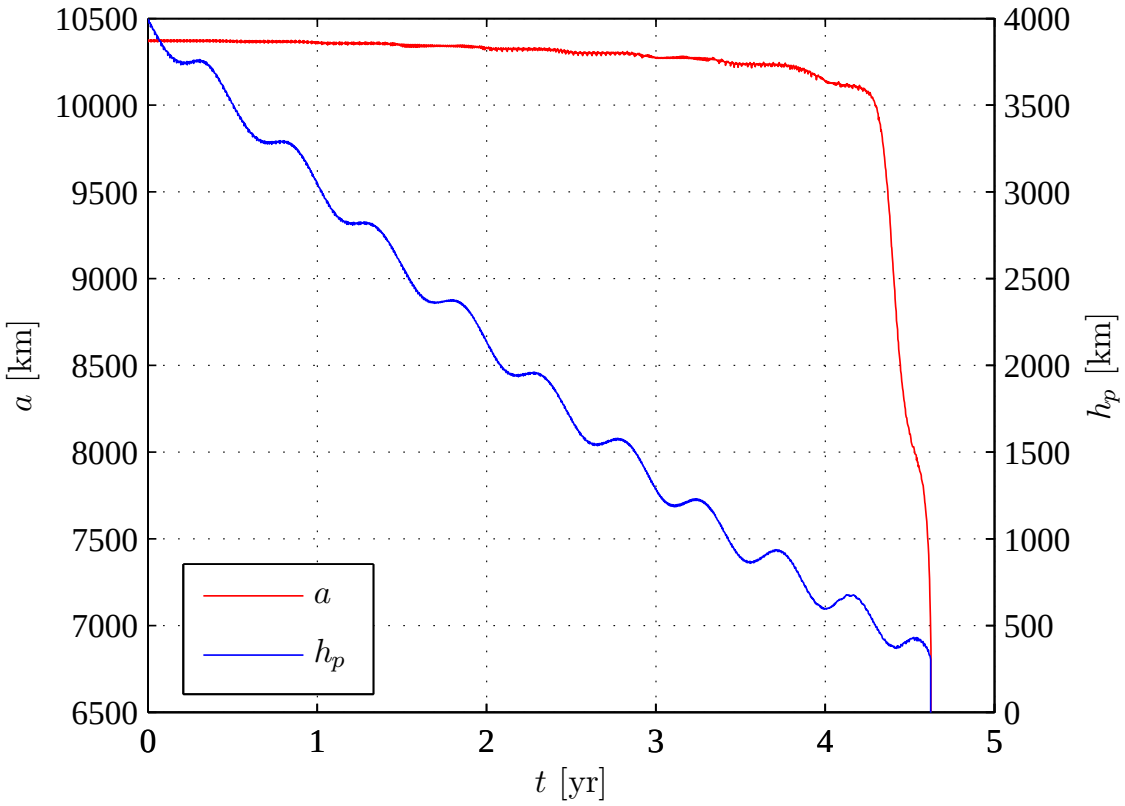

Figure 4.24: Evolution of the perigee altitude and semi-major axis of a 4000 km polar orbit for a spacecraft with an effective area-to-mass-ratio of $6\,\mathrm{m^2\,kg^{-1}}$

the transition between the two phases is not as clear at 2000 km. This is likely due to the closer initial distance of the perigee to the Earth which means that drag will set in less suddenly if the perigee is decreased over a similar time span as in the previous case.

Finally, a polar orbit ($i = 90°$) is investigated. From Fig. 4.16 a 4000 km altitude orbit is selected with a predicted required area-to-mass-ratio of $6\,\mathrm{m^2\,kg^{-1}}$. For a polar orbit the analytical model developed in Sec. 4.1.1 is not applicable any more. This is because the J_2 effect does not work as formulated in this model. It will rotate the orbit perigee in a plane normal to the ecliptic, while this plane will rotate with respect to the Sun mainly due to the Earth's motion around the Sun. The method of SRP-augmented deorbiting can still be effectively applied as the perigee is rotated due to SRP as well as the J_2 effect. If the rate of this rotation is close to the rate of the Earth's motion around the Sun, then as a result the spacecraft will experience an eccentricity increasing effect from solar radiation pressure when SRP acts in the orbit plane.

Figure 4.5 shows the resulting trajectory for this test case. It can be seen that the perigee altitude has phases of strong decrease and phases of quasi-stagnation which alternate approximately

twice per year. This is the effect described above. Furthermore, as the perigee enters the regime of atmospheric drag, the semi-major axis decreases and the rate of change of the argument of perigee is no longer the same as the rotation of the Earth around the Sun. This means that the decrease becomes less pronounced while there are even small increases in altitude discernible. The period of the oscillations becomes shorter towards the end of the manœuvre, which is completed within the required five years time.

4.6 Conclusions

This chapter introduced a new concept for SRP-augmented deorbiting and investigates its applicability to MEO spacecraft. SRP-augmented deorbiting is a passive deorbiting technique which can be applied to small spacecraft in high altitude orbits. Its main advantage, apart from the applicability to high altitude, is the fully passive nature of the manœuvre, which allows the spacecraft to remain switched off for the entire duration of the deorbit. This means that the method could be used in a fail-safe device which deploys when a spacecraft is unresponsive for a given time. This is particularly beneficial for small satellites, which, as discussed in Sec. 1.2, are typically built with a low-cost and low reliability philosophy and thus cannot claim with sufficient certainty that they will be able to perform an active deorbit manœuvre. It is less likely to be adapted by larger spacecraft such as Galileo and other GNSS satellites, as the size of the sail or balloon required is not feasible by the current state of technology.

The Hamiltonian dynamics of the orbit evolution were used to provide an analytical analysis of the method. An expression for the required area-to-mass-ratio was derived for planar orbits. This expression was then verified numerically for equatorial orbits. Next, numerical propagation was used to determine the required area-to-mass-ratio for inclined orbits. The results were dependent on inclination. The sensitivity of the method with respect to initial time of year and planar orientation with respect to the Sun was investigated. Two regions in the inclination and semi-major axis parameter space were identified in which the requirements and the sensitivity are low. Finally, three test cases were analysed in a high precision orbit propagator. It was shown that for all three the numerical results are accurate and the spacecraft deorbited within the required five years time.

Considering the survey of current MEO objects presented in Sec. 1.2.2, the important regions identified in this section can be assessed for deorbiting with the method presented in this chapter. GNSS satellites in high inclination orbits of approximately 20 000 km altitude and sub-GEO orbits with low inclination and approximately 34 000 km altitude are not suitable for deorbiting with solar radiation pressure and the J_2 effect only, as the required effective area-to-mass-ratios would be in

the region of $50\,\mathrm{m}^2\,\mathrm{kg}^{-1}$. This is larger than realistically achievable with current solar sail materials. However, the effectiveness in the identified low MEO regions enable small satellite missions in that region which meet deorbiting standards, leading to new applications for the small satellite industry.

In order to be able to use this method in the regimes identified as effective, the technology readiness of ultra-lightweight inflatable or deployable structures needs to be increased. The device needs to be light enough to not contribute greatly to the overall the system mass. It also needs to be fully functional after the mission is completed. The mechanism therefore require a long shelf-life.

Chapter 5

SRP-Augmented Deorbiting from High Sun-synchronous Orbits

In this chapter the SRP-augmented deorbiting method introduced in the Chapter 4 is applied to high altitude Sun-synchronous orbits (SSO). SSOs are typically retrograde orbits of a fixed inclination which depends on the semi-major axis for which the J_2 effect causes the line of nodes to precess at the same rate as the Earth's orbital motion about the Sun. Thus the orbit plane always has the same aspect angle with respect to the Sun (see Sec. 1.2.2). This is useful for many Earth observation missions and makes SSOs the most popular of low Earth orbits (LEO). This popularity means that SSOs are at a particular risk of space debris collisions and so end-of-life disposal is essential for spacecraft in these orbits. However, as discussed in Sec. 1.2.2, drag augmentation is infeasible at high altitudes and electrodynamic tethers cannot be used at high inclinations. This arguably makes SRP-augmented deorbiting the only feasible passive deorbiting method for these critical orbits.

In the first section the Hamiltonian model of the orbital dynamics is modified for Sun-synchronous orbits. In Sec. 5.2 a numerical propagation is used to find an estimate for the required area-to-mass-ratio to deorbit. These results are also compared to the analytical results. Finally, in Sec. 5.3 the results from the previous section are verified for three cases with a high precision orbit propagator.

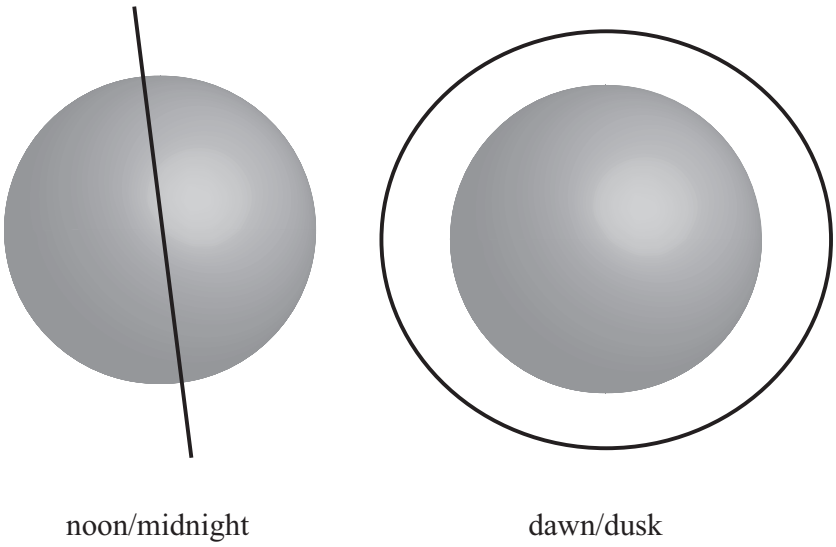

Figure 5.1: Sun-synchronous orbits: noon/midnight orbit and dawn/dusk orbit as seen from the direction of the Sun

5.1 Modified Hamiltonian model

In order to assess the problem analytically some assumptions and simplifications have to be made. As already assumed in Eq. (2.9), the tilt of the Earth's axis and the effect of eclipses are neglected. Furthermore, out-of-plane effects are not considered in the analytical SRP model. Therefore, the predicted behaviour will be most accurate for a noon/midnight orbit, as this orbit predominantly faces the Sun edge-on and thus experiences only small SRP forces along the normal of the orbit plane. Dawn/dusk orbits however experience mainly out-of-plane forces. This is illustrated in Fig. 5.1.

The first step in the creation of a modified analytical model is to consider the components of the Hamiltonian for planar orbits in Eq. (2.9) in Sec. 2.1.1:

$$H(\phi, e) = \alpha e \cos\phi - \frac{\kappa}{3\sqrt{1-e^2}^3} - \sqrt{1-e^2}$$

The first term represents for the effect of solar radiation pressure and is dependent on the SRP parameter α. The second term represents the effect of the Earth's oblateness and is dependent on the J_2 effect parameter κ. The final term represents the orbital motion of the Earth around the Sun. For Sun-synchronous orbits the SRP term remains the same because out-of-plane forces are neglected.

When orbits are inclined out of the plane, the Sun-perigee angle is redefined as $\phi = \Omega + \omega - \lambda_\odot - \pi$ (Eq. (2.1)). Sun-synchronous orbits are designed such that $\Omega - \lambda_\odot$ is constant. The rate of change in right ascension of the ascending node and the the rate of change in true longitude of the position of the Sun are equal and opposite. Thus, the last term of Eq. (2.9) can be removed so that the second term only needs to consider the change in the argument of perigee. The modified Hamiltonian can be written as:

$$H_{\text{sync}}(e, \omega) = \alpha e \cos\omega - \frac{\kappa_{\text{sync}}}{3\sqrt{1-e^2}} \tag{5.1}$$

with

$$\kappa_{\text{sync}} = \frac{d\omega}{dt}\frac{\left(1-e^2\right)^2}{n_\odot} = \frac{3}{2n_\odot} J_2 {R_E}^2 \sqrt{\frac{\mu}{a^7}} \left(2 - \frac{5}{2}\sin i_{\text{sync}}\right) \tag{5.2}$$

The Sun-synchronous inclination i_{sync} for circular orbits can be calculated for a given semi-major axis using the following expression:

$$\cos i_{\text{sync}} = -\frac{2n_\odot}{3J_2{R_E}^2}\sqrt{\frac{a^7}{\mu}} \tag{5.3}$$

With this term the following expression for κ_{sync} can then be found:

$$\kappa_{\text{sync}}(a) = 3\sqrt{\frac{{J_2}^2{R_E}^4\mu}{{n_\odot}^2 a^7}} - \frac{15}{4}\sqrt{\frac{{J_2}^2{R_E}^4\mu}{{n_\odot}^2 a^7} - \frac{4}{9}} \tag{5.4}$$

Next, the required area-to-mass-ratio for deorbiting is derived in a way analogous to Eqs. (4.1) and (4.2). The value of the Hamiltonian for a circular orbit is calculated by setting the eccentricity to zero in Eq. (5.1), so that:

$$H_{\text{sync,circ}} = \frac{\kappa_{\text{sync}}}{3} \tag{5.5}$$

The Hamiltonian in Eq. (5.1) is then set equal to Eq. (5.5) in order to isolate the phase line in the orbital element phase space of eccentricity e and argument of perigee ω which passes through $e = 0$. As shown in Sec. 4.1.1, the maximum eccentricity can only be reached at either $\phi = 0$ or $\phi = \pi$. Thus, using Eqs. (2.4) and (2.6) the following expression for the required effective area-to-mass-ratio σ can be found:

$$\sigma_{\text{sync}}(a) = \frac{2n_\odot c}{F_\odot}\sqrt{\frac{\mu}{a}}\left|\left(1 - \left(1 - \left(1 - \frac{R_E}{a}\right)^2\right)^{-\frac{3}{2}}\right)\frac{\kappa_{\text{sync}}(a)}{\left(1-\frac{R_E}{a}\right)}\right| \tag{5.6}$$

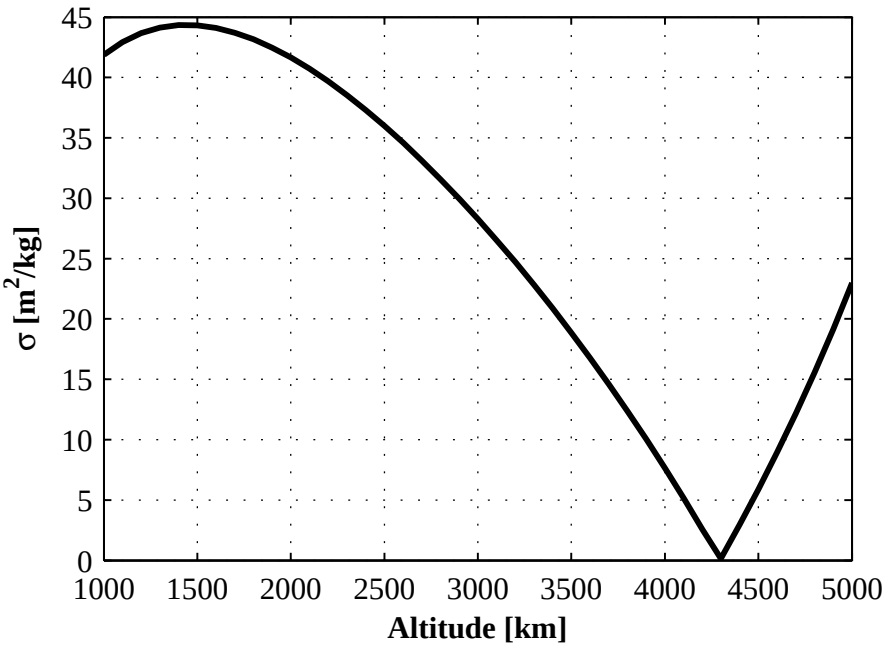

Figure 5.2: The analytical results for the required effective area-to-mass-ratio σ to deorbit a Sun-synchronous orbit

The results of the analytical approach are represented in Fig. 5.2. They are similar to those for planar orbits presented in the previous section, but the location of the minimum is at 4300 km rather than 7500 km as in the planar case.

In the next section the analytical results are compared to a numerical solution. In this case, it is not expected that the analytical prediction is very accurate as several simplifications and assumptions had to be made. In particular, the out-of-plane forces due to SRP are neglected. This assumption is most accurate for noon/midnight orbits although not even then is the orbit normal permanently orthogonal to the solar radiation. Due to the tilt of the Earth's axis, the aspect angle with respect to the Sun also oscillates over the year. Neither is the assumption that the orbits remain Sun-synchronous throughout the deorbit accurate. As soon as the eccentricity begins to increase the Sun-synchronous inclination changes and a progression of the line of nodes begins. However, the analytic approximation does provide an initial estimate.

5.2 Numerical analysis

In this model, the orbital dynamics are propagated numerically by integrating the semi-analytical equations for the secular orbit evolution in non-singular elements, which are introduced in Sec.2.2.2.

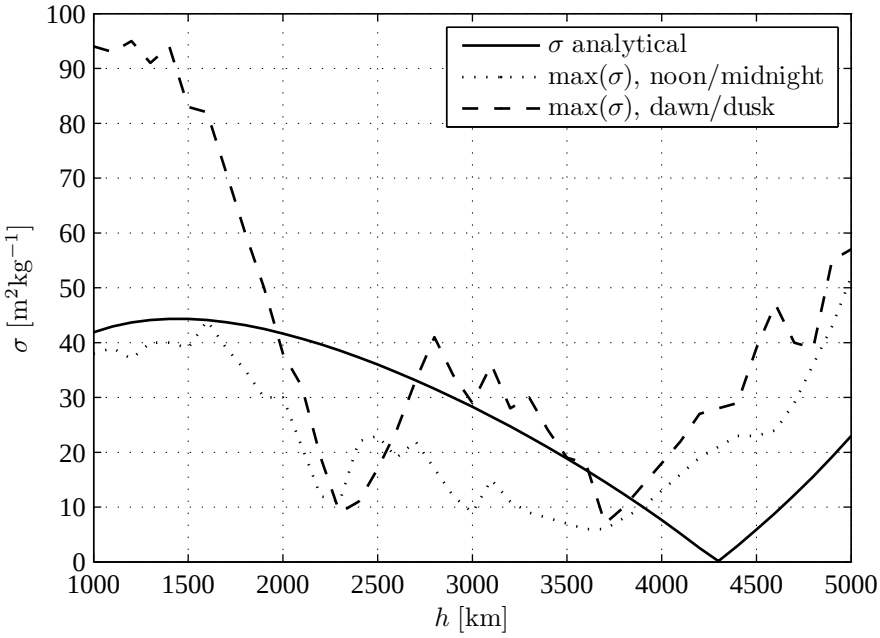

Figure 5.3: Analytical and maximum numerical results for the required effective area-to-mass-ratio to deorbit a Sun-synchronous noon/midnight and dawn/dusk orbit with respect to initial true longitude of the Sun

Initially, the numerical propagation considers only the perturbations of solar radiation pressure and the J_2 effect. The effect of drag and eclipses are neglected to save computational time and to allow a comparison with the analytical model. The criterion for a successful deorbit is a perigee altitude of zero and the maximum propagation time is set to five years, as in chapter 4.

In order to find the required effective area-to-mass-ratio, a numerical search is implemented. The scenario is simulated starting from the analytical best guess for σ from Eq. (5.6) and, depending on whether the deorbit is successful or not, a higher or lower σ is chosen for the next run. This is continued until the required σ is determined within an accuracy of $1\,\mathrm{m^2\,kg^{-1}}$. Using this method the required effective area-to-mass-ratio for deorbit is calculated for a range of initial altitudes and local times of the ascending node. For each case the result is found for eight different starting dates equally spread throughout the year starting from the spring equinox. The maximum required area-to-mass ratio for noon/midnight and dawn/dusk orbits are shown in Fig. 5.3 and compared to the analytical prediction. It can be seen that, as expected, the analytical model is not very accurate. However, the general magnitude of the results for noon/midnight orbits is shown and also the v-shaped trend. The minimum required area-to-mass-ratio occurs at an altitude 600 km, lower than predicted by the simple analytical model. As expected the method is less effective for dawn/dusk orbits than for noon/midnight orbits at lower altitudes because out-of-plane forces are higher for

dawn/dusk orbits. However, this difference in area-to-mass-ratio shrinks for increasing altitude. This is due to fact that the Sun-synchronous inclination increases with larger altitudes, and thus the orbital plane becomes more aligned with the equator. This means that even dawn/dusk orbits will experience stronger in-plane SRP effects.

Figure 5.4 shows the required effective area-to-mass-ratio for all Sun-synchronous orbit altitudes between 1000 km and 5000 km. The result shown is the maximum for the different manœuvre starting times throughout the year. The greatest difference between starting at different times is experienced by dawn/dusk orbits of altitudes between 1000 km and about 1500 km. In this region the deviation of the results with respect to the initial true longitude of the Sun is high (see Fig. 5.5). This means that the effectiveness of the manœuvre is highly dependent on the time of year when it is initiated. The required effective area-to-mass-ratio is lowest for 6:00 h orbits when the manœuvre starts in autumn and, symmetrically, lowest for 18:00 h orbits when the manœuvre starts in spring.

It can be seen from both figures that SRP-augmented deorbiting is most effective and reliable for Sun-synchronous orbits with semi-major axes between approximately 2000 km and 4500 km. In this region the maximum required effective area-to-mass-ratio is predominantly below $20\,\mathrm{m^2\,kg^{-1}}$ and always below $40\,\mathrm{m^2\,kg^{-1}}$. The sensitivity to the starting date of the manœuvre is also low. This is an advantage when a fail-safe deorbiting mechanism is applied for a system which automatically deploys when the satellite fails. With systems which are deployed on command from ground this characteristic is irrelevant as the operator can simply wait until the best time to start the deorbiting manœuvre.

5.3 Verification

In this section the numerical results presented in the previous section are verified using Satellite Tool Kit (STK v9.2.2). This is necessary to test the assumption that perturbations other than SRP and the J_2 effect (such as luni-solar perturbation) and the effect of eclipses can be neglected when performing an approximate analysis of SRP-augmented deorbiting. The propagation in STK is performed with the HPOP propagator as described in Sec. 2.3.2. Three different scenarios are tested as shown in Fig. 5.6. In all cases the Spring equinox is chosen as the manœuvre start date, i.e. $\lambda_{\odot,0} = 0$.

The selected test cases are all high altitude Sun-synchronous orbits starting at 1000 km. This is because for lower SSOs the effect of solar radiation pressure is insignificant to the effect of

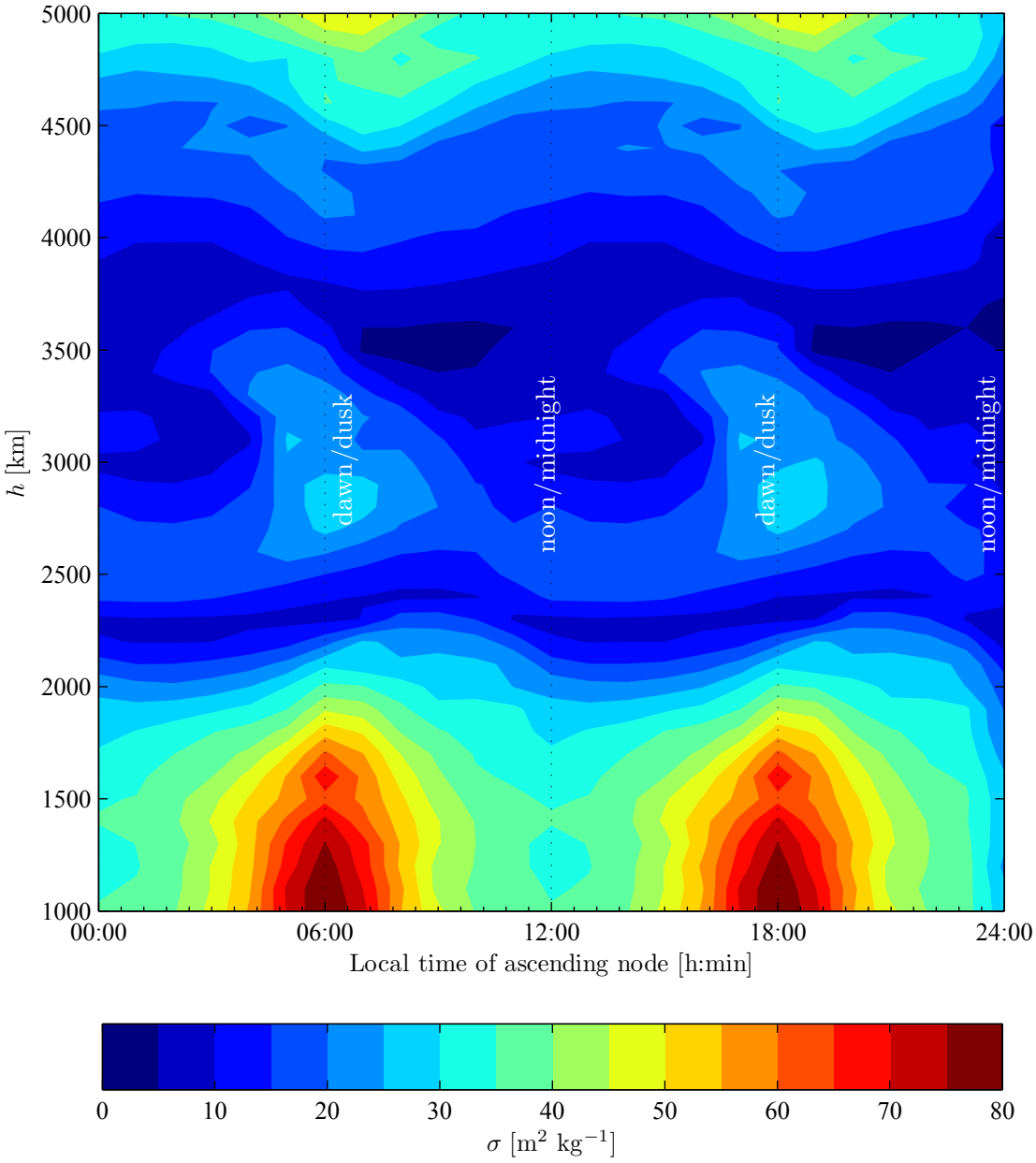

Figure 5.4: Contour plot of the numerical results for the maximum required effective area-to-mass-ratio to deorbit for Sun-synchronous orbits

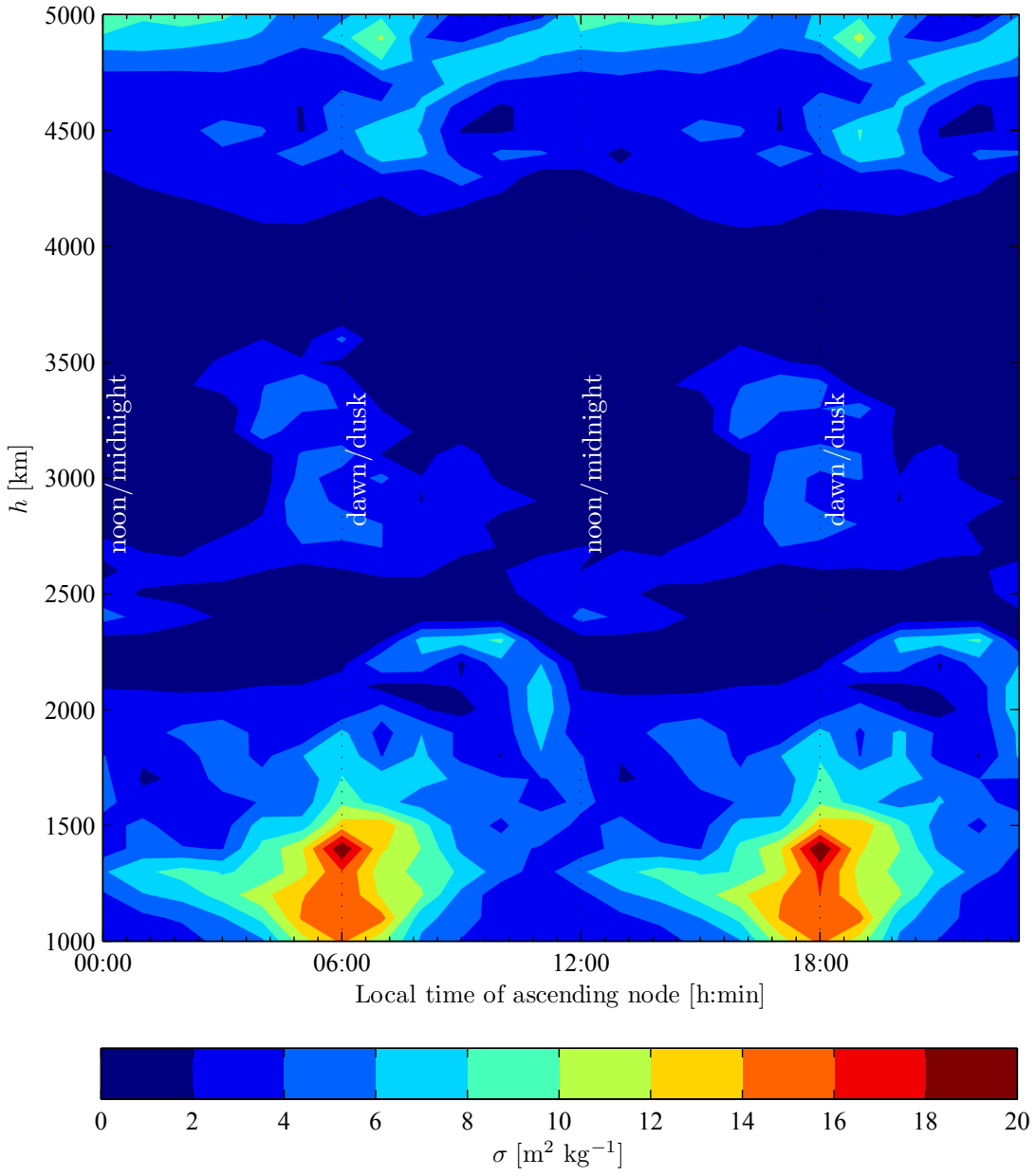

Figure 5.5: Contour plot of the standard deviation of the required effective area-to-mass-ratio to deorbit Sun-synchronous orbits with respect to initial true longitude of the Sun

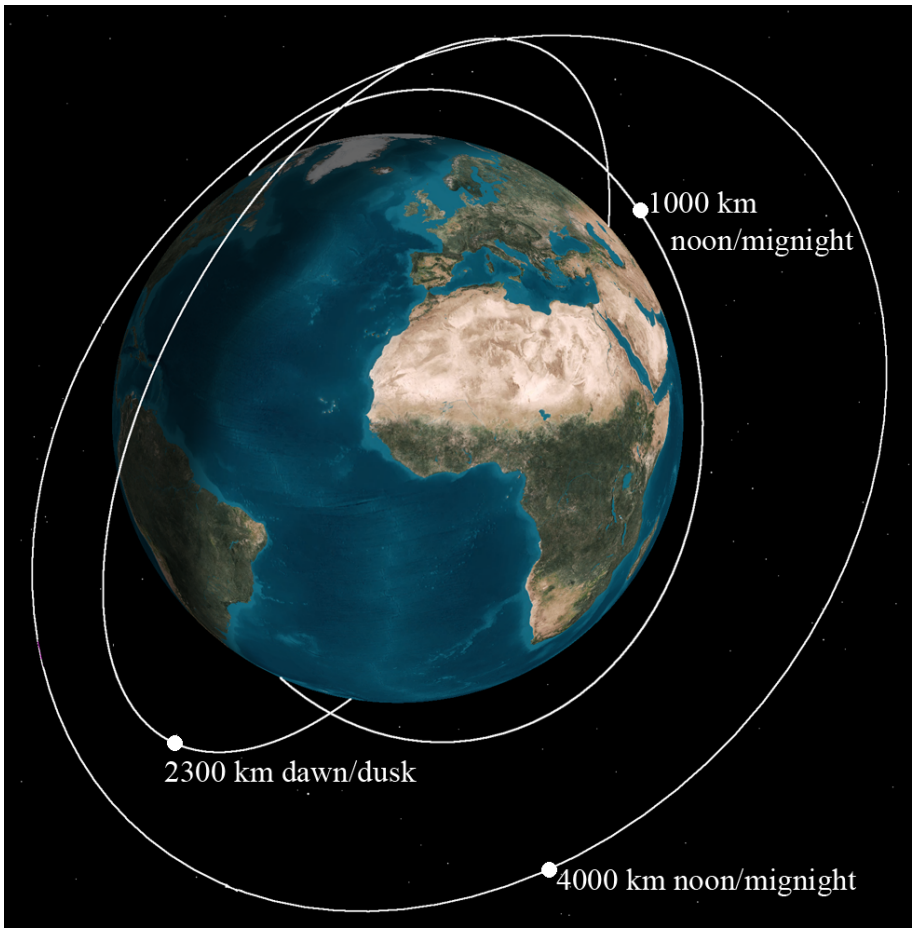

Figure 5.6: The three test case Sun-synchronous orbits with different initial altitudes and local times of the ascending node (STK)

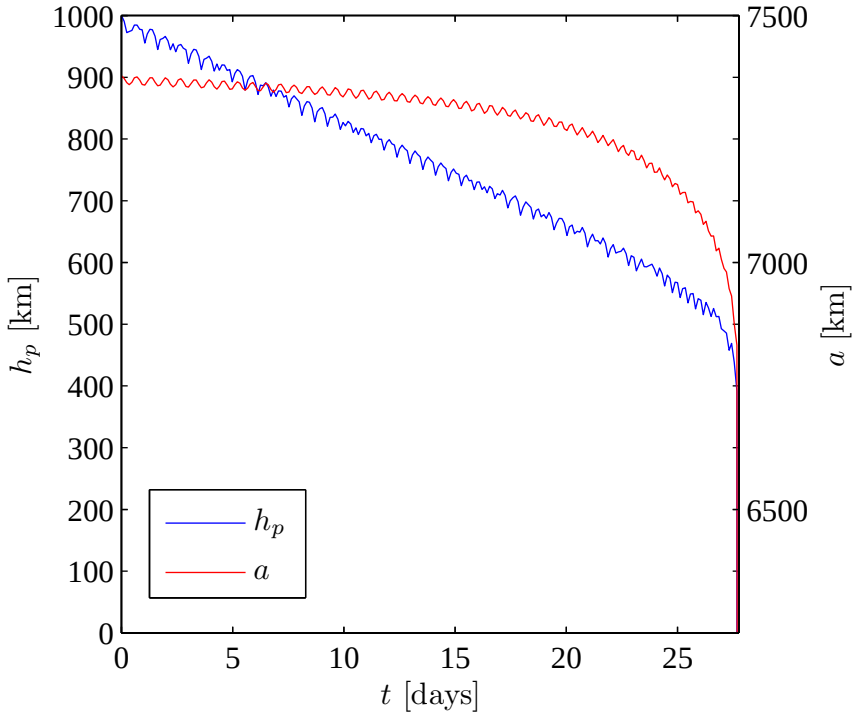

Figure 5.7: Evolution of the perigee altitude and semi-major axis of a 1000 km noon/midnight Sun-synchronous orbit for a spacecraft with an effective area-to-mass-ratio of $35\,\mathrm{m^2\,kg^{-1}}$

aerodynamic drag. At 1000 km both effects are important and above this altitude SRP becomes the single most important perturbation.

5.3.1 Low altitude SSO test case

For the first test case a noon/midnight Sun-synchronous orbit with an altitude of 1000 km is chosen. The results of the numerical model predicted a required effective area-to-mass-ratio of $35\,\mathrm{m^2\,kg^{-1}}$ for this orbit. When a spacecraft with these characteristics is propagated in STK it deorbits within just 28 days as shown in Fig. 5.7. This is due to the strong effect of drag which is neglected in the numerical model but which affects a spacecraft of a very large area-to-mass-ratio even at an altitude of 1000 km. To verify, the same simulation is run without the effect of SRP and a similar deorbit time is recorded.

To assess by how much the area-to-mass-ratio can be decreased owing to aerodynamic drag the scenario is run again repeatedly within STK with different area-to-mass-ratios until the requirements are found with an accuracy of $1\,\mathrm{m^2\,kg^{-1}}$. The deorbiting is successful within 3.5 years for a $2\,\mathrm{m^2\,kg^{-1}}$ spacecraft. Figure 5.8a shows the results for the perigee altitude and the semi-major

axis throughout the manœuvre for this case. The effect of SRP which causes the eccentricity to librate can be seen in the periodic variation in perigee altitude while the decline in semi-major axis is more uniform. The evolution of the orbit altitude as seen in Fig. 5.8a does not bring the perigee down into the lower atmosphere or even to a zero altitude as required in the MATLAB simulation in Section 5.2, but it is enough to periodically increase the effect of drag and thus speed up the final decay. The same simulation is then run again, neglecting solar radiation pressure. In this case the spacecraft did not deorbit within the same time span, as can be seen in Fig. 5.8(b). In this case the spacecraft still experiences librations in eccentricity but not as strongly as the SRP case. These librations occur due to the diurnal and seasonal variations in atmospheric density. This means that for the lower altitudes the numerical model overestimates the required effective area-to-mass-ratio. In this simulation a coefficient of reflectivity of one is assumed. For a device providing a higher reflectivity the enhancing effects of SRP will be further increased.

5.3.2 Medium altitude SSO test case

For the next test case a 2300 km dawn/dusk orbit is chosen. At this altitude the required area-to-mass-ratio shows a local minimum for dawn/dusk orbits. The predicted required effective area-to-mass-ratio is $10\,\mathrm{m^2\,kg^{-1}}$. Propagating this scenario with STK shows that as predicted a successful deorbiting manœuvre is completed within 3.5 years (see Fig. 5.9a).

Again this result is compared to a simulation in which solar radiation pressure is neglected. In this case drag has a minimal effect on the orbit evolution as shown in Fig. 5.9(b). In this figure the slight oscillations in perigee altitude are due to third body effects. For this scenario the numerical prediction is accurate and the effect of solar radiation pressure is essential to the eventual re-entry.

5.3.3 High altitude SSO test case

For the final test case a 4000 km noon/midnight orbit is chosen. The predicted required effective area-to-mass-ratio for this scenario is $15\,\mathrm{m^2\,kg^{-1}}$ maximum. The simulation in STK shows that this prediction is justified. The manœuvre is completed within one year as shown in Fig. 5.10(a). A comparison to the simulation without SRP shows again that the effect of solar radiation pressure is instrumental in the manœuvre as the semi-major axis and eccentricity hardly vary at all in the latter case as shown in Fig. 5.10(b).

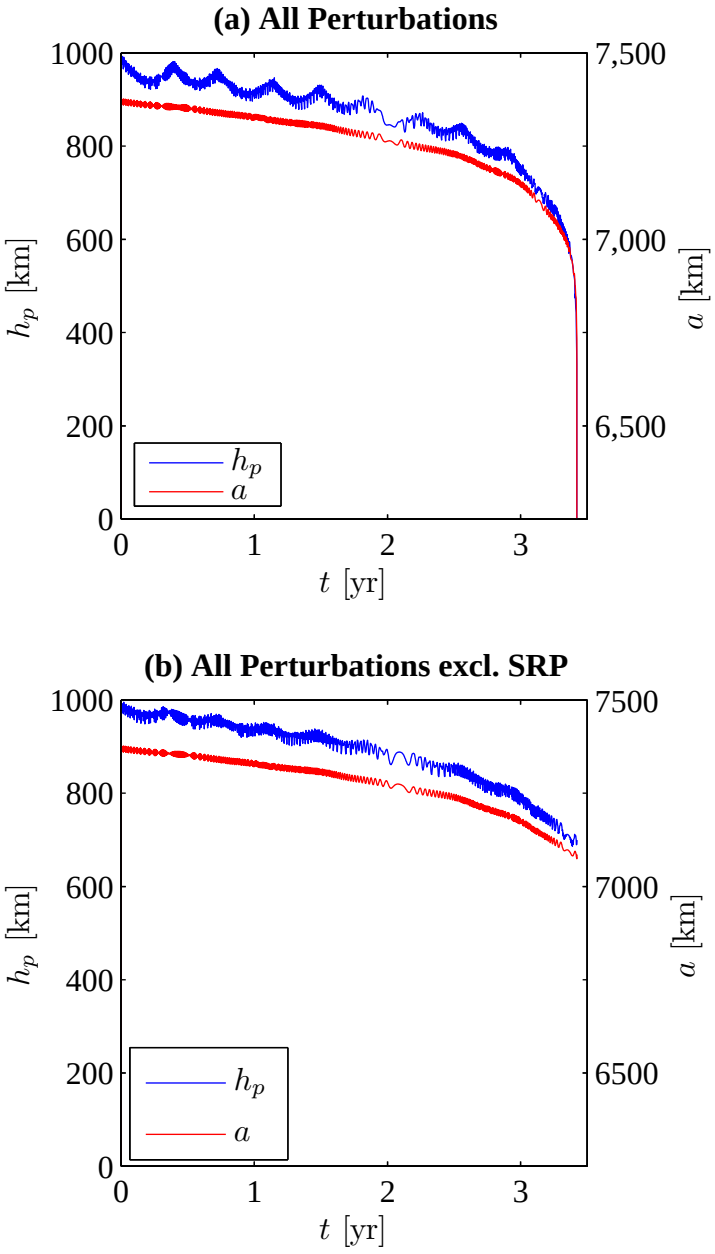

Figure 5.8: Evolution of the perigee altitude and semi-major axis of a 1000 km noon/midnight Sun-synchronous orbit for a spacecraft with an effective area-to-mass-ratio of $2\,\mathrm{m}^2\,\mathrm{kg}^{-1}$ (a) including the effect of SRP and (b) excluding the effect of SRP

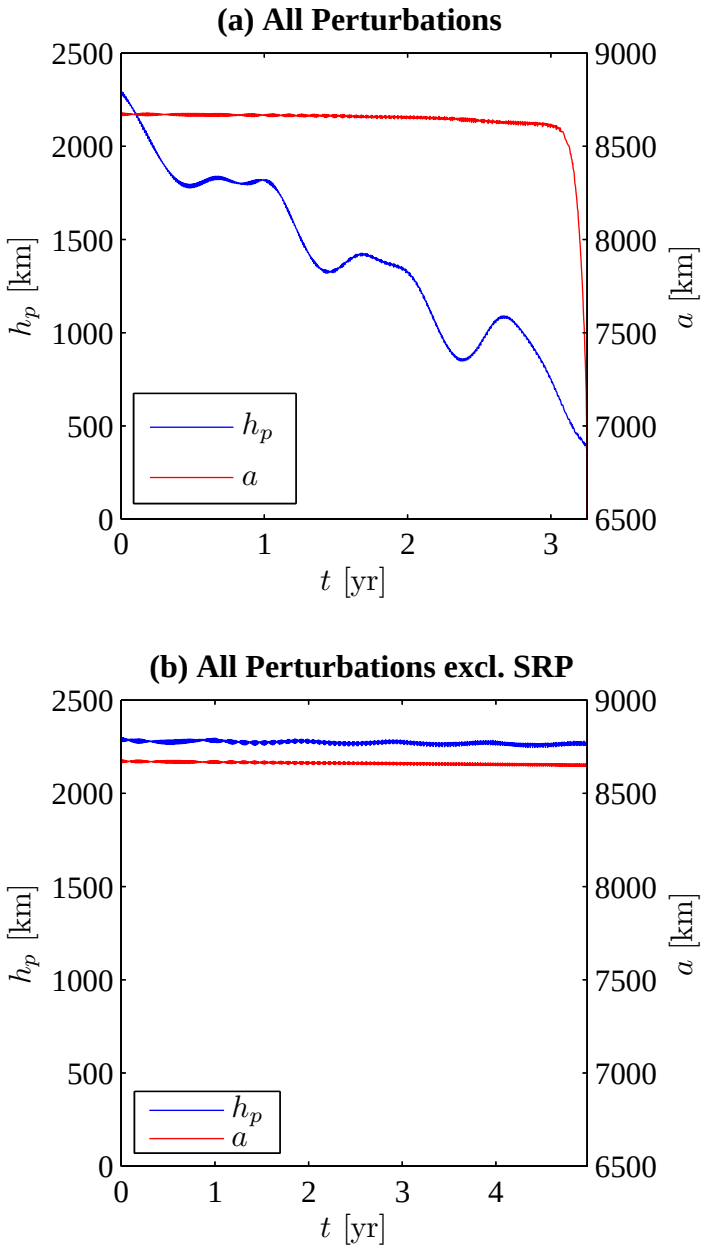

Figure 5.9: Evolution of the perigee altitude and semi-major axis of a 2000 km dawn/dusk Sun-synchronous orbit for a spacecraft with an effective area-to-mass-ratio of $10\,\mathrm{m^2\,kg^{-1}}$ (a) including the effect of SRP and (b) excluding the effect of SRP

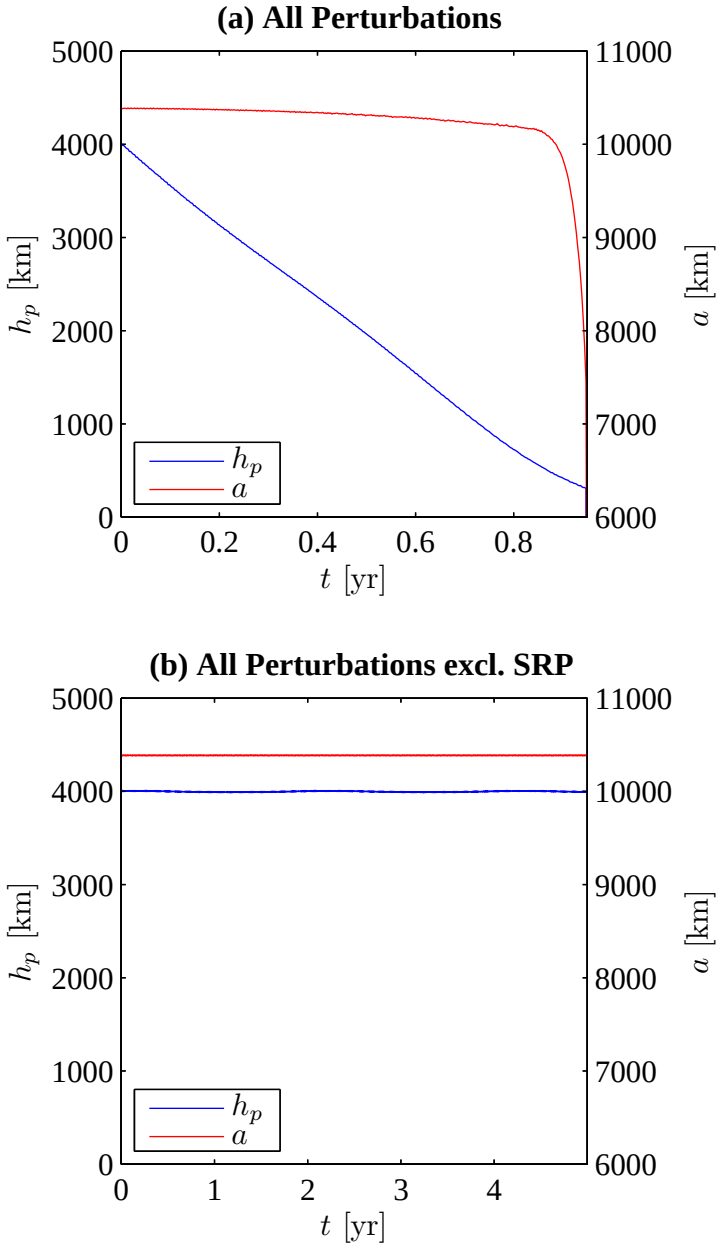

Figure 5.10: Evolution of the perigee altitude and semi-major axis of a 4000 km noon/midnight Sun-synchronous orbit for a spacecraft with an effective area-to-mass-ratio of $15\,\mathrm{m^2\,kg^{-1}}$ including the effect of SRP (a) and excluding the effect of SRP (b)

5.4 Conclusions

Solar radiation pressure-augmented deorbiting was introduced in Chapter 4 with an analytical Hamiltonian model for planar orbits, which is then adapted for Sun-synchronous orbits. The analytical results were compared to numerical results and three test cases are investigated using a high precision orbit propagator. Solar radiation pressure augmented deorbiting was shown to be an effective method to passively deorbit spacecraft from high altitude orbits. The effectiveness is dependent on altitude and inclination. For orbits with altitudes of order 1000 km it will accelerate orbital decay due to aerodynamic drag by causing the orbit eccentricity to oscillate. For higher altitudes solar radiation pressure is the dominating factor in the deorbiting manœuvre. Solar radiation pressure-augmented deorbiting is most effective for Sun-synchronous orbits of altitudes between 2000 km and 4500 km. Simulations run which neglected solar radiation pressure effects showed only very minor variations in semi-major axis and eccentricity. Moreover, the deorbiting simulation performed through Satellite Tool Kit allowed a validation of the analytical model which considered only solar radiation pressure and the J_2 effect.

Again, solar radiation pressure-augmented deorbiting has the potential to unlock new small satellite missions as it may allow small systems without propulsion subsystems to access high altitude orbits while still complying to the Inter-agency Space Debris Coordination Committee deorbiting guidelines. A further advantage of the method is that it is entirely passive. This would allow the method to be applied to a fail-safe deorbiting system which automatically removes spacecraft from orbit when they fail. This is possible as solar radiation pressure-augmented deorbiting does not require any active control.

The application of SRP-augmented deorbiting to high altitude SSOs is particularly relevant to the current international efforts to reduce space debris, as Sun-synchronous orbits are the most popular LEO orbits and thus the most populated. The SSOs with altitudes below 2000 km fall under the protected regions as defined in the space debris mitigation standards [35]. This means that deorbiting is mandatory in these orbits. Small satellite missions carrying an SRP-augmentation subsystem would thus be conforming to international guidelines if launched to one of these orbits.

PART II

Millimetre-scale:

Orbit Control for SpaceChips

Chapter 6

Electrochromic Orbit Control using a Potential Controller

In the second part of this thesis, applications of HAMR orbital dynamics for the control of SpaceChips are investigated. SpaceChips, as introduced in Sec. 1.3, are millimetre-scale spacecraft which can be deployed in large numbers, but typically lack orbit control systems. A new control method is proposed which exploits the dynamics of orbital evolution due to solar radiation pressure. This effect is modulated using electrochromic coatings to alter the optical properties of the SpaceChip. Electrochromic materials (EM) change their optical properties when a voltage or current is applied, thus modulating the fraction of light which is transmitted, absorbed and reflected, effectively changing the coefficient of reflectivity c_R of the body. The effect remains until a voltage or current in the opposite sense reverses it [120].

This chapter proposes to use electrochromic coatings to exploit the perturbing effect of solar radiation pressure for orbit stabilisation and manœuvres of SpaceChips. A spacecraft thus coated can change its coefficient of reflectivity between two set values. For a SpaceChip the ideal value for minimum reflectance is one, completely absorptive, because a lower value would mean that it were partially transmissive, and an ideal value for maximum reflectance is two. In this thesis only orbits in the region of 30 000 km to geosynchronous altitude are investigated for illustration. It is noted that possible SpaceChip missions have been proposed in the LEO regime [59] and very high elliptical Sun-pointing orbits. The latter are used in the GEOSAIL mission [100] to monitor the Earth's magnetic tail and can be utilised by a swarm of SpaceChip devices. The orbit control developed in this part of the thesis is applicable to these very high altitude orbits but not to

the LEO orbits, as the latter are strongly affected by aerodynamic drag and thus unstable in the long-term. Two different applications are discussed: orbit stabilisation and orbit manœuvres.

6.1 Analysis of the control potential

A spacecraft on a high Earth-centred orbit lying in the ecliptic plane is considered, subject to solar radiation pressure. The effects of other perturbations are neglected, as, according to Atchison and Peck [1], SRP is the dominant force in this scenario. In particular, the orbit is chosen with a perigee above LEO, so as to avoid aerodynamic drag. The orbit geometry, represented in Fig. 6.1, can be expressed through three in-plane orbital elements, semi-major axis a, eccentricity e, and the angular displacement between the orbit pericentre and the direction of the solar radiation through the centre of the Earth ϕ. The acceleration an object receives from solar radiation pressure (SRP) is given by:

$$a_{\mathrm{SRP}} = c_R \frac{F_\odot}{c} \frac{A}{m} \cos^2 \gamma \tag{6.1}$$

where c_R is the coefficient of reflectivity, $F_\odot$ the solar flux, c the speed of light, A the surface area receiving solar radiation, m the mass of the object and γ the incident angle of the Sunlight. It can be seen that the value of a_{SRP} in Eq. (6.1) depends on the area-to-mass-ratio of the object. Conventional spacecraft experience SRP only as a perturbing force, whereas the effect on micro-scale satellites becomes dominant. Solar sail technology exploits the acceleration due to solar radiation pressure by attaching a large light-weight reflective film to the satellite bus and controlling the thrust vector by varying the sail attitude (i.e. the angle γ). Electrochromic orbit control (EOC) instead modifies the reflectivity coefficient c_R, with the advantage that mechanical attitude control actuators and complex sail deployment mechanisms are not necessary. A constant attitude of the SpaceChip with respect to the Sun is assumed, which can be achieved with one of the methods discussed in Sec. 1.3.2. The SpaceChip's surface is therefore assumed to be normal to the incident solar radiation. In this case, $\gamma = 0$ and the area-to-mass-ratio with respect to the Sun is constant.

Because of the discrete nature of the reflectivity change, the orbit control has the characteristics of a bang-bang controller with the lower reflectivity state ($c_{R,\mathrm{off}}$) of the electrochromic thin-film defined as the off-state and the higher reflectivity state ($c_{R,\mathrm{on}}$) as the on-state. The two values of reflectivity used here are $c_{R,\mathrm{off}} = 1$ (completely absorptive) and $c_{R,\mathrm{on}} = 2$ (completely reflective). It is assumed that during each orbit the reflectivity is be switched twice. The true anomalies at which these changes take place are used as control parameters (f_{on} and f_{off} in Fig. 6.1).

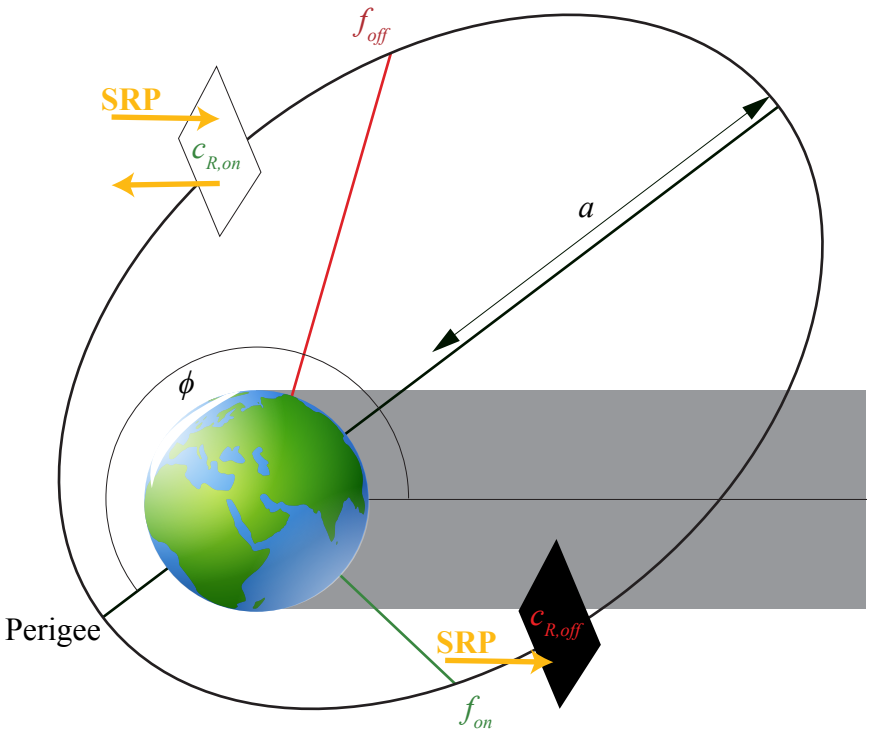

Figure 6.1: Diagram of an electrochromic orbit control controlled orbit: The control parameters, the switching angles f_{on} and f_{off} are marked. The shadow of the Earth indicated the direction of Sunlight.

6.1.1 SpaceChip model

The spacecraft model considered here is based on the Cornell University *Sprite* SpaceChip [61]. The spacecraft is a Silicon microchip (density of $2330\,\mathrm{kg\,m^{-3}}$) of $1\,\mathrm{cm}^2$ area by $25\,\mu\mathrm{m}$ thickness and resulting area-to-mass-ratio $17.4\,\mathrm{m}^2\,\mathrm{kg}^{-1}$. Because of its passively Sun-pointing design a constant area-to-mass-ratio is assumed, as discussed earlier.

Orbits with a semi-major axis of 30 000 km in the ecliptic plane are considered for illustration. A large semi-major axis is preferable because at a greater distance from the main gravitational body the ratio between the acceleration due to SRP and the acceleration due to gravity is greater and thus the effectiveness of the control method is higher. This is appropriate, as for orbits with $a \geq 30\,000\,\mathrm{km}$ SRP has an influence significantly larger than all other perturbations for the size of spacecraft considered here [1]. The secular effect of SRP on the orbit is approximated using a set of 2D analytical equations neglecting any out-of-plane forces, as introduced in Sec. 2.2.1. For orbits in the ecliptic plane which neglect the Earth's gravitational harmonics this is a valid reduction of the problem.

The simulation later in Sec. 6.2.3 on the other hand uses a 3D model of the orbital geometry and includes the J_2 perturbation as well as SRP, while the control algorithm is still based on the planar analytical model without J_2. This is to demonstrate the robustness of the algorithm for stabilisation and the validity of the assumption of SRP as the dominant perturbation.

6.1.2 Control potential of in-plane orbital elements

To analyse the usefulness of electrochromic orbit control (EOC) for orbit stabilisation, firstly its control potential has to be assessed. This requires the maximum and minimum change in the Keplerian elements (Δa, Δe, $\Delta\phi$) achievable for any initial set of elements (a_0, e_0, ϕ_0) and spacecraft parameters ($\frac{A}{m}$, $c_{R,\mathrm{on}}$, $c_{R,\mathrm{off}}$) to be determined.

The first step is to determine for each position (in true anomaly f) on an orbit whether the change in the Keplerian elements ($\frac{\mathrm{d}a}{\mathrm{d}t}$, $\frac{\mathrm{d}e}{\mathrm{d}t}$, $\frac{\mathrm{d}\phi}{\mathrm{d}t}$) is positive, negative or whether the spacecraft is in eclipse (and the orbital elements consequently remain constant since only SRP induced perturbations are considered).

Next, the maximum change in orbital elements for a certain orbit can be determined by using $c_{R,\mathrm{on}}$ when the change is positive to achieve the largest possible effect, and using $c_{R,\mathrm{off}}$ when the change is negative to minimise the negative effect. The minimum change can be obtained with the

opposite strategy, using $c_{R,\text{on}}$ when the change is negative and $c_{R,\text{off}}$ when the change is positive. The maximum and minimum change in orbital elements is computed through Eq. (6.2) where K represents any orbital element.

$$\begin{aligned}\Delta K_{\max} &= \int\limits_{\left[\frac{\mathrm{d}K}{\mathrm{d}f}<0\right]} \frac{\mathrm{d}K(c_{R,\text{off}})}{\mathrm{d}t}\left(\frac{\mathrm{d}f}{\mathrm{d}t}\right)^{-1}\mathrm{d}f + \int\limits_{\left[\frac{\mathrm{d}K}{\mathrm{d}f}>0\right]} \frac{\mathrm{d}K(c_{R,\text{on}})}{\mathrm{d}t}\left(\frac{\mathrm{d}f}{\mathrm{d}t}\right)^{-1}\mathrm{d}f \\ \Delta K_{\min} &= \int\limits_{\left[\frac{\mathrm{d}K}{\mathrm{d}f}<0\right]} \frac{\mathrm{d}K(c_{R,\text{on}})}{\mathrm{d}t}\left(\frac{\mathrm{d}f}{\mathrm{d}t}\right)^{-1}\mathrm{d}f + \int\limits_{\left[\frac{\mathrm{d}K}{\mathrm{d}f}>0\right]} \frac{\mathrm{d}K(c_{R,\text{off}})}{\mathrm{d}t}\left(\frac{\mathrm{d}f}{\mathrm{d}t}\right)^{-1}\mathrm{d}f\end{aligned} \tag{6.2}$$

The term $\frac{\mathrm{d}K}{\mathrm{d}t}$ is the variation of Keplerian elements, given by the Gauss' equations in Sec. 2.3.1 [53]. In particular, $\frac{\mathrm{d}f}{\mathrm{d}t}$ is given by Eq. (2.28). The disturbing acceleration due to solar radiation pressure is given by Eq. (6.1). The radial and transversal accelerations, a_r and a_θ, are the components of the SRP acceleration in the radial and transversal directions in the orbital plane:

$$\begin{aligned}a_r &= a_{\text{SRP}}\cos\left(f+\phi\right) \\ a_\theta &= -a_{\text{SRP}}\sin\left(f+\phi\right)\end{aligned} \tag{6.3}$$

The integrals in Eq. (6.2) are evaluated over the arc of a single orbit revolution $0 < f < 2\pi$ where $\frac{\mathrm{d}K}{\mathrm{d}f}$ is greater or smaller than zero. The resulting map allows an assessment of possible points for stabilisation. These can only be orbits for which, for all three in-plane elements, the minimum change is negative and the maximum change is positive so that a net change of zero is possible. This can be seen as a necessary criterion for stabilisation.

Semi-major axis

The semi-major axis is directly related to the energy of an orbit ε. This relationship is described as for elliptical orbits:

$$\varepsilon = -\frac{\mu}{2a} \tag{6.4}$$

where μ is the gravitational parameter of the central body, in this case the Earth.

It can be seen that the specific orbital energy increases and decreases with semi-major axis. When solar radiation pressure is acting against a component of the spacecraft velocity vector the spacecraft's orbital energy is decreased. This means that the specific orbital energy is decreased

and thus the change in semi-major axis is negative. The opposite is true when SRP is acting in the direction of the spacecraft's velocity vector and the spacecraft is accelerated. The spacecraft orbital energy then increases and the change in semi-major axis is positive. Without the effect of eclipses the total change of semi-major axis due to SRP after one orbital period is zero. However, when eclipses are considered, they will block out Sunlight on part of the spacecraft's orbit. If the orbit is not symmetrical with respect to the Sun-line, i.e. if the eccentricity is larger than zero and $\phi \notin \{0, \pi\}$, this will result in an overall change in semi-major axis, which can be positive or negative depending on ϕ. The rate of change of the semi-major axis at any point in the orbit is given by Eq. (2.23) in Sec. 2.3.1 as:

$$\frac{\mathrm{d}a}{\mathrm{d}t} = \frac{2a^2}{\sqrt{\mu p}} \left(e \sin(f)\, a_r + \frac{p}{r} a_\theta \right)$$

Figure 6.2 shows the sign of $\frac{\mathrm{d}a}{\mathrm{d}t}$ as a function of the true anomaly along an orbit and the initial value of ϕ, for an initial semi-major axis of 30 000 km. Note that the sign of $\frac{\mathrm{d}a}{\mathrm{d}t}$ along a single orbit can be determined from a vertical section in Fig. 6.2, for a fixed value of ϕ. Figure 6.2a shows the result for a nearly circular orbit, Fig. 6.2b corresponds to a highly elliptical orbit with eccentricity 0.78 (the eccentricity at which the perigee lies in the Earth's lower atmosphere, without considering drag). For all orbits, positive and negative $\frac{\mathrm{d}a}{\mathrm{d}t}$ values exist. Figure 6.3 shows the maximum and minimum change in semi-major axis achievable for all orbits with a semi-major axis of 30 000 km and an eccentricity between 0.01 and 0.78 calculated with Eqs. (6.2) and (2.23). The semi-transparent dark plane indicates a zero change of semi-major axis. It can be seen that at every point in the (e, ϕ)-phase space the minimum change is negative and the maximum change positive. Thus, it is possible for any orbit to achieve a constant semi-major axis by electrochromic orbit control.

Eccentricity

The variation of eccentricity is given by Gauss' equation Eq. (2.24) in Sec. 2.3.1 as:

$$\frac{\mathrm{d}e}{\mathrm{d}t} = \frac{p \sin f a_r + ((p + r)\cos f + er)\, a_\theta}{\sqrt{\mu p}}$$

Figure 6.4 shows the sign of $\frac{\mathrm{d}e}{\mathrm{d}t}$ for a nearly circular and a highly-eccentric orbit. It can be seen that only small areas exist in which negative and positive change is experienced during one orbit (i.e. a vertical line in Figure 6.4 with a fixed value of ϕ) around $\phi = 0°$ and $\phi = 180°$. These are consequently the only areas in which a positive $\Delta e_{\max}$ and a negative $\Delta e_{\min}$ can be found to stabilise the spacecraft. Figure 6.5 shows the minimum and maximum Δe achievable for the

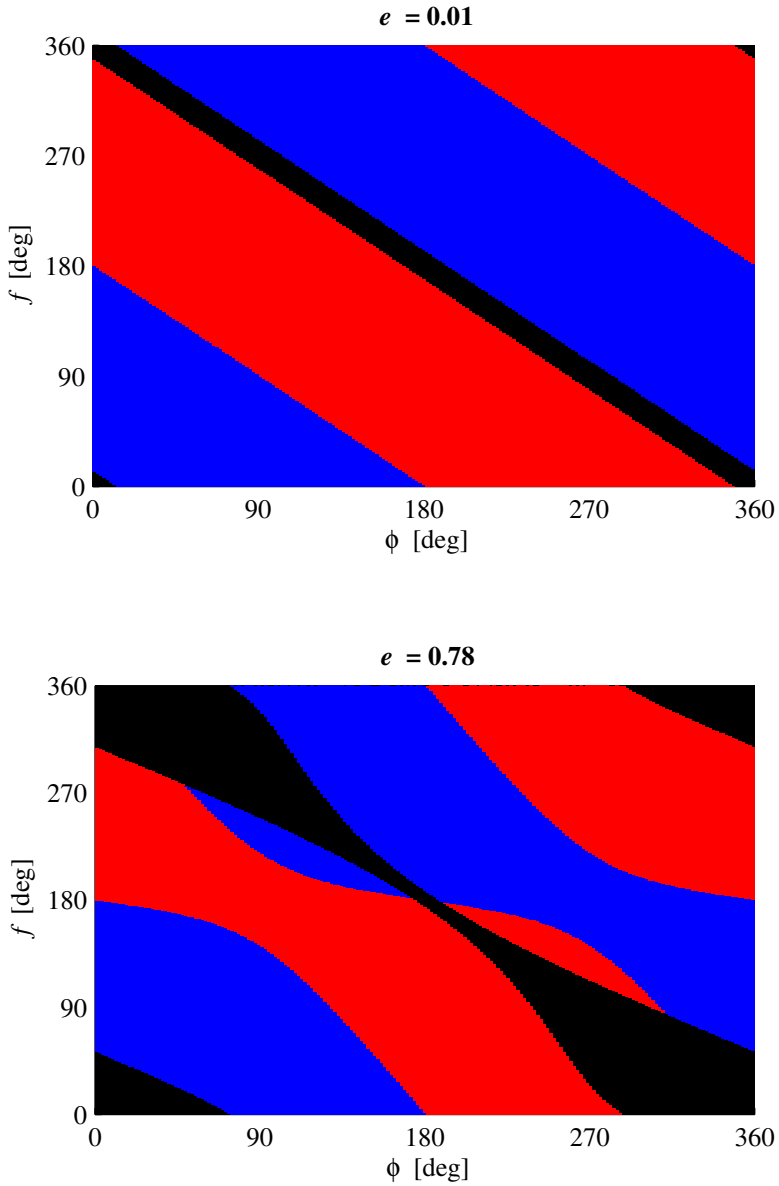

Figure 6.2: Zones of positive (red), negative (blue) and zero (black) $\frac{\mathrm{d}a}{\mathrm{d}t}$ due to SRP as a function of true anomaly f for orbits of different initial ϕ with eccentricities $e = 0.01$ (a) and $e = 0.78$ (b) and 30 000 km semi-major axis. Zero $\frac{\mathrm{d}a}{\mathrm{d}t}$ zones are due to eclipses.

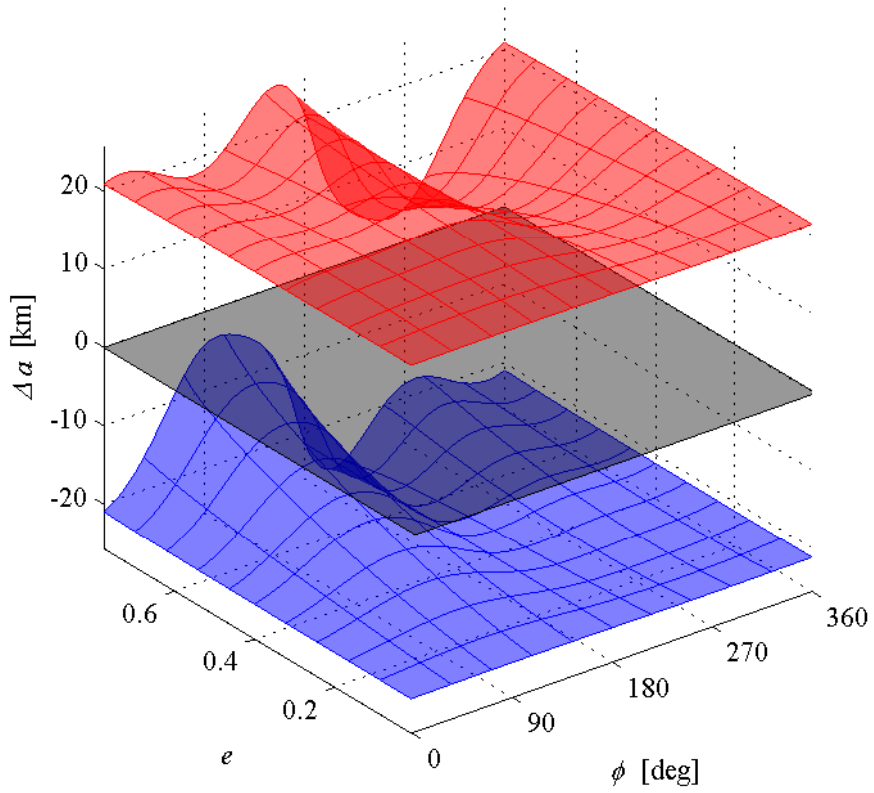

Figure 6.3: Maximum (red) and minimum (blue) change in semi-major axis over one orbit for different initial orbits in the (e, ϕ) phase space portraying the floor and the ceiling of possible control options, for a semi-major axis of 30 000 km

spacecraft considered; the narrow gap between the two layers around zero at $\phi = 0°$ and $\phi = 180°$ reflects the control potential in eccentricity limited to these regions.

Sun-perigee angle

The determination of the areas of positive or negative $\frac{\mathrm{d}\phi}{\mathrm{d}t}$ is also not trivial and using Eq. (2.1) in Sec. 2.1.1 it is described by the sum of the rate of change of argument of perigee, right ascension of the ascending node and the progression rate of the position of the Sun, $\frac{\mathrm{d}\lambda_\odot}{\mathrm{d}t} = -n_\odot$. The rate of change of the argument of perigee is given by the Gauss' equation Eq. (2.27) in Sec. 2.3.1 as:

$$\frac{\mathrm{d}\omega}{\mathrm{d}t} = \frac{-p\cos f a_r + (p+r)\sin f a_\theta}{e\sqrt{\mu p}} - \frac{r\sin\omega + f}{\sqrt{\mu p}\tan i} a_n$$

While the rate of change of right ascension of the ascending node is given by Eq. (2.26) as:

$$\frac{\mathrm{d}\Omega}{\mathrm{d}t} = \frac{r\sin\omega + f}{\sqrt{\mu p}\sin i} a_n$$

It can be seen that the change in right ascension is only dependent on the out-of-plane component of the perturbing force, a_n, and thus equals zero here, as only an in-plane model is considered. The out-of plane term in the rate of change of argument of perigee is also neglected, while the inclination is set equal to zero in this model to derive the following term for $\frac{\mathrm{d}\phi}{\mathrm{d}t}$:

$$\frac{\mathrm{d}\phi}{\mathrm{d}t} = \frac{\mathrm{d}\Omega}{\mathrm{d}t} + \frac{\mathrm{d}\omega}{\mathrm{d}t} - n_\odot = \frac{-p\cos f a_r + (p+r)\sin f a_\theta}{e\sqrt{\mu a(1-e^2)}} - n_\odot \tag{6.5}$$

It can be noted that the singularity at $i = 0$ in Eqs. (2.27) and (2.26) is not found in Eq. (6.5), as the force normal to the orbit plane, a_n, is assumed to be zero. Figure 6.6 shows the sign of $\frac{\mathrm{d}\phi}{\mathrm{d}t}$ for a quasi-circular and a highly-eccentric orbit as a function of the Sun-perigee angle. It appears similar to the results for the eccentricity, albeit phase shifted. The significant difference is the fact that there is also a fixed rate of change in ϕ due to the Earth's motion around the Sun, $n_\odot$. In order to fix the orbit geometry, the SRP needs to counteract this natural progression of ϕ. This leads to a zone where a stabilisation in ϕ is possible that is not only found around $\phi = 90°$ and $\phi = 270°$ but also in a semi-circular shape around $\phi = 180°$. Figure 6.7 shows the ceiling and floor of possible $\Delta\phi$ values for different positions in the phase space.

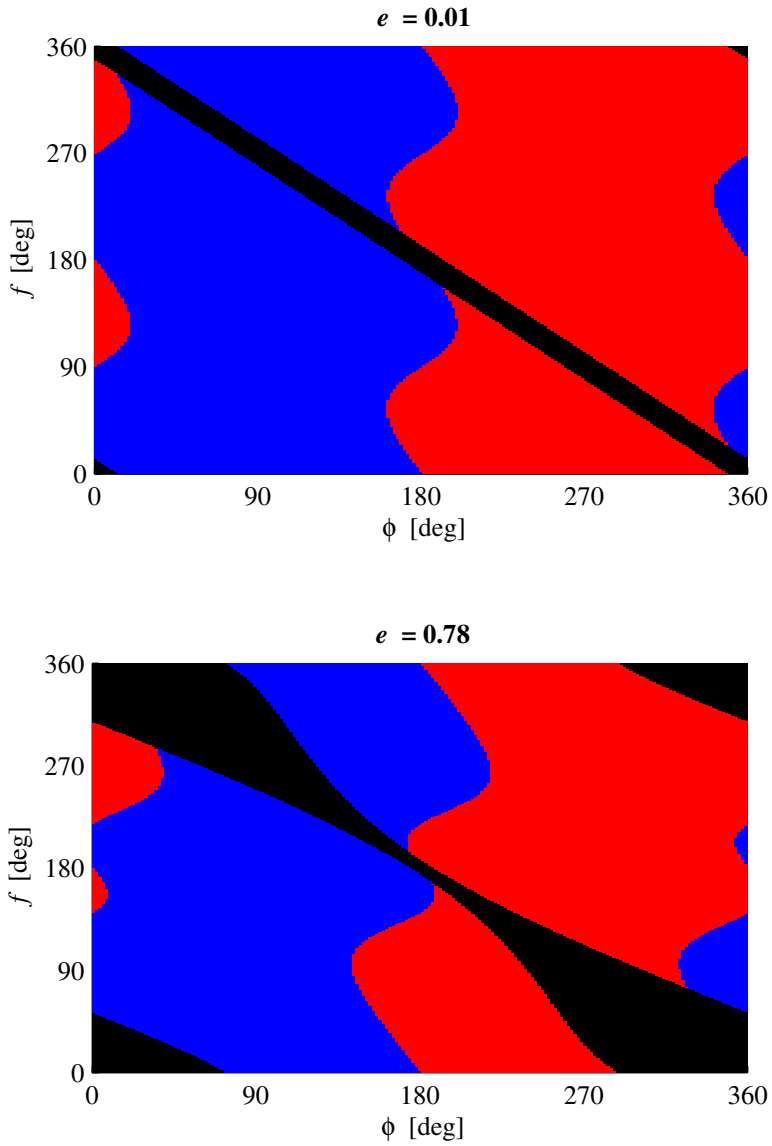

Figure 6.4: Zones of positive (red), negative (blue) and zero (black) $\frac{\mathrm{d}e}{\mathrm{d}t}$ due to SRP as a function of true anomaly f for orbits of different initial ϕ with eccentricities $e = 0.01$ (a) and $e = 0.78$ (b) and 30 000 km semi-major axis. Zero $\frac{\mathrm{d}e}{\mathrm{d}t}$ zones are due to eclipses.

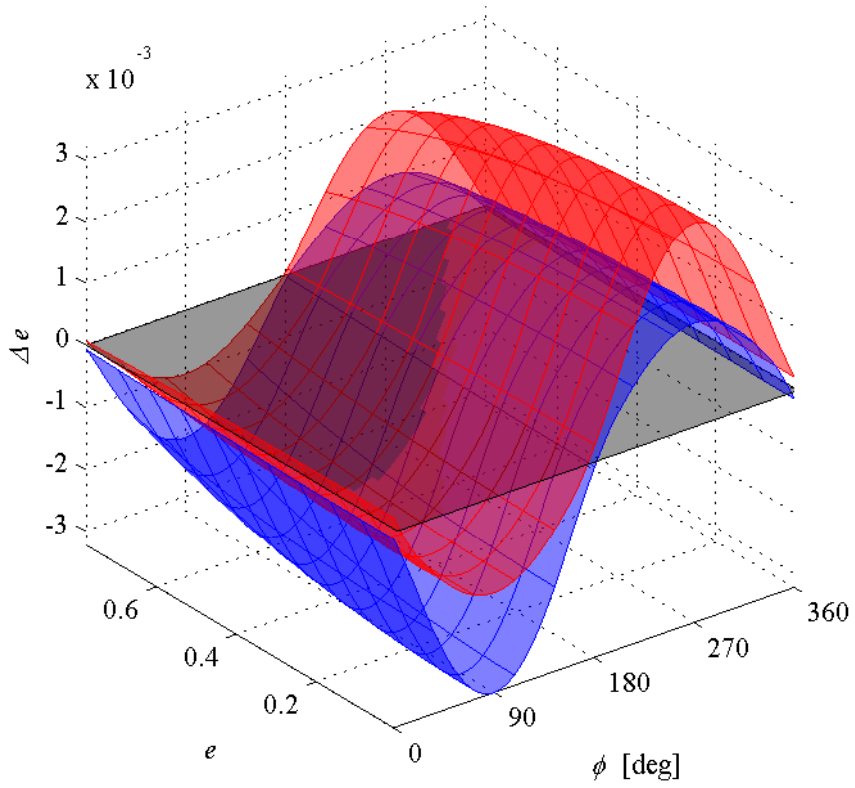

Figure 6.5: Maximum (red) and minimum (blue) change in eccentricity over one orbit for different initial orbits in the (e, ϕ) phase space portraying the floor and the ceiling of possible control option, for a semi-major axis of 30 000 km

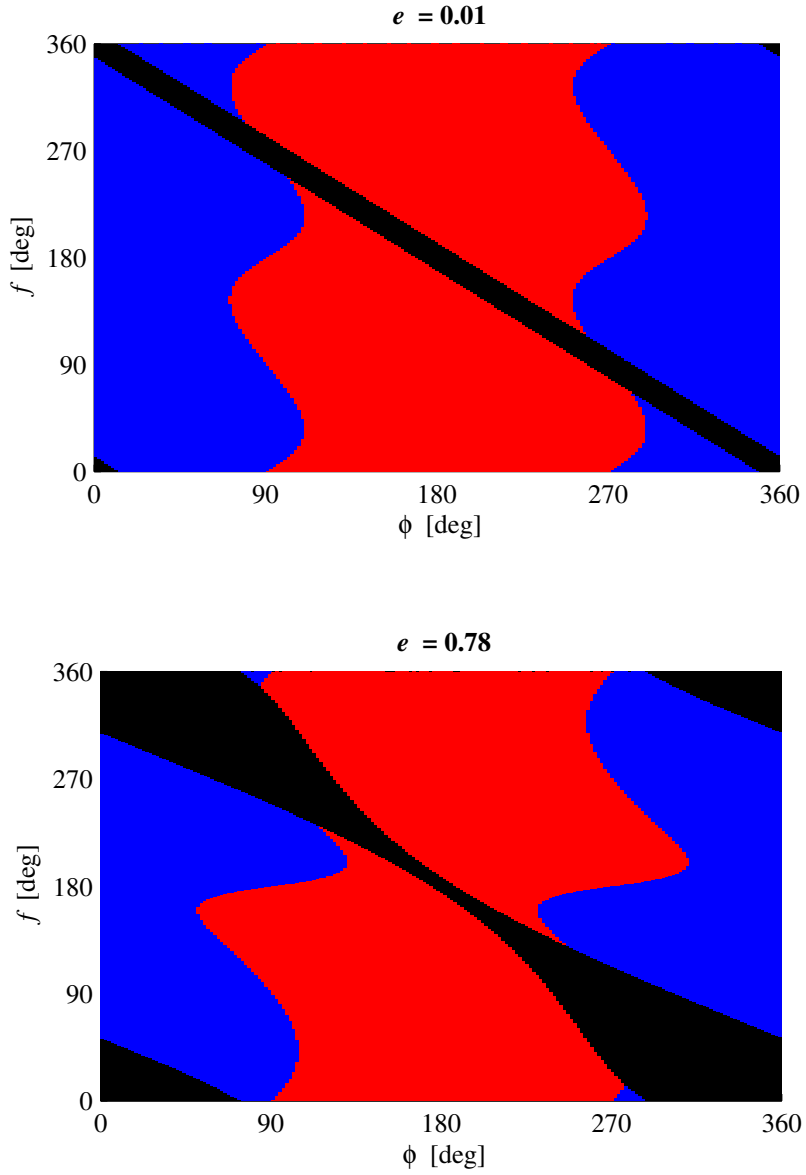

Figure 6.6: Zones of positive (red), negative (blue) and zero (black) $\frac{\mathrm{d}\phi}{\mathrm{d}t}$ due to SRP as a function of true anomaly f for orbits of different initial ϕ with eccentricities $e = 0.01$ (a) and $e = 0.78$ (b) and 30 000 km semi-major axis. Zero $\frac{\mathrm{d}\phi}{\mathrm{d}t}$ zones are due to eclipses. The change due to the progression of the Earth around the Sun is not included.

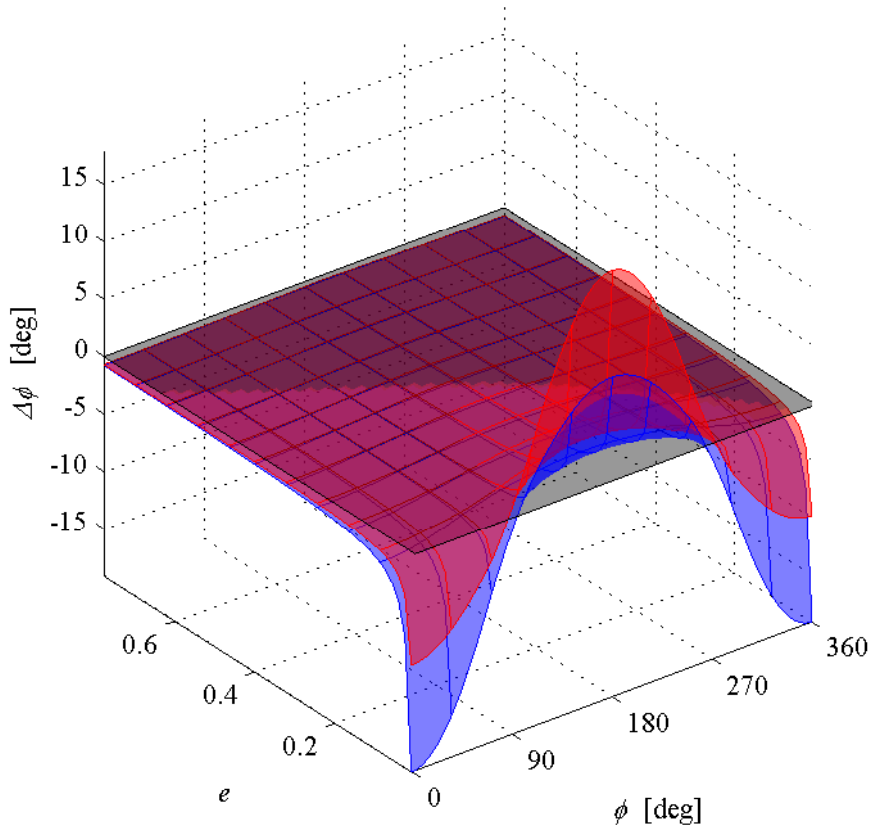

Figure 6.7: Maximum (red) and minimum (blue) change in eccentricity over one orbit for different initial orbits in the (e, ϕ) phase space portraying the floor and the ceiling of possible control options, for a semi-major axis of 30 000 km

6.1.3 The potentially stabilisable zone

The results in Sec. 6.1.2 can be combined to find possible points in the (e, ϕ) phase space where stabilisation is possible. To assess an orbit's usefulness for stabilisation of the three orbital elements considered, a new parameter is introduced. S_K is the lower value of the positive $\Delta K_{\max}$ and the negative $\Delta K_{\max}$, if this term is positive. If the term is negative the point is not useful for stabilisation because zero change is not within the range of possible control options. If this is the case, the control potential parameter S_K becomes zero to indicate that stabilisation of the orbital element K is not possible.

$$S_K = \begin{cases} \min\{\Delta K_{\max}, -\Delta K_{\min}\} & \text{, if } \min\{\Delta K_{\max}, -\Delta K_{\min}\} > 0 \\ 0 & \text{, if } \min\{\Delta K_{\max}, -\Delta K_{\min}\} \leq 0 \end{cases} \tag{6.6}$$

with ΔK_{max} and ΔK_{min} defined by Eq. (6.2).

Figure 6.8 contains the results for all possible in-plane orbits with a semi-major axis of 30 000 km. The thick red line indicates the eccentricity above which the radius of the perigee is smaller than the radius of the Earth, R_E. Only orbits below this line are possible. S_a is portrayed in red contour lines. Since the semi-major axis can always be kept constant using EOC (see Sec. 6.1.2) all positions in the phase space are acceptable for stabilisation when only considering this parameter. The regions in which $S_e > 0$, and thus the eccentricity can be kept constant, are highlighted in blue. In addition, unmarked darker blue contour lines trace the S_e values. As expected, these areas are thin stripes around $\phi = 0°$ and $\phi = 180°$ (see Sec. 6.1.2). The region in which $S_\phi > 0$ is highlighted in green. In addition, unmarked darker green contour lines trace the S_ϕ values. The resulting shape resembles a semi-circle with the highest S_ϕ values towards the centre of the region.

Complete stabilisation is only possible in regions where all S_K values are larger than zero. This is possible in a near rectangular shape with approximately $175° < \phi < 185°$ and $0.15 < e < 0.3$, defined by the potentially stabilisable zone (PSZ). This area is highlighted in bright cyan with a thick black border.

Figure 6.9 shows the range in eccentricity of the PSZ for the spacecraft parameters given in 6.1.1 and varying semi-major axes. The rise in eccentricity and the extension of the range of the stable zone can be seen.

Finally, the maximum values for the control potential parameter S_K can be seen in Fig. 6.10 and Fig. 6.11. All three grow with increasing semi-major axis. The maximum S_a is at $e \approx 0$, the

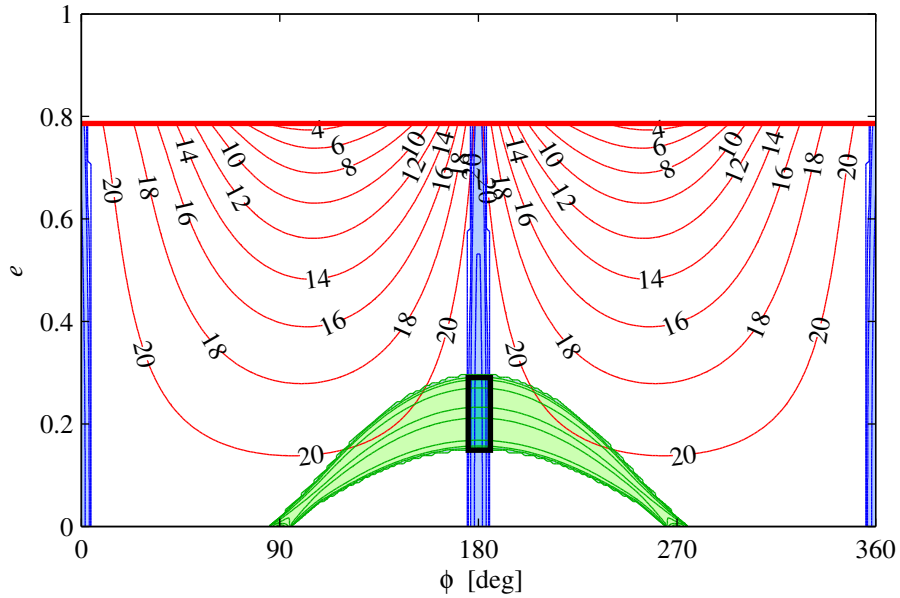

Figure 6.8: S_a (red) S_e (blue) and S_ϕ (green) for $a = 30\,000\,\text{km}$ orbits in the (e, ϕ) phase space: The thick red line indicates the critical eccentricity e_{crit}, where $r_p = R_E$. The potentially stabilisable zone (PSZ) where the necessary criterion for stabilisation is fulfilled is marked in cyan with thick black border. The contour values on the red thin lines indicate the maximum positive or negative change achievable in semi-major axis in kilometres using electrochromic control.

maximum S_e can be found at $e \approx 0$ and $\phi = 0°$ or $180°$ and the maximum S_ϕ at $\phi = 180°$ and e between the boundaries shown in Fig. 6.9.

6.2 Orbit stabilisation using an artificial potential field controller

The potentially stabilisable zone identified in the previous section includes all in-plane orbits of a given semi-major axis for which stabilisation using electrochromic coatings is not impossible due to the initial assessment presented in Sec. 6.1.2. However, this assessment considers each of the three in-plane orbital elements separately. Next, the possibility of controlling all three elements is analysed. This is necessary to truly stabilise the orbit. In this section an artificial potential field in the orbital element phase space is introduced which is then used to control the orbit of a SpaceChip with an electrochromic coating on orbits of the PSZ.

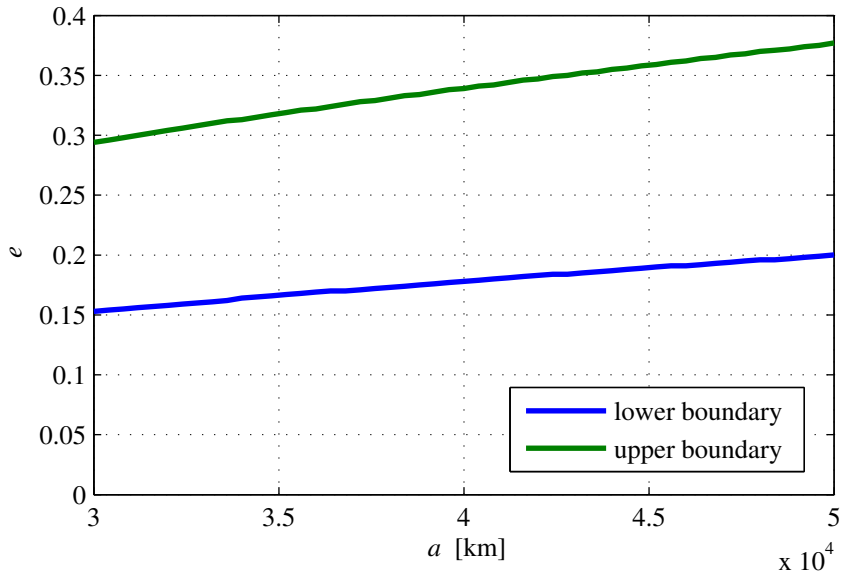

Figure 6.9: The eccentricity value of the lower (blue) and upper (green) boundary of the PSZ at $\phi = 180°$ as a function of semi-major axis.

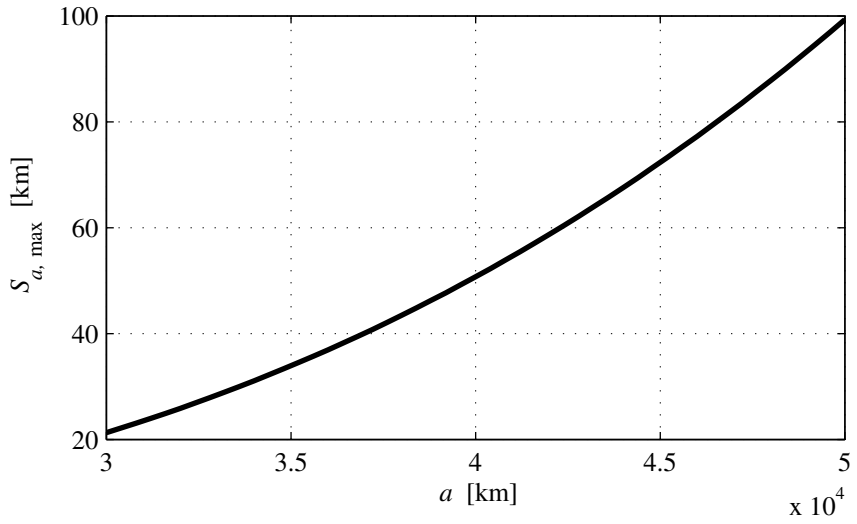

Figure 6.10: Maximum values of semi-major axis control potential parameter S_a as a function of semi-major axis.

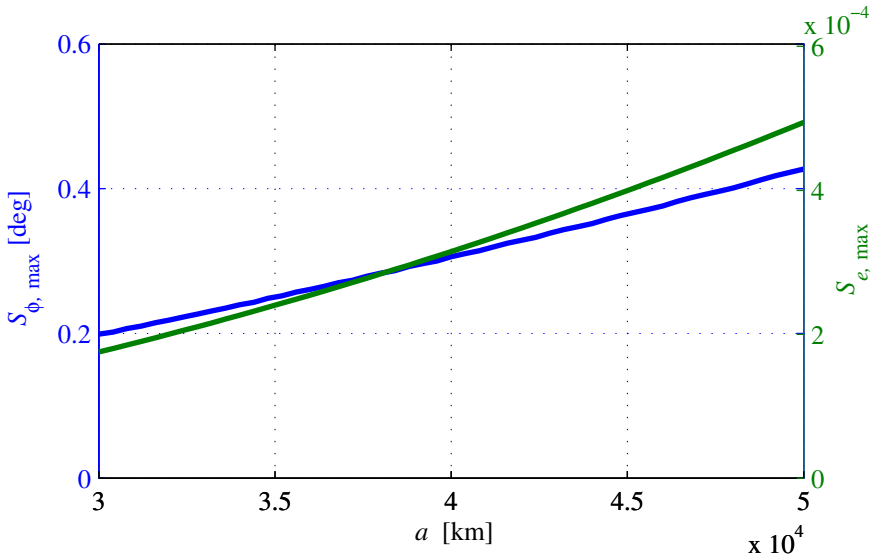

Figure 6.11: Maximum values of control potential parameters S_ϕ (blue) and S_e (green) as a function of semi-major axis.

6.2.1 Controller design

In Sec. 6.1.3 the area in the phase space that fulfils the necessary criterion for stabilisation (PSZ) has been identified. The next step is to determine which of these orbits can be stabilised using an artificial potential field based electrochromic orbit controller. Figure 6.12 shows the principle of the controller. The control loop operates in discrete time steps of one orbit. First, the initial orbit state is defined. Then, the optimum control parameters (f_{on} and f_{off}) are determined. Finally, the next orbit state is determined exactly using the numerical integration of the 3D Gauss' equations, as introduced in Sec. 2.3.1, and the loop repeats itself.

The different steps of the control algorithm are now explained in detail: initially the orbital elements at the end of a single orbit revolution for different sets of ($f_{\text{on}}, f_{\text{off}}$) are estimated using the set of analytical equations introduced in Sec. 2.2.1, which describe the secular variation of orbital elements due to SRP. The analytical approach is quicker than the numerical integration of the full dynamical model, and thus preferable for the search for the optimum control parameters.

Next, the values of a control function $U\,(f_{\text{on}}, f_{\text{off}})$ are calculated. A search for the local minimum of $U\,(f_{\text{on}}, f_{\text{off}})$ delivers the required control parameters f_{on} and f_{off}. The control function is based on an artificial potential field approach in the orbital element space. The desired position $[a_0, e_0, \phi_0]$ is at the bottom of a parabolic artificial potential well:

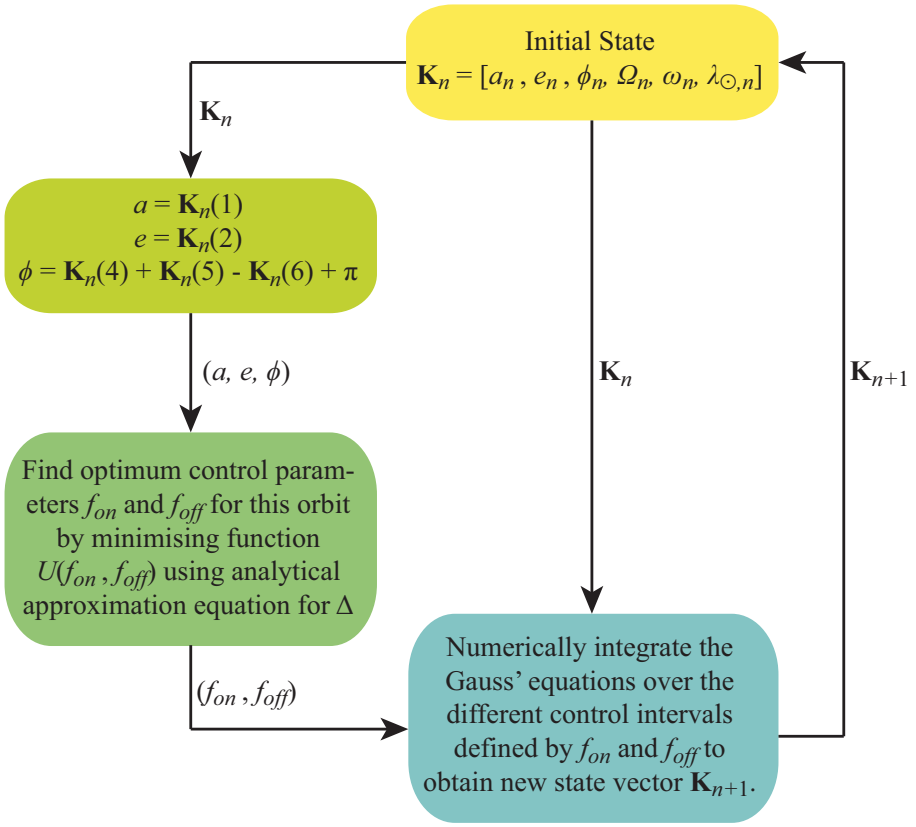

Figure 6.12: Diagram of the closed control loop for the artificial potential field controller.

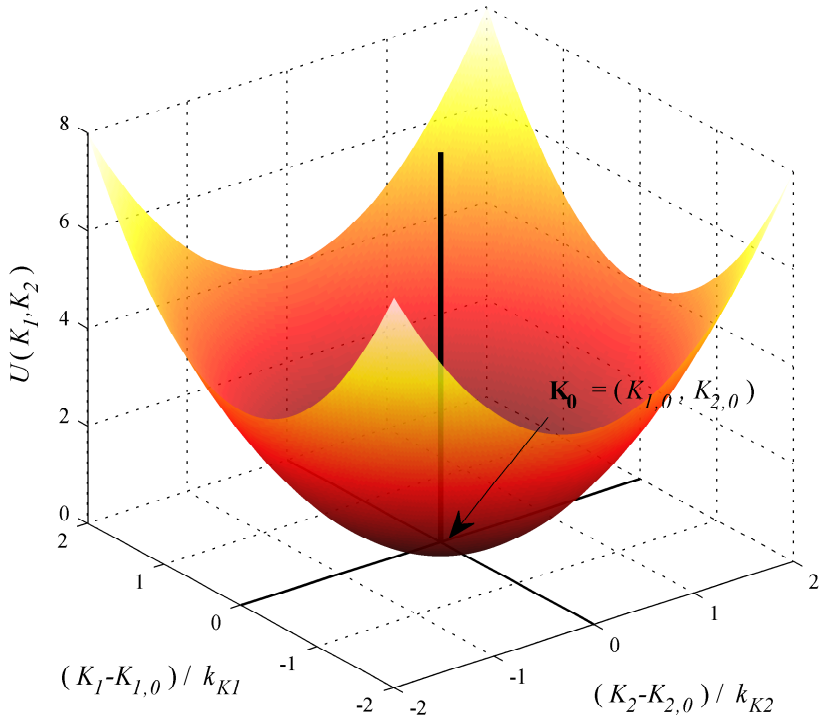

Figure 6.13: The artificial potential field control function in a two dimensional orbital element phase space for $\mathbf{K} = (K_1, K_2)$.

$$\begin{aligned} U\left(f_{\text{on}}, f_{\text{off}}\right) =& k_a^2 \left(a\left(f_{\text{on}}, f_{\text{off}}\right) - a_0\right)^2 \\ &+ k_e^2 \left(e\left(f_{\text{on}}, f_{\text{off}}\right) - e_0\right)^2 \\ &+ k_\phi^2 \left(\phi\left(f_{\text{on}}, f_{\text{off}}\right) - \phi_0\right)^2 \end{aligned} \tag{6.7}$$

where the term $K(f_{\text{on}}, f_{\text{off}})$ decribes the the value of the Keplerian element K after one orbit, if the control parameters f_{on} and f_{off} were applied. As only in-plane parameters are considered, K stands for a, e, and ϕ, while k_a, k_e and k_ϕ are weight parameters, whose values are expressed as function of the control potential parameter defined. Figures 6.10 and 6.11 show the maximum values for S_K as an indicator of the magnitude of the maximum step size in orbital elements over one orbit within the PSZ. The parameters k_K are defined as:

$$k_K = \frac{1}{\max\left(S_K\right)^2} \tag{6.8}$$

so that $k_K \left(K(f_{\text{on}}, f_{\text{off}}) - K_0\right)^2 = 1$, if the distance between the actual and desired position $|K(f_{\text{on}}, f_{\text{off}}) - K_0|$ is of order one step size.

After the required set of control parameters has been determined, the orbit is then propagated through the numerical integration of the 3D Gauss' equations as introduced in Sec. 2.3.1, including the perturbations of solar radiation pressure and the J_2 effect [84]. The consideration of the J_2 effect in the stability simulation, despite neglecting it in the controller design, is done to test the robustness of the controller to unpredicted influences and perturbations.

The simulation employs the electrochromic orbit control by switching reflectivity at the chosen positions. Because the analytical expressions used to predict the variation of Keplerian elements only consider the secular rate of change, neglecting the periodic variations and ignoring the J_2 effect and any out-of-plane effects [103], the predicted variation of elements is not exactly equal to the variation computed through numerical integration of the full model. This new state vector is then input into the beginning of the control loop again leading to a closed loop system which is robust towards errors in orbit prediction, as will be shown in Sec. 6.2.3.

6.2.2 Stability conditions

A measure of stability is the destabilisation time, the time until a simulated spacecraft exits a pre-defined sphere around its starting position in the orbital element space. If this simulation is performed at a multitude of points in the potentially stabilisable zone (PSZ) for controlled and

uncontrolled cases, profiles of the actual stability domain can be constructed. The controlled and uncontrolled profiles can be compared to assess the usefulness of the method for orbit stabilisation described in this section.

The dimensions of the sphere around the position to be tested for stability are directly related to the control function. As defined in the previous subsection, the part of the control function corresponding to any orbital element is equal to one when the distance between the actual position and the required position equals $\max(S_K)$. It is reasonable to size the sphere as a multiple of this distance by a size factor of the stability sphere. This factor can in principle be chosen almost arbitrarily because if the position is unstable then the spacecraft will eventually exit the sphere, however large it is, as long as it is not big enough to distort the result by enclosing a different position that is indeed stable. Likewise, if the position is stable, the spacecraft will stay within the sphere as long as it is not small enough to exclude positions around the initial state that the spacecraft may jump to and from while staying close to the desired position. It is, however, desirable to have a sphere as small as possible to reduce the simulation time until a conclusion about stability can be drawn. Stability is assumed if the spacecraft does not exit the sphere for at least fifty orbits (approximately one month) for a semi-major axis of 30 000 km. The resulting dimensions of the stability sphere can be seen in Fig. 6.14.

Figure 6.15 shows the percentage of points in the PSZ that destabilise according to these criteria within certain times (measured as the number of orbits) for controlled and uncontrolled spacecraft. It can be seen that the vast majority of uncontrolled points destabilise within ten orbits ($\approx 99\%$). The other regimes have far smaller percentages but there are at least some points that last for longer than fifty orbits. For the uncontrolled spacecraft approximately one third of points are stable. The unstable ones destabilise mostly within ten orbits. The sharp drop in points when looking at larger destabilising times suggest that the one-third defined as stable would not destabilise within just over one hundres orbits, but remain within the stability sphere indefinitely. Thus, both the size of the sphere and the maximum time of propagation are shown to be adequate.

6.2.3 Stability simulation results

The results of the simulation highlight the significant difference between the destabilising times of controlled and uncontrolled SpaceChips. Figure 6.16 visualises the results for both cases at a semi-major axis of 30 000 km. The uncontrolled SpaceChip destabilises typically within ten orbits apart from an equilibrium point at $\phi = 180°$ and $e \approx 0.22$. Around this point the destabilising times become longer but the rise is very steep as can also be seen in Fig. 6.15. This is the stable point for the GEOSAIL mission [100].

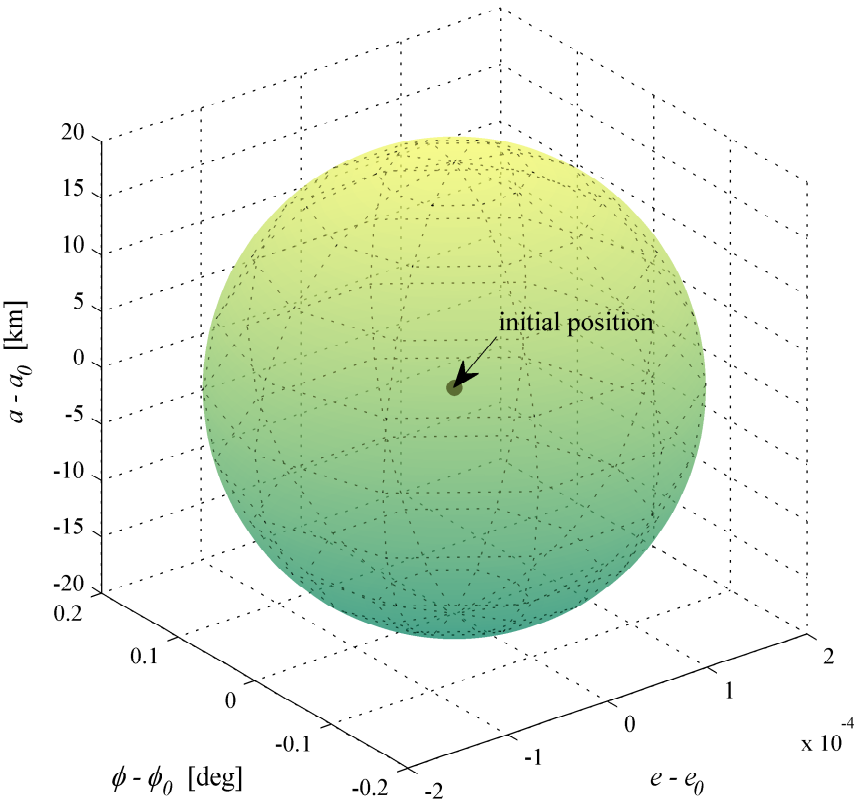

Figure 6.14: Dimensions of the stability sphere at $a = 30\,000\,\text{km}$

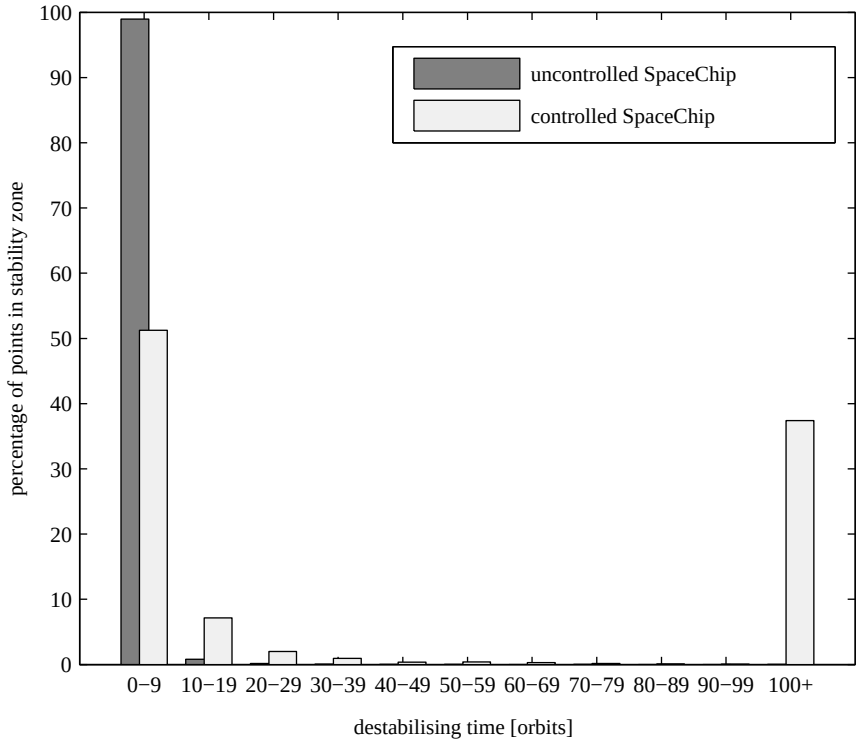

Figure 6.15: Percentage of orbits in potentially stabilisable zone with given destabilising times at $a = 30\,000\,\mathrm{km}$ for *Sprite* SpaceChips with area-to-mass-ratio $17.4\,\mathrm{m^2\,kg^{-1}}$.

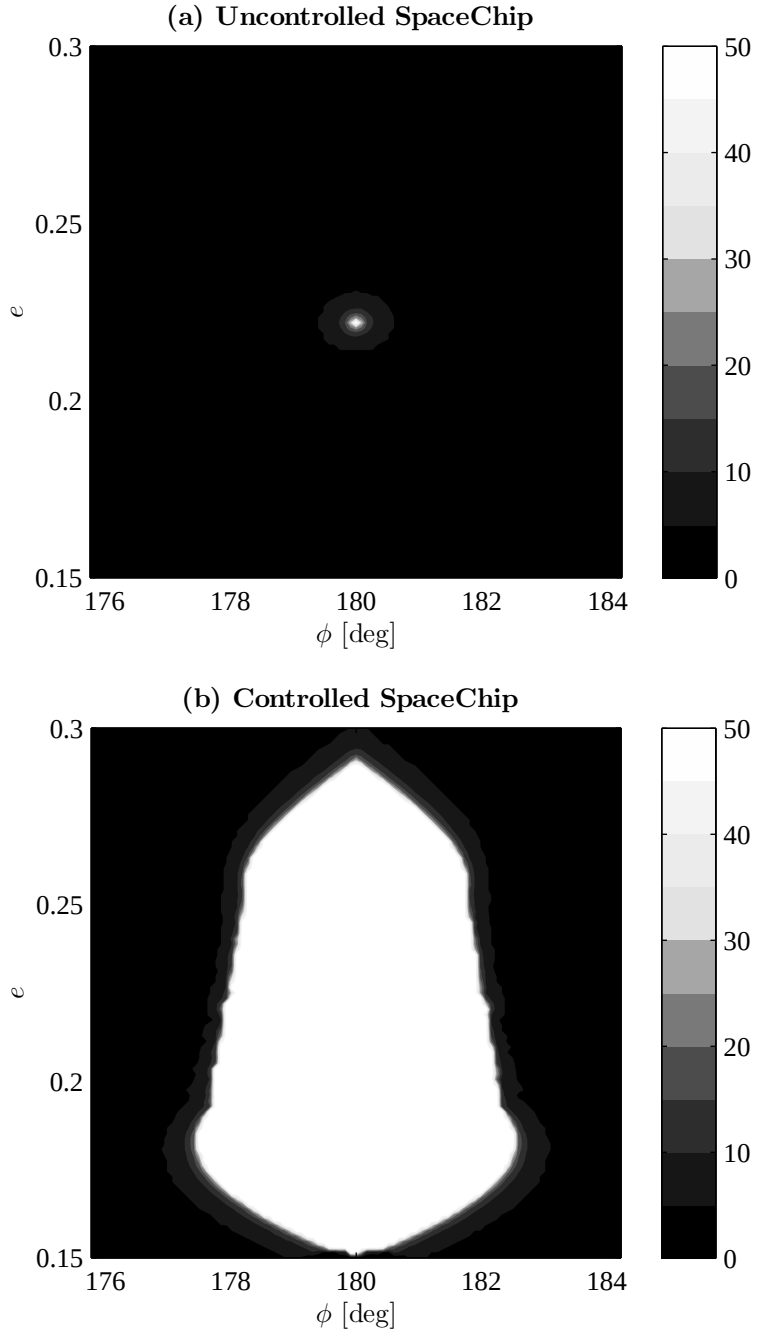

Figure 6.16: Stability profile of controlled (a) and uncontrolled (b) orbits in potentially stabilisable zone at $a = 30\,000\,\mathrm{km}$ for SpaceChips with area-to-mass-ratio $17.2\,\mathrm{m^2\,kg^{-1}}$. The area shade indicates the number of orbits before destabilising to a maximum of 50.

In contrast, the controlled SpaceChips have a large area (approximately one third of the PSZ) in which the orbital lifetime exceeds one hundred orbits. Around the edges of this shape the destabilising time decreases rapidly so that half of the PSZ destabilises within ten orbits. It is interesting to note that the semi-major axis rarely exceeds more than 10 % of its allowed deviation in both the controlled and uncontrolled case. If an orbit is unstable it is always due to high deviations in e, ϕ or both.

Figure 6.17 visualises the relation between Δe and $\Delta\phi$ with respect to the initial orbit when the SpaceChip exits the stability sphere. Blue areas indicate orbits for which the eccentricity exceeded the bounds, while orange indicates orbits for which the Sun-perigee angle exceeded the bounds. Intermediate colours indicate orbits in which both violate the stability sphere in combination, with the colour shade showing the ratio of Δe and $\Delta\phi$ when exiting the stability sphere, as can be seen in the colour bars to the right of the figures. The pattern for the uncontrolled SpaceChip is very regular. Along $\phi = 180°$, ϕ is the unstable parameter, and horizontally along the eccentricity of the equilibrium point e is the unstable parameter. Between these two directions the transition between the parameters is smooth resulting in a circular domain. The controlled spacecraft's pattern appears less smooth. In the upper and lower quarter of the diagram it appears similar to the uncontrolled case. In the middle, however, it results in a chaotic pattern. This can be explained with the randomness in the position of the spacecraft when leaving the sphere. During the orbits until destabilisation, the controller will fight against a drift in eccentricity and Sun-perigee angle. When one is corrected, the other one will decay. Thus the spacecraft's orbit will jump back and forth between positions in the phase space, either favouring the eccentricity or favouring ϕ, thus moving in a zig-zag path from the starting point within the stability sphere. The moment the SpaceChip leaves the sphere can be at either position.

The results of the simulation show that using electrochromic orbit control a SpaceChip may be stabilised in a variety of different orbits within a certain area of the (e, ϕ) phase space, as opposed to the uncontrolled case that only offers one equilibrium orbit for a given semi-major axis corresponding to the equilibrium point in the (e, ϕ) phase space discussed in Sec. 2.1.1, and used for the GEOSAIL mission [100]. This is an advantage for formation flying SpaceChips to account for insertion inaccuracies or to allow a spread in stable orbits. It is also shown that the algorithm is robust with respect to other perturbations, such as the J_2 effect, and orbit prediction uncertainties as the algorithm for selection of the control variables is based on simplified analytical expressions, while the simulation is conducted using a numerical propagation of the 3D Gauss' equations, as discussed in Sec. 6.2.1.

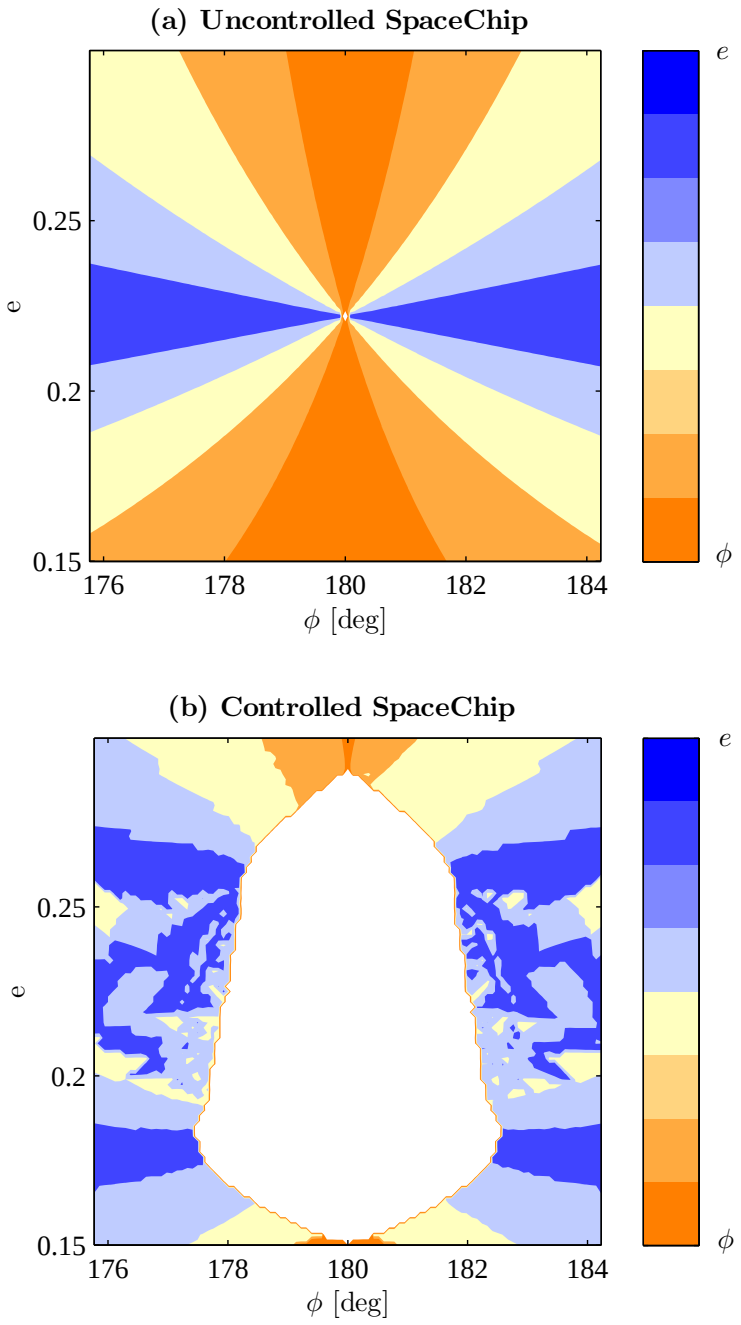

Figure 6.17: Colour interpretation of the relation of e and ϕ when the SpaceChips exceeded the stability boundaries.

6.3 Orbit manœuvres using an artificial potential field controller

Electrochromic Orbit Control using the artificial potential field controller as described in the previous section can also be used for orbit manœuvres. In this section two types of manœuvres are investigated: (e, ϕ) translations and an orbit raising manœuvre. In all simulations the controller design described Sec. 6.2.1 is used, including the propagation of the full set of Keplerian elements. The results are displayed in the three planar elements a, e and ϕ.

6.3.1 Electrochromic (e, ϕ) translation using an artificial potential field controller

An (e, ϕ) translation is a manœuvre between two orbits of the same semi-major axis but with different eccentricities and Sun-perigee angles. To investigate the effectiveness of the artificial potential field electrochromic orbit control method described in the previous section two test case are simulated. In each case a formation of four passively Sun-pointing SpaceChips with area-to-mass-ratio $15\,\mathrm{m^2\,kg^{-1}}$ occupy four different near geo-synchronous orbits ($a = 42\,000\,\mathrm{km}$) differing in e and ϕ so that they are located on the corners of a rectangle in the (e, ϕ) phase space around the desired goal orbit. The goal orbit is stabilisable. Their relative spacing within the final orbit is not considered. The SpaceChips have the ability to switch their coefficients of reflectivity between $c_{R,\mathrm{on}} = 2$ and $c_{R,\mathrm{off}} = 1$ using electrochromic coating.

In both cases the goal orbit is at $\phi = 180°$ and $e = 0.25$. However, in the second case, the far case, the starting orbits are tenfold further away from the goal orbit than in the first case, the close case. A manœuvre is considered successful when the spacecraft enters a sphere around the desired goal position in the orbital element phase space of the following dimensions: $a_{\mathrm{thresh}} = 50\,\mathrm{km}$, $e_{\mathrm{thresh}} = 1 \times 10^{-4}$ and $\phi_{\mathrm{thresh}} = 0.1°$. This is similar to the stability conditions defined in Sec. 6.2.2.

6.3.1.1 The close case

In this case the starting distances from the goal orbits are: $\Delta\phi = \pm 0.5° \approx 2S_\phi$ and $\Delta e = \pm 8.7 \times 10^{-3} \approx 2S_e$. Figure 6.18 shows the evolution of the orbital elements over time and Fig. 6.19 the evolution of the spacecraft in the (e, ϕ) phase space. It can be seen that within 70 days all four SpaceChips are assembled in the stable goal orbit. The controller first moves the spacecraft

towards $\phi = \pi$ and then adjusts the eccentricity while allowing the semi-major axis to librate. From Sec. 6.1.2 it is known that the possible changes in eccentricity over one orbit are smallest at $\phi = 0$ and $\phi = 180°$. Therefore the control path is not time optimal.

6.3.1.2 The far case

In this case the starting distances from the goal orbits are: $\Delta\phi = \pm 5°$ and $\Delta e = \pm 8.7 \times 10^{-2}$. Figure 6.20 shows the evolution of the orbital elements over time and Fig. 6.21 the evolution of the spacecraft in the (e, ϕ) phase space. It can be seen that within 700 days all four SpaceChips are assembled in the stable goal orbit. In the first part of the manœuvre the controller again moves the SpaceChips to orbits with $\phi = 180°$. However, in the far case the path is not a direct one. The spacecraft's orbits circle the goal orbit in the phase space. The final part of all four manœuvres again consists in correcting the eccentricity only. During the first part of the manœuvre the semi-major axis is allowed to deviate up to 700 km from the required value. This is because of the laxer threshold of this parameter compared to eccentricity and Sun-perigee angle (see Sec. 6.3.1). The behaviour of the SpaceChips in the phase space follows the natural phase flow which can be understood using the Hamiltonian orbital dynamics introduced in Sec. 2.1.1. These dynamics are exploited later in Sec. 7.2 for a more efficient electrochromic orbit control manœuvre algorithm.

6.3.2 Electrochromic orbit raising using an artificial potential field controller

As seen in the previous subsection, the artificial potential field controller is not ideally suited for orbital manœuvres in the (e, ϕ) phase space. In this subsection it is instead applied to an orbit raising manœuvre. A passively Sun-pointing SpaceChip with area-to-mass-ratio of $15\,\mathrm{m^2\,kg^{-1}}$ is considered which has the ability to switch its coefficient of reflectivity between $c_{R,\mathrm{on}} = 2$ and $c_{R,\mathrm{off}} = 1$ using an electrochromic coating. The SpaceChip starts in a stabilisable orbit with a semi-major axis of 30 000 km. The goal orbit has a semi-major axis of 50 000 km. Both initial and goal orbits are set at $\phi = 180°$ and $e = 0.25$. The threshold values for eccentricity and Sun-perigee angle are relaxed to allow the controller to affect the orbit raising manœuvres instead. The thresholds are set at $a_{\mathrm{thresh}} = 100\,\mathrm{km}$, $e_{\mathrm{thresh}} = 0.05$ and $\phi_{\mathrm{thresh}} = 5°$.

Figure 6.22 shows the evolution of the semi-major axis over time. It can be seen that the manœuvre could be completed in 450 days. The ascent is almost linear. Figure 6.23 shows the evolution of the orbit in the (e, ϕ) phase space during this manœuvre. The spacecraft first drifts

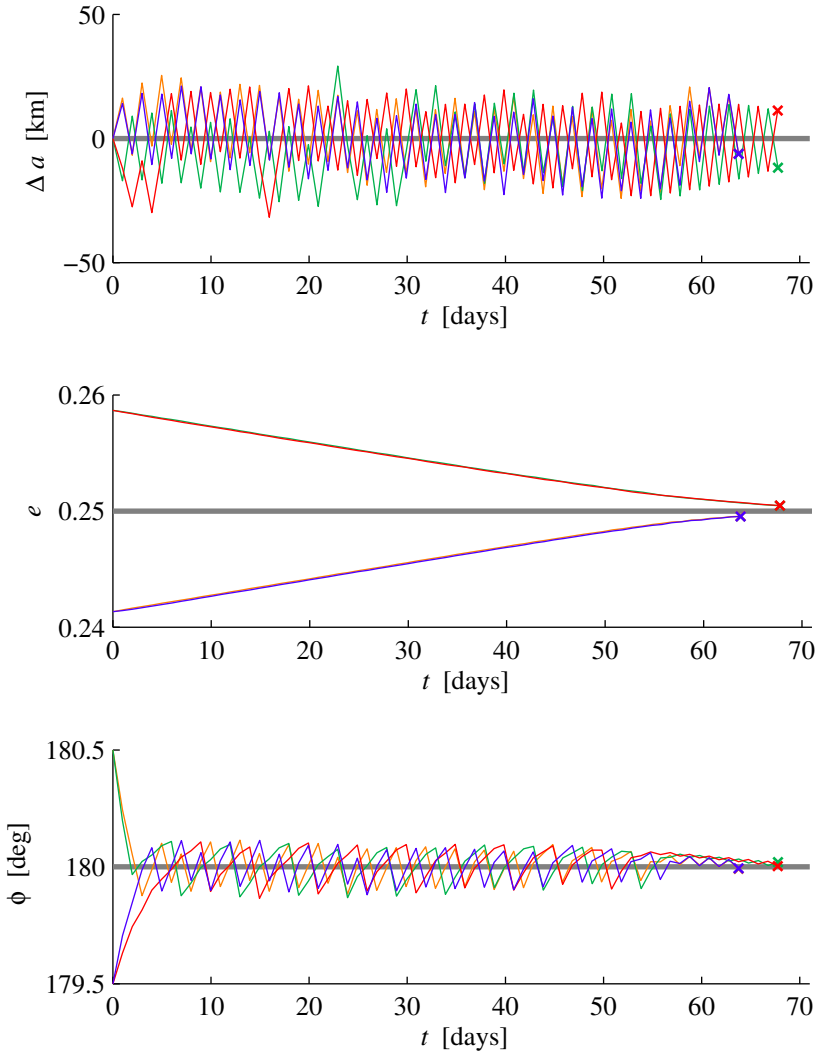

Figure 6.18: Evolution of the spacecraft's in-plane orbital elements over time for the close case – the different line colours indicate the four different spacecraft and are consistent with the colours used in Fig. 6.19

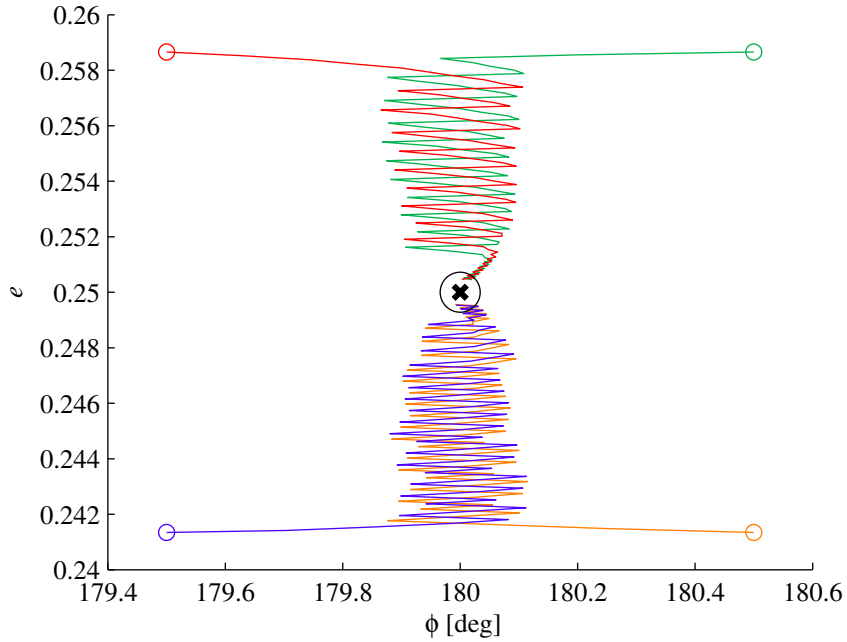

Figure 6.19: Evolution of the spacecraft's orbits in the (e, ϕ) phase space for the close case – the different line colours indicate the four different spacecraft and are consistent with the colours used in Fig. 6.18

out of the goal circle and librates in the phase space, and finally is corrected in the last 10 days after the SpaceChip reaches the desired semi-major axis.

The artificial potential field controller works well for this type of manœuvre. However, there are no built-in constraints to prevent the SpaceChip from reaching the critical eccentricity and impinging on the Earth's atmosphere. The potential field will steer the SpaceChip away from high eccentricities but it cannot prevent the spacecraft from manœuvring towards undesired regions of the phase space. For this reason it is important to understand the dynamics of the phase space better and to build the knowledge of the dynamics into the control algorithm. Chapter 7 will apply the Hamiltonian dynamics described in Sec. 2.1.1 to the electrochromic control problem to formulate an intelligent stabilisation controller and an algorithm for time efficient navigation in the (e, ϕ) phase space.

6.4 Conclusions

In this chapter the concept of controlling the orbit of a SpaceChip using electrochromic coatings was introduced. The control potential in the orbital element phase space was analysed and it was shown

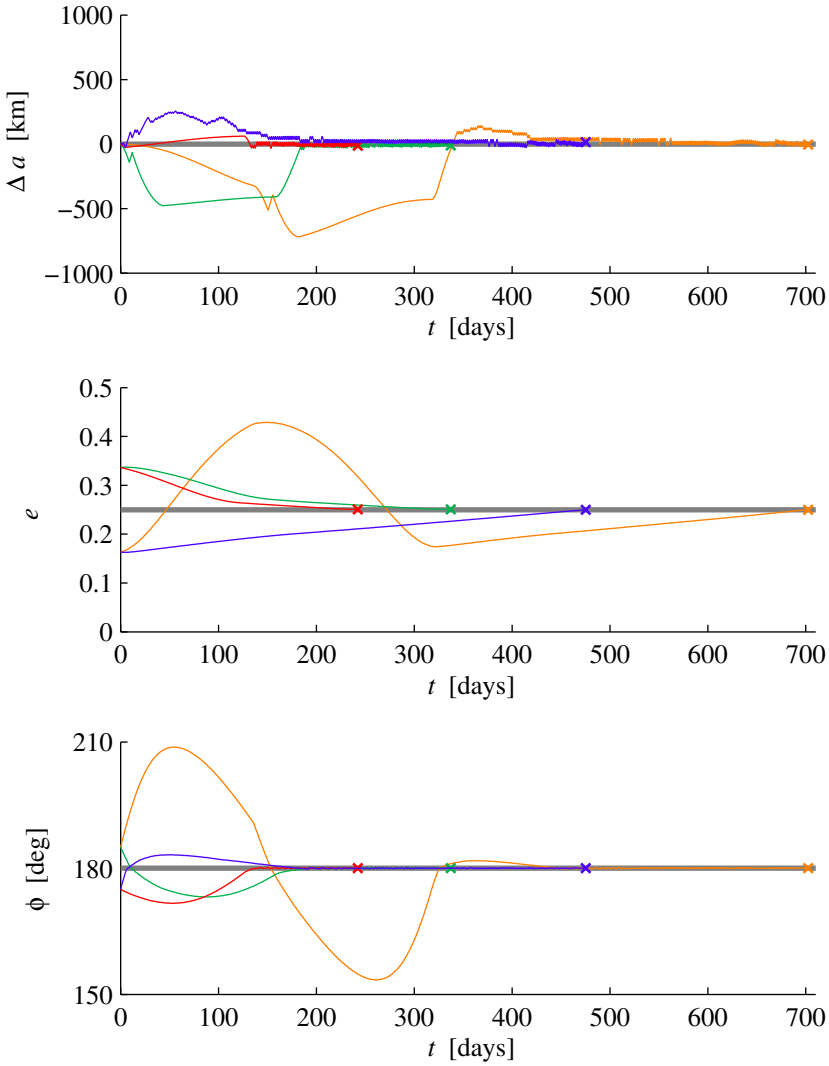

Figure 6.20: Evolution of the spacecraft's in-plane orbital elements over time for the far case – the different line colours indicate the four different spacecraft and are consistent with the colours used in Fig. 6.21.

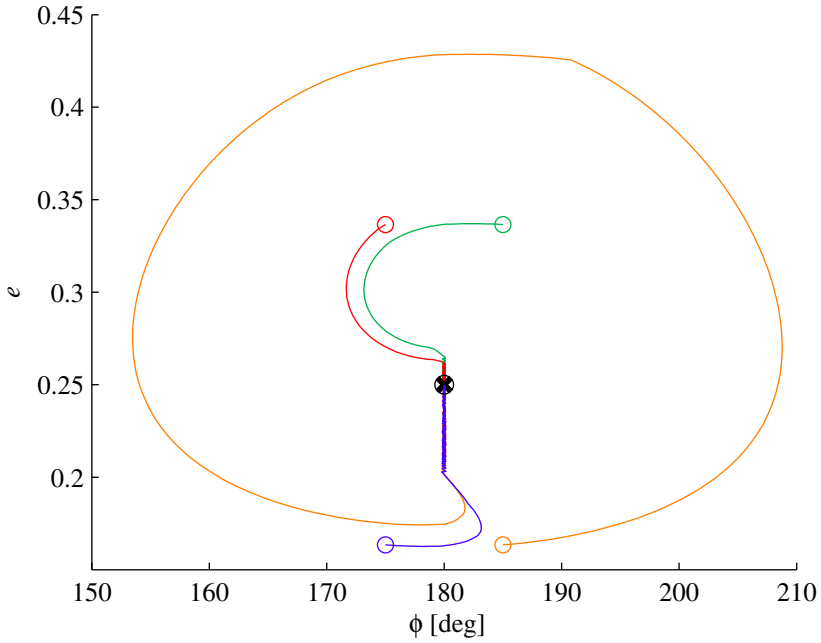

Figure 6.21: Evolution of the spacecraft's orbits in the (e, ϕ) phase space for the far case – the different line colours indicate the four different spacecraft

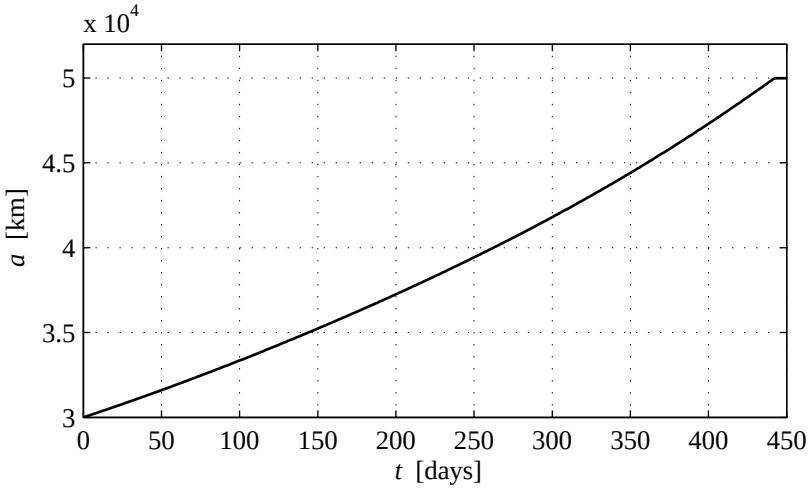

Figure 6.22: Evolution of the spacecraft's semi-major axis over time during the electrochromic orbit raising manœuvre.

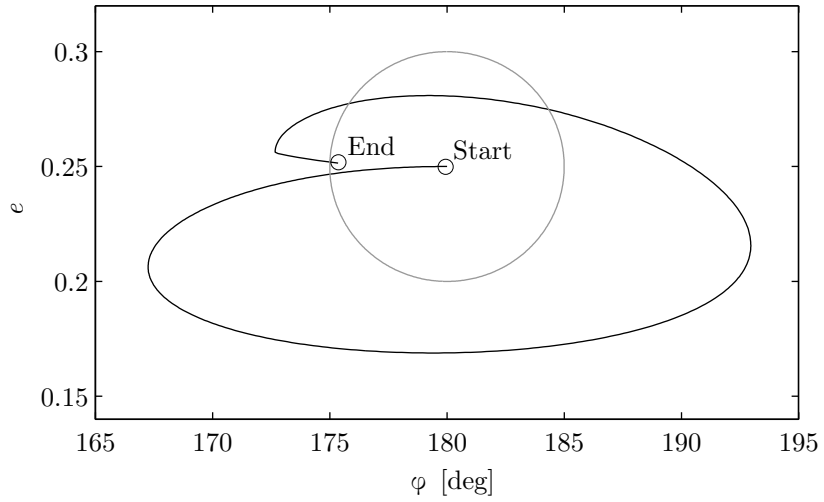

Figure 6.23: Evolution of the spacecraft's orbits in the (e, ϕ) phase space during the electrochromic orbit raising manœuvre: The large circle indicates the threshold zone in e and ϕ.

that there is a region of orbits in the (e, ϕ) phase space in which high area-to-mass-ratio spacecraft can be stabilised using electrochromic coating. This region includes the passive equilibrium orbits of the spacecraft in the (e, ϕ) phase space with either reflectivity state.

An artificial potential field in the orbital element phase space was formulated and applied to orbit stabilisation. It was shown that using this control method, a range of orbits around the natural equilibria can be stabilised. Next, the artificial potential field controller was applied to orbit control. A scenario of six spacecraft in orbits with the same semi-major axis but differing in eccentricity and Sun-perigee angle was devised. These spacecraft then used electrochromic orbit control to attain the same goal orbit and stabilise in this orbit. The control algorithm was successful in performing this task. Finally, the artificial potential field controller was used for orbit raising. A SpaceChip in an initially stable orbit at 30 000 km semimajor axis employs electrochromic orbit control to reach 50 000 km. This was achieved in less than 450 days.

This Chapter showed that electrochromic orbit control is a viable, efficient method for orbit manœuvres of SpaceChips with large semi-major axes. It can be implemented using an artificial potential field controller in orbital elements. However, this control algorithm requires the reflectivity to be changed twice every orbit which could lead to a deterioration of the coating. Furthermore, it is not time-efficient. In the following chapter knowledge of the Hamiltonian phase space dynamics is applied to the problem to derive a more effective control algorithm.

Chapter 7

Electrochromic Orbit Control using a Hamiltonian Controller

In this chapter a control algorithm for SpaceChips with electrochromic coating is proposed, which is based on the Hamiltonian dynamics of high area-to-mass-ratio spacecraft introduced in Sec. 2.1.1. This method uses knowledge of the phase space to perform the manoeuvres in a more time-efficient and less computationally expensive way than the artificial potential field approach presented in Chap. 6. This approach uses knowledge the Hamiltonian equation provides about the dynamics in the phase space to navigate it elegantly and efficiently. In the first section of this chapter the Hamiltonian control is applied to orbit stabilisation as an alternative to the algorithm discussed in Sec. 6.2. In Sec. 7.2 a control algorithm for translations in the (e, ϕ) phase space is developed and tested.

7.1 Orbit stabilisation using a Hamiltonian dynamics approach

Instead of the full Hamiltonian, Eq. (2.9), given in Sec. 2.1.1, a reduced model is considered for the control algorithm which neglects the J_2 effect and only considers solar radiation pressure. This simplification is necessary, so that the problem can be reduced to a linear oscillator in the phase space and equivalent control laws can be defined. In the next subsection the validity of neglecting the J_2 effect is investigated.

7.1.1 Orbital dynamics with and without J_2

The behaviour of spacecraft with the area-to-mass-ratios investigated in this thesis (less than $20\,\mathrm{m^2\,kg^{-1}}$) follow the behaviour shown in Fig. 2.3(g-i) in Sec. 2.1.1 for high-altitude orbits ($a > 30\,000\,\mathrm{km}$). This behaviour is dominated by solar radiation pressure with the Earth's oblateness only having a small effect on the orbit evolution. This means that for the orbits and spacecraft investigated here the J_2 perturbation can initially be neglected when devising the control strategy and the Hamiltonian (Eq. (2.9) in Sec. 2.1.1) can be reduced to:

$$H_{\mathrm{SRP}}(e,\phi) = -\sqrt{1-e^2} + \alpha e \cos\phi \tag{7.1}$$

where α is the solar radiation pressure parameter defined in Eq. (2.4) in Sec. 2.1.1 and is a function of the area-to-mass-ratio and semi-major axis.

Equation (7.1) is used by Oyama et al. [101] to describe solar sail orbits for geomagnetic tail exploration at apogee distances of 30 Earth radii. The resulting phase space diagram can be divided into three regions. For $H_{\mathrm{SRP}} \leq -1$ it can be shown that the behaviour is librational. This means that the orbital eccentricity and perigee angle librate between two values in the form of a loop in the phase space. These orbits have a perigee within 90° of the direction of the Sun, while the perigee angle ϕ and eccentricity e librate around the stable equilibrium at $\phi = \pi$, as discussed in Sec. 2.1.1. For $-1 < H_{\mathrm{SRP}} \leq -\alpha$ it can be shown that the behaviour is rotational. This means the perigee angle will continually regress while the eccentricity periodically librates. These orbits are most eccentric when the perigee is Sun-pointing and least eccentric when the apogee is Sun-pointing. The last region is for orbits with $H_{\mathrm{SRP}} > -\alpha$. These will eventually reach $e = 1$ and decay as the orbit perigee intersects the surface of the Earth.

To test the premise that for large semi-major axes the J_2 perturbation can be neglected a comparison between Eq. (2.9) and Eq. (7.1) is performed. The normalised distance between the positions in the phase space can be calculated with the two different equations averaged over one loop. Since the time for the completion of a full loop varies for the SRP and J_2 case, the positions are not compared at the same time step but rather the same fraction of loop completion. First, the evolution of orbits with an initially Sun-facing perigee ($\phi = 180°$) and different starting eccentricities is reported in Fig. 7.1 for four different semi-major axes. In this figure the inaccessible regions are shaded in grey with the critical eccentricity e_{crit} marked in a dark grey, which represents the eccentricity at which the perigee equals the Earth's radius R_E, as defined in Eq. (2.11) in Sec. 2.2.2, defined as $e_{crit} = 1 - \frac{R_E}{a}$.

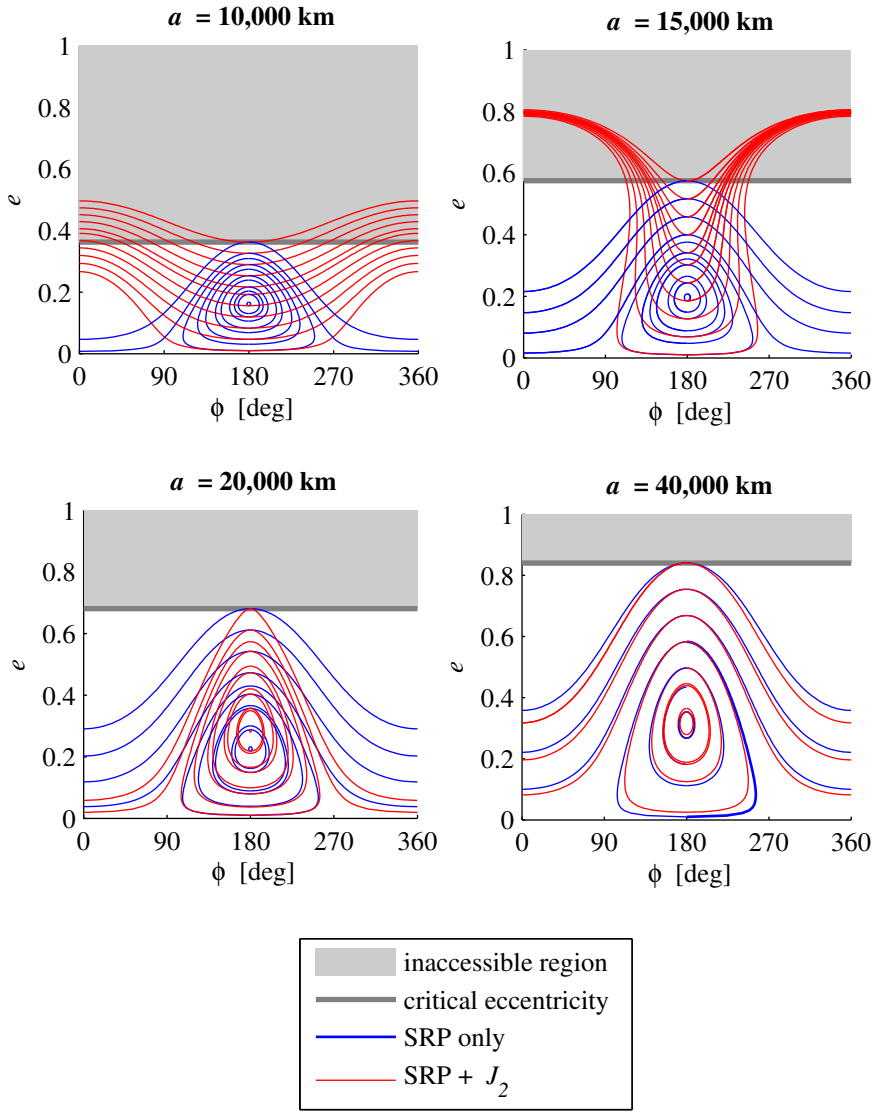

Figure 7.1: Evolution of the orbit of a $20\,\mathrm{m}^2\,\mathrm{kg}^{-1}$ spacecraft with $c_R = 1.5$ in the (e, ϕ) space with SRP and J_2 Hamiltonian and SRP only Hamiltonian for four different semi-major axes.

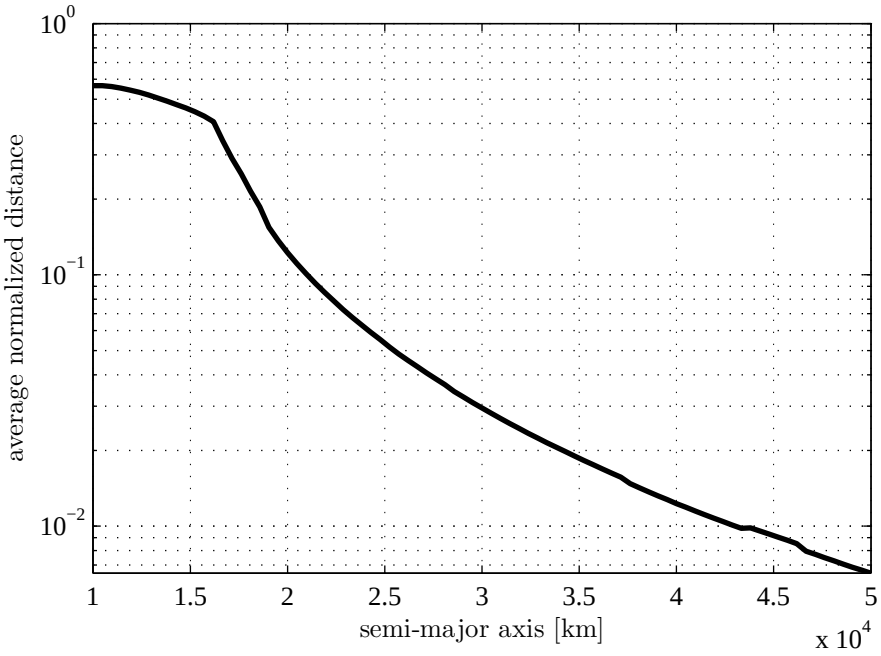

Figure 7.2: Average normalized distance (logarithmic) between points in the Hamiltonian phase space with and without J_2 effect over one period loop in the phase space as a function of semi-major axis.

It is clear that the two evolutions differ significantly for the 10 000 km orbits but become more similar with increasing semi-major axis. This can also be seen in Fig. 7.2 which shows the average normalised distance in the phase space between the two orbit evolutions, i.e. the relative error, as a function of semi-major axis. For high semi-major axis orbits this is small enough to be neglected.

7.1.2 Stabilisation algorithm

In this subsection the areas in the orbital element phase space in which a spacecraft can be stabilised are identified. This is necessary in order to define a goal orbit for orbital control manœuvres. Such manœuvres seek to navigate SpaceChips towards a long-term stable position.

Hamilton and Krivov [7] and Krivov and Getino [8] show that the secular rate of change of the eccentricity and Sun-perigee angle with respect to the true longitude of the Sun, $\lambda_\odot$, as defined in Fig. 2.2 in Sec. 2.1.1, in the solar radiation pressure only case are:

$$\begin{aligned}\frac{\mathrm{d}e}{\mathrm{d}\lambda_\odot} &= -\alpha\sqrt{1-e^2}\sin\phi \\ \frac{\mathrm{d}\phi}{\mathrm{d}\lambda_\odot} &= -\alpha\frac{\sqrt{1-e^2}}{e}\cos\phi - 1\end{aligned} \tag{7.2}$$

This is the rate of change of the spacecraft's orbital parameters averaged over one orbital revolution around the Earth. It can be seen that the eccentricity has a stable point at $\phi \in \{0, \pi\}$ whereas the change in Sun-perigee angle can only be zero for $\frac{\pi}{2} < \phi < \frac{3\pi}{2}$. Therefore, a phase space equilibrium point can only exist at $\phi_0 = \pi$ and a fixed equilibrium eccentricity e_0. This equilibrium position is previously identified as stable for the GEOSAIL solar sail mission [100]:

$$e_0 = \frac{\alpha}{\sqrt{1+\alpha^2}} \tag{7.3}$$

The Hamiltonian then has its lowest value of $\sqrt{1+\alpha^2}$ at this phase space equilibrium point.

When considering electrochromic control, instead of a single point, a line of possible stable points emerge which span the two equilibria resulting from different reflectivity values provided by the spacecraft coating. Here two different solar radiation pressure parameters are selected, α_{off} and α_{on}, corresponding to two different reflectivity states with $\alpha_{\text{off}} < \alpha_{\text{on}}$. The condition on the orbit eccentricity for a stable controlled equilibrium is then

$$\frac{\alpha_{\text{off}}}{\sqrt{1+\alpha_{\text{off}}^2}} < e_S < \frac{\alpha_{\text{on}}}{\sqrt{1+\alpha_{\text{on}}^2}} \tag{7.4}$$

At these points only the change in eccentricity is zero while the change in Sun-perigee angle with one reflectivity has the opposite sign to that with the other, as illustrated in Fig. 7.3. The stabilisation at the point $P_S = (\pi, e_S)$ with e_S defined in Eq. (7.4) can be achieved with a very simple switching control law for $c_{R,\text{off}} < c_{R,\text{on}}$:

$$\begin{aligned}&c_{R,\text{off}} \text{ when } \phi \leq \pi \\ &c_{R,\text{on}} \text{ when } \phi > \pi\end{aligned} \tag{7.5}$$

Using this strategy a SpaceChip experiences a controlled equilibrium as the derivative of ϕ is positive for $\phi < 0$ and negative for $\phi > 0$. This causes the Sun-perigee angle to oscillate closely around π and thus the eccentricity to remain constant. The orbital parameters are evaluated once per orbital revolution to avoid a jittering control response. Alternatively a dead-band could be introduced.

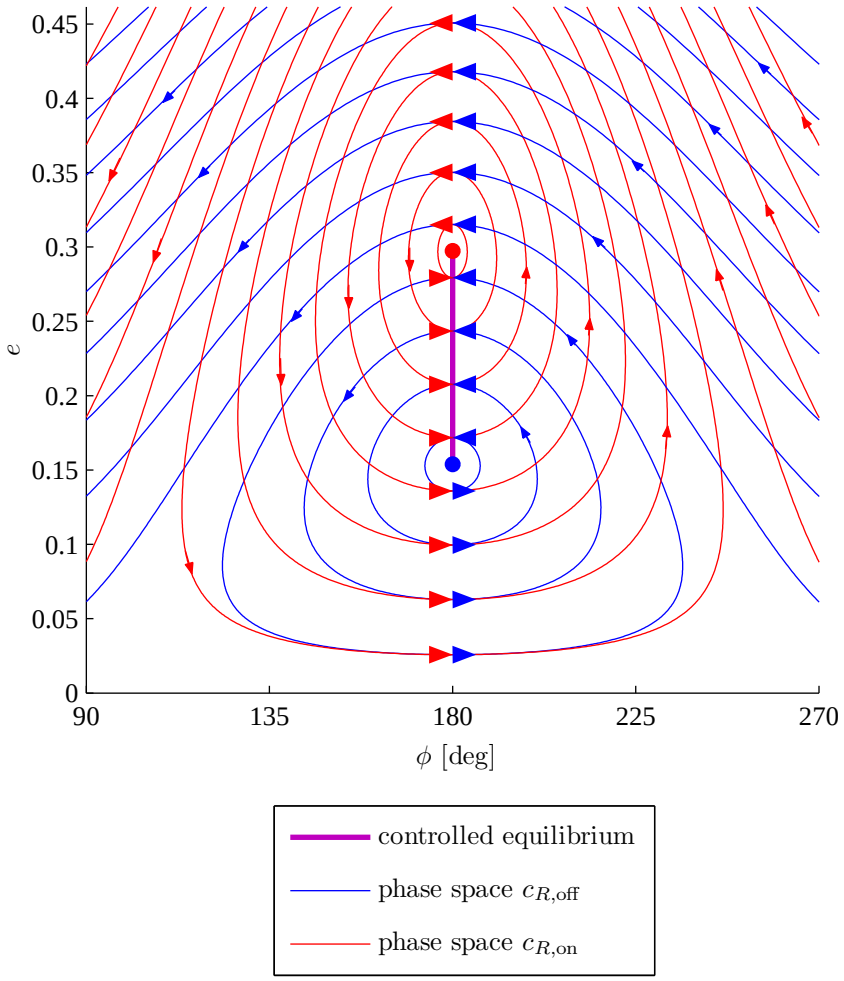

Figure 7.3: Phase space for a $20\,\mathrm{m}^2\,\mathrm{kg}^{-1}$ spacecraft at $a = 42\,000\,\mathrm{km}$ with two different reflectivity coefficients $c_{R,\mathrm{on}} = 2$ and $c_{R,\mathrm{off}} = 1$ highlighting the region in which the orbit can be stabilised using the simple switching control law.

In Sec 6.2 an artificial potential field control algorithm in the orbital element phase space was used to stabilise spacecraft at a greater range of points. It allows a reflectivity change twice per orbit and uses the angles of true anomaly where the switch takes place as control parameters. The resulting area in the phase space in which stabilisation is possible includes the range described in Eq. (7.4). However, the control algorithm is more complex and requires the solution of a two-dimensional optimisation problem. This is computationally far more expensive than the algorithm described in Eq. 7.5 and possibly not suited for SpaceChips with limited computing capabilities.

7.1.3 Stabilisation simulation results

In this subsection the long-term orbit stability of a spacecraft stabilised using the control algorithm introduced in the previous section is investigated. A SpaceChip with area-to-mass-ratio $15\,\mathrm{m}^2\,\mathrm{kg}^{-1}$ and $c_{R,\mathrm{on}} = 2$ and $c_{R,\mathrm{off}} = 1$ is placed in near geosynchronous orbit ($a = 42\,000\,\mathrm{km}$) at $\phi = \pi$ and $e = 0.25$. The starting orbit is chosen in accordance with the stability criteria identified in Sec. 7.1.2, so that the eccentricity is between the stable eccentricities with $c_{R,\mathrm{on}}$ and $c_{R,\mathrm{off}}$ respectively. The orbit is then propagated for fifty years using a numerical integration of the Gauss' equations, as introduced in Sec. 2.3.1, and taking into account solar radiation pressure and the J_2 effect, while the control algorithm described in Eq. (7.5) is applied.

The results of this simulation can be seen in Fig. 7.4. It can be seen that the controlled parameters e and ϕ remain close to their initial value while the other uncontrolled orbital parameters oscillate within bounds.In particular, the semi-major axis varies despite ϕ remaining close to π because of the definition of the angle in three dimensions: $\phi = \Omega + \omega - (\lambda_\odot - \pi)$ (Eq. (2.1)). As the inclination is not zero, the projection of the perigee onto the ecliptic is not directly between the Sun and the Earth. This means that for long durations the orbit will be asymmetrical with respect to the direction of the Sunlight. Therefore, eclipses will cause a long-term change in the semi-major axis which is periodic and synchronised with the variations of Ω and ω. It can be concluded that a SpaceChip orbit at geosynchronous altitude can be stabilised in eccentricity and ϕ in the long-term using the proposed control algorithm, for the orbits identified as suitable in the previous section.

7.2 Orbital manœuvres using a Hamiltonian dynamics approach

In this section the Hamiltonian orbital dynamics introduced in Sec. 7.1.1 are used to formulate a control law for manœuvres in the (e, ϕ) phase space.

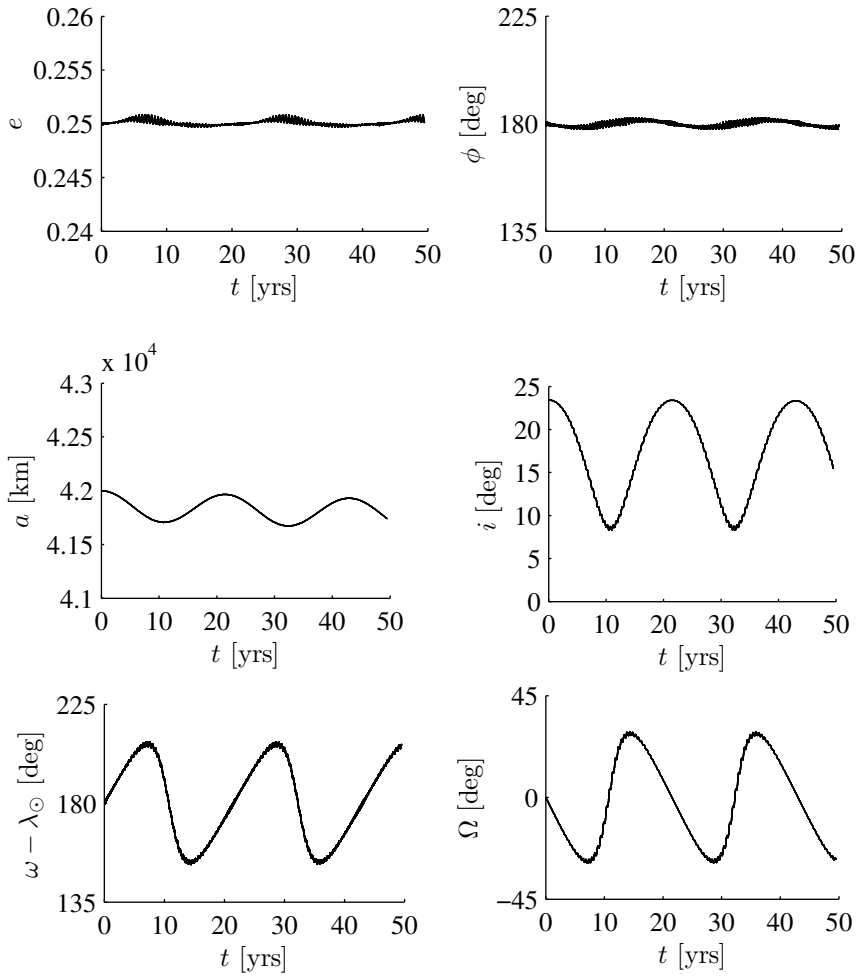

Figure 7.4: Long-term evolution of a controlled SpaceChip at an artificial stable orbit.

7.2.1 Orbit Control Law

The simple switching control defined in Eq. (7.5) can stabilise at a point in the orbital element phase space. A control law for navigation through the phase space is now sought, which can be applied to transfer a spacecraft from any orbit onto a stabilisable orbit, as defined in Sec. 7.1.2. In this section it will be shown that a bang-bang control, similar to the time-optimal control of a linear oscillator, can be applied to the problem. The control of a linear oscillator is discussed in detail by King et al. [121].

The application of this controller to the orbital manœuvre problem is possible because the Hamiltonian for solar radiation pressure and J_2 in a polar plot, with coordinates $e\sin\phi$ and $e\cos\phi$ (Fig. 7.5), can be isomorphically projected onto the classical pendulum phase space which consists of concentric circles around the stable equilibrium position. The superposed phase flow field lines of the orbital evolution with two different values for α correspond to the phase space of a linear oscillator with two different centres of oscillation. In both cases the two equilibria lie on an axis around which all phase lines are symmetrical. No phase line can cross another and there are no other equilibria.

To navigate a spacecraft to any stable point P_S identified in Eq. (7.4), the values of the Hamiltonian at the point with α_{off} and α_{on} need to be identified:

$$\begin{aligned} H_{S,\text{on}} &= -\sqrt{1-e_S^2} - \alpha_{\text{on}} e_S \\ H_{S,\text{off}} &= -\sqrt{1-e_S^2} - \alpha_{\text{off}} e_S \end{aligned} \tag{7.6}$$

With these values the control law can then be formulated. The desired position can be reached by using $c_{R,\text{off}}$ when $\phi \geq \pi$, unless the current orbit is within the loop described by $H_{S,\text{off}}$, and by using $c_{R,\text{on}}$ when $\phi < \pi$, unless the correct orbit is within the loop described by $H_{S,\text{on}}$. Figure 7.6 illustrates this control law as formulated below:

$$\begin{aligned} &\text{if } (\phi < \pi) \wedge (H_{\text{off}} \geq H_{S,\text{on}}) \rightarrow c_{R,\text{on}} \\ &\text{if } (\phi < \pi) \wedge (H_{\text{off}} < H_{S,\text{on}}) \rightarrow c_{R,\text{off}} \\ &\text{if } (\phi \geq \pi) \wedge (H_{\text{off}} \geq H_{S,\text{off}}) \rightarrow c_{R,\text{off}} \\ &\text{if } (\phi \geq \pi) \wedge (H_{\text{off}} < H_{S,\text{off}}) \rightarrow c_{R,\text{on}} \end{aligned} \tag{7.7}$$

where H_{off} is the value of the Hamiltonian with α_{off} at the current position and H_{on} is the value of the Hamiltonian with α_{on} at the current position. H_{off} and H_{on} change during the

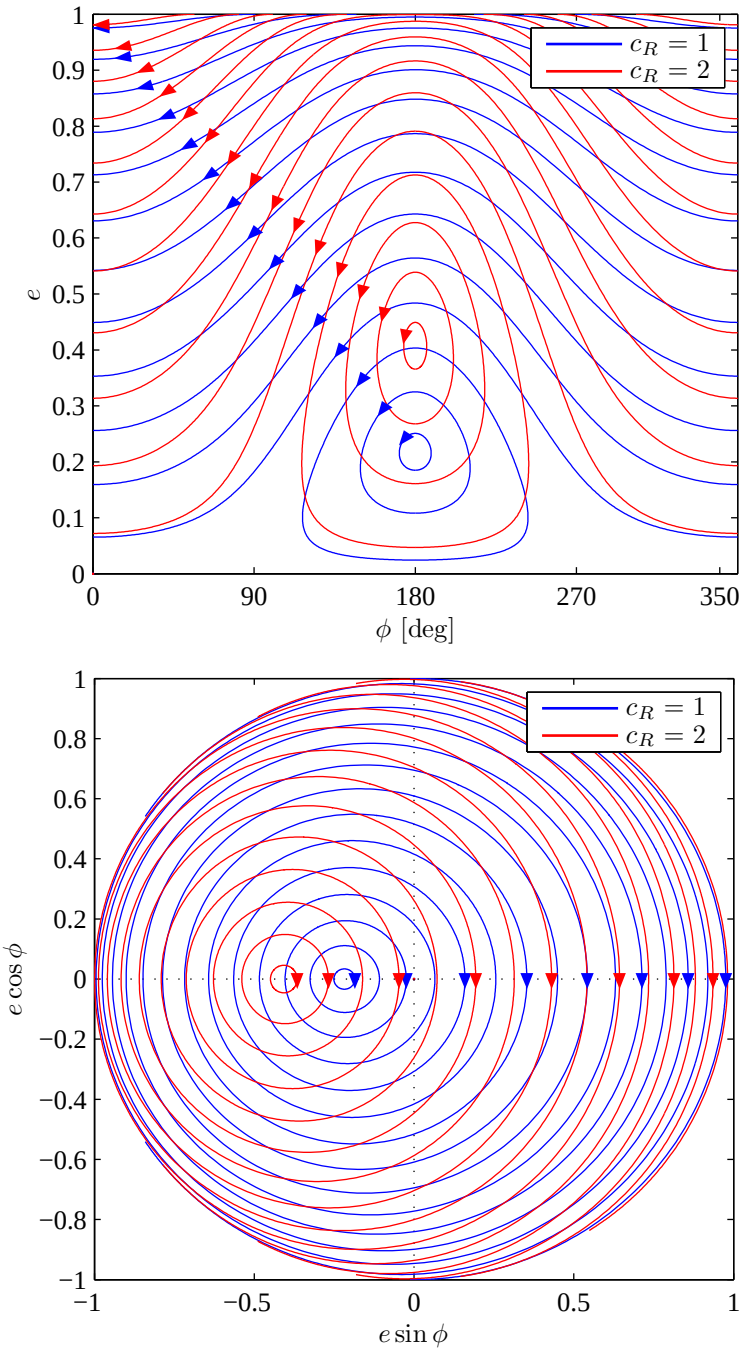

Figure 7.5: Phase space plot (above) and polar plot (below) for a $20\,\mathrm{m}^2\,\mathrm{kg}^{-1}$ spacecraft on a geosynchronous orbit.

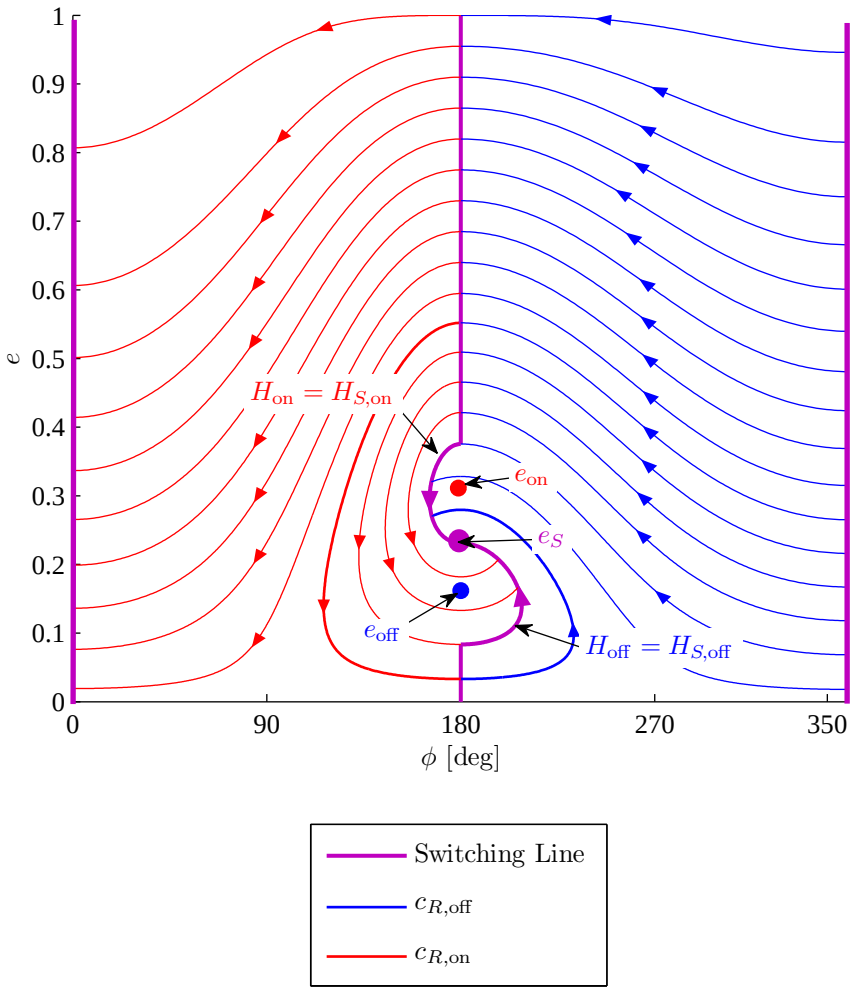

Figure 7.6: Bang-bang switching law in the phase space to navigate a $20\,\mathrm{m}^2\,\mathrm{kg}^{-1}$ spacecraft on a geosynchronous orbit to the stable position, marked with a large magenta circle

manœuvre as they depend on the current position, while $H_{S,\text{off}}$ and $H_{S,\text{on}}$ remain constant as they depend on the desired goal position. Figure 7.6 displays the phase space dynamics when applying the control law formulated above. It can be seen that the desired final position can be reached from all initial positions in the phase space excluding those which would inevitably lead to the eccentricity exceeding unity.

7.2.2 Comparison with a linear oscillator

The proposed switching control algorithm with two fixed reflectivity parameters is equivalent to the optimal control of a linear oscillator. In this subsection the two are compared to estimate how close the proposed control algorithm comes to be being time optimal.

The orbit evolution is considered in eccentricity and orientation alone, which occurs naturally when eclipses are neglected and reflectivity switches do not occur more than once over several orbits. In this case the algorithm is time-optimal in most of the phase space as it represents the only viable control path. There are two regions in the phase space in which time-optimality is non-trivial. These are the areas in which two possible paths exist to connect two points within the respective region. These regions are highlighted in Fig. 7.7. In the case of a linear oscillator the switching solution is always time-optimal even within the highlighted areas because the period of one oscillation is constant and equal for both control options, and the speed along each control path is constant. Therefore, in the linear oscillator problem the shortest path connecting two points is always the fastest [121]. These conditions do not universally apply to the phase space control which is considered here. In this section it will be investigated how close the phase space control comes to fulfilling the two conditions:

(1) How far from equal are the phase space periods with two different reflectivity coefficients?

(2) How far from constant is the speed along a phase curve?

These two conditions will be addressed in the following subsections. The term ‘phase space period’ is used to describe the period in which one complete loop in the phase space is covered; this is far longer than the period for completing one single orbit around the Earth.

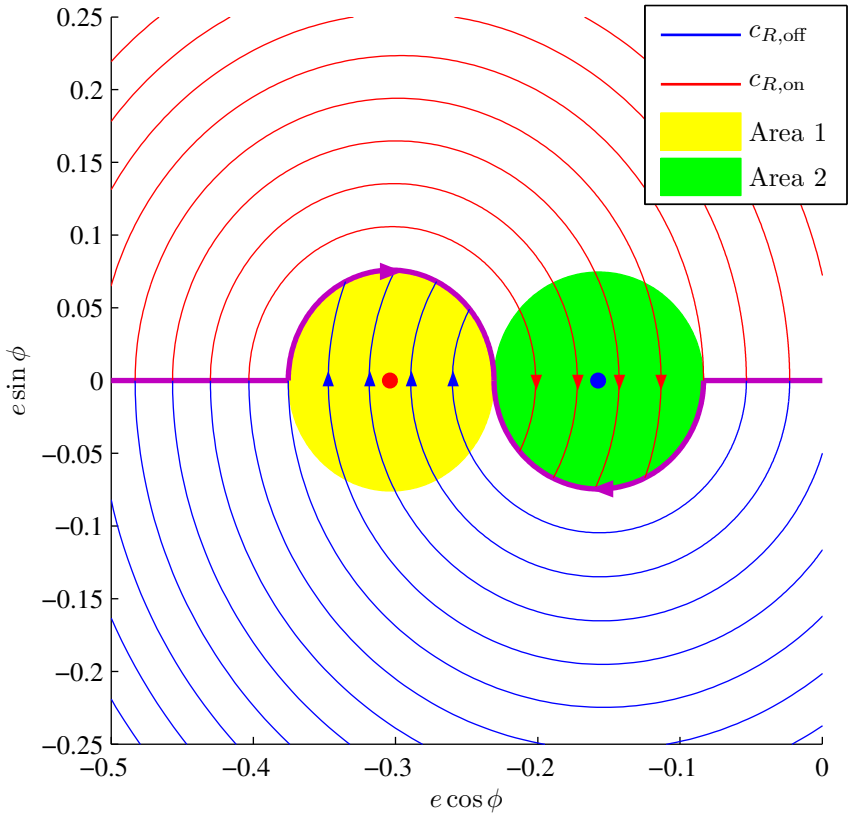

Figure 7.7: Switching law with areas in which proof of time-optimal control is not trivial highlighted.

7.2.2.1 Duration of the period in the phase space

First the condition on the period of the phase space evolution is investigated. For time-optimality it is required that the period is the same for both values of reflectivity and regardless of the starting position. Oyama et al. [101] find an expression for the period of time T to follow a closed phase path in the case of SRP only:

$$T = \frac{2\pi}{n_{\odot}\sqrt{1+\alpha^2}} \tag{7.8}$$

This means that for a given area-to-mass-ratio, semi-major axis and reflectivity the period to complete one phase space period is constant and not dependent on the starting orbit. However, higher α SpaceChips complete one period around a closed phase curve faster. The difference is small: a $10\,\mathrm{m^2\,kg^{-1}}$ geosynchronous spacecraft would only be 1.8 % faster with $c_R = 2$ than with $c_R = 1$. A $20\,\mathrm{m^2\,kg^{-1}}$ spacecraft could increase its libration period by just 6.8 %.

7.2.2.2 Rate of orbit evolution

The second condition to investigate is how the rate of orbit evolution in the polar plot deviates from the average. In order to find an analytical expression for the speed of orbital evolution in polar coordinates for a given initial condition, a coordinate transformation has to be performed from (e, ϕ) to $(\varepsilon, \varphi)_{\alpha}$. The latter point is a polar coordinate system with the centre at the equilibrium point for a given α, as shown in Fig. 7.8. The following expressions are found which define the transformation:

$$\begin{aligned} e(\varepsilon,\varphi)_{\alpha} &= \sqrt{\varepsilon^2 + \frac{\alpha^2}{1+\alpha^2} - 2\varepsilon\frac{\alpha}{\sqrt{1+\alpha^2}}\cos\varphi} \\ \phi(\varepsilon,\varphi)_{\alpha} &= \arccos\frac{\varepsilon\cos\varphi - \frac{\alpha}{\sqrt{1+\alpha^2}}}{e(\varepsilon,\varphi)_{\alpha}} \end{aligned} \tag{7.9}$$

with

$$e\cos\phi = \varepsilon\cos\phi - e_0 \tag{7.10}$$

An expression for ε as a function of α, H and φ is found by inserting Eq. (7.9) and Eq. (7.10) into Eq. (7.1) and then solving for ε so that

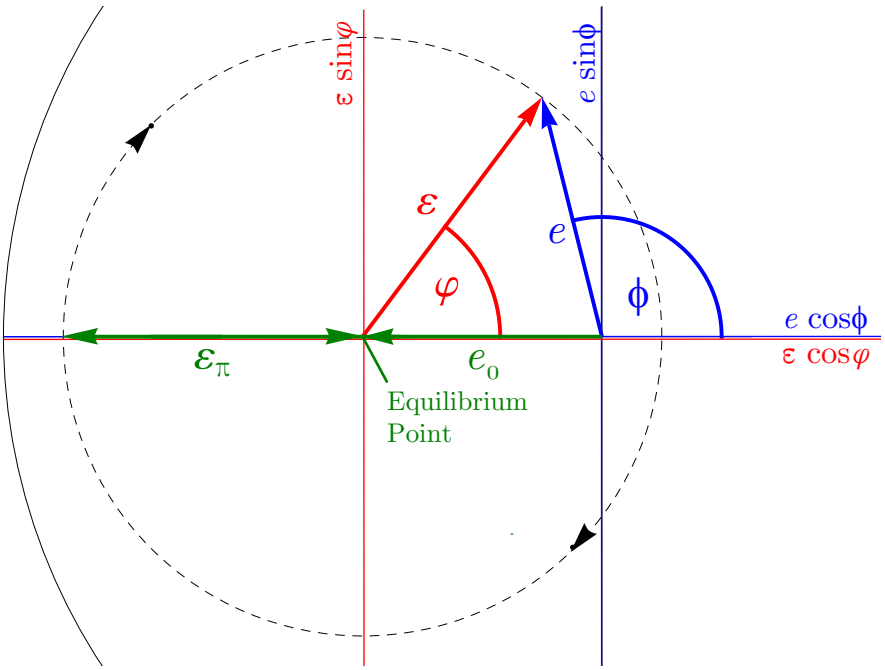

Figure 7.8: Coordinate transformation from (e,ϕ) (blue) to equilibrium centred coordinates (ε,φ) (red)

$$\begin{aligned}\varepsilon\left(\alpha,H,\varphi\right) =& \frac{\alpha}{\sqrt{1+\alpha^2}}\frac{\left(1+\alpha^2+H\sqrt{1+\alpha^2}\right)\cos\varphi}{1+\alpha^2\cos^2\varphi} \\ &+\frac{\sqrt{1-\left(1+\frac{\alpha}{\sqrt{1+\alpha^2}}\right)H^2+\alpha^2\left(1+\frac{H}{\sqrt{1+\alpha^2}}\right)\cos 2\varphi}}{1+\alpha^2\cos^2\varphi}\end{aligned} \tag{7.11}$$

Defining $\varepsilon_\pi = (e-e_0)_{\phi=\pi}$ as the difference between the eccentricity at $\phi=\pi$ and the equilibrium eccentricity gives the value of the Hamiltonian as a function of ε_π:

$$H\left(\alpha,\varepsilon_\pi\right) = -\sqrt{1-\left(\frac{\alpha}{\sqrt{1+\alpha^2}}+\varepsilon_\pi\right)^2}-\alpha\left(\frac{\alpha}{\sqrt{1+\alpha^2}}+\varepsilon_\pi\right) \tag{7.12}$$

Next the speed of progression along the phase curves in the polar plot $(x,y)=(e\cos\phi, e\sin\phi)$ is derived using:

$$v=\sqrt{\dot{x}^2+\dot{y}^2}=\sqrt{\left(\dot{e}\cos\phi-e\dot{\phi}\sin\phi\right)^2+\left(\dot{e}\sin\phi+e\dot{\phi}\cos\phi\right)^2} \tag{7.13}$$

and using Eq. (7.2) this reduces to:

$$v\left(e,\phi\right)=\sqrt{\left(e\sin\phi\right)^2+\left(-\sqrt{1-e^2}\alpha-e\cos\phi\right)^2} \tag{7.14}$$

From Eq. (7.9) the following equation can be derived in the transformed polar coordinates system:

$$v(\varepsilon_\pi, \varphi)_\alpha = \sqrt{(1-\alpha^2)\, e(\varepsilon_\pi, \varphi)_\alpha{}^2 + \alpha^2 + 2\alpha e(\varepsilon_\pi, \varphi)_\alpha \sqrt{1 - e(\varepsilon_\pi, \varphi)_\alpha{}^2}\cos\phi(\varepsilon_\pi, \varphi)_\alpha} \tag{7.15}$$

This equation can be numerically evaluated to find the average, the minimum and the maximum speed over one evolution period (i.e. one loop in the phase space) for a given initial orbit and spacecraft characteristics. Using this information the maximum relative divergence from the average speed can be found as a function of area-to-mass-ratio and reflectivity. Figure 7.9 shows the results of this analysis. It depicts the maximum relative difference, $\frac{\max|v-v_{avg}|}{v_{avg}}$, between the actual and average speed of progression calculated using Eq. (7.15) along any phase curve for different area-to-mass-ratio spacecraft with coefficients of reflectivity of 1 or 2. It can be seen that a $10\,\mathrm{m^2\,kg^{-1}}$ spacecraft will never diverge more than 1.5% from the average progression speed and a $20\,\mathrm{m^2\,kg^{-1}}$ spacecraft stays within $\pm 5\,\%$.

It can be seen that for both conditions of the linear controller optimality, as presented in Sec. 7.2.3, the deviation from time optimality is limited with the parameters used. It can therefore be assumed that the resulting manœuvre times are approaching the optimum.

7.2.3 Modifications to the Hamiltonian model

In this section the original Hamiltonian model of the orbit evolution described with Eq. (7.1) is modified to account for the effect of eclipses.

Effect of eclipses on the orbital evolution

There are several effects which have not been taken into account in the Hamiltonian model. The most dominant of these effects is eclipses, which will occur each orbit since the orbit is assumed to lie in the ecliptic plane. Eclipses have two main effects on the Hamiltonian dynamics. They compress the phase space in the direction of eccentricity, so that the equilibrium eccentricity is lower and it adds a periodic change of the semi-major axis. The change of the semi-major axis is positive for $0 < \phi < \pi$, negative for $\pi < \phi < 2\pi$ and zero if $\phi \in \{0, \pi\}$. The effect is such that a spacecraft will return to the semi-major axis it started from after the completion of a full loop in the phase space during which the semi-major axis varies, as shown by Colombo and McInnes [103]. Both effects are small at the distances considered in this thesis but are still problematic. The change in semi-major axis during the period further shifts the equilibrium point as e_0 is a

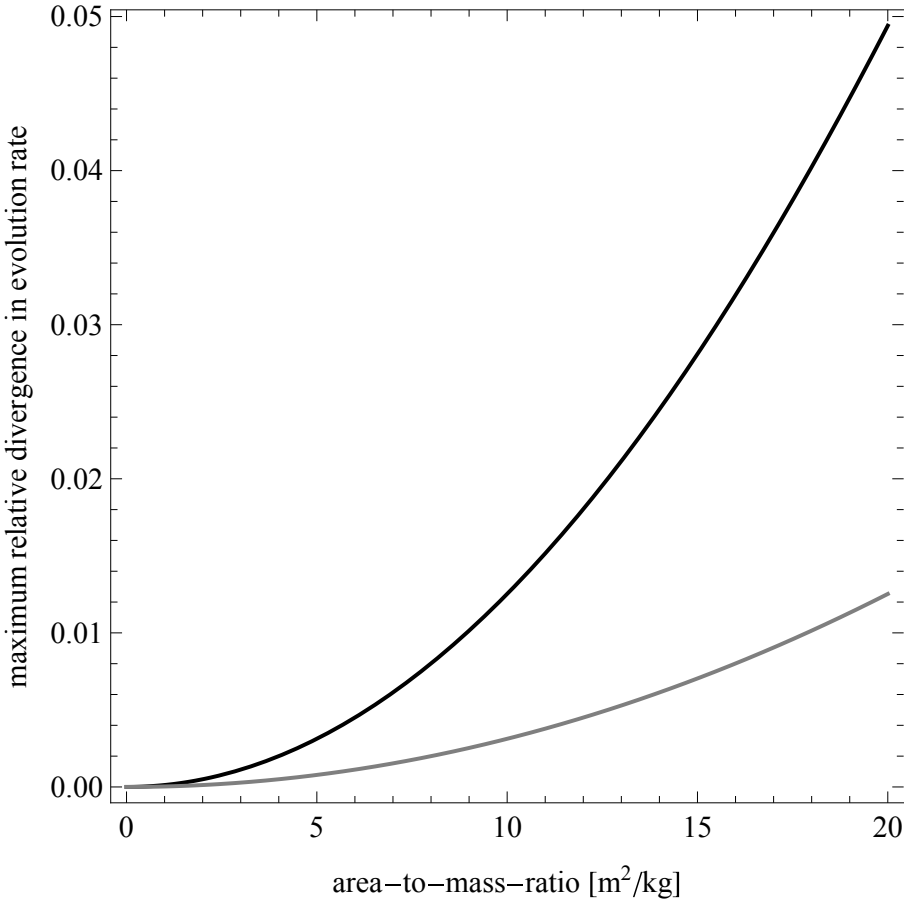

Figure 7.9: Maximum divergence from average progression speed normalised relative to the average along polar phase lines for geosynchronous spacecraft with reflectivity of 1 (grey) and 2 (black).

function of α which in turn is dependent on the semi-major axis. With decreasing semi-major axis the eccentricity of the equilibrium point will also decrease. Furthermore, additional perturbations act on the spacecraft. Atchison and Peck show that in the case of SpaceChips with area-to-mass-ratios in the order of $10\,\mathrm{m^2\,kg^{-1}}$ and in high altitude orbits the strongest of these effects is the J_2 precession [1], as discussed in Sec. 7.1.1.

Although small, the effects of neglecting eclipses and additional perturbations can increase the transfer time considerably because they can lead to the spacecraft missing its target equilibrium point and having to complete another phase space loop until it reaches the goal. Since the period of evolution along a closed phase curve is the same regardless of the size of the loop when only SRP is considered, as shown in Eq. (7.8), this can lead to a doubling of the transfer time. One solution is to add a margin to the control algorithm that is linearly proportional to the difference between actual and desired eccentricity. This way, a spacecraft would switch its reflectivity earlier rather than later.

Linearised Phase Space Equations to Account for Eclipses

In this and the following subsection, approaches are discussed to account for the effects of eclipses. The phase space perturbed by the effect of eclipses can be approximated by a linearisation process. The original Hamiltonian is linearised around the equilibrium condition in a Cartesian coordinate system based on the polar plot, as shown in Fig. 7.5. The linearised equations are then modified to account for a shift in the centre of rotation away from the equilibrium point. The expression for the rotational centre is a function of position and the true equilibrium point location. The effect of eclipses can then be approximated by substituting the analytical equilibrium eccentricity e_0 with the real equilibrium which is found numerically taking into account eclipses.

First, the polar coordinates (e, ϕ) are again transformed into a set of auxiliary Cartesian coordinates (x, y).

$$\begin{aligned} x &= e\cos\phi \\ y &= e\sin\phi \end{aligned} \tag{7.16}$$

$$\begin{aligned} e &= \sqrt{x^2+y^2} \\ \phi &= \arctan\frac{y}{x} \end{aligned} \tag{7.17}$$

The derivatives of the Cartesian coordinates are (with Eq. (7.2)):

$$\begin{aligned} \dot{x} &= e \sin\phi \\ \dot{y} &= -\alpha\sqrt{1-e^2} - e\cos\phi \end{aligned} \tag{7.18}$$

Inserting Eq. (7.17) yields:

$$\begin{aligned} \dot{x} &= y \\ \dot{y} &= -\alpha\sqrt{1-x^2-y^2} - x \end{aligned} \tag{7.19}$$

Linearising Eq. (7.19) around the equilibrium point (e_0, ϕ) then defines Cartesian coordinates $(\hat{x}, \hat{y})$ for any initial radial distance r along the x-direction ($\phi = 0 \vee \phi = \pi$):

$$\begin{aligned} \hat{x}(\varphi) &= -e_0 + r\cos\varphi \\ \hat{y}(\varphi) &= -r\sqrt{1+\alpha^2}\sin\varphi \end{aligned} \tag{7.20}$$

It can be seen that the radial distance in the y-direction is $r\sqrt{1+\alpha^2}$. The linearisation defined by Eq. (7.20) assumes a static centre of rotation, e_0. A hypothetical point is then introduced with $\phi = \pi$ and $e = e_c$, the central eccentricity which has equal distance to the maximum and minimum eccentricity within one loop in the phase space. Note that e_c is equal to the equilibrium eccentricity e_0 at the equilibrium point, but decreases with distance from e_0 in the polar plot. Figure 7.10 shows the position of e_c and r in the polar plot for two different phase lines. The central eccentricity e_c can be found as a function of an initial set of orbital parameters (e, ϕ) by solving Eq. (7.1) for e with $\phi = \pi$:

$$e_{c,i}(e,\phi) = -\frac{H_{\mathrm{SRP}}(e,\phi)}{\sqrt{1+{\alpha_i}^2}} e_0 \qquad (i = \mathrm{off}, \mathrm{on}) \tag{7.21}$$

where the index i indicates the control mode, such that $i = \mathrm{off}$ corresponds to $c_{R,\mathrm{off}}$ and $i = \mathrm{on}$ to $c_{R,\mathrm{on}}$. Next the radius of rotation in the x-direction can be calculated:

$$r_i(e,\phi) = \sqrt{\left(e\cos\phi + e_{c,i}(e,\phi)\right)^2 + \frac{e^2 \sin^2\phi}{1+{\alpha_i}^2}} \tag{7.22}$$

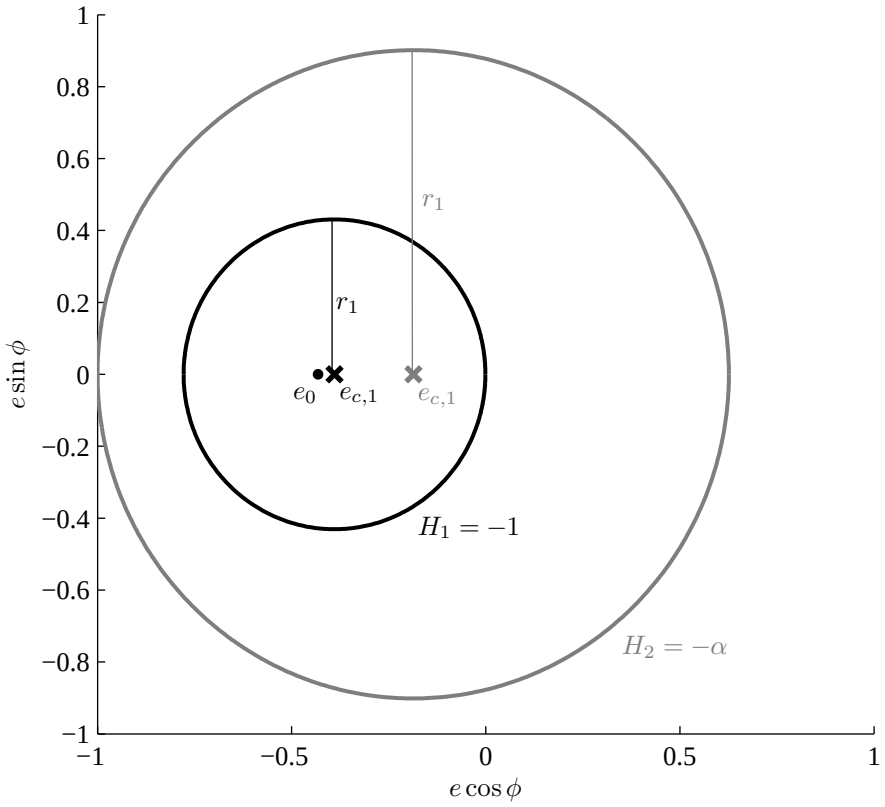

Figure 7.10: Position of the central eccentricities e_c and radial distances in x-direction r for two different phase lines H_{off} and H_{on} for the same area-to-mass-ratio and reflectivity in a polar plot.

When using two different coefficients of reflectivity any set of orbital coordinates can be transformed into radial coordinates which are unique within one half of the phase space ($\phi \in (0,\pi) \vee \phi \in (\pi, 2\pi)$). The coordinates are $(r_{\text{off}}, r_{\text{on}})$ and correspond to the radial distance in the x-direction with $c_{R,\text{off}}$ and $c_{R,\text{on}}$. Using Eqs. (7.21) and (7.22), Eq. (7.20) can be revised to:

$$\begin{aligned} \hat{x}_i(\varphi) &= -e_{c,i} + r_i \cos\varphi \\ \hat{y}_i(\varphi) &= -r_i \sqrt{1+{\alpha_i}^2} \sin\varphi \end{aligned} \tag{7.23}$$

By substituting the analytical result for the equilibrium point e_0 with a numerical solution $e_{0,ecl}$ which takes into account the eclipses when computing $e_{c,i}$ in Eq. (7.21), the linearisation Eq. (7.23) becomes an accurate approximation of the perturbed phase space resulting from the compensation for eclipses. Although the real equilibrium $e_{0,ecl}$ is close to the analytical equilibrium e_0, this step is necessary because manœuvres in the vicinity of the equilibrium point are sensitive to exact position. If an incorrect value for the equilibrium eccentricity is assumed the control algorithm could in certain cases fail to complete the manœuvre. To find $e_{0,ecl}$, ϕ is set equal to π in the expression for $\frac{\mathrm{d}\phi}{\mathrm{d}t}$ in Eq. 2.12 in Sec. 2.2.1, which calculates the secular change in ϕ. Then the eccentricity $e_{0,ecl}$ can be found numerically by setting the equation equal zero and solving for e.

Figure 7.11 shows the results of the linearisation superimposed on those of a numerical simulation with eclipses. The model used in this simulation is the model introduced in Sec. 2.2.1 neglecting the effects of J_2 and aerodynamic drag but considering eclipses. It can be seen that the linearised phase lines in Fig. 7.11(b) match the numerical results far better than the Hamiltonian phase lines in Fig. 7.11(a).

Using this approach the control algorithm in Eq. (7.7) can be revised to:

$$\begin{aligned} &\text{if}(\phi < \pi) \wedge (r_{\text{on}} \geq r_{S,\text{on}}) \rightarrow c_{R,\text{on}} \\ &\text{if}(\phi < \pi) \wedge (r_{\text{on}} < r_{S,\text{on}}) \rightarrow c_{R,\text{off}} \\ &\text{if}(\phi \geq \pi) \wedge (r_{\text{off}} \geq r_{S,\text{off}}) \rightarrow c_{R,\text{off}} \\ &\text{if}(\phi \geq \pi) \wedge (r_{\text{off}} < r_{S,\text{off}}) \rightarrow c_{R,\text{on}} \end{aligned} \tag{7.24}$$

where $(r_{\text{off}}, r_{\text{on}})$ are the radial coordinates of the current orbit as described above and $(r_{S,\text{off}}, r_{S,\text{on}})$ are the radial coordinates of the desired stable goal point.

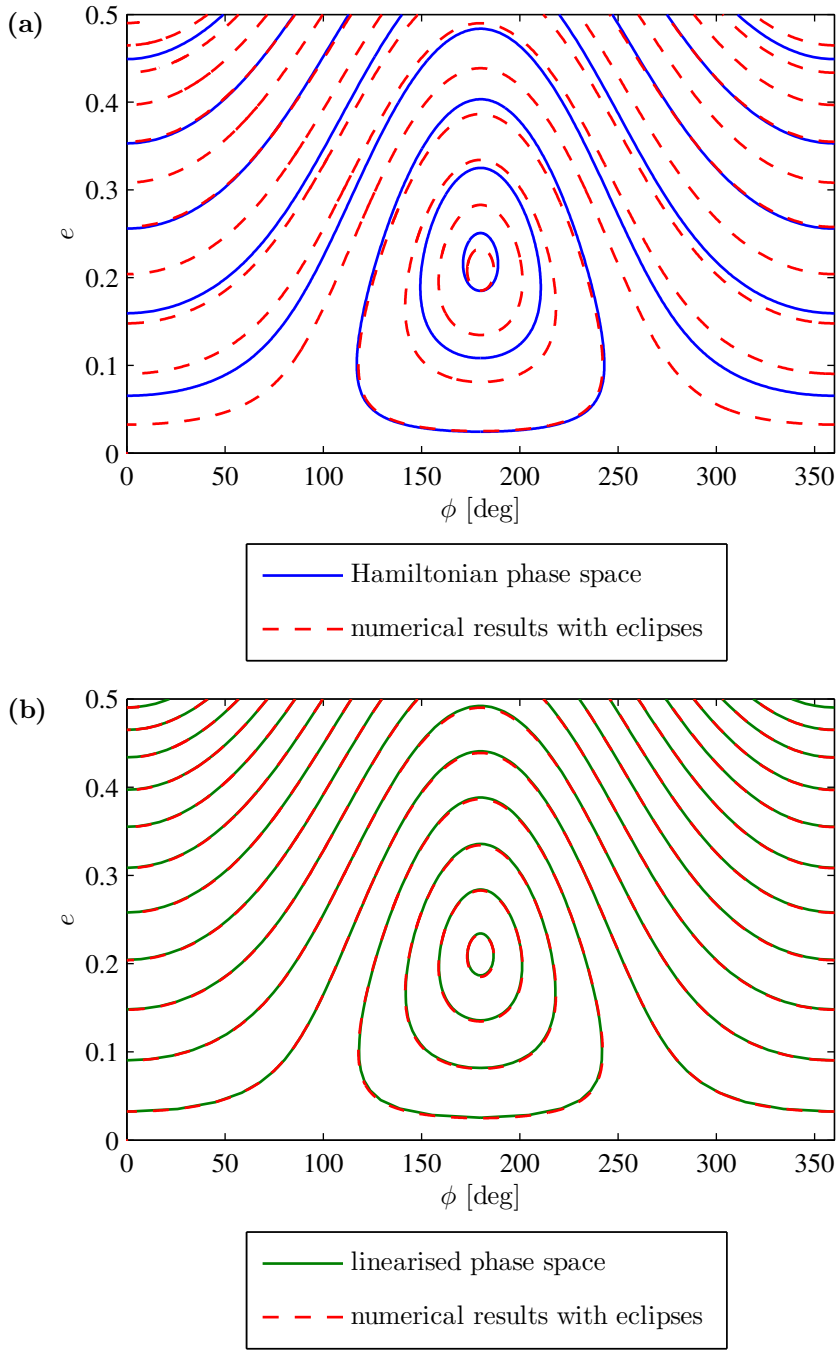

Figure 7.11: Comparison of the numerically computed phase space with eclipses with Hamiltonian phase space (a) and with the phase space resulting from the approximating linearisation (b) for a spacecraft with area-to-mass-ratio $20\,\mathrm{m^2\,kg^{-1}}$ and $c_R = 1$

Control algorithm for constant semi-major axis

The method described in the previous subsection can account for the inaccuracies caused by the effect of eclipses to allow more precision in the selection of the control path. However, it does not remove all effects of eclipses and the spacecraft arrives at the correct position in the (e, ϕ) phase space, but with a different semi-major axis. In this subsection it is shown how the electrochromic properties of the spacecraft can be used to keep the semi-major axis constant as well as efficiently navigating the spacecraft through the (e, ϕ) phase space. To achieve this, the reflectivity has to be switched twice per orbit. That way there are always two possible control modes. One in which the reflectivity is predominantly high, control mode 'on', and one in which the reflectivity is predominantly low, control mode 'off'. In both modes a short interval of the orbit will be spent with the other respective reflectivity to offset the change in semi-major axis caused by the eclipses. The switching angles, f_{off} and f_{on} have to fulfil the following expression in which $f_{e,\text{in}}$ and $f_{e,\text{in}}$ represent the angles of true anomaly at which the eclipse is entered and exited:

$$\begin{aligned}
\text{control mode 'off':} \quad & \int_{f_{\text{on}}}^{f_{\text{off}}} \frac{\mathrm{d}a}{\mathrm{d}f}(c_{R,\text{on}})\ \mathrm{d}f - \int_{f_{\text{on}}}^{f_{\text{off}}} \frac{\mathrm{d}a}{\mathrm{d}f}(c_{R,\text{off}})\ \mathrm{d}f = -\int_{f_{e,\text{in}}}^{f_{e,\text{in}}} \frac{\mathrm{d}a}{\mathrm{d}f}(c_{R,\text{off}})\ \mathrm{d}f \\
\text{control mode 'on':} \quad & \int_{f_{\text{off}}}^{f_{\text{on}}} \frac{\mathrm{d}a}{\mathrm{d}f}(c_{R,\text{on}})\ \mathrm{d}f - \int_{f_{\text{off}}}^{f_{\text{on}}} \frac{\mathrm{d}a}{\mathrm{d}f}(c_{R,\text{off}})\ \mathrm{d}f = -\int_{f_{e,\text{in}}}^{f_{e,\text{in}}} \frac{\mathrm{d}a}{\mathrm{d}f}(c_{R,\text{on}})\ \mathrm{d}f
\end{aligned} \tag{7.25}$$

where $\frac{\mathrm{d}a}{\mathrm{d}f}(c_R)$ is the derivative of the semi-major axis with respect to the true anomaly due to solar radiation pressure for the given reflectivity.

The interval of the eclipses and the switching interval, the orbit arc in which the non-dominant reflectivity is used ($[f_{\text{on}}, f_{\text{off}}]$ for control mode 'off', and $[f_{\text{off}}, f_{\text{on}}]$ for control mode 'on'), may not overlap. To find close to optimal switching angles with as little computational expense as possible the problem is reduced from two to one dimensions. Instead of searching for both switching angles as proposed in Sec. 6.3.1, the switching interval is redefined as $[f_c - \Delta f, f_c + \Delta f]$ where f_c is the angle in the centre of the interval and $\Delta f = |f_{\text{off}} - f_c| = |f_{\text{on}} - f_c|$ determines the size of the interval. Of these two variables only f_c needs to be found numerically, since Δf is found analytically by a linear approximation.

First f_c is determined. For the manœuvre to be most effective means the interval is to be as small as possible so that the orbit evolution will follow closely the behaviour predicted by the Hamiltonian. To achieve this, f_c is chosen as the angle at which the positive or negative change of semi-major axis over true anomaly is greatest. Whether the direction of the change is negative or positive depends on the control mode and the change in semi-major axis which would occur

without control, Δa. Using this definition, f_c can be found using:

$$\begin{aligned}
&\text{control mode 'off':}\\
&0 < \phi < \pi \Rightarrow f_c = f_{\min \frac{\mathrm{d}a}{\mathrm{d}f}}\\
&\pi < \phi < 2\pi \Rightarrow f_c = f_{\max \frac{\mathrm{d}a}{\mathrm{d}f}}\\
&\\
&\text{control mode 'on':}\\
&0 < \phi < \pi \Rightarrow f_c = f_{\max \frac{\mathrm{d}a}{\mathrm{d}f}}\\
&\pi < \phi < 2\pi \Rightarrow f_c = f_{\min \frac{\mathrm{d}a}{\mathrm{d}f}}
\end{aligned} \tag{7.26}$$

where $f_{\max \frac{\mathrm{d}a}{\mathrm{d}f}}$ is the true anomaly where the greatest positive rate of change of semi-major axis over true anomaly occurs, and $f_{\min \frac{\mathrm{d}a}{\mathrm{d}f}}$ is the angle of true anomaly where the greatest negative change occurs. The change of semi-major axis is positive when the velocity vector of the spacecraft is pointing away from the Sun and negative if it is pointing towards it. The angles at which the largest positive and negative change occur can be found by maximising or minimising the following equation which has been derived by combining Gauss' equation for variation of semi-major axis in Eq. (2.23) in Sec. 2.3.1 with the in-plane force components of solar radiation pressure as shown in Eq. (6.3) in Sec. 6.1.2, so that the rate of change of semi-major axis scales as:

$$\frac{\mathrm{d}a}{\mathrm{d}f} \propto e\sin(2f+\phi) + \sin(f+\phi) \tag{7.27}$$

Next Δf, the size of the interval in true anomaly on each side of the central angle f_c, is determined. It is found by linear approximation:

$$\begin{aligned}
&\text{control mode 'off': } 2\Delta f \left(\frac{\mathrm{d}a(f_c)}{\mathrm{d}f}(c_{R,\mathrm{on}}) - \frac{\mathrm{d}a(f_c)}{\mathrm{d}f}(c_{R,\mathrm{off}}) \right) = -\int_{f_{e,\mathrm{in}}}^{f_{e,\mathrm{in}}} \frac{\mathrm{d}a(c_{R,\mathrm{off}})}{\mathrm{d}f}\,\mathrm{d}f\\
&\text{control mode 'on': } 2\Delta f \left(\frac{\mathrm{d}a(f_c)}{\mathrm{d}f}(c_{R,\mathrm{on}}) - \frac{\mathrm{d}a(f_c)}{\mathrm{d}f}(c_{R,\mathrm{off}}) \right) = -\int_{f_{e,\mathrm{in}}}^{f_{e,\mathrm{in}}} \frac{\mathrm{d}a(c_{R,\mathrm{on}})}{\mathrm{d}f}\,\mathrm{d}f
\end{aligned} \tag{7.28}$$

where the right hand term is the change in semi-major axis which would occur due to eclipses over one orbit if the reflectivity is constant. The integral does not have to be calculated numerically. Instead the analytical expressions by Colombo and McInnes [103], introduced in Sec. 2.2.1, are used. The left term corresponds to the difference in change of semi-major axis caused by using the other reflectivity. This is assuming a constant rate of change of semi-major axis over that interval. This assumption can be made because the interval is small. A comparison with the exact results

for the required Δf obtained using a numerical simulation has been conducted and it is found that at geosynchronous semi-major axis and eccentricities below 0.5 this simplification is appropriate. At higher eccentricities a numerical approach can be used to find Δf using the value calculated in Eq. (7.28) as an initial guess.

Using this method, eclipses can be accounted for with low computational expense, as all but one step in the control algorithm are analytical and the numerical step is a simple one-dimensional optimisation. Since a linear approximation is used to determine Δf, and because any out-of-plane dynamics are neglected, there will still be a change in semi-major axis. However, this change is small in comparison to the change occurring when using the method in which the reflectivity is switched only depending on the position in the phase space, as described in the Sec. 7.2.1. Figure 7.12 shows the results for the two control modes for a geosynchronous orbit with an eccentricity of 0.3 and two different initial perigee angles. For eccentricities below 0.5 at geosynchronous semi-major axis it is found that $\Delta f \leq 2.5°$. The arc of the orbit with $c_{R,\text{off}}$ is drawn in blue and $c_{R,\text{on}}$ in red. The positions at which the reflectivity is switched are marked with crosses. Figures 7.12(a) and (b) show the control strategy when the change in semi-major axis over one orbit would be positive and (c) and (d) show the control strategy when the change in semi-major axis would be negative. The left column of figures shows the control strategy with mainly reflectivity $c_{R,\text{off}}$ and the right column shows the control strategy with mainly reflectivity $c_{R,\text{on}}$. This control method forces the evolution of the orbital elements to follow closely the evolution with eclipses and the linearised approach to the control algorithm described in the previous section.

7.2.4 Test case manœuvre

To show the effectiveness of the proposed control method a test case is devised and simulated. The mission scenario consists of six SpaceChips with an area-to-mass-ratio of $15\,\text{m}^2\,\text{kg}^{-1}$ which are initially in six different orbits with a semi-major axis of 42 000 km, with eccentricity ranging from close to circular to under 0.5 and perigee angle between 90° and 270°. They are to be collected into a stable goal orbit with $e_S = 0.25$ and $\phi = 180°$. The manœuvre is performed using the linearised phase space with and without the constant semi-major axis control derived in Sec. 7.2.3. The orbit is propagated numerically taking solar radiation pressure and the Earth oblateness into account, while the control algorithms use the linearised phase space introduced in Sec. 7.2.3. The numerical propagation is performed using the Gauss' equations as introduced in Sec. 2.3.1, while taking out-of-plane dynamics into account. When using a full set of Keplerian orbital parameters, the angle ϕ can is calculated according to Eq. (2.1) in Sec. 2.1.1.

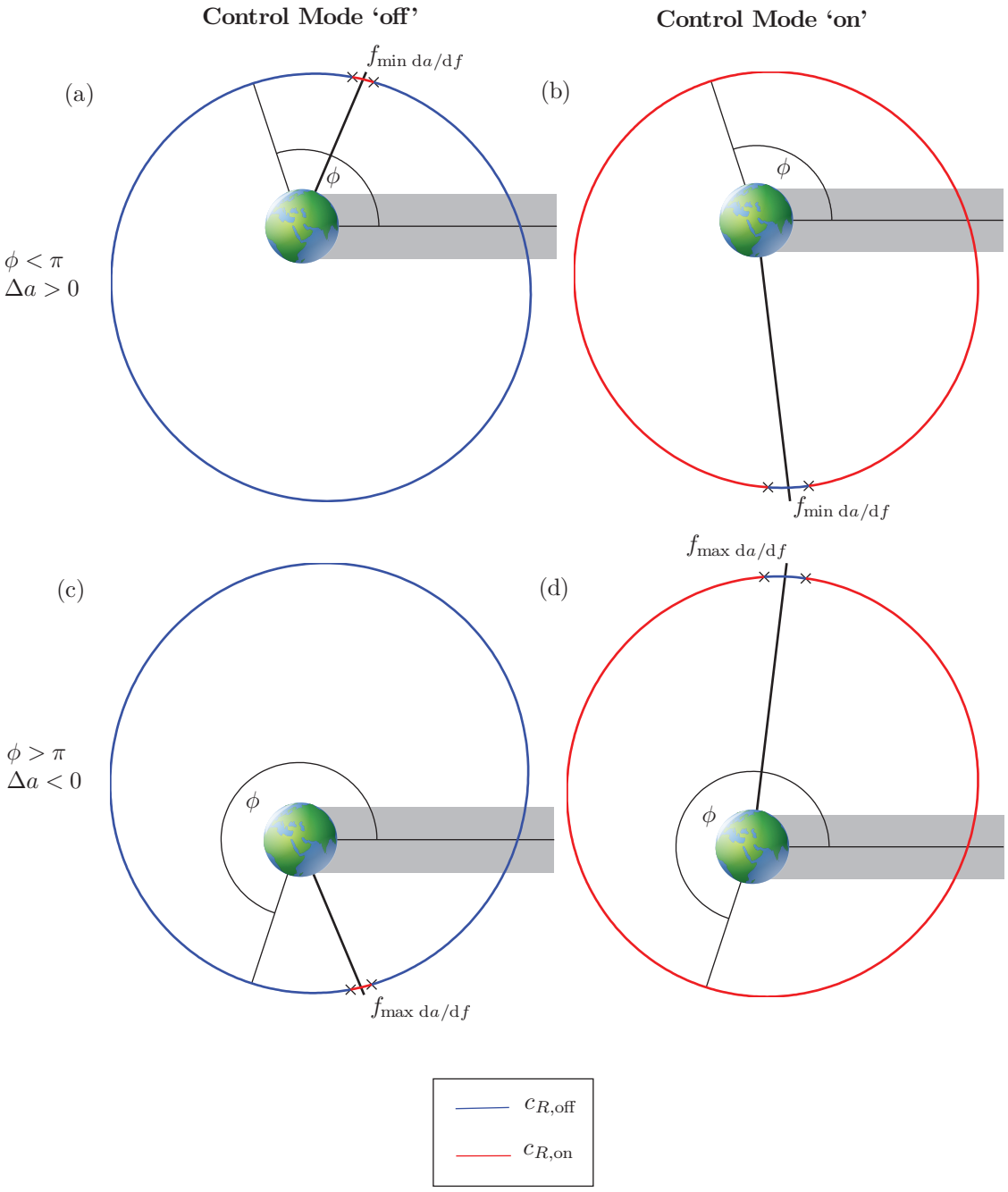

Figure 7.12: Switching law in control mode 'off' and 'on' for two example orbits. The arc of the orbit with $c_{R,\text{off}}$ is drawn in blue and $c_{R,\text{on}}$ in red. The positions at which the reflectivity is switched are marked with crosses. Figures (a) and (b) show the control strategy when the change in semi-major axis over one orbit would be positive and (c) and (d) show the control strategy when the change in semi-major axis would be negative. The left column of figures shows the control strategy with mainly reflectivity $c_{R,\text{off}}$ and the right column shows the control strategy with mainly reflectivity $c_{R,\text{on}}$.

The control algorithm uses the linearised phase space model. It is assumed that the spacecraft receive accurate information about their current eccentricity and ϕ once every orbit and then decide on the control mode using the algorithm detailed in this chapter. This way it can be shown that the control method is also robust towards perturbations which have not been taken into account in the control algorithm such as eclipses, the J_2 effect and out-of plane dynamics.

The control algorithm accomplished the objective to assemble all six spacecraft at the desired eccentricity and orbit orientation. This is achieved in less than 1.3 years. However, the SpaceChips which do not use the constant semi-major axis control ended up at different semi-major axes of between 41 000 km and 43 000 km. This can be avoided using the computationally more expensive (i.e., the reflectivity coefficient is changed twice per orbit) constant semi-major axis control. The evolution in the phase space in the latter case is shown in Fig. 7.13. The evolution of all orbital parameters over the course of the manœuvre is shown in Fig. 7.14. In this case the semi-major axis only varies on the order of 100 km. The cause for this small variation is the change in inclination which changes the actual eclipse angles from the ones calculated analytically in the plane within the control loop. For the eclipse calculation in the control algorithm an analytical solution found by Colombo and McInnes [103] was used, as it is the least computationally expensive. Figure 7.15 visualises the evolution of the orbits during the manœuvre.

7.2.5 Manœuvre time

Figure 7.16 shows the time until the completion of a manœuvre using the linearised phase space control algorithm without controlling the semi-major axis starting from different points in the phase space. The hatched areas indicate the position from which a manœuvre is impossible because impact with the Earth is inevitable ($e < e_{crit}$). The stable eccentricity can be reached from any position within three years.

7.3 Conclusions

In this chapter a deeper understanding of the orbital dynamics of high area-to-mass-ratio spacecraft gained through the study of the Hamiltonian dynamics was used to design an alternative control algorithm to the potential controller discussed in Chap. 6. The Hamiltonian dynamics were first applied to an alternative stabilisation algorithm. This algorithm has the advantage of being a very simple bang-bang switch law only dependent on the orientation of the orbit with respect to the

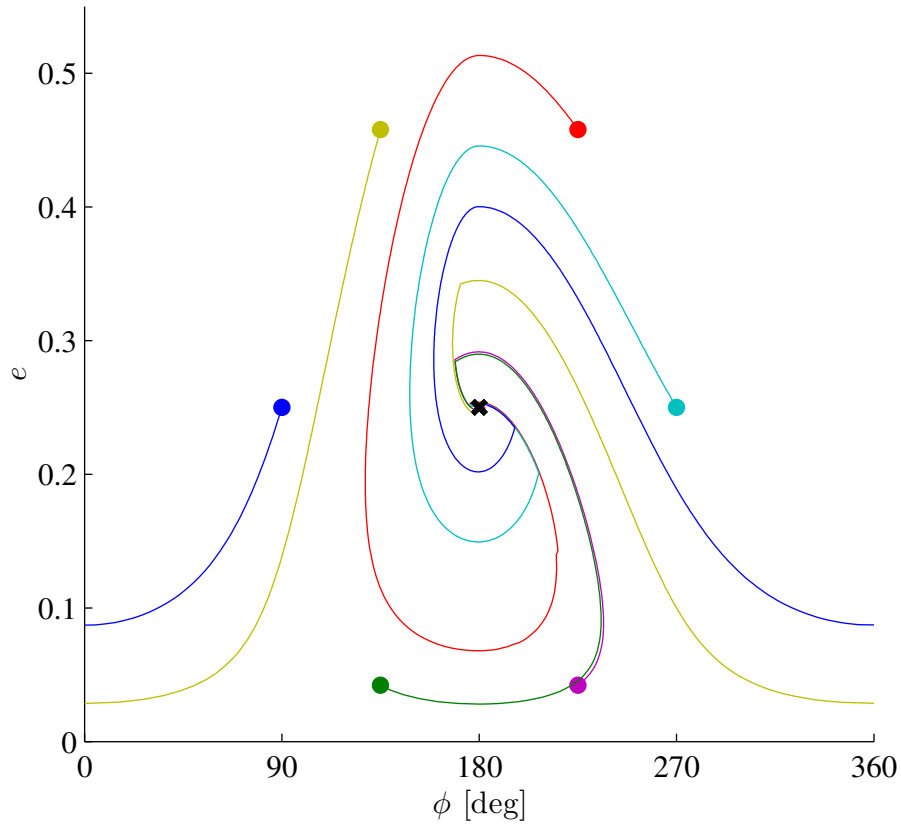

Figure 7.13: Manœuvres of six SpaceChips with area-to-mass-ratio $15\,\mathrm{m}^2\,\mathrm{kg}^{-1}$ toward the same orbit in the phase space using the control algorithm described in Sec. 7.2.3: the different line colours indicate the four different spacecraft and are consistent with the colours used in Figs. 7.14 and 7.15.

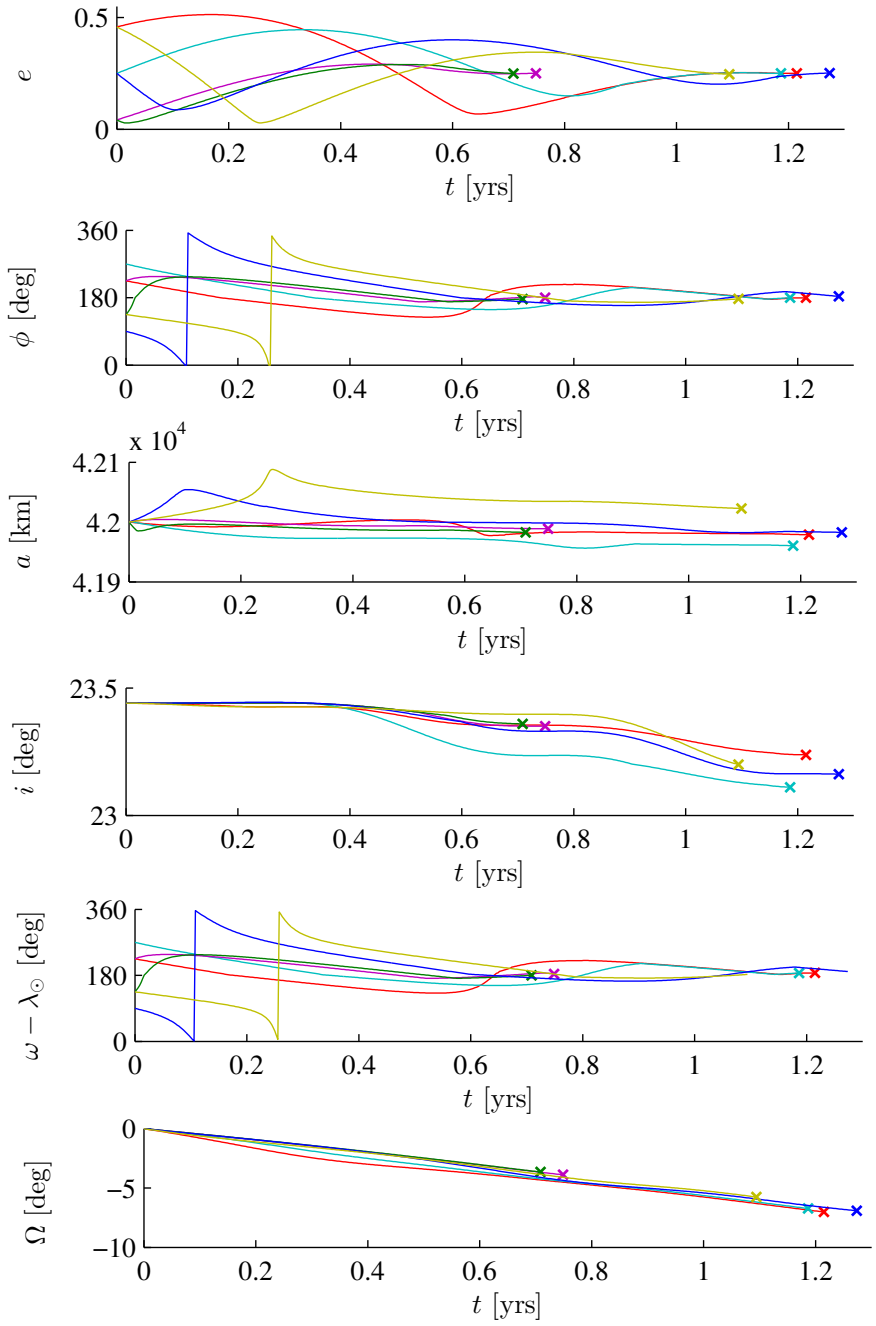

Figure 7.14: Evolution of orbital parameters during the manœuvres of six SpaceChips with area-to-mass-ratio $15\,\mathrm{m^2\,kg^{-1}}$ toward the same orbit in the phase space using the linearised control algorithm

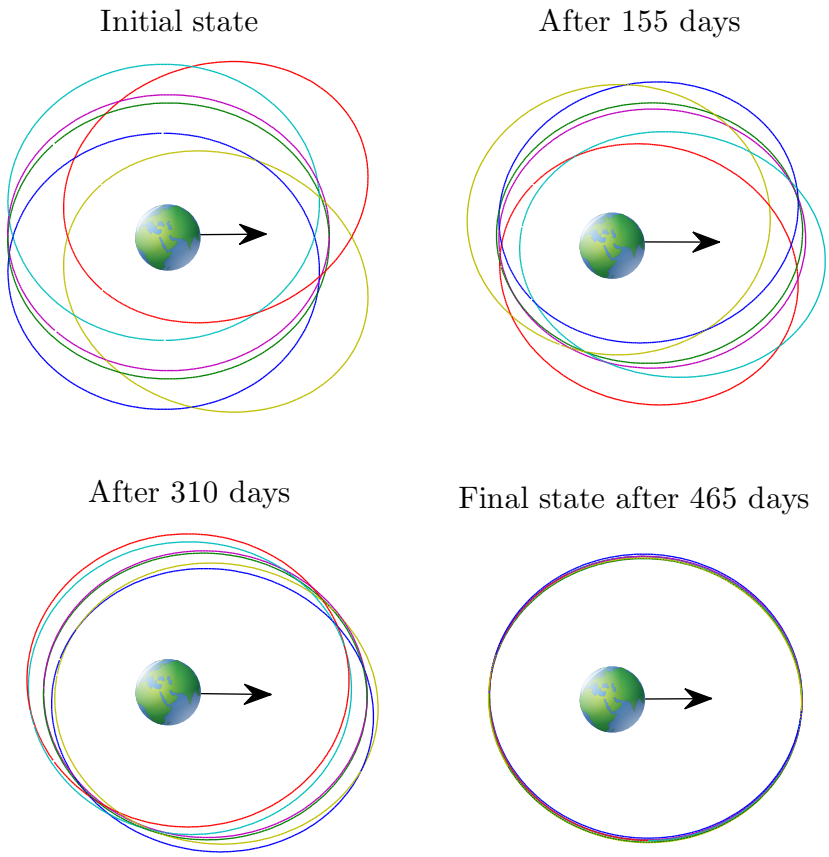

Figure 7.15: Evolution of the orbits of the six spacecraft during the manœuvre as a projection onto the ecliptic plane in a Sun-following reference frame. The arrow indicates the direction of the solar radiation: : the different line colours indicate the four different spacecraft and are consistent with the colours used in Figs. 7.13 and 7.14.

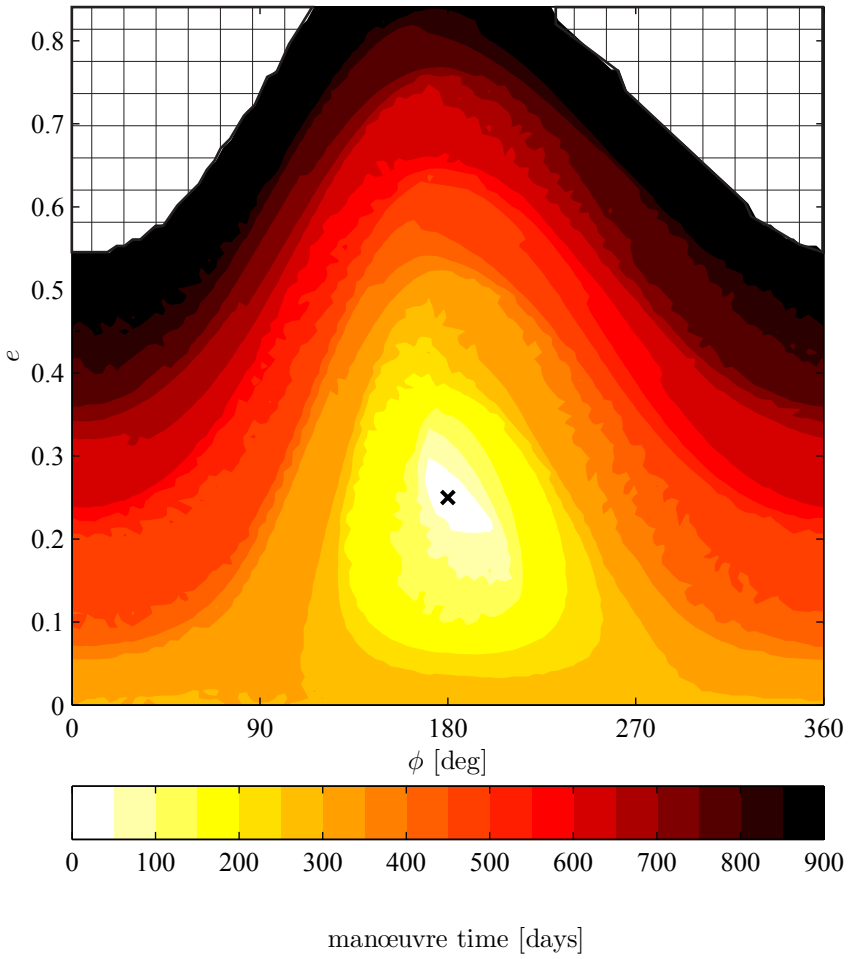

Figure 7.16: Time until reaching goal orbit marked with **x** from different positions in the phase space ($a = 42\,000\,\mathrm{km}$) using the linearised phase space control for a SpaceChips with area-to-mass-ratio $15\,\mathrm{m^2\,kg^{-1}}$.

Sun. However, the range of orbits which can be stabilised is smaller than for the artificial potential field controller.

Two models of a Hamiltonian-based electrochromic (e, ϕ) translation control strategy were also proposed, one based on linearised phase space dynamics, while the other also takes into account the effect of eclipses. The first control algorithm is purely analytical and requires a change in reflectivity approximately twice per year. The latter control algorithm requires the spacecraft to switch reflectivity twice per orbit and uses a numerical search of the control parameter in a one-dimensional search space. Both control algorithms were tested in a simulated scenario in which a group of SpaceChips with different initial orbits are gathered into the same goal orbit. All SpaceChips reached the desired position within a reasonable time. In the simulation, the SpaceChips are propagated using Gauss' equations in three dimensions with a differential equation solver considering solar radiation pressure and the Earth's oblateness. The scenario results showed that the control algorithm can cope with other minor perturbing effects at high semi-major axis. The Hamiltonian control algorithm is better suited to (e, ϕ) translations than the artificial potential field controller as it has a shorter manoeuvre time and works reliably from almost all points in the phase space.

The two methods for electrochromic orbit control presented in this thesis are fundamentally different. While the artificial potential field controller discussed in chapter 6 requires no prior knowledge about the underlying dynamics, it is more computationally expensive and less time efficient that the Hamiltonian controller introduced in this chapter. The two methods were compared using the same test cases.

PART III

Micrometre-scale:

Orbital Dust for Geo-engineering

Chapter 8

Asteroid Dust in Heliotropic Orbits for Climate Engineering

In this final part of this thesis a novel problem of orbital dynamics on the micrometre-scale is investigated. The smaller the length-scale, the more futuristic the applications discussed in this thesis. While an orbit control device making use of solar radiation pressure (chapters 3 to 5) may be developed within this decade, SpaceChips with electrochromic orbit control (chapters 6 and 7) lie further from our grasp. The application discussed in this part shall be even further in the future. A truly 'visionary space system' as the project under which this PhD was conducted is titled. This chapter discusses the use of dust, mined from a captured asteroid, to offset terrestrial climate change by reducing the inbound solar radiation.

The use of asteroid dust for geoengineering has been proposed previously as discussed in Sec. 1.4. The dust can be extracted from a captured asteroid or obtained from the Moon, which has a lower gravity well than the Earth. Previous proposals have suggested placing a dust cloud at the Sun-Earth L_1 point [80], the Earth-Moon $L_{4,5}$ points [77] or in an Earth orbit [76]. The last option has the advantage of providing constant shade and being potentially long-term stable. However, in the proposal by Pearson et al. [76] the effect of solar radiation pressure on the dust ring stability was not considered. Furthermore, a deployment strategy was not elaborated on. In this chapter the concept of an a dust ring around the Earth for climate engineering is investigated from an orbital dynamics perspective and a novel scheme for maintenance and deployment is developed using *heliotropic* orbits.

8.1 In-plane orbital evolution of dust

For a certain range of semi-major axis and area-to-mass-ratios, the Hamiltonian in Eq. (2.9) allows, among all its stationary points, a stable equilibrium (i.e., $\frac{\mathrm{d}e}{\mathrm{d}\lambda_\odot} = 0$ and $\frac{\mathrm{d}\phi}{\mathrm{d}\lambda_\odot} = 0$), at $\phi = 0$ with eccentricity e_0 as shown in Sec. 1.1. This equilibrium point represents frozen orbits with their apogee pointing in the direction of the Sun. These orbits are therefore termed *heliotropic* orbits. If the solar radiation pressure parameter is zero, $\alpha = 0$ (i.e. without the effect of SRP), the equilibrium at e_{0,J_2} corresponds to an orbit with a frozen orientation with respect to the Sun solely due to the J_2 effect. Such an orbit would have its apse-line precessing at the same rate as the Earth's motion around the Sun. While the SRP parameter is zero, the equilibrium exists for any orbit orientation. However, as soon as the SRP parameter is non-zero the equilibrium can only be found for Sun-pointing apogees. For increasing values of the SRP parameter, the equilibrium eccentricity e_0 increases, with the J_2-only equilibrium eccentricity e_{0,J_2} (i.e., $\alpha = 0$) being the minimum boundary value at a given semi-major axis.

Figure 8.1 shows e_0 as a function of semi-major axis for different dust grain radii. This corresponds to Fig. 2.4 in Sec. 2.1.1, showing equilibria in the phase space. It also shows e_{0,J_2}, the minimum possible equilibrium eccentricity. The background shading indicates perigee altitude. Dark grey marks orbits with $h_p \leq 0\,\mathrm{km}$ and light grey marks orbit with $h_p \leq 2000\,\mathrm{km}$. An altitude of 2000 km is approximately the altitude below which the effect of drag on the orbital evolution is not negligible [96]. A ring of dust at or beyond this distance from the Earth will remain in place indefinitely regardless of the sizes of dust grains, as long as other perturbations do not cause the perigee altitude to decrease.

It can be seen from the Fig. 8.1 that *heliotropic* orbits do not exist for any grain size above approximately 16 000 km semi-major axis. Above c. 13 500 km semi-major axis they become unstable due to drag. It can also be seen that $e_{0,J_2} = 0$ for $a \leq 12\,300\,\mathrm{km}$. This means that for these semi-major axes the *heliotropic* orbit does not exist without the effect of solar radiation pressure.

From the required e_0 with solar radiation pressure it can be seen that the equilibrium eccentricity increases with decreasing grain size. For $r_g = 5\,\mu\mathrm{m}$ there exists no semi-major axis at which the perigee altitude of the equilibrium is above 2000 km. This means that dust grains of this size or smaller will always decay due to drag, regardless of their initial orbit.

In the following section this phenomenon is investigated further and the minimum stable dust grain size as a function of semi-major axis is determined. This is important as smaller dust grains offer a higher mass efficiency for climate engineering as their cross-sectional area is larger in relation to their mass.

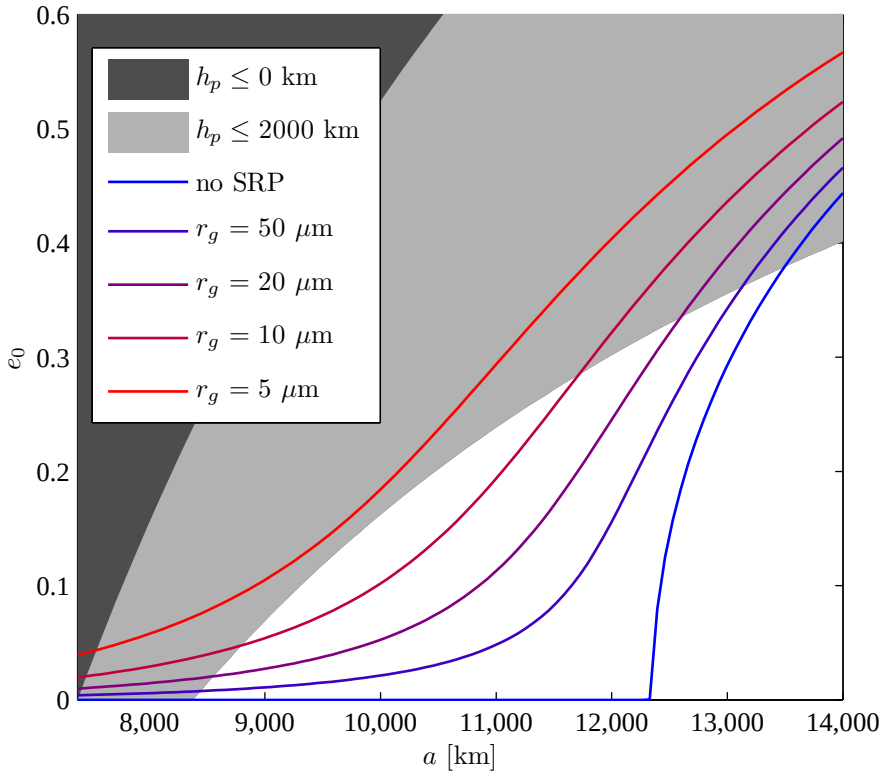

Figure 8.1: Eccentricity of the *heliotropic* equilibrium orbit as a function of semi-major axis without SRP and with SRP for different grain sizes – the background shading indicates the perigee altitude

8.1.1 Circular versus eccentric release orbit

If a grain with a specific area-to-mass ratio is released in any orbit, its orbit will then evolve by librating or rotating around its equilibrium eccentricity (see Sec. 1.1). The greater the initial distance from the libration point in the phase space the larger the maximum eccentricity reachable. Therefore, it is more efficient to release the dust grains (with different area-to-mass-ratios) at a higher initial eccentricity to prevent them from deorbiting due to drag (see Chapters 4 and 5).

Figure 8.2 compares the orbital evolution of grains with different radii when they are released in a circular and elliptical orbit with the same semi-major axis. A grey colour marks the area in which the orbits will experience drag, and grains which pass through this area are considered as "lost". It can be seen that while for an initially circular orbit all grains with a radius smaller than 13 µm will be lost (see Fig. 8.2a), in the elliptical case grains as small as 6.5 µm survive (see Fig. 8.2b). It follows that release at the critical eccentricity yields the best results and that the smallest possible grain radius at any semi-major axis is the one which has its equilibrium point at the critical eccentricity.

8.2 Geoengineering scenario

In this section the general scenario of the proposed scheme is explained and a suitable semi-major axis for the ring chosen.

8.2.1 Baseline concept

Previous space-based geoengineering (SBGE) concepts have suggested the use of dust sourced from the Earth, Moon, asteroids and comets [80, 76, 77]. It has been shown that the amount of asteroid material that can be captured into a weakly bound Earth orbit with a threshold velocity lower than that of lunar escape velocity, $2.37\,\mathrm{km\,s^{-1}}$, is $6 \times 10^{13}\,\mathrm{kg}$ [122]. For the material required in this SBGE scenario an extra velocity increment of $2.7\,\mathrm{km\,s^{-1}}$ would be required to lower the orbit to the position of the feeder orbit, therefore doubling the velocity requirement.

Despite the additional costs of transporting asteroid material to a medium Earth orbit, the use of captured asteroid resources would still be more efficient than lifting material from the surface of the Earth. This also applies for schemes that require solid reflectors to block solar radiation where large devices must be manufactured and then launched into the correct position. Lifting such large

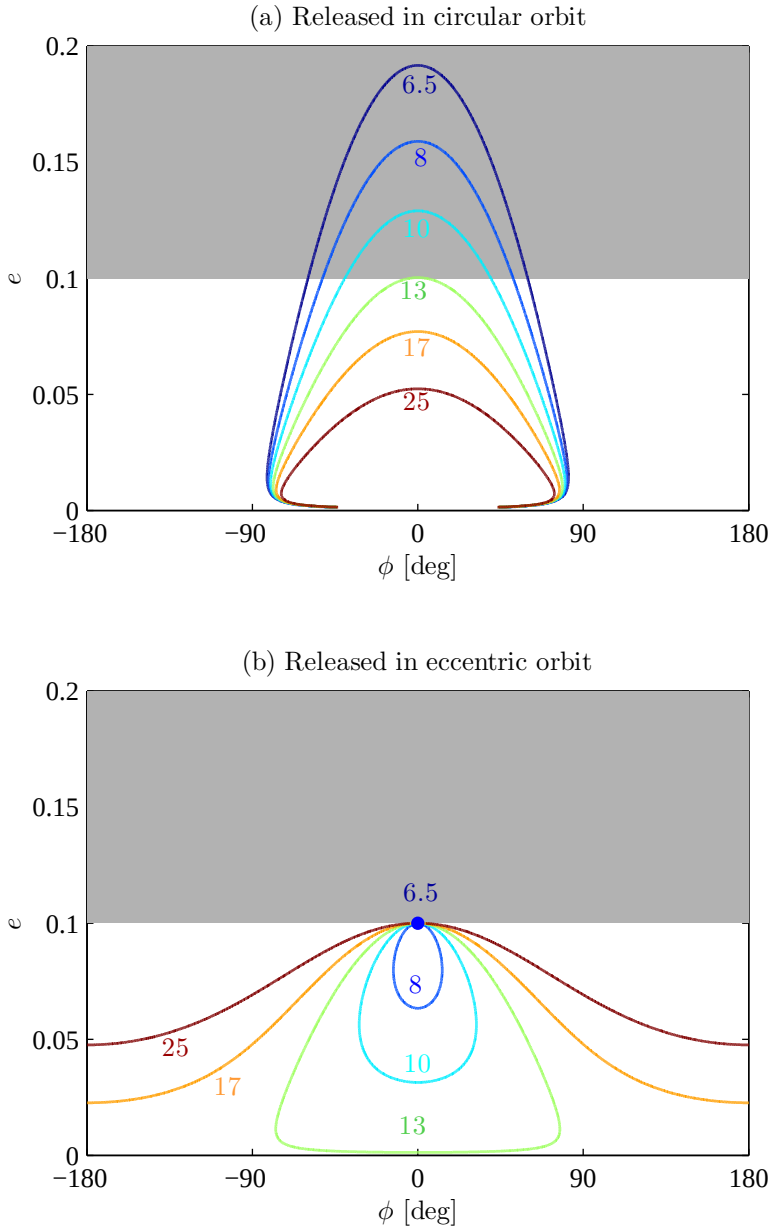

Figure 8.2: Evolution due to SRP and J_2 of the orbits of dust grains of different grain radii in the (e, ϕ)-phase space with (a) release in a circular orbit and (b) release in an eccentric orbit with Sun-facing apogee. The semi-major axis is 9300 km and the shaded area represents the orbits with a perigee lower the 2000 km.

masses (of the order of 1×10^{10} kg) is beyond current launch capabilities. Using asteroid material rather than lunar dust has the added benefit that the material can be sourced and ground to finer grain sizes, if required, whilst in the feeder orbit before being released, thus removing the requirement to transport material from the Moon.

The asteroid is envisaged to be captured into a circular, equatorial generator orbit with semi-major axis a_G (see Fig. 8.3). Since the area-to-mass ratio of an asteroid is clearly small, the effect of solar radiation pressure is negligible. The generator orbit is thus assumed to be unperturbed. In order to continually release dust in a Sun-pointing elliptical feeder orbit, the dust must be ejected into this orbit with a specific Δv from an initially circular orbit with an altitude of either the feeder orbit's perigee or apogee altitude. The apogee is chosen for two reasons: It allows the manœuvre to always be performed in Sunlight thus guaranteeing power generation during the ejection. It also means that the asteroid which is used as the source of the dust can be kept further away from the Earth. It follows that a_G is also the radius of the apogee for the feeder orbit with semi-major axis a_F and perigee at $R_E + 2000$ km to avoid decay due to drag.

The dust grains will be continuously extracted from the asteroid, milled to achieve a certain radii distribution and collected during one orbit. Whenever the generator passes the apogee of the feeder orbit, i.e. when $\theta = \pi$, it ejects the collected dust with the correct Δv to inject it into the feeder orbit using a mass driver [81]. From this feeder orbit the grains will then evolve and spread due to their different area-to-mass ratios and thus form the dust ring. Because the period of the generator orbit and the feeder orbit are different, grains will be distributed at all positions in the orbit. After approximately one year all positions on the libration curves in the phase space will be filled as this is the period of one evolution in the phase space. Figure 8.3 shows a scale illustration of the concept.

In the following subsections the choice of altitude for the feeder orbit is justified. For this a trade-off is made between the minimum stable grain size and the geometric efficiency of the orbit.

8.2.2 Minimum grain size

The smallest possible grain radius can be determined as a function of semi-major axis by finding the particle radius for which the equilibrium eccentricity e_0 is equal to e_p, the eccentricity corresponding to the smallest allowable perigee height h_p:

$$e_p(a) = 1 - \frac{R_E + h_p}{a} \tag{8.1}$$

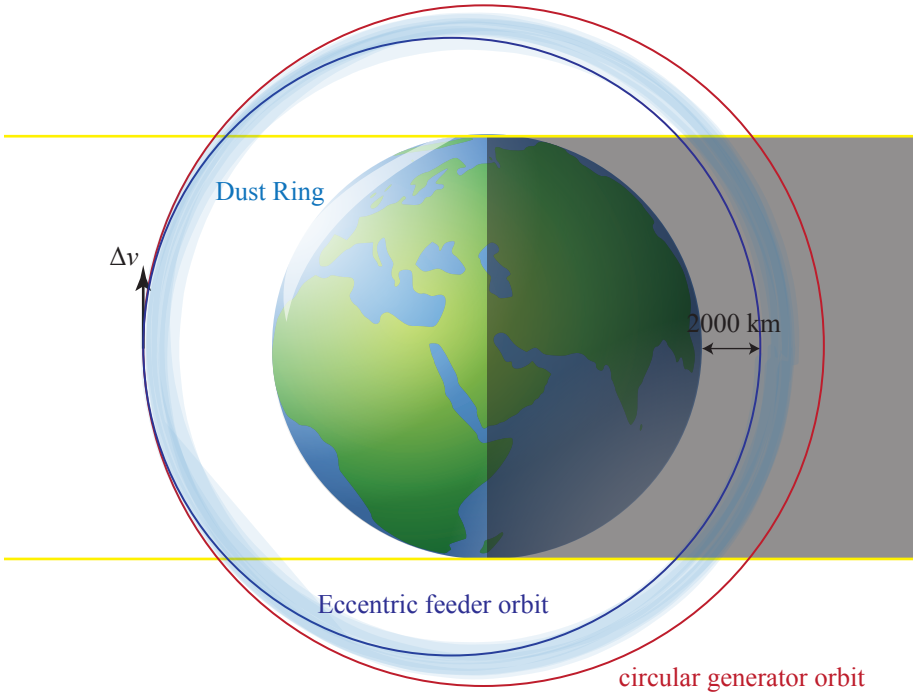

Figure 8.3: Ring generation baseline concept: The asteroid is "parked" in a circular equatorial generator orbit. Mined dust is expelled with a given Δv each time the asteroid is exactly between the Earth and the Sun. From this feeder orbit the dust ring evolves naturally until a steady state is reached.

To find the minimum particle radius which for a given semi-major axis can be inserted in an orbit such that its perigee altitude will never dip below a given r_p, Eq. 2.3 is used which describes the secular variation of the Sun-perigee-angle over time:

$$\frac{\mathrm{d}\phi}{\mathrm{d}\lambda_\odot} = -\alpha\frac{\sqrt{1-e^2}}{e}\cos\phi + \frac{\kappa}{(1-e^2)^2} - 1$$

An orbit orientation of $\phi = 0$ is inserted to obtain only orbits with an apogee pointing in the direction of the Sun. Eq. (2.3)is then set equal to zero to find the orbit which is fixed in this orientation, as from Equation 2.2 it is already known that for $\phi = 0$ the change in eccentricity is zero. Finally e is substituted with e_p in Eq. 8.1, solved for α and combined with Eqs. 2.4 and 2.6 to obtain:

$$r_{\min(a)} = \frac{2F_\odot}{cn_\odot\delta_g}\sqrt{\frac{a}{\mu}}\frac{(\sqrt{1-e_p(a)^2})^{\frac{5}{2}}}{e_p(a)(\kappa(a)-(1-e_p(a)^2)^2} \tag{8.2}$$

where δ_g is the density of the asteroid grains. In this chapter $\delta_g = 3500\,\mathrm{kg\,m^{-3}}$ is used as in the study by Wilck and Mann [123]. This expression is later used for a trade-off to find the most appropriate semi-major axis for the dust ring. The other trade-off parameter is the geometrical efficiency which shall be discussed in the following subsection.

8.2.3 Geometrical efficiency

Another measure of the efficiency of a ring for geoengineering is how much of its orbital period a grain spends blocking solar radiation. This is dependent on the orbit geometry and takes into account that the velocity at which the grain travels, v_g, is lower at apogee than at perigee. Figure 8.4 shows the useful region of an orbit for geoengineering.

The ratio of the time a grain spends in the useful part of the orbit over the total orbital period is termed geometrical efficiency. To determine it, first the entry and exit angles into the useful zone $f_{u,1}$ and $f_{u,2}$ need to be calculated. For an orbit with Sun-pointing apogee the angles can be found geometrically from the relation of radial distance from the centre of the Earth r and the radius of the Earth R_E:

$$\frac{R_E}{r} = \sin f_u \tag{8.3}$$

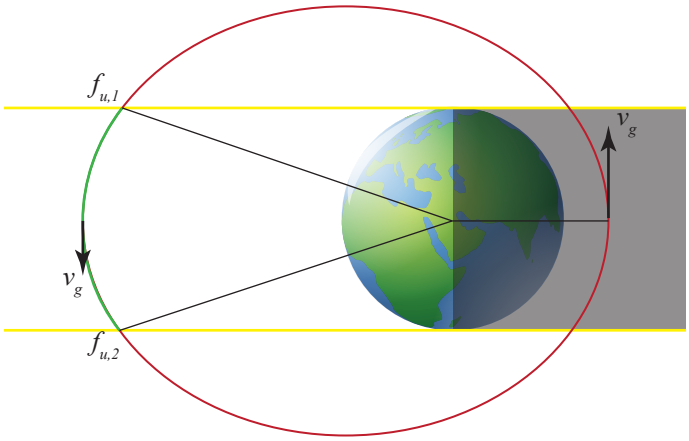

Figure 8.4: Useful region (green) of an orbit for geoengineering – the geometrical efficiency is the proportion of one orbit a grain spends in the useful region

Together with the expression for the radial distance:

$$r = \frac{a(1-e^2)}{1+e\cos f_u} \tag{8.4}$$

the following expression for the angle can be derived:

$$\cos f_u = -\frac{eR_E^2 + a(1-e^2)\sqrt{a^2(1-e^2)^2 - R_E^2(1-e^2)}}{a^2(1-e^2)^2 + e^2R_E^2} \tag{8.5}$$

with $f_{u,1} < \pi$ and $f_{u,2} > \pi$. This is the same equation used to compute the eclipse angles in Sec. 2.2.1. The true anomaly can then be transformed into mean anomaly, M, from which the geometric efficiency ε_G, the proportion of time spent between the two angles, can easily be calculated:

$$\varepsilon_G = \frac{M_{u,2} - M_{u,1}}{2\pi} \tag{8.6}$$

with

$$M = E - e\sin E \tag{8.7}$$

and

$$E = 2\arctan\sqrt{\frac{1-e}{1+e}}\tan\frac{f}{2} \tag{8.8}$$

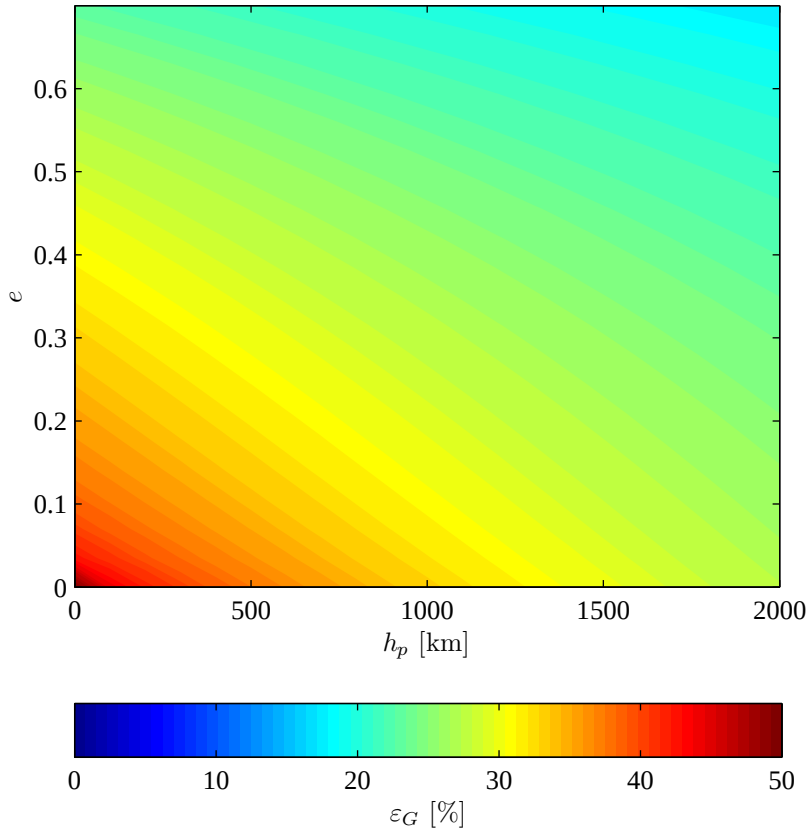

Figure 8.5: Geometric efficiency as a function of eccentricity and perigee altitude

Figure 8.5 shows the geometric efficiency of orbits with Sun-pointing apogee as a function of perigee altitude h_p and eccentricity e. It can be seen that small circular orbits are the most efficient with decreasing efficiency for higher eccentricity and perigee altitudes. For a fixed semi-major axis the efficiency would increase with eccentricity. However, it is not the semi-major-axis but the perigee altitude which limits the lifetime of a dust grain orbit. Therefore, smaller eccentricities are preferable.

8.2.4 Selection of semi-major axis

Using the minimum grain size and the geometric efficiency as the two figures of merit, a trade-off can be performed to choose the semi-major axis likely to be most efficient for geoengineering. Figure 8.6 shows the dust grain minimum radius and the geometrical efficiency of a circular orbit and an orbit with $e = e_p$ with $h_p = 2000\,\mathrm{km}$ as a function of semi-major axis. These two orbits were chosen as they describe the maximum and minimum eccentricity of the future dust ring because the grains shall be released with a distribution of radii and not all of them have an equilibrium

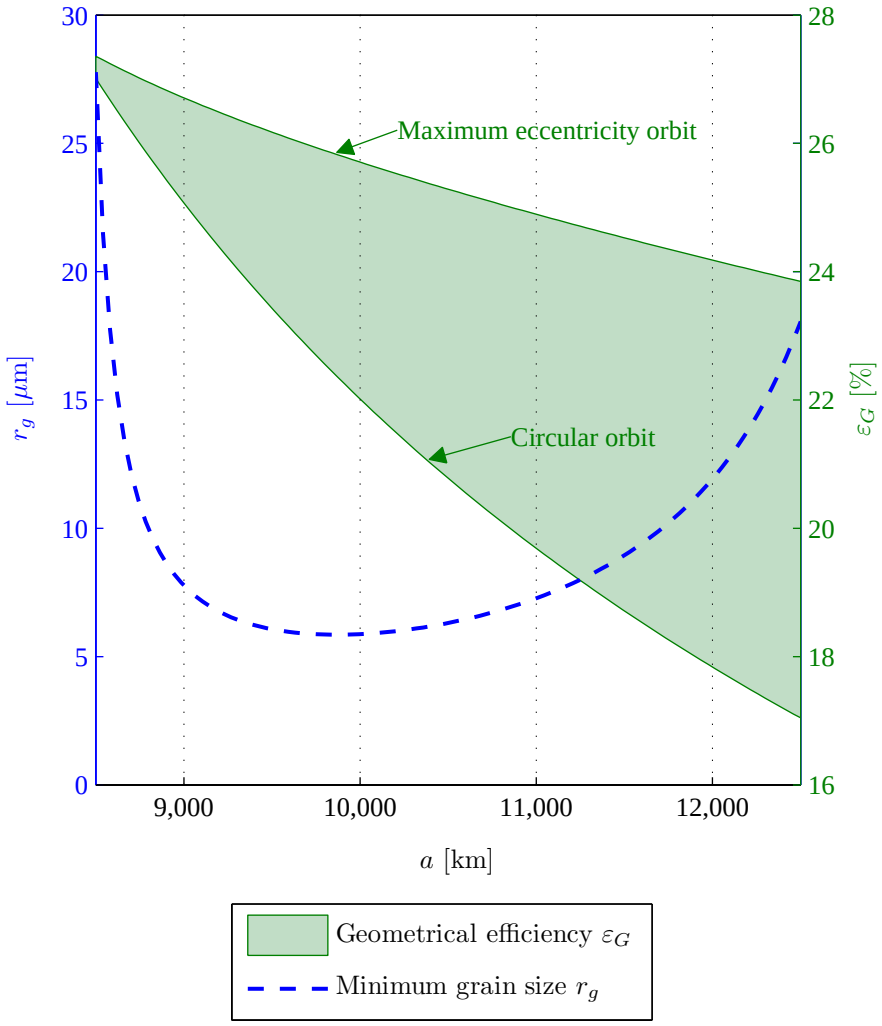

Figure 8.6: Minimum grain radius and geometric efficiency of circular and maximum stable eccentricity e_p orbits over semi-major axis

condition at the critical eccentricity. Thus, some grains will librate in eccentricity between $e \geq 0$ and $e = e_0$. A good compromise between low minimum grain size and high geometrical efficiency is desired. Considering the results in Figure 8.6, it can be seen that above a semi-major axis of order 9800 km the total efficiency goes down because the minimum grain size increases while the geometrical efficiency decreases. Below that value the minimum grain size is close to the absolute minimum before rising sharply for semi-major axes below 8000 km. From this graph a qualitative choice of semi-major axis of 9300 km is made with $e_p = 0.1$. This orbit is referred thereafter as the feeder orbit. It has a Sun-pointing apogee with a radius of approximately 10 250 km. The feeder semi-major axis is not further optimised as this chapter aims to assess the order of magnitude of mass required for geoengineering using a dust ring and the feasibility of the method proposed.

Table 8.1: Dust distributions

Distribution	μ_g	σ_g
D1	-11.5	0.1
D2	-11.35	0.15
D3	-11.2	0.25

8.3 Ring Model

In this section an attenuation model of the ring resulting from the scenario derived in Sec. 8.2 is obtained. For this the distribution of the grain sizes after milling and their dispersion along the ring are combined to derive an attenuation map.

8.3.1 Dust grain size distributions

As discussed in Bewick et al. [75], the milled dust is assumed to be distributed log-normally in grain radius r:

$$f_{\mu_g,\sigma_g}(r) = \frac{1}{r\sigma_g\sqrt{2\pi}} e^{-\frac{(\ln r-\mu_g)^2}{2{\sigma_g}^2}} \tag{8.9}$$

where μ_g is the natural logarithm of the mean grain size and σ_g the natural logarithm of the standard deviation of the distribution.

Three possible distributions have been chosen. D1 is an optimistic estimate with small mean and low standard deviation. D2 is a realistic distribution and achievable with existing terrestrial particle size reduction machinery [124]. D3 is a pessimistic estimate with high mean and large standard deviation. Table 8.1 shows the chosen values for mean and standard deviation and Fig. 8.7 shows the three distributions as probability density functions.

The probability of any grain having a radius within the interval $[r_{g,1}, r_{g,2}]$ can be found with the cumulative probability density function:

$$P\left(r_g \in [r_{g,1}, r_{g,2}]\right) = F_{\mu_g,\sigma_g}(r_{g,1}) - F_{\mu_g,\sigma_g}(r_{g,2}) \tag{8.10}$$

with

$$F_{\mu_g,\sigma_g}(r_g) = \frac{1}{\sqrt{2\pi}} e^{-\frac{(\ln r_g-\mu_g)^2}{2{\sigma_g}^2}} \tag{8.11}$$

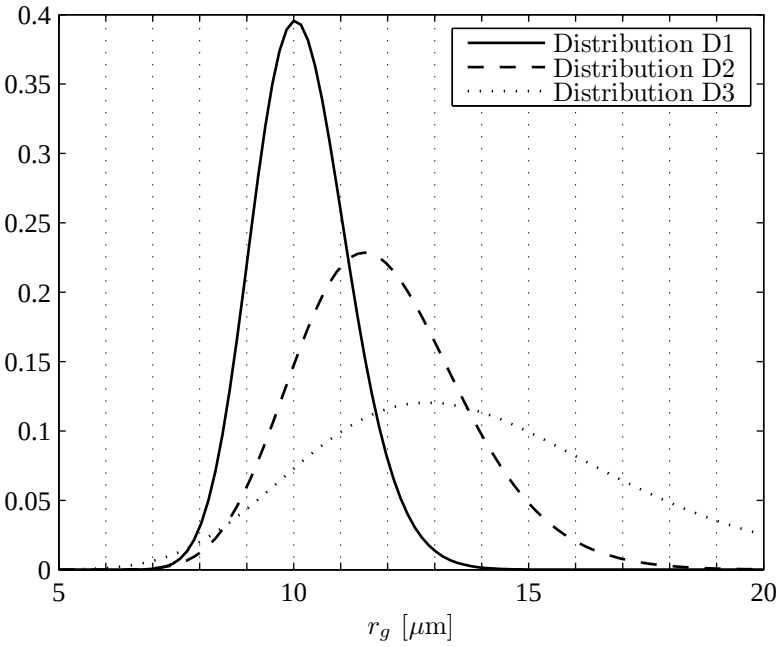

Figure 8.7: Probability density function of three different grain size distributions

8.3.2 Solar attenuation due to dust

In order to offset the effects of global warming caused by the current concentration of CO_2 in the atmosphere an average insolation reduction of 1.7 % is necessary [125]. To derive the mass of dust required to achieve this, the Beer-Lambert law is applied [126, Chap. 4]:

$$I = I_0 e^{-\Lambda l} \tag{8.12}$$

where I_0 is the solar constant before passing through the ring, Λ is the attenuation coefficient and l is the path length. The attenuation coefficient at any given point is calculated from:

$$\Lambda = \int_{r_{g,1}}^{r_{g,2}} \pi {r_g}^2 \rho(r_g) \mathrm{d}r_g \tag{8.13}$$

where $\rho(r_g)$ is the number density of grains as a function of grain radius r_g. Since the attenuation coefficient is likely to change through the ring, it must be integrated over the path length and hence Eq. (8.13) becomes

$$I = I_0 e^{-\int_0^l \Lambda(l) dl} \tag{8.14}$$

To determine the attenuation coefficient for the different distributions a phase space density model must to be built. To achieve this, a two dimensional model of the ring will be constructed, using the in-plane dynamics discussed before. The attenuation coefficient is then calculated for this in-plane evolution of the dust. Then, the orbital plane is tilted with respect to the ecliptic plane and the inclination change added. Thus, a third dimension is added by approximating the out-of-plane evolution with a change of plane.

8.3.3 In-plane model

In this subsection a density model of the ring is derived. To achieve this, firstly two different phase space densities as a function of eccentricity e and Sun-perigee-angle ϕ need to be found. The grain size density expresses the likelihood of any grain passing through a point in the phase space during its orbit evolution. The specific phase space density is then an expression of the probability that a grain is at a given point in its orbital evolution at any given time.

Grain Size Phase Space Density

An expression is needed to find the radius of a grain passing through any point (ϕ, e) in the phase space. This can be derived by setting the Hamiltonian Eq. (2.9) with (ϕ, e) equal to the Hamiltonian of the feeder orbit with $(0, e_F)$ and solving for α:

$$\alpha(e,\phi) = \frac{e_F - e\cos\phi}{3\left(\sqrt{1-{e_F}^2} - \sqrt{1-e^2}\right) + \kappa\left(\frac{1}{(1-{e_F}^2)^{\frac{3}{2}}} - \frac{1}{(1-e^2)^{\frac{3}{2}}}\right)} \tag{8.15}$$

The solar radiation pressure parameter α is a function of the acceleration due to SRP, a_{SRP}, as expressed in Eq. (2.6). This acceleration is inversely proportional to the grain radius r_g and can be expressed as follows for circular dust grains:

$$a_{\mathrm{SRP}} = \frac{F_\odot}{c}\frac{4}{3\rho_g r_g} \tag{8.16}$$

where ρ_g is the material density of the dust grain approximated as $3500\,\mathrm{kg\,m^{-3}}$. It is important to note the difference between the material density ρ_g and the density of dust grains in the ring ρ. With Eqs. (2.6) and (8.16), Eq. (8.15) can be rewritten as:

$$r_g(\phi,e) = \frac{\frac{6F_\odot}{cn_\odot\delta}\sqrt{\frac{a}{\mu}}(e_F - e\cos\phi)}{3\left(\sqrt{1-{e_F}^2} - \sqrt{1-e^2}\right) + \kappa\left(\frac{1}{(1-{e_F}^2)^{\frac{3}{2}}} - \frac{1}{(1-e^2)^{\frac{3}{2}}}\right)} \tag{8.17}$$

The probability of finding any grain in a differential element around a given (ϕ, e) in the phase space can then be determined. This is achieved by finding the range of grain radii which pass through the differential element using Eq. (8.17). This results in a middle value $r_{g,0}$ and a differential corresponding to the phase space element of $\pm \mathrm{d}r_g$ The probability of any grain having the calculated differential radius can be found with the cumulative probability density function in Eq. (8.10):

$$P\left(r_g \in [r_{g,0} - \mathrm{d}r_g, r_{g,0} + \mathrm{d}r_g]\right) = F_{\mu,\sigma}(r_{g,0} + \mathrm{d}r_g) - F_{\mu,\sigma}(r_{g,0} - \mathrm{d}r_g) \tag{8.18}$$

This expression gives the fraction of all grains whose evolution passes through the considered differential phase space element.

Specific phase space density

Next the specific phase space density at the differential phase space element is calculated. This is the fraction of grains passing through the differential box in the phase space. Combining the orbital evolution density at the location in the phase space with the grain size density derived in Sec. 8.3.3 will later deliver the total fraction of grains in this element of the phase space.

The orbital evolution density is found numerically by first calculating the libration period, in the phase space, with a grain of a given size. This is then compared with the time derivative of the orbital parameters in the phase space at the given position calculated using Eqs. (2.2) and (2.3). The time a grain spends in the differencial box in the phase space can be calculated from the velocity in the phase space at the given point and the size of the differential box. This is then divided by the total phase space libration period to obtain the likelihood of a grain of the given size being in the required orbit at any time during its orbital evolution. This information is necessary to calculate the global phase space density.

In-plane number density

The grain size density and specific phase space density can now be multiplied to find the global phase space density. This figure does not depend on the total number of grains in the ring. Instead it is normalised over the full grain population.

Figure 8.8 shows the resulting global phase space density for the three distributions of grain radii introduced in the previous section. It is shown relative to the average number density in the phase space. As expected the highest density can be found in the release position, the feeder orbit,

at $(0, e_F)$. The narrowest distribution, D1, shows high density in higher eccentricity orbits with the apogee facing within 45° of the Sun. The wider the grain size distribution the more dispersed the dust cloud is in the phase space. It can be assumed that the narrowest distribution has the highest proportion of grains blocking sunlight. To ascertain this assumption the dust density around the Earth in polar coordinates is calculated next.

The polar coordinate system chosen is a rotational reference frame with fixed orientation towards the Sun. Any position in the orbital plane is determined by R, the distance to the centre of the Earth, and θ, the angle with respect to the direction of solar radiation as shown in Figure 8.9.

Figure 8.10 shows the deviation of accumulated in-plane number density from the orbit average as a function of θ for the three different initial distributions. The values are accumulated over radius R for each angle θ to visualise the advantage a *heliotropic* ring has over a circular ring of the same semi-major axis. It can be seen that the narrowest distribution D1 indeed has the largest number of particles on the Sun-side of the Earth, about 15 % more than the orbit average. But even the widest distribution still has 12 % more grains than average on the Sun-side of the Earth. The difference is because of the wider spread in the phase space as shown in Fig. 8.8 which is caused by larger deviations in grain size from the minimum grain size which has its equilibrium in the feeder orbit.

In-plane attenuation coefficient

Finally the in-plane number density is used to calculate the in-plane attenuation coefficient. Again, the coefficient is not an absolute value as it is independent of the total mass of material ejected and the extension of the ring out of the feeder orbit plane. This figure is then used to size the ring in a such a way as to cause a 1.7 % reduction in insolation and to assess the mass of material required to do so.

The in-plane number density, which is the probability of finding a grain in a given area of the orbital plane, can then be used to calculate Λ_0, the in-plane attenuation coefficient, using Eq. (8.13). The in-plane coefficient differs from the final value to be used as here the number density is in terms of area not volume and hence there is an intermediate step to calculate the true attenuation coefficient.

Figure 8.11 shows the in-plane attenuation coefficient relative to the maximum attenuation for the three different distributions. The maximum attenuation occurs predictably at the intersec-

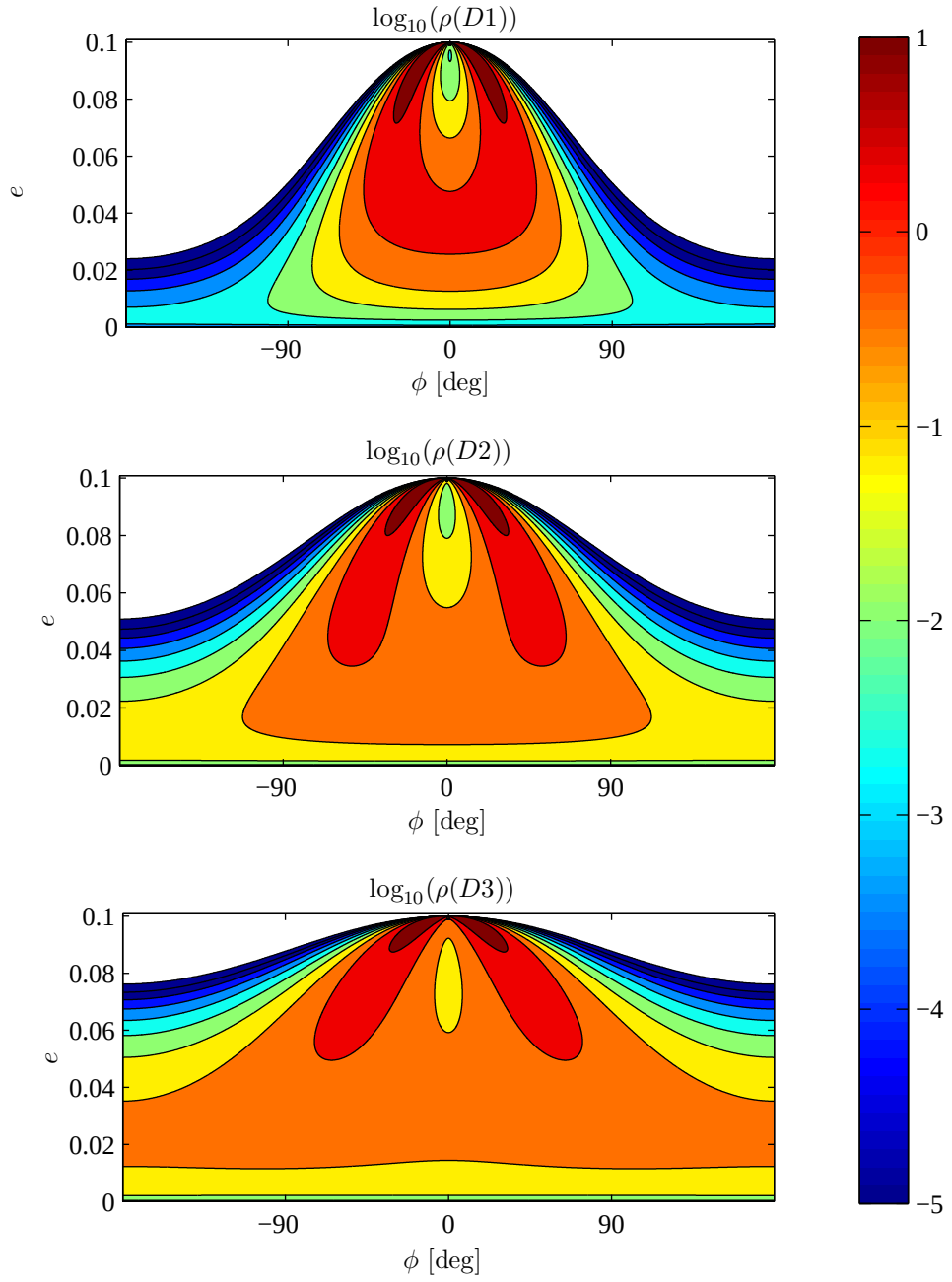

Figure 8.8: Global phase space density of dust grain orbits for the three different grain size distributions

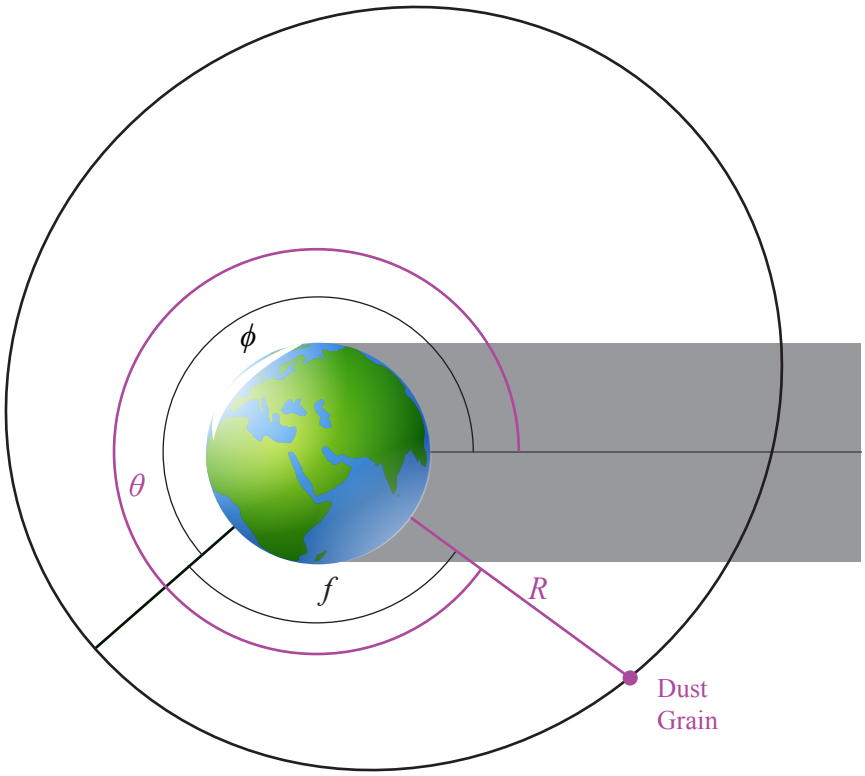

Figure 8.9: Polar coordinates in rotational reference frame defining position of a dust grain as (R, θ)

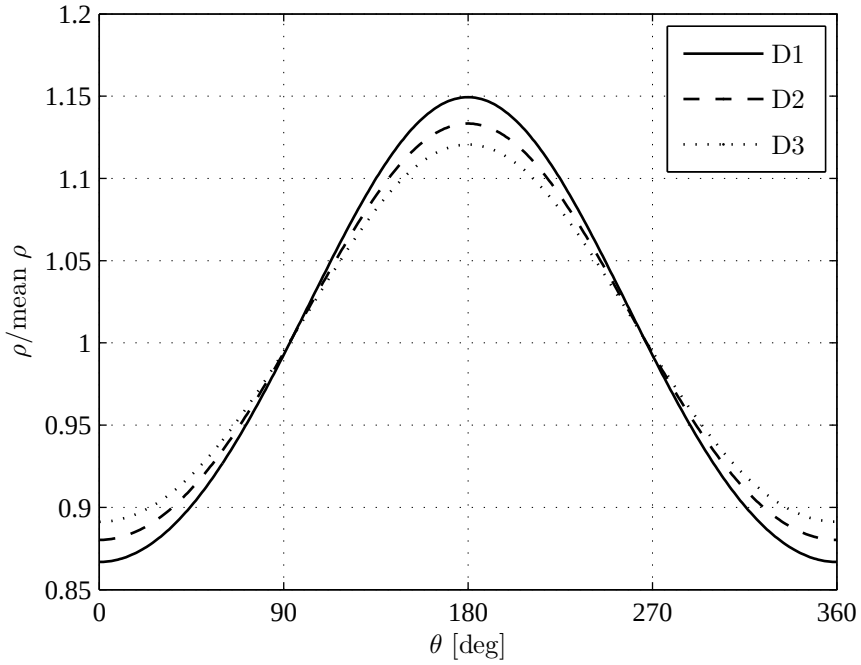

Figure 8.10: Deviation of the accumulated in-plane number density of dust grains from the orbit average for the three different distributions of grain radii

tion with the generator orbit at $\theta = \pi$ and $R = a_F(1 + e_F)$. The feeder orbit itself can also be seen in all three figures. Apart from the feeder orbit, a wider dust ring is discernible in all three figures with attenuation values of order 10 % of the maximum. The narrowest distribution D1 has the narrowest ring measuring approximately 600 km. The ring of the widest distribution D3 is about twice as wide at approximately 1200 km. Although distribution D1 is favourable because of its small average grain radius and its higher geometrical efficiency, D3 could have an advantage with the wider ring allowing the burden of the reduced insolation to be stretched over a larger area of the Earth, thus making the shadowing effect less pronounced.

An investigation into the 3D dynamics of the ring was conducted by Bewick et al. [75]. It was shown that the three-dimensional evolution of the dust closely follows the two-dimensional assessment presented in this Chapter. The maximum deviation of the inclination can be seen for the smallest dust grains and is less than $\pm 0.2°$.

With these results Bewick et al. [75] calculated the attenuation over the Earth's surface [75] for the different distributions and the amount of mass required to achieve the desired 1.7 % average reduction of incident Sunlight on the Earth. It was found that the total attenuation of the incident Sunlight on Earth varies over the time of one year, as can be seen in Fig. 8.12. It is lowest in spring and autumn, when the Sun is in the equatorial plane and the ring thus faces the Sun edge-on.

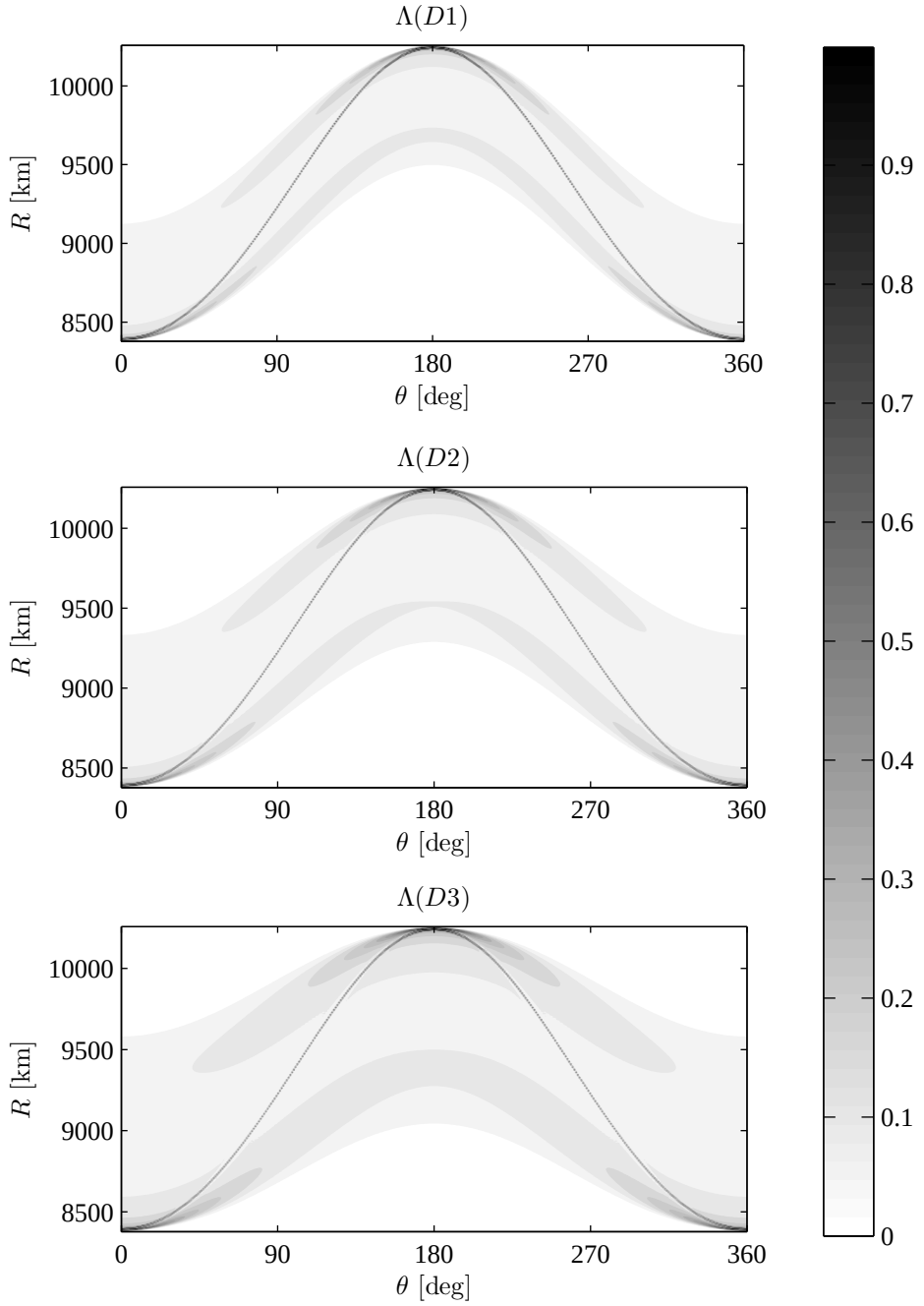

Figure 8.11: In-plane attenuation coefficient of the dust ring for the three different distributions of grain radii relative to the maximum attenuation

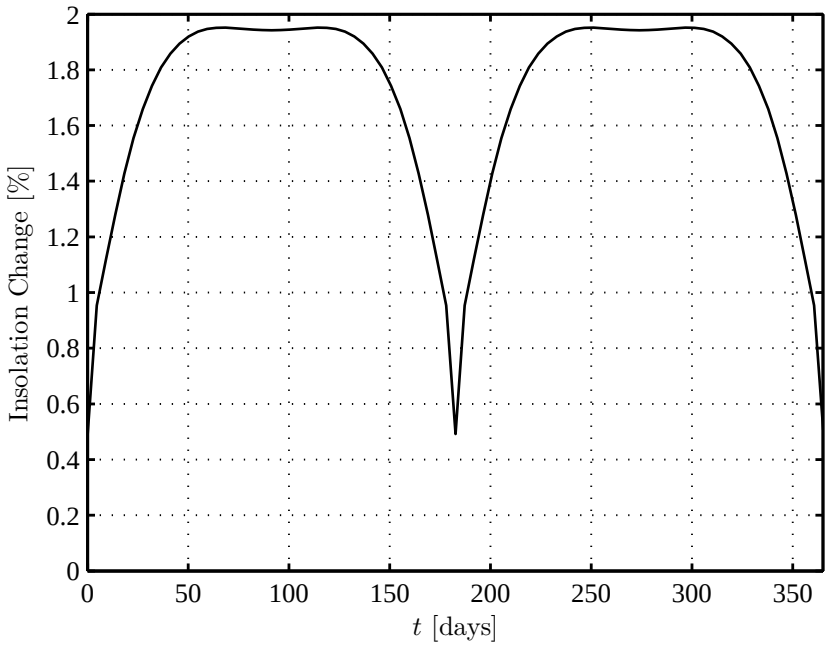

Figure 8.12: Average attenuation coefficient over time [75]

In this time only a small band at the equator is shadowed, while in summer and winter a larger portion of the winter hemisphere is shadowed.

The total mass for the different distributions was found to be 5.9×10^{11} kg (D1), 6.6×10^{11} kg (D2) and 9.1×10^{11} kg (D3). These values are lower the those estimated by Pearson et al. [76].

8.4 Conclusions

In this chapter the new concept of a *heliotropic* dust ring for climate engineering was introduced. The proposed method is to deploy and disperse asteroid dust in such a way that it blocks part of the Sunlight incident on Earth. The aim is to reduce the insolation by 1.7 % at as a low a total mass as possible.

The concept of a dust ring for geoengineering, which was first proposed by Pearson et al. [76], is enhanced by taking into account solar radiation pressure. Its effect on the orbital evolution and lifetime on dust particles is significant and increases with decreasing dust grain radius. In this chapter it was proposed to make use of this effect to create a new, stable Sun-pointing ring of dust. The orbital dynamics were investigated, a semi-major axis selected and from this an in-plane attenuation model calculated.

The results presented in this chapter were then used to find the required mass for such a dust ring depending on dust grain size distribution. The results were presented by Bewick et al. [75] and lie between 5.9×10^{11} kg and 9.1×10^{11} kg. This is less than the results obtained by Pearson but more than solar reflector methods proposed by McInnes [74] and Angel [79] among others.

Chapter 9

Conclusions

In this chapter an overview of the thesis is provided, the main results of which are summarised and commented and their limitations discussed. On the basis of the findings of this thesis, an outline of future work and some recommendations are given.

This thesis detailed novel orbital dynamics and applications for high area-to-mass-ratio spacecraft. To identify these applications a multi-step approach was used to model the underlying orbital dynamics. Each step increases the problem's complexity but reduces the size of the parameter space examined.

The first step in most of the applications is the analytical approach based on the Hamiltonian model of orbital dynamics due to solar radiation pressure and the J_2 effect, introduced by Hamilton and Krivov [7]. In this model a number of influences are neglected, most notably the orbit's inclination and all out-of-plane forces, but also the effect of eclipses. Hence, this model cannot accurately predict the orbital evolution but only grant an insight into the global behaviour. It is thus used to identify applications and analytically derive first guesses for the required area-to-mass-ratio and starting conditions or to formulate control laws.

In a second step semi-analytical equations are used to verify the new orbits and applications and to further investigate their behaviour. Two different models are used. One developed by Colombo and McInnes [103] expresses the in-plane secular change of Keplerian elements due to solar radiation pressure, the J_2 effect and aerodynamic drag while also taking account of the effect of eclipses. The other model developed by Krivov et al. [6] is formulated in non-singular elements and considers the effect of SRP and J_2 only on an inclined orbit, taking also into account the obliquity of the Earth's rotational axis with respect to the ecliptic.

The semi-analytical equations are computationally efficient to integrate as both neglect the periodic changes during the orbit evolution. This allows the investigation of a large parameter space to gain an overview of the evolution for different area-to-mass-ratios, starting orbits and starting dates depending on the application investigated. The equations were also used to enhance the effectiveness of the control algorithm for SpaceChips by accounting for the effect of eclipses on the orbital evolution.

Finally, applications are verified for a number of test case scenarios using a model with higher precision. For the small satellite applications, Analytical Graphics, Inc.'s high precision orbit propagator (HPOP) was used which takes into account a large number of orbital perturbations and also seasonal variations of the atmospheric density. For the SpaceChip application, a Gauss' equation model in Keplerian elements was used which was propagated in true anomaly in MATLAB. Finally, the planetary dust scenario is not validated in this way within the scope of the thesis, as only the initial analytical analysis is provided.

9.1 Summary of findings

In the following sections the different novel orbits and applications are discussed separately. For each application, the results presented in this thesis are summarised and evaluated and their implications on future space missions is discussed.

9.1.1 Passive orbit transfers for small satellites

Small satellites are spacecraft with masses of 1000 kg or less. Due to advances in miniaturisation and the commercialisation of space there has recently been a surge in small satellite activities. These systems have the advantage of being orders of magnitude lower cost and having significantly shorter development time than conventional spacecraft. They can usually be launched at low cost as a secondary payload with a larger satellite. However, they also have draw-backs. Apart from the limitations caused by lower power, restricted dimensions and satellite payload mass, they typically have limited influence over the orbit in which they are inserted as they have to accept orbit of the prime payload of the launcher. Furthermore, they often lack propulsion systems and cannot perform orbital manœuvres. This is due to their small size and simple design which are hard to combine with the complexity of an active propulsion subsystem. This is particularly the case for CubeSats which have a mass in the order of 1 kg to 10 kg.

The main orbital region of interest for CubeSat operators is low Earth orbit (LEO). This is due to several reasons. The limited power available for communications and the lack of high performance antennae require a short path length to the receiving ground station to transfer data at acceptable data rates. A further reason are the deorbiting requirements in LEO, which mean that small satellites are usually restricted to an altitude where orbit decay due to atmospheric drag can be guaranteed. In addition, the future growth of the CubeSat market is restricted by the number of launch opportunities to low LEO. Two solutions to this problem have been developed in this thesis. A passive GTO-to-LEO transfer has the potential to expand the piggy-back launch opportunities to include geostationary transfer launches. Furthermore, SRP-augmented deorbiting can expand the range of operational orbits for CubeSats to include higher altitudes. This because it offers a fail-safe deorbiting method for propellantless re-entry from orbits above the aerodynamic drag regime.

GTO to LEO transfer

In Chapter 3, the passive GTO-to-LEO transfer was discussed. The concept initially discussed by Colombo and McInnes [32] is to deploy a large light-weight structure in GTO to increase the spacecraft area-to-mass-ratio. The enhanced effect of aerodynamic drag will then cause the apogee to decrease, while solar radiation pressure is exploited to raise the perigee. When the desired quas-circular orbit in LEO is achieved, the device is ejected. The original work does not consider other orbit perturbations apart from solar radiation pressure, the J_2 effect and aerodynamic drag. It found that the manœuvre can only be successfully performed for a specific orientation of the orbit with respect to the Sun. This has the consequence that the spacecraft is forced to wait in GTO for up to 600 days until the correct orientation is reached.

In this thesis the concept was analysed in detail using a high performance orbit propagator including a full set of orbital perturbations. It was found that the the strongest secondary perturbation was the third body effect of the Sun. It causes the orbit eccentricity to librate during the waiting time in GTO. This means that the manœuvre success depends on the initial launch date. It was found that a lower perigee at the beginning of the manœuvre yields a higher final perigee altitude. This is due to the relative strength of the effects of drag and SRP. Colombo and McInnes [32] noted that the manœuvre is best performed for a reflectivity below 1, i.e. when the device is partially transparent. This is due to SRP affecting the spacecraft stronger than drag in the initial phase of the manœuvre, and causing the perigee altitude to rise to quickly.

In this thesis two different launch dates were considered: the 1$^{\text{st}}$ of October 2014 and the 1$^{\text{st}}$of January 2015. It was found that the transfer can be performed successfully for the October

launch, but is less effective for the January launch. For the October launch the waiting time and the orbit transfer were simulated in STK, with a final perigee altitude of approximately 330 km.

In the second part of the chapter design options for the deorbiting device and the orbit transfer module were discussed. The effect that different device shapes have on the coefficient of reflectivity were calculated. It was concluded that a spherical device was best suited to passive orbit transfers, as it has the same area-to-mass-ratio regardless of aspect angle. However, it requires more material than a flat sail of the same effective area-to-mass-ratio, due to the larger surface area and lower coefficient of reflectivity. Different methods of rigidisation were introduced and cold curing resin was chosen for the design. It has the advantage of a long shelf-life and offers reversable rigidisation which is advantageous for pre-flight testing. A thermal analysis of the heating process and a steady state thermal analysis of the deployed balloon were performed. It has been shown that a device capable of transporting a 3U CubeSat from GTO to LEO using the proposed method, can be accomodated in 1U volume of the CubeSat.

SRP-augmented deorbiting

In Chapters 4 and 5, a novel method for propellantless deorbit for small satellites was presented. SRP-augmented deorbiting is a type of area-to-mass-ratio augmented deorbiting that can be applied to high altitude missions. As opposed to drag-augmented deorbiting, it also uses the effect of solar radiation pressure to perform the re-entry. The manœuvre has two phases. In phase one, solar radaition pressure is exploited to increase the orbit eccentricity until the perigee is affected by drag. In phase two drag then rapidly reduces the orbit apogee until the spacecraft re-enters the Earth's atmosphere.

In Chapter 4, the method was initially developed analytically using equations derived from the Hamiltonian dynamics of the problem. An expression for the required area-to-mass-ratio to deorbit from any given altitude was found for planar orbits. This expression was then verified using a numerical propagator. Next, the required area-to-mass-ratio was calculated for inclined orbits in the three dimensional model of the orbital dynamics. It was found that in three dimensions the effectiveness of the method also depends on the right ascension of the ascending node and the initial time of the manœuvre. Regions of inclination and semi-major axis were identified in which the method is particularly effective. Three scenarios were devised and evaluated in STK to verify the numerical results.

In Chapter 5, deorbiting from high altitude Sun-synchronous orbits was investigated. The analytical model developed in the previous chapter was modified to take into account the orbital

dynamics of Sun-synchronous orbits. In the next step the orbits were investigated using a three dimensional numerical propagation. It was shown that the effectiveness of the deorbiting manœuvre depends on the local time of ascending node as well as on the orbit altitude. Noon/midnight orbits are more suitable for SRP-augmented deorbiting than terminator orbits, due to the orientation of the orbit plane with respect to the Sun.

It was shown that for a range of high altitude orbits SRP-augmented deorbiting is a viable option for end-of-life disposal. Due to the passive nature of the method it can be used as part of a fail-safe system which activates automatically when the spacecraft becomes unresponsive. However, it is not applicable to large spacecraft with mass above approximately 1 tonne, as the re-entry point is not controllable and spacecraft which have parts that can survive re-entry which could then pose a risk to human life should the satellite re-enter above populated areas.

9.1.2 Orbit control for SpaceChips

In Chapters 6 and 7, a new orbit control strategy for SpaceChips was developed. SpaceChips are millimetre-scale satellites on a silicon chip. Due to their small length-scale they have very high area-to-mass-ratios and are thus strongly affected by surface force perturbations. Furthermore, they lack the ability to accommodate traditional orbit control actuators which means they need to utilise natural forces to stabilise and control their orbits. The method proposed in this thesis is termed Electrochromic Orbit Control and works by fitting the SpaceChip with an electrochromic coating. These coatings have the ability to change their optical properties when a voltage or current is applied. This would allow them to modulate the solar radiation pressure perturbation on their orbit. In the method proposed in this thesis a SpaceChip has the ability to switch its coefficient of reflectivity between two discrete values, 'off' and 'on'.

In Chapter 6, the control potential of the method was analysed and an artificial potential field control algorithm presented which can be applied to orbit stabilisation and manœuvres. The control potential was assessed by evaluating the extremes of change for the individual in-plane orbital elements that can be achieved by changing the reflectivity twice per orbit. This was calculated for different orbits in the (e, ϕ) phase space, where e is the eccentricity and ϕ the Sun-perigee angle. The regions in which a zero change was possible were highlighted and combined for all three in-plane elements to identify the potentially stabilisable zone (PSZ). The PSZ is a rectangular region in the phase space centred around $\phi = 0$. It includes both natural equilibria in the Hamiltonian phase space for the two reflectivity values. Next, the artificial potential field controller was applied to stabilise the spacecraft within the PSZ. It was found that a region exists in which the SpaceChips can use electrochromic orbit control to maintain their orbits. The controller was then applied to

manœuvres in the (e, ϕ) phase space and for orbit raising. It was shown that a SpaceChip is able to perform the desired manœuvres in equatorial orbits using electrochromic orbit control.

In Chapter 7, a control algorithm based on the Hamiltonian orbital dynamics was developed. It is used to navigate SpaceChips to orbits with Sun-pointing apogee and stabilise them there. The model of the dynamics used by the control algorithm are based on the simplified in-plane dynamics, while the propagation was performed using the Gauss' equations in three dimensions. It was shown that the algorithm is able to compensate the difference in predicted and actual evolution in a closed-loop feedback control with an update time interval of one orbit. In order to further improve the performance of the controller the Hamiltonian phase space was linearised and adapted to account for the effect of eclipses. The advantage of this control algorithm is that it is closed to the actual orbit evolution. However, it requires a switch of reflectivity twice per orbit, whereas the pure Hamiltonian controller only needs to change approximately twice per year during orbit transfer.

Electrochromic orbit control is a promising method of performing orbit manœuvres with SpaceChips. However, there are a number of limitations. The control was analysed only for high altitude equatorial orbits. It cannot be applied in its current form to inclined orbits or orbits with lower semi-major axes. As semi-major axis decreases, the effect of J_2 increases, which was neglected in the design of the controller. Furthermore, there are a number of technical issues in practice which would need to be overcome. An electrochromic coating needs to be developed which offers a reflectivity change as large as possible and which is long-term resistant to radiation damage. A reliable passive Sun-pointing attitude control method needs to be developed. Some concepts for this are discussed in Sec. 1.3.2. A balance between power generation with solar cells and the electrochromic coating needs to be found. One possible solution would be to use an electrochromic coating which can switch between mirrored and transmissive, and layer it over the solar cells. That way, however, the SpaceChip generates energy only when in the 'off' state.

9.1.3 Climate engineering using dust grains

Finally, a geoengineering application of the Hamiltonian orbital dynamics is presented in Chapter 8. An artificial dust ring was proposed as a method of solar radiation management to combat climate change. The ring is designed to reduce the incident Sunlight on Earth to mitigate rising average temperatures on Earth. It is envisaged that the dust is extracted from an asteroid captured in an equatorial circular generator orbit. The dust is milled to a micrometre-scale grain size and then ejected into an eccentric feeder orbit with Sun-pointing apogee. The injection orbit is chosen such as to create an artificial ring, which is quasi-*heliotropic* through the effects of SRP and J_2. This way the average attenuation can be maximised. The work was conducted in collaboration

with other researchers. The contribution in this thesis is the development of the dispersal strategy, the novel *heliotropic* ring, and the computation of the in-plane density and attenuation coefficient.

First the generator and feeder orbits were chosen as a compromise between the minimum grain size and the geometric efficiency of a dust ring. The mass efficiency of the ring improves with decreasing grain size. However, the higher area-to-mass-ratio of smaller grains affects their orbital evolution. An area-to-mass-ratio which is too large leads to rapid orbit decay. After a mission scenario was selected the density of the ring was calculated for three log-normal grain size distributions. Initially the density in the (e, ϕ) phase space was calculated, and from this the in-plane attenuation coefficient was computed. Further analysis by Bewick et al. [75] yield a required mass of approximately 6×10^{11} kg for the finest grain size distribution. This value is better than the estimate by Pearson et al. [76].

One common concern about a dust ring strategy is that it will affect everyday space operations. It is feared that the dust could collide operational spacecraft and cause damage to these systems. However, the altitude of the ring is above the LEO regime. Should grains sink lower they will quickly deorbit due to their very high area-to-mass-ration.

9.2 Future Work

In this section a collection of ideas for future work is outlined, which will help to better understand the concepts and applications developed in this thesis.

GTO to LEO transfer

The next step for the GTO-to-LEO transfer is to analyse in detail the effect that launch date has on the mission success. The launch date affects the perigee altitude and solar activity at the start of manœuvre. As discussed earlier, the correct ratio of the effects of aerodynamic drag and solar radiation pressure is vital to the effectiveness of the manœuvre. Both perigee altitude and solar activity influence the effect of drag on the spacecraft orbit. An in-depth study into the applicability of the passive GTO-to-LEO transfer will be useful to future CubeSat mission designers.

SRP-augmented deorbiting

Solar radiation pressure augmented deorbiting is a type of area-to-mass-ratio augmentation. These deorbiting methods often draw criticism for the fact that a larger surface area sweeps out a greater volume of space and could thus have a larger on-orbit collision probability over its lifetime than the un-augmented spacecraft. This poses more questions: As area-to-mass-ratio increases, deorbit time decreases. Is there an optimum area-to-mass-ratio for a minimum collision probability? What is the optimum deorbiting time in this case and how does it change for different spacecraft masses and initial altitudes? A study into this topic is currently in progress. First results were presented in April 2013 [127].

Electrochromic orbit control

The next step in the development of electrochromic orbit control for SpaceChips is the extension to inclined and low altitude orbits. This is particularly relevant, as SpaceChips are mainly envisaged for LEO applications. One particularly exciting prospect form an astrodynamics perspective is the use of SpaceChips in orbit regimes in which a change of reflectivity causes a bifurcation of the phase space with the appearance of new equilibria due to J_2. One possible application would be the controlled dispersal of SpaceChips from a common injection orbit. While the SpaceChips' orbit evolves at regular time intervals, SpaceChips could change their reflectivity to enter different phase lines. This could provide a method of creating a network of dispersed SpaceChips without using several launches. Finally, SpaceChips could be used for solar system exploration. An analysis into the use of electrochromic control in Sun-centred orbits could yield new ways of interplanetary travel for high area-to-mass-ratio spacecraft.

Climate engineering using dust grains

The simulations performed for the dust ring application do not consider any perturbations apart from solar radiation pressure and the J_2 effect. Therefore the next step would be to analyse the long-term stability of the ring under the influence of other forces. In particular, it is assumed that the third body effect of the Sun will affect the orbit due to its quasi-Sun-synchronous orientation. Furthermore, the mass of this scheme could likely be further reduced by applying a global optimisation algorithm.

Bibliography

[1] Justin A. Atchison and Mason A. Peck. Length-scaling in spacecraft dynamics. *Journal of Guidance, Control, and Dynamics*, 34(1):231–246, 2011. doi: 10.2514/1.49383.

[2] Richard Greenberg and Andre Brahic. *Planetary Rings*. Space Science Series. University of Arizona Press, Tucson, 1984.

[3] Nikolai N. Gor'kavyi, Leonid M. Ozernoy, and John C. Mather. A new approach to dynamical evolution of interplanetary dust. *Astrophysical Journal*, 474(1):496–496, 1997. doi: 10.1086/303440.

[4] J. E. Howard, M. Horanyi, and G. R. Stewart. Global dynamics of charged dust particles in planetary magnetospheres. *Physical Review Letters*, 83(20):3993–3996, 1999. doi: 10.1103/PhysRevLett.83.3993.

[5] C. Grotta-Ragazzo, M. Kulesza, and P. A. S. Salomao. Equatorial dynamics of charged particles in planetary magnetospheres. *Physica D: Nonlinear Phenomena*, 225(2):169–183, 2007. doi: 10.1016/j.physd.2006.10.009.

[6] Alexander V. Krivov, Leonid L. Sokolov, and Valeri V. Dikarev. Dynamics of Mars-orbiting dust: Effects of light pressure and planetary oblateness. *Celestial Mechanics and Dynamical Astronomy*, 63(3):313–339, 1995. doi: 10.1007/bf00692293.

[7] Douglas P. Hamilton and Alexander V. Krivov. Circumplanetary dust dynamics: effects of solar gravity, radiation pressure, planetary oblateness, and electromagnetism. *Icarus*, 123(2): 503–523, 1996. doi: 10.1006/icar.1996.0175.

[8] Alexander V. Krivov and Juan Getino. Orbital evolution of high-altitude balloon satellites. *Astronomy and Astrophysics*, 318:308–314, 1997.

[9] William C. Jakes. Project Echo. Technical report, 1961. Bell Laboratories Record 19620022405.

[10] Irwin I. Shapiro and Harrison M. Jones. Perturbations of the orbit of the Echo balloon. *Science*, 132(3438):1484–1486, 1960. doi: 10.1126/science.132.3438.1484.

[11] A. C. B. Lovell and M. Ryle. West Ford Project, Interference to Astronomy from Belts of Orbiting Dipoles (Needles). *Quarterly Journal of the Royal Astronomical Society*, 3:100 – 108, 1962.

[12] Irwin I. Shapiro, Harrison M. Jones, and C. W. Perkins. Orbital properties of the West Ford dipole belt. In *IEEE*, volume 52, pages 469–518, 1964.

[13] Bendisch J. Krag H. Wegener P. Wiedemann, C. and D. Rex. Modeling of copper needle clusters from the West Ford Dipole experiments. In *3rd Third European Conference on Space Debris*, pages 315 – 320, 2001.

[14] Colin R. McInnes. *Solar sailing: technology, dynamics and mission applications*. Springer Praxis Books. Springer-Verlag, New York, 1st edition.

[15] National Aeronautics and Space Administration. National Space Science Data Centre, ID: 1957-001B (Sputnik-1), 2013. URL: http://nssdc.gsfc.nasa.gov/nmc/. Last accessed: 25/02/2013.

[16] Jasper Bouwmeester and Jian Guo. Survey of worldwide pico- and nanosatellite missions, distributions and subsystem technology. *Acta Astronautica*, 67(7-8):854–862, 2010. doi: 10.1016/j.actaastro.2010.06.004.

[17] Herbert J. Kramer and Arthur P. Cracknell. An overview of small satellites in remote sensing. *International Journal of Remote Sensing*, 29(15):4285–4337, 2008. doi: 10.1080/01431160801914952.

[18] Hans Dodel and Dieter Häupler. *Galileo*. Springer, Berlin/Heidelberg, Germany, 2010. doi: 10.1007/978-3-540-79444-8_10.

[19] G.D. Racca, A Marini, L Stagnaro, J van Dooren, L di Napoli, B.H Foing, R Lumb, J Volp, J Brinkmann, R Grnagel, D Estublier, E Tremolizzo, M McKay, O Camino, J Schoemaekers, M Hechler, M Khan, P Rathsman, G Andersson, K Anflo, S Berge, P Bodin, A Edfors, A Hussain, J Kugelberg, N Larsson, B Ljung, L Meijer, A Mörtsell, T Nordebäck, S Persson, and F Sjöberg. SMART-1 mission description and development status. *Planetary and Space Science*, 50(14-15):1323–1337, 2002. doi: 10.1016/S0032-0633(02)00123-X.

[20] Hank Heidt, Jordi Puig-Suari, Augustus S. Moore, Shinichi Nakasuka, and Robert J. Twiggs. CubeSat: A new generation of picosatellite for education and industry low-cost space experimentation. In *14th Annual AIAA/USU Conference on Small Satellites*, Logan (UT), USA, August .

[21] Armen Toorian, Emily Blundell, and Robert Puig Suari, Jordiand Twiggs. CubeSats as responsive satellites. In *3rd AIAA Responsive Space Conference*, Los Angeles (CA), USA, 2005.

[22] Craig Clark and Steven Greenland. UKube-1: The first TechDemoCube multi-payload nanosatellite. In *20th ESA/CNES 4S Symposium*, Portorož, Slovenia, 5 June 2012.

[23] David J. Barnhart, Tanya Vladimirova, and Martin N. Sweeting. Satellite-on-a-chip: a feasibility study. In *5th Round Table on Micro/Nano Technologies for Space*, Noordwijk, The Netherlands, 2005.

[24] Justin A. Atchison, Zachary R. Manchester, and Mason Peck. Microscale atmospheric reentry sensors. 7th International Planetary Probe Workshop (IPPW), Barcelona, Spain, 14-18 June 2007.

[25] Chris Verhoeven, Bert Monna, Steven Engelen, Arash Noroozi, Prem Sundaramoorthy, Mark Bentum, and Robert J. Meijer. Emerging eco-system: nano-satellite swarms and large satellites. In *62nd International Astronautical Congress*, Cape Town, South Africa, 2011. IAC-11-A6.4.

[26] Frank te Hennepe, R. Rinaldo, A. Ginesi, Carsten Tobehn, M. Wieser, Ø. Olsen, Ø. Helleren, R. Challamel, and F. Storesund. Space-based detection of AIS signals: Results of a feasibility study into an operational space-based AIS system. In *Advanced satellite multimedia systems conference (ASMA) and the 11th signal processing for space communications workshop (SPSC)*, pages 17 –24, September 2010. doi: 10.1109/ASMS-SPSC.2010.5586862.

[27] Angel Borja and Dionisio Tun. Deorbit process using solar radiation force. *Journal of Spacecraft and Rockets*, 43:685–687, 2006. doi: 10.2514/1.9508.

[28] Daniel Oltrogge and Kyle Leveque. An evaluation of CubeSat orbital decay. In *25th AIAA/USU Conference on Small Satellites*, Logan, Utah, USA, 8-12 August 2011. SSC11-VII-2.

[29] Skrobot Garrett. ELaNa Educational Launch of Nanosatellite enhance education through space flight. In *25th AIAA/USU Conference on Small Satellites*, Logan, Utah, USA, 8-12 August 2011. SSC11-II-2.

[30] Richard Fleeter, Daviel B. DeBra, Paul Gloyer, Zeno Wahl, and Goldstein. Aerobraking orbit transfer vehicle. US Patent No. 6,550,720 B2, 22 April 2003.

[31] Juergen Mueller, Richard Hofer, and John Ziemer. Survey of propulsion technologies applicable to CubeSats. Technical report, NASA Technical Report, 3 May 2010.

[32] Camilla Colombo and Colin R. McInnes. Propellant-free GTO to LEO transfers. In *Desktop Delta V Workshop*, Providence, RI, USA, 17 February 2011.

[33] Donald J. Kessler and Burton G. Cour-Palais. Collision frequency of artificial satellites: The creation of a debris belt. *Journal of Geophysical Research*, 83(A6):2637–2646, 1978. doi: 10.1029/JA083iA06p02637.

[34] IADC. IADC Space Debris Mitigation Guidelines. Technical report, 15 October 2002.

[35] ISO. Space systems – space debris mitigation requirements. ISO 24113:2010, International Organization for Standardization, Geneva, Switzerland, 2010.

[36] Holger Burkhardt, Martin Sippel, Gerhard Krülle, Ralf Janovsky, Martin Kassebom, Hendrik Lübberstedt, Oliver Romberg, and Ben Fritsche. Evaluation of propulsion systems for satellites end-of-life de-orbiting. In *38th AIAA/ASME/SAE/ASEE Joint Propulsion Conference & Exhibit*, Indianapolis, USA, 2002. AIAA. AIAA-2002-4208.

[37] Rolf Janovsky, M. Kasseborn, H. Lübberstedt, O. Romberg, H. Burkhardt, and M. Sippel. End-of-life de-orbiting strategies for satellites. In *Deutscher Luft-und Raumfahrtkongress*, 2002. DGLR-JT-2002-028.

[38] Vaios Lappas, Nasir Adeli, Lourens Visagie, Juan Fernandez, Theodoros Theodorou, Willem Steyn, and Matthew Perren. CubeSail: A low cost CubeSat based solar sail demonstration mission. *Advances in Space Research*, 48(11):1890–1901, 2011. doi: 10.1016/j.asr.2011.05.033.

[39] Clyde Space Ltd. AEOLDOS: Aerodynamic end-of-life deorbit system. Technical report, 2012. URL: http://www.clyde-space.com. Last accessed: 02.12.2012.

[40] Peter C. E. Roberts and Patrick G. Harkness. Drag sail for end-of-life disposal from low Earth orbit. *Journal of Spacecraft and Rockets*, 44(6):9, 2007. doi: 10.2514/1.28626.

[41] Daan C. Maessen, Eddie D. van Breukelen, Barry T.C. Zandbergen, and Otto K. Bergsma. Development of a generic inflatable de-orbit device for CubeSats. In *International Astronautical Congress*, 24-28 September 2007. IAC-07-A6.3.6.

[42] Kerry T. Nock, Kristin L. Gates, Kim M. Aaron, and Angus D. McRonald. Gossamer Orbit Lowering Device (GOLD) for safe and efficient de-orbit. In *AIAA Astrodynamics Specialists Conference*, Toronta, Canada, 2-5 August 2010. AIAA-2010-7824.

[43] Jason Andrews, Krissa Watry, and Kevin Brown. Nanosat deorbit and recovery system to enable new missions. In *25th Annual AIAA/USU Conference on Small Satellites*, Logan, Utah, USA, 2011. SSC11-X-3.

[44] Luciano Iess, C. Claudio Bruno, Carlo Ulivieri, U. Ponzi, M. Parisse, G. Laneve, G. Vannaroni, M. Dobrowolny, F. De Venuto, B. Bertotti, and L. Anselmo. Satellite de-orbiting by means of electrodynamic tethers - Part I: General concepts and requirements. *Acta Astronautica*, 50(Compendex):399–406, 2002. doi: 10.1016/S0094-5765(01)00180-1.

[45] Luciano Iess, C. Claudio Bruno, Carlo Ulivieri, and G. Vannaroni. Satellite de-orbiting by means of electrodynamic tethers - Part II: System configuration and performance. *Acta Astronautica*, 50(Compendex):407–416, 2002. doi: 10.1016/S0094-5765(01)00181-3.

[46] Carmen Pardini, Toshiya Hanada, and Paula H. Krisko. Benefits and risks of using electrodynamic tethers to de-orbit spacecraft. In *57th International Astronautical Congress*, 2006. IAC-06-B6.2.10.

[47] Robert P. Hoyt, Ian M. Barnes, Nestor R. Voronka, and Jeffrey T. Slostad. The Terminator Tape: a cost-effective de-orbit module for end-of-life disposal of LEO satellites. In *AIAA Space Conference and Exposition*, Pasadena, CA, United states, 2009. American Institute of Aeronautics and Astronautics Inc.

[48] Center for Space Standards and Innovation (CSSI). CelesTrak, 2012. URL: http://www.celestrak.com/. Last accessed: 13/01/2013.

[49] P. Daly. Navstar GPS and GLONASS: global satellite navigation systems. *Electronics Communication Engineering Journal*, 5(6):349–357, 1993.

[50] B.W. Parkinson and S.W. Gilbert. NAVSTAR: Global positioning system – ten years later. *Proceedings of the IEEE*, 71(10):1177–1186, 1983. doi: 10.1109/PROC.1983.12745.

[51] P. Jain. Architectural trends in military satellite communications systems. *Proceedings of the IEEE*, 78(7):1176–1189, 1990. doi: 10.1109/5.56931.

[52] Pavel Podvig. History and the current status of the russian early-warning system. *Science and Global Security*, 10:21:60, 2002. doi: 10.1080/08929880290008395.

[53] David A. Vallado. *Fundamentals of astrodynamics and applications*. Space Technology Library, City, third edition edition, 2007.

[54] Brett A. Warneke, Matt Last, Brian Liebowitz, and Kristofer S. J. Pister. *Smart Dust*: communicating with a cubic-millimeter computer. *Computer*, 34(1):44–51, 2001. doi: 10.1109/2.963443.

[55] Brett A. Warneke and Kristofer S. J. Pister. MEMS for distributed wireless sensor networks. In *9th International Conference on Electronics, Circuits and Systems*, volume 1, pages 291–294, 2002.

[56] Michael J. Sailor and Jamie R. Link. *Smart dust*: nanostructured devices in a grain of sand. *Chemical Communications*, (11):1375–1383, 2005. doi: 10.1039/b417554a.

[57] David J. Barnhart, Tanya Vladimirova, and Martin N. Sweeting. Very-small-satellite design for distributed space missions. *Journal of Spacecraft and Rockets*, 44(6):1294–1306, 2007. doi: 10.2514/1.28678.

[58] David J. Barnhart, Tanya Vladimirova, Adam M. Baker, and Martin N. Sweeting. A low-cost femtosatellite to enable distributed space missions. *Acta Astronautica*, 64(11-12):1123–1143, 2009. doi: 10.1016/j.actaastro.2009.01.025.

[59] Mason A. Peck. A vision for milligram-scale spacecraft. In *ChipSat - Space Horizons Workshop*, Providence, RI, USA, 18$^{\text{th}}$ February 2010.

[60] Justin A. Atchison and Mason Peck. A millimeter-scale Lorentz-propelled spacecraft. AIAA Guidance, Navigation, and Control Conference, pages 5041–5063, Hilton Head, SC, United states, 2007.

[61] Justin A. Atchison and Mason A. Peck. A passive, Sun-pointing, millimeter-scale solar sail. *Acta Astronautica*, 67(1-2):108–121, 2009. doi: 10.1016/j.actaastro.2009.12.008.

[62] Brett Streetman and Mason A. Peck. General bangbang control method for Lorentz augmented orbits. *AIAA Journal of Spacecraft and Rockets*, 47(3):484–492, 2010. doi: 10.2514/1.45704.

[63] Iverson Bell, Brian Gilchrist, Sven Bilen, Robert P. Hoyt, Nestor A. Voronka, and Mason A. Peck. Enabling Ultra-small Sensor Spacecraft for the Space Environment using Small-Scale Electrodynamic Tethers. In *AIAA SPACE Conference & Exposition*, Long Beach, CA, USA, 2011. AIAA 2011-7322.

[64] Iverson Bell, Brian Gilchrist, Sven Bilen, and Jesse McTernan. Investigating the use of miniaturized electrodynamic tethers to enhance the capabilities of femtosatellites and other ultra-small satellites. In *26th AIAA Conference on Small Satellites*, Logan UT, USA, 2012. SSC12-X-6.

[65] Hanspeter Schaub, Gordon G. Parker, and Lyon B. King. Challenges and prospects of Coulomb spacecraft formation control. *AAS Journal of the Astronautical Sciences*, 52(1-2): 169–193, 2004.

[66] Junichiro Kawaguchi, Yuya Mimasu, Osamu Mori, Ryu Funase, Takayuki Yamamoto, and Yuichi Tsuda. IKAROS - Ready for lift-off as the world's first solar sail demonstration in interplanetary space. In *60th International Astronautical Congress*, Daejeon, Korea, 2009. IAC-09-D1.1.3.

[67] Hulya Demiryont and David Moorehead. Electrochromic emissivity modulator for spacecraft thermal management. *Solar Energy Materials and Solar Cells*, 93(12):2075–2078, 2009. doi: 10.1016/j.solmat.2009.02.025.

[68] Maria de Juan Ovelar, Jose Llorens Montolio, Chit Hong Yam, and Dario Izzo. Transport of nanoparticles in the interplanetary medium. In *60th International Astronautical Congress*, Daejeon, Republic of Korea, 12-16 October 2009.

[69] John Cook, Dana Nuccitelli, Sarah A Green, Mark Richardson, Bärbel Winkler, Rob Painting, Robert Way, Peter Jacobs, and Andrew Skuce. Quantifying the consensus on anthropogenic global warming in the scientific literature. *Environmental Research Letters*, 8(2), 2013.

[70] Intergovernmental Panel on Climate Change (IPCC). Contribution of working groups I, II and III to the fourth assessment report. Technical report, Core Writing Team, Pachauri, R.K. and Reisinger, A. (Eds.), IPCC, Geneva, Switzerland. pp 104, 2007.

[71] John Shepherd, Ken Caldeira, Peter Cox, and Joanna Haigh. Geoengineering the climate. *Report of Royal Society working group of geo-engineering*, 2009.

[72] Hashem Akbari, Surabi Menon, and Arthur Rosenfeld. Global cooling: increasing world-wide urban Albedos to offset CO_2. *Climatic Change*, 94:275–286, 2009. doi: 10.1007/s10584-008-9515-9.

[73] Philip J. Rasch, John Latham, and Chih-Chieh Chen. Geoengineering by cloud seeding: influence on sea ice and climate system. *Environmental Research Letters*, 4(4), 2009. doi: 10.1088/1748-9326/4/4/045112.

[74] Colin R. McInnes. Space-based geoengineering: challenges and requirements. *Proceedings of the Institution of Mechanical Engineers, Part C: Journal of Mechanical Engineering Science*, 224(3):571–580, 2010.

[75] Russell Bewick, Charlotte Lücking, Camilla Colombo, Joan-Pau Sanchez, and Colin R. McInnes. Heliotropic dust rings for Earth climate engineering. *Advances in Space Research*, 51(7):1132–1144, 2013. doi: 10.1016/j.asr.2012.10.024.

[76] Jerome Pearson, John Oldson, and Eugene Levin. Earth rings for planetary environment control. *Acta Astronautica*, 58(1):44–57, 2006. doi: 10.1016/j.actaastro.2005.03.071.

[77] Curtis Struck. The feasibility of shading the greenhouse with dust clouds at the stable lunar Lagrange points. *Journal of the British Interplanetary Society*, 60(3):82–89, 2007.

[78] Colin R. McInnes. Minimum mass solar shield for terrestrial climate control. *Journal of the British Interplanetary Society*, 55(9-10):307–311, 2002.

[79] Roger Angel. Feasibility of cooling the Earth with a cloud of small spacecraft near the inner Lagrange point (L_1). *Proceedings of the National Academy of Sciences*, 103(46):17184–17189, 2006. doi: 10.1073/pnas.0608163103.

[80] Russell Bewick, Joan-Pau Sanchez, and Colin R. McInnes. The feasibility of using an L_1 positioned dust cloud as a method of space-based geoengineering. *Advances in Space Research*, 49(7):1212–1228, 2012. doi: 10.1016/j.asr.2012.01.010.

[81] John R. Olds, A.C. Charania, and Mark G. Schaffer. Multiple mass drivers as an option for asteroid deflection missions. In *Planetary Defense Conference*, Washington, DC, USA, March 2007.

[82] Alison Gibbings, J.M. Hopkins, D. Burns, M. Vasile, and I. Watson. On testing laser ablation processes for asteroid deflection. In *IAA Planetary Deference Conference*, 2011.

[83] Massimiliano Vasile, Christie Maddock, and C. Saunders. Orbital debris removal with solar concentrators. In *61st International Astronautical Congress*, Prague, Czech Republic, 2010. IAC-10-A6.4.

[84] Camilla Colombo, Charlotte Lücking, and Colin R. McInnes. Orbital dynamics of high area-to-mass-ratio spacecraft with J_2 and solar radiation pressure for novel Earth observation and communication services. *Acta Astronautica*, 81(1):137–150, 2012. doi: 10.1016/j.actaastro.2012.07.009.

[85] Colin R. McInnes, Matteo Ceriotti, Camilla Colombo, Joan-Pau Sanchez, Russell Bewick, Jeannette Heiligers, and Charlotte Lücking. Micro-to-macro: Astrodynamics at extremes of length-scale. *Acta Futura*, 4:81–97, 2011. doi: 10.2420/AF04.2011.81.

[86] Charlotte Lücking, Camilla Colombo, and Colin R. McInnes. A passive satellite deorbiting strategy for medium Earth orbits using solar radiation pressure and the J_2 effect. *Acta Astronautica*, 77(1):197–206, 2012. doi: 10.1016/j.actaastro.2012.03.026.

[87] Charlotte Lücking, Camilla Colombo, and Colin R. McInnes. Electrochromic orbit control for SpaceChip swarms. *AIAA Journal of Guidance, Control and Dynamics*, 35(5):1548–1558, 2012. doi: 10.2514/1.55488.

[88] Camilla Colombo, Charlotte Lücking, and Colin R. McInnes. Orbit evolution, maintenance and disposal of SpaceChip swarms through electrochromic control. *Acta Astronautica*, 82(1): 25–37, 2012. doi: 10.1016/j.actaastro.2012.05.035.

[89] Charlotte Lücking, Camilla Colombo, and Colin R. McInnes. Solar radiation pressure augmented deorbiting: Passive end-of-life disposal from high altitude orbits. *AIAA Journal of Spacecraft and Rockets*, in press, 2013. doi: 10.2514/1.A32478.

[90] Charlotte Lücking, Camilla Colombo, and Colin R. McInnes. Orbit control of high area-to-mass-ratio spacecraft using electrochromic coating. In *61st International Astronautical Congress*, Prague, Czech Republic, 2010. IAF. IAC10-C1.2.7.

[91] Camilla Colombo, Charlotte Lücking, and Colin R. McInnes. Orbit evolution, maintenance and disposal of SpaceChip swarms. In *6th International Workshop on Satellite Constellation and Formation Flying (IWSCFF 2010)*, Taipei, Taiwan, 1-3 November 2010. IWSCFF-Paper-2010-2-2.

[92] Charlotte Lücking, Camilla Colombo, and Colin R. McInnes. A passive de-orbiting strategy for high altitude CubeSat missions using a deployable reflective balloon. In *8th IAA Symposium on Small Satellites for Earth Observation*, Berlin, Germany, 4-8 April 2011. IAA-B8-0504.

[93] Charlotte Lücking. A passive high altitude deorbiting strategy. In *25th AIAA/USU Conference on Small Satellites*, Logan, Utah, USA, 8-12 August 2011. SSC11-VIII-6.

[94] Charlotte Lücking, Camilla Colombo, and Colin R. McInnes. A passive satellite deorbiting strategy for MEO using solar radiation pressure and the J_2 effect. In *62nd International Astronautical Congress*, Cape Town, South Africa, 2011. IAC-11-A6.4.6.

[95] Russell Bewick, Charlotte Lücking, Camilla Colombo, Joan-Pau Sanchez, and Colin R. McInnes. Geo-engineering using dust grains in heliotropic elliptical orbits. In *62nd International Astronautical Congress*, Cape Town, South Africa, 2011. IAC-11-D1.1.9.

[96] Camilla Colombo, Charlotte Lücking, and Colin R. McInnes. Orbital dynamics of high area-to-mass-ratio spacecraft under the influence of J_2 and solar radiation pressure. In *62nd International Astronautical Congress*, Cape Town, 3-7 October 2011. IAC-11-C1.4.8.

[97] Charlotte Lücking, Camilla Colombo, and Colin R. McInnes. Solar radiation pressure augmented deorbiting from high altitude sun-synchronous orbits. In *4S Symposium*, Portorož, Slovenia, 4 June 2012. ESA/CNES.

[98] Charlotte Lücking, Camilla Colombo, and Colin R. McInnes. Mission and system design of a 3U CubeSat for passive GTO to LEO transfer. In *63rd International Astronautical Congress*, Naples, Italy, 1-5 October 2012. IAF. IAC-12-E2.1.4.

[99] Luciano Anselmo and Carmen Pardini. Long-term dynamical evolution of high area-to-mass ratio debris released into high earth orbits. *Acta Astronautica*, 67(1-2):204–216, 2010. doi: 10.1016/j.actaastro.2009.10.017.

[100] Colin R. McInnes, Malcolm Macdonald, Vassilis Angelopolous, and David Alexander. GEOSAIL: Exploring the geomagnetic tail using a small solar sail. *Journal of Spacecraft and Rockets*, 38(4):622–629, 2001. doi: 10.2514/2.3727.

[101] Teppei Oyama, Hiroshi Yamakawa, and Yoshiharu Omura. Orbital dynamics of solar sails for geomagnetic tail exploration. *Journal of Guidance, Control and Dynamics*, 45(2):316–323, 2008. doi: 10.2514/1.31274.

[102] Yuri Kuznetskov. *Elements of applied bifurcation theory*, volume 112 of *Applied mathematical sciences*. Springer-Verlag, New York.

[103] Camilla Colombo and Colin R. McInnes. Orbital dynamics of *Smart Dust* devices with solar radiation pressure and drag. *Journal of Guidance, Control and Dynamics*, 34(6):1613–1631, 2011. doi: 10.2514/1.52140.

[104] Desmond King-Hele. *Theory of satellite orbits in an atmosphere*. Butterworths, London, 1964.

[105] Analytical Graphics, Inc. STK High-Precision Orbit Propagator (HPOP), 2012. URL: www.stk.com/resources/help/online/stk/source/hpop/hpop.htm. Last accessed: 17/01/2013.

[106] Erwin Fehlberg. Klassische Runge-Kutta-Formeln vierter und niedrigerer Ordnung mit Schrittweiten-Kontrolle und ihre Anwendung auf Wärmeleitungsprobleme. *Computing*, 6 (1-2):61–71, 1970. doi: 10.1007/BF02241732.

[107] Charles E. Roberts, Jr. An analytic model for upper atmosphere densities based upon Jacchia's 1970 models. *Celestial Mechanics*, 4(3-4):368–377, 1971. doi: 10.1007/BF01231398.

[108] European Space Agency. The Space Environment Information System, 2013. URL: http://www.spenvis.oma.be/. Last accessed: 17/01/2013.

[109] James R. Wertz and Wiley J. Larson. *Space Mission Analysis and Design*. Microcosm Press and Kluwer Academic Publisher, El Segundo, Dordrecht, 3^{rd} edition, 1999.

[110] Ruaridh Clark. Residual air inflated system for passive deorbiting of CubeSats. MEng Aero-Mechanical Engineering Thesis, University of Strathclyde, 2012. Glasgow, UK.

[111] Roy M. Young and Charles L. Adams. TRL assessment of solar sail technology development following the 20 meter system ground demonstrator hardware testing. In *Proc. of the 2^{nd} International Symposium on Solar Sailing*, New York, USA, 20-22 July 2010.

[112] Marco C. A. M. Van Der List, L. D. Van Vliet, H. M. Sanders, P. Van Put, and J. W. E. C. Elst. Applications for solid propellant cool gas generator technology. In *4^{th} International Spacecraft Propulsion Conference*, European Space Agency, (Special Publication) ESA SP, pages 897–904, Sardinia, Italy, 2004. European Space Agency.

[113] Dave P. Cadogan and Stephen E. Scarborough. Rigidizable materials for use in gossamer space inflatable structures. In *42^{nd} AIAA Structures, Structural Dynamics, and Materials Conference*, 2001. AIAA-2001-1417.

[114] Brigitte Defoort, Vincent Peypoudat, Marco C. Bernasconi, K. Chuda, and Xavier Coqueret. *Recent Advances in the Rigidization of Gossamer Structures*, volume 3 of *Computational Methods in Applied Sciences*, pages 259–283. Springer, Netherlands, 2005.

[115] Philipp Reiß. Development and implementation of new methodologies for the thermal analysis of CubeSats. MSc Aerospace Engineering Thesis, Technische Universitt Mnchen, 2012.

[116] David G. Gilmore. *Spacecraft Thermal Control Handbook, Vol. 1.* American Institute of Aeronautics and Astronautics/Aerospace Press, 2002.

[117] ITP Engines. ESATAN Thermal Modelling Suite, 2012. URL: www.esatan-tms.com/. Last accessed: 17/01/2013.

[118] Hugh G. Lewis, Adam E. White, Richard Crowther, and Hedley Stokes. Synergy of debris mitigation and removal. *Acta Astronautica*, 81(1):62–68, 2012. doi: 10.1016/j.actaastro.2012.06.012.

[119] Peter Fortescue, John Stark, and Graham Swinerd. *Spacecraft System Engineering.* Wiley, Chichester, 3^{rd} edition, 2003.

[120] Claes-Göran Granqvist, Esterban Avendaño, and Andris Azens. Electrochromic coatings and devices: survey of some recent advances. In 4^{th} *International Conference on Coating*, volume 442 of *Thin Solid Films*, pages 201–211, Braunschweig, Germany, 2002. Elsevier.

[121] Andrew C. King, John Billingham, and Steven R. Otto. *Differential Equations: linear, nonlinear, ordinary, partial.* Cambridge University Press, 2003.

[122] Joan-Pau Sanchez and Colin R. McInnes. Asteroid resource map for near-Earth space. *Journal of Spacecraft and Rockets*, 48(1):153–165, 2011.

[123] Martin Wilck and Ingrid Mann. Radiation pressure forces on "typical" interplanetary dust grains. *Planetary and Space Science*, 44(5):493–499, 1996.

[124] Ashok Baria, Nikunjana Patel, and Rakesh Patel. An overview of size reduction technologies in the field of pharmaceutical manufacturing. *Asian Journal of Pharmaceutics*, 2(4):216–220, 2008. doi:10.4103/0973-8398.45033.

[125] Bala Govindasamy and Ken Caldeira. Geoengineering Earth's radiation balance to mitigate CO_2-induced climate change. *Geophysical Research Letters*, 27(14):2141–2144, 2000.

[126] J.C. Kotz, P.M. Treichel, and J.R. Townsend. *Chemistry and Chemical Reactivity.* Brooks Cole Publishing Company, 2011.

[127] Charlotte Lücking, Camilla Colombo, Colin R. McInnes, and Hugh Lewis. Collision probability of satellite re-entry with area-to-mass-ratio augmentation. In 9^{th} *IAA Symposium on Small Satellites for Earth Observation*, Berlin, Germany, 8-12 April 2013. IAA-B9-0504.